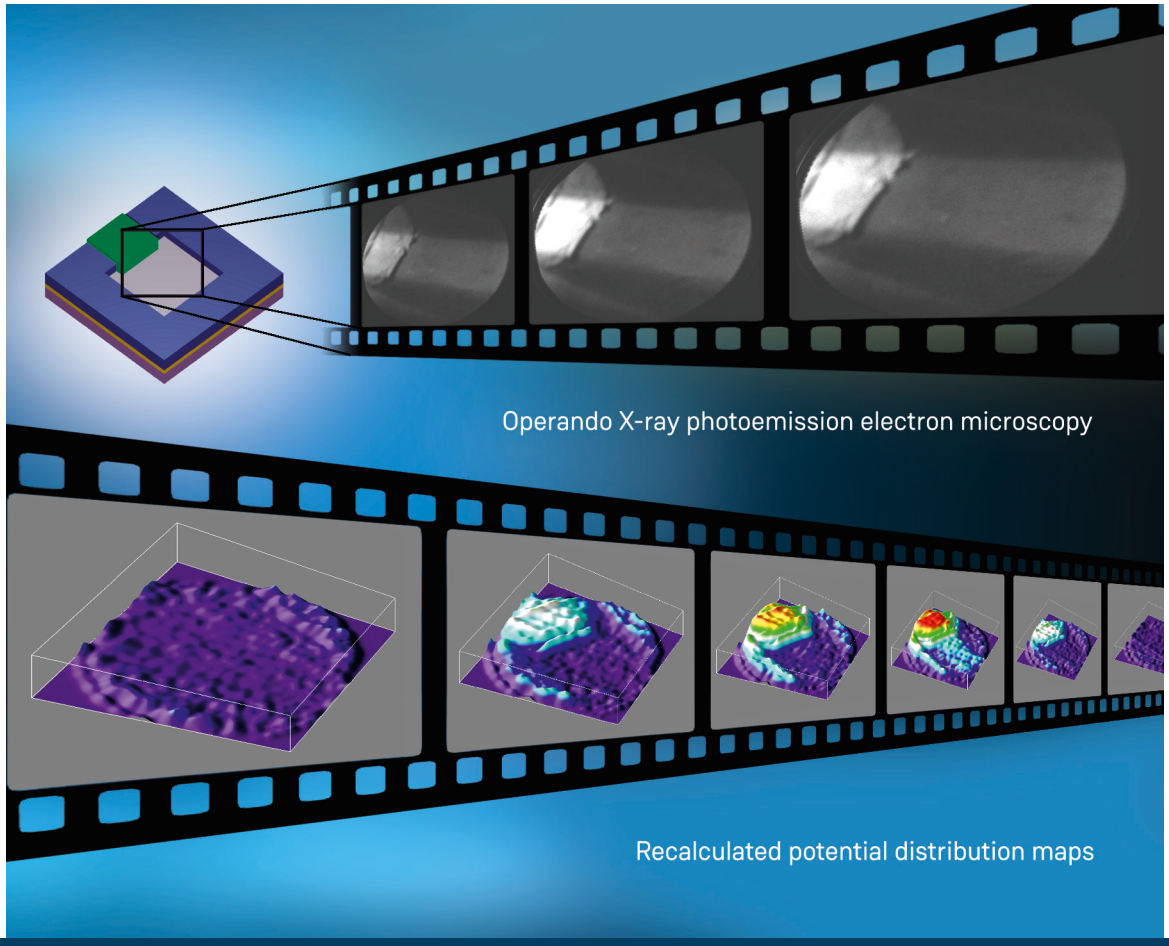

Operando X-ray photoemission electron microscopy (XPEEM) investigations of resistive switching metal-insulator-metal devices

Christoph Jan Schmitz

Information
Band / Volume 53
ISBN 978-3-95806-283-2

Mitglied der Helmholtz-Gemeinschaft

JÜLICH
Forschungszentrum

Schriften des Forschungszentrums Jülich
Reihe Information / Information Band / Volume 53

Forschungszentrum Jülich GmbH
Peter Grünberg Institute (PGI)
Electronic Properties (PGI-6)

Operando X-ray photoemission electron microscopy (XPEEM) investigations of resistive switching metal-insulator-metal devices

Christoph Jan Schmitz

Schriften des Forschungszentrums Jülich
Reihe Information / Information Band / Volume 53

ISSN 1866-1777 ISBN 978-3-95806-283-2

Bibliografische Information der Deutschen Nationalbibliothek.
Die Deutsche Nationalbibliothek verzeichnet diese Publikation in der
Deutschen Nationalbibliografie; detaillierte Bibliografische Daten
sind im Internet über http://dnb.d-nb.de abrufbar.

Herausgeber und Vertrieb:	Forschungszentrum Jülich GmbH Zentralbibliothek, Verlag 52425 Jülich Tel.: +49 2461 61-5368 Fax: +49 2461 61-6103 zb-publikation@fz-juelich.de www.fz-juelich.de/zb
Umschlaggestaltung:	Grafische Medien, Forschungszentrum Jülich GmbH
Druck:	Grafische Medien, Forschungszentrum Jülich GmbH
Copyright:	Forschungszentrum Jülich 2018

Schriften des Forschungszentrums Jülich
Reihe Information / Information, Band / Volume 53

D 464 (Diss., Duisburg, Univ., 2017)

ISSN 1866-1777
ISBN 978-3-95806-283-2

Vollständig frei verfügbar über das Publikationsportal des Forschungszentrums Jülich (JuSER)
unter www.fz-juelich.de/zb/openaccess.

Kurzzusammenfassung

Resistive Schaltmaterialien – einschließlich resistiver Oxide - erlangen zunehmende wissenschaftliche und industrielle Bedeutung aufgrund ihrer vielfältigen Anwendungsmöglichkeiten in nichtflüchtigen Datenspeichern der nächsten Generation und als neuartige Logikelemente. Obwohl bereits zahlreiche Schaltmaterialien ihren Weg in die Anwendung gefunden haben, sind die zugrunde liegenden physikalischen Mechanismen nicht vollständig verstanden. Während die elektronischen Eigenschaften, wie z.B. die Antwort auf externe elektrische Anregung, in der Literatur gut dokumentiert sind, gibt es bisher nur wenige experimentelle Studien zu den mikroskopischen und chemischen Ursachen des Schaltvorgangs.

Ziel dieser Arbeit ist es mittels chemisch-sensitiver und ortsaufgelöster Röntgen-Photoelektronenemissionsmikroskopie (XPEEM) ein tieferes physikalisches Verständnis der elektronischen und chemischen Prozesse während des Schaltvorgangs zu gewinnen. XPEEM wird verwendet, um chemische und elektronische Veränderungen zwischen EIN und AUS Zuständen an dysfunktionalen, delaminerten $SrTiO_3$ Zellen zu identifizieren. Für den niederohmigen (AN) Zustand werden sub-mikrometer große, filamentäre Bereiche mit beträchtlichen Anteilen an dreiwertigem Titan beobachtet. Vergleichbare Strukturen und Zustände lassen sich für den hochohmigen (AUS) Zustand nicht finden. Die experimentellen chemischen und räumlichen Signaturen deuten in Übereinstimmung mit dem Valence Change Model auf eine Anreicherung bzw. Verarmung von Sauerstoffleerstellen am Metall/Oxid Übergang hin. Die weitere Untersuchung der filamentären Bereiche zeigt, dass die oftmals makroskopisch homogen angenommen Strukturen aus einer Matrix mit nanoskaligen Einschlüssen bestehen. Die gewonnenen Erkenntnisse tragen zum Verständnis des Schaltmechanismus bei, welcher wesentlich für die Simulation von Bauteilen und für die Identifizierung von Skalierungslimits ist.

Über die Charakterisierung der statischen EIN und AUS Zustände dysfunktionaler Zellen hinaus liegt der Schwerpunkt der Arbeit darin, zu untersuchen, ob und wie der hochoberflächensensitive XPEEM-Ansatz verbessert werden kann, um die erwarteten chemischen Veränderungen auch während des Betriebs eines Bauteils zu beobachten („operando“). Mit dem Ziel die hohe Oberflächensensitivtät photoemissions-basierter Experimente zu überwinden, werden verschiedene experimentelle Ansätze und Bauteilgeometrien diskutiert und ausgewertet. Ultradünne Graphen Top-Elektroden sind für Elektronen hinreichend transparent und erlauben in Kombination mit Absorptionsspektroskopie die chemisch-sensitive Abbildung aktiver Grenzflächen in Metall-Isolator-Metall Strukturen. Basierend auf den erarbeiteten Strategien wurden neue funktionale Speicherzellen entwickelt. Ein PEEM zum Einsatz an einem Synchrotron wurde entsprechend der neuen Methodik technisch aufgerüstet. Mit dem verbesserten Aufbau ist es erstmals gelungen, ein Bauteil während des Betriebs gleichzeitig chemisch und elektronisch ortsaufgelöst zu charakterisieren. Insbesondere konnte eine Verknüpfung der elektrischen Strom-Spannungskennlinie (I-V) und dem vorherrschenden mikroskopischen Zustand hergestellt werden. Variationen zwischen verschieden Zellen können durch die Messung an einer einzelnen Zelle mit der neuen Methodik umgangen werden.

Die in dieser Arbeit dokumentierten Verbesserungen der XPEEM Methodik ermöglichen die operando Charakterisierung funktionaler Bauteile. Dies ist ein bedeutender Schritt in Richtung des langfristigen Ziels der ortsaufgelösten Visualisierung ultraschneller Schaltvorgänge.

Abstract

Resistive switching materials - including resistive oxides - raise significant scientific and industrial interest due to their potential applications in next generation non-volatile data storage devices and as building blocks for novel logic elements. Even though numerous resistive switching materials already found their way into application, the underlying physical mechanisms still remain highly elusive. While the electronic response of these systems is well-documented throughout literature, experimental data on microscopic and chemical origin of resistive switching is rare.

Scope of the present work is to gain a deeper physical understanding of chemical and electronic changes taking place during the switching process by means of chemically-sensitive and spatially resolving X-ray photoelectron emission microscopy (XPEEM). This technique is used to identify chemical and electronic changes between the ON and OFF states of non-functional delaminated memristive $SrTiO_3$ devices. For the low resistive (ON) state, sub-micron filamentary regions are observed showing significant contributions of trivalent Ti, whereas the high resistive (OFF) state lacks these states and structures. The experimentally derived chemical and spatial fingerprints provide evidence for oxygen vacancy accumulation respectively depletion being predicted by the valence change model. Further analysis of the observed filament substructure indicates that the observed macroscopic filaments consist of an inhomogeneous matrix of nanoscale islands. These findings contribute to the fundamental understanding of the switching mechanism being essential to improve device simulations and to identify scaling limits.

Beyond the conventional static characterization of the ON and OFF states of non-functional devices, the focus of the thesis is to evaluate how the highly surface-sensitive PEEM approach can be improved to allow monitoring the anticipated chemical changes also during operation of a device ('operando'). In this context different experimental approaches and device geometries are discussed and evaluated, which have the potential to circumvent the top electrode surface sensitivity dilemma in photoemission-based techniques. Ultra-thin graphene top electrodes are demonstrated to be sufficiently transparent for electrons and thus allow to image chemical signals originating from the buried active interface of a metal-insulator-metal structure by means of X-ray absorption spectroscopy. The novel strategies and concepts are realized into a set of functional devices. Additional technical modifications are implemented into a PEEM instrument operated at a synchrotron facility. Using this new setup chemical and electronic characterization of a working device are simultaneously performed in a single experiment providing a direct correlation between current-voltage (I-V) response and chemical state for the first time. Results from the operando and in-situ experiments are obtained from single devices and thus exclude typically observed device-to-device variations and experimental artifacts typically hampering the analysis.

The instrumental advances and improved methods documented in this thesis enable operando characterization of functional devices using PEEM. They are not limited to resistive switching and they present a significant step towards the long-term goal of visualizing the switching dynamics on a nanosecond timescale with sub-micron spatial resolution.

Contents

Executive Summary

The present work deals with the characterization of resistive switching metal-insulator-metal devices during operation using time-resolved, chemical sensitive and spatially resolving photoemission electron microscopy (PEEM). The goal is to identify chemical and spatial fingerprints characteristic for high and low resistance states in resistive oxide materials. These fingerprints are intended to be used as tracers for filament formation of oxygen vacancy rich regions during device operation. Major effort was dedicated to the development of new approaches to visualize the dynamics by time-resolved PEEM (tr-PEEM), as information about the switching dynamics, filament localization and quantification of the switching process using spatially resolving techniques is believed to be key to explain strong device-to-device and cycle-to-cycle variations in resistive switching currently hampering these devices from application in novel data storage devices.

Chapter 1 addresses the need for novel data storage materials and logic concepts with respect to the continuously increasing demand for computational power, especially in the field of Big Data. In this context, memory devices based on resistive switching materials (ReRAM) may offer a non-volatile, energy efficient, highly scalable alternative to silicon based technologies. In a ReRAM device the resistance of a nanoscale volume is modified between different values by chemical or structural ordering on the atomic level: A high device resistance represents a binary “1”, a low device resistance is equal to a binary “0”. The key challenge in making resistive switching materials competitive to the well-established silicon technologies, is to achieve a similar, yet unparalleled level of understanding of the underlying physical processes. The current understanding of these processes and the technological state-of-the-art in the field of resistive switching are reviewed in chapter 2. It is general consensus that the resistive switching phenomenon is caused by local modifications of atomic arrangements. These rearrangements occur under high electric fields and at elevated temperatures. Strong correlations between atomic arrangement and device current materialize in a hysteric and non-linear I-V characteristics. In the special case of *resistive switching metal oxides,* the atomic rearrangements responsible for the local conductivity modulations are related to the formation of oxygen vacancies and their redistribution under high electric fields and temperature gradients. These oxygen vacancies are point defects in the crystal lattice and act as local electron donors. Local charge transfer from the vacancy onto the neighboring metal atom leads to a formal change in the metal valence - known as *valence change mechanism (VCM)* - making the initially insulating material locally n- or p-type conductive. Vacancy clustering and ordering under electric stress leads to the formation of conductive filaments. Furthermore, the presence of oxygen vacancies modifies the width and height of the Schottky barrier at the metal/oxide interface. The barrier is a space charge layer and acts as tunnel barrier for the electronic transport. Overall, switching between high resistive states

(HRS) and low resistive states (LRS) in oxides is attributed to the interplay between Schottky barrier modulations due to oxygen vacancies accumulation near the interface and filament percolation. In chapter 3 the concepts of switching in oxides are transferred to the perovskite model system $SrTiO_3$. The influence of vacancy formation with respect to the electronic structure is analyzed and simulated. Based on model simulations of the absorption process of the TiO_6 octahedra we identified features in the Ti L- absorption edge, which may act as indirect spectral fingerprints of vacancy formation. Thus, spatially resolved X-ray absorption spectroscopy (XAS) enables experimental detection, quantification and tracking of oxygen vacancy formation and movement also during device operation. Filament position, doping concentrations and other key parameters, which are required for reasonable device simulation and rational device design, can be derived from these measured vacancy profiles. Surface-sensitive *Photoemission Electron Microscopy (PEEM)* with synchrotron radiation as the experimental method of choice is introduced in chapter 4. The method is highly sensitive to chemical changes on the micron scale and provides access to spatially resolved X-ray absorption spectroscopy (XAS) and X-ray photoemission (XPS).

Chapter 5 evaluates chemical fingerprints present in the absorption spectra of $SrTiO_3$, which are related to the formation or depletion of oxygen vacancies and can be observed with XPEEM. Initial results are based on thermal reduction of a $SrTiO_3$ single crystal and on ex-situ switched and delaminated thin film devices. Within these results regions with highest contrast for changes in the oxygen vacancy ($V_O^{\cdot\cdot}$) concentration are identified being of utmost relevance with respect to the in-operando characterization of working devices. For $V_O^{\cdot\cdot}$ concentrations below 10% modifications are primarily observed at the *O K-edge*. For vacancy concentrations above 10 % also deviations at the *Ti L-edge* become visible. The microscopic investigations on delaminated, pre-switched thin film devices show that the modifications of the oxygen vacancy concentration are confined to filamentary regions with diameters between $500-1500$ nm. Within these modified regions the *work function* of the material is lowered. The results indicate that the observed filamentary regions consist of many nanosized islands with less than 100 nm in diameter being below the experimental resolution. Both derived fingerprints - chemical and microscopic - serve as basis for in-situ and operando characterization. With respect to the expected signal intensities, the delaminated devices represent a best case scenario as the filaments are directly accessible.

Chapter 6 addresses the question how the identified fingerprints on delaminated devices can be transferred to the characterization of working devices. The main challenge arises from the limited probing depth of photoemission experiments - typically below $6-10$ nm - combined with a top electrode of several ten of nanometer thickness damping the chemically relevant signal. This *top-electrode surface sensitivity dilemma* cannot be resolved completely, as it is a consequence of electron scattering effects, but its effects can be minimized by selecting viable combinations of experimental approach and device geometry. Three different approaches were identified to be capable of bypassing the physical limitations imposed by the photoemission process: (i) *hard x-ray PEEM (HAXPEEM)* (ii) *lateral devices* and (iii) *ultra-thin electrode* devices. All three approaches have been implemented and experimentally evaluated with respect to their potential application in in-situ and time-resolved studies. The findings for $SrTiO_3$ based system are condensed in Tab. 0.1 taking different, multidimensional aspects (e.g. device fabrication, chemical contrast...) into account. It turns out that some of the approaches work better than others and the ideal combination of device geometry and experimental method strongly depends on the material system under investigation.

		Methology & Fabrication		Resistiv Switching related aspects			PEEM related aspects		
device type		method	fabrication	oper. devices	chemical [4] contrast	reported endurance	ex. feature size [5]	ex. Intensity of Interface [6]	suitabilty [7] for TR-PEEM
lateral configuration		XAS [1]	basic, optical lithography	yes, but not in this thesis [3a]	o/+	no operational devices	<10 nm, below PEEM res.	very high	++
		SX-XPS			o/-			high	+
		HX-XPS			-/--			avg./low	-
vertical configuration	thin TE > 2nm	XAS [1]	basic, optical lithography	yes, well known from Lit. [3b]	o/+	10^9 cycles, reduced under UHV	observed up to 1µm	avg./low	o
		SX-XPS			o/-			avg./low	-
		HX-XPS			-/--			low/v. low	- -
	ultra-thin TE < 2nm	XAS [1]	multi-step, optical lithography [2]	yes	o/+	$10-10^4$ cycles, red. under UHV	observed up to 1µm	high/v. high	++
		SX-XPS			o/-			avg.	o
		HX-XPS			-/--			avg./low	-

1) soft x-ray XAS < 1000 eV 2) know-how for thin electrodes required 3a) working devices reported in literature 3b) standard devices in literature
4) material dependent (here shown for SrTiO3), here it implies real chemical contrast, but also involves instrumental resolution and statistics
5) the expected feature size is based on experiments and models, the ranking is based on a comparison to PEEM resolution of 50-150nm
6) the intensity ranking is referenced to best S2N ratios for a aquistion times in the order of seconds 7) The suitability for time-resolved PEEM is a product of chemical contrast and expected signal intensity

Figure 0.1. – Evaluation of the operando suitability of different device-method pairs for a $SrTiO_3$ based system.

In general, *HAXPEEM* is the most versatile approach and can be applied to almost any device geometry and material combination. It is demonstrated that the probing depth in *HAXPEEM* can be increased up to 15 nm relaxing the constraints on the top electrode fabrication. Simultaneously it is observed that the photoemission cross sections for hard x-ray excitation are reduced by orders of magnitude resulting in very low counting statistics in the current setup. Extrapolation of the measured intensities leads to an average acquisition time of ≈ 10 h for a single, high resolution spectrum, presenting an insurmountable obstacle for time-resolved measurements unless the signal intensity can be significantly enhanced.

Lateral devices provide highest intensities as the active area remains uncovered. While in previous works lateral devices have been successfully employed in the characterization of initial filament formation, we find the geometry is not suitable to characterize the reversible switching process between LRS and HRS using XPEEM, as the oxygen vacancy redistribution is expected to take place in confined regions of less than 10 nm near the electrode/filament interface. Thus, the approach was discarded as the expected feature size during reversible ON/OFF switching is below the average resolution limit of a PEEM instrument amounting to $50-100$ nm.

Ultra-thin electrodes allow one to maintain the well-established vertical stacking geometry, extensively studied over the past years. As the ultimate limit in top electrode thickness, *sheets of graphene* were used for device fabrication providing a highly electron transparent and conductive top electrode. In combination with x-ray absorption (XAS) experiments the devices provide high intensity signals and reasonable chemical contrast. In view of the scope of in-operando measurements we opted for the graphene contacted $SrTiO_3$ devices in the current thesis.

In chapter 7 a single, novel graphene contacted device is *switched between LRS and HRS in-situ* in a PEEM microscope. XAS measurements were performed before and after a switching event. In this configuration, device to device (D2D) variations and external influences to the device resistance state can be excluded. Within a confined region of about 500 nm changes in the occupation of the hybridized Ti 3d - O 2p states at the oxygen K edge are identified. The observed changes are

correlated to a change in vacancy concentration. By comparing the spectral changes to the annealed single crystal "calibration" sample oxygen vacancy of $4.5 \pm 0.5\%$ for the LRS and of $2 \pm 0.5\%$ for the HRS are extracted. Based on these concentrations the charge carrier density in the conduction band was calculated to $1.5 \times 10^{21}\,\mathrm{cm}^{-3}$ (LRS) and $6.7 \times 10^{20}\,\mathrm{cm}^{-3}$(HRS), respectively. The modulations of the charge carrier density in the conduction band go hand in hand with measured resistance change. Using the derived charge carrier concentrations in simulations based on Schottky barrier modulations, good agreement between experimental I-V and simulated I-V curves is found for the low voltage regime. During four cycles of switching the identified filament position remains unaltered , Fig. 0.2.

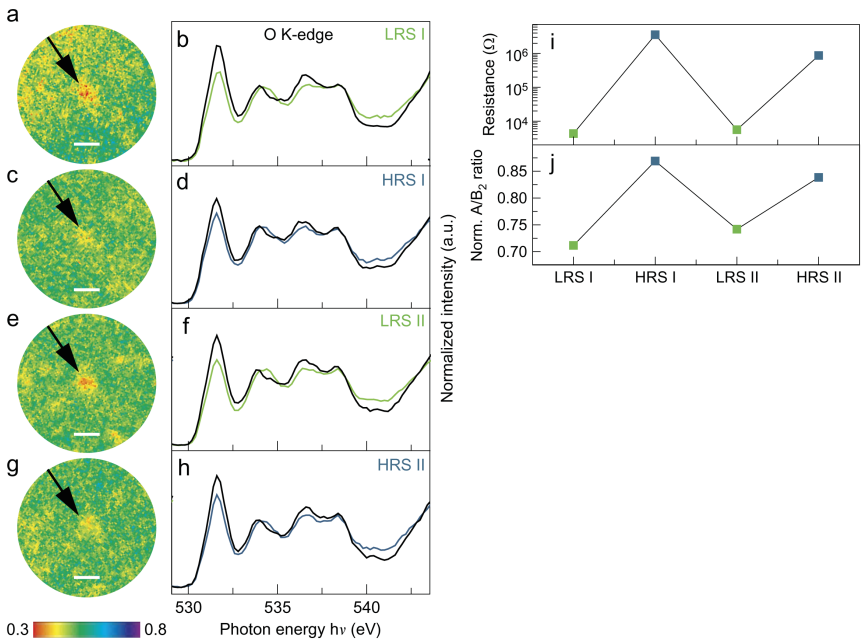

Figure 0.2. – In-situ experiments on a graphene contacted device. Accumulation and depletion of oxygen vacancies in filament like regions of 500 nm in diameter under reversible LRS to HRS switching (a,c,e,g). The first peak of the O K-edge, representing the Ti 3d - O 2p hybridization, is modified by a few percent (b,d,f,h). The measured change in device resistance correlates with the peak intensity modifications. Taken from Bäumer, Schmitz et al. [1]

Chapter 8 summarizes necessary *instrumental modifications for operando experiments*. A novel and powerful *method for potential analysis* in XPEEM is presented. Two operational modes are distinguished: A *voltage mode*, sensitive to potential modulations in the device during operation and a *chemical mode*, sensitive to the formation of oxygen vacancies. The exceptional benefit of the new setup is that externally measured I-V curves can be directly correlated to microscopic changes in the device. In the *voltage mode*, graphene contacted devices are subjected to external pulse characterization. The recalculated voltages provide *evidence for dynamic switching in front of the microscope* and allow determining the voltage drop across the device without parasitic influences. Fitting of these recalculated I-V curves in forward bias direction to a Schottky barrier model, results

in a lowering of the transport barrier in between HRS and LRS. Further, an increase in tunneling contributions is observed. Both effects can be explained by an increase/decrease of donor density in the order of 2-3 being in close agreement with the measured density modulation derived from the XPEEM measurements in chapter 7. The chemical characterization remained without visible outcome. *No filament could be identified during the switching process.* The lack of filament formation is attributed to a filament formation within the Au lead and graphene electrode overlap regions inaccessible by PEEM. These assertions are supported by *hard break down (HBD) experiments*, where single devices are driven into thermal break down by stepwise removal of the protecting current limitation. Complementary to the extracted I-V curves, the HBD experiments provide solid evidence for operando device operation in front of the microscope: Specifically, physical modifications of the top electrode are observed in the high current, break down regime including the *evolution of a diffusion front* and characteristic *bubble formation* at the top electrode being a common fingerprint for the ex-corporation of oxygen. Scanning electron microscopy (SEM) *studies on post-mortem* devices confirm filamentary regions underneath the Au/graphene contact.

Part I.

Theoretical Background

CHAPTER 1

Introduction & Motivation

In the past 30 years the available and accessible knowledge has grown exponentially in all scientific disciplines. This knowledge has driven most of the technological progress, which in turn is the foundation of our modern life. Today, even the amount of information available in a special and narrow field of interest exceeds the capability of a single human by orders of magnitude. Consequently, the generation of new insights will strongly depend on the pace in which our brain will adapt to the new circumstances. Unfortunately, it seems as if we are getting close to a physical limit. Despite spending a lifetime reading, it will never be possible to keep up with the rate of publication. Without technical assistance the technological evolution will start to stagnate due to the increase in complexity each progress brings along. While a wagon from the Middle Ages required only wheels and some basic tools to craft, a car engine fabricated in the early 60s could only be repaired by a mechanic with knowledge on fuel engines. Nowadays engines are equipped with various electronics in order to optimize fuel consumption and CO_2 emission. Now, both mechanical understanding and a basic knowledge of electronics are necessary to repair it, which usually requires a specialist. Each improvement in efficiency comes along with an increase of complexity. To keep up with this complexity we have to specialize, but in the future we will reach a moment where we will not be able to specialize any further. At this point artificial and computational tools, which can assist us, will be needed.

In the 1950's, a 'digital revolution' started which evolved into an exponential increase of computing power. A modern computer can perform billions of operations per second outperforming a human brain by orders of magnitude regarding addition and multiplication. Yet, modern computers cannot compete with the human brain when it comes to logical understanding, pattern recognition or creativity. The task of recognizing human faces in a photograph requires sophisticated programming and many millions of operations, whereas a 5-year-old child can perform this task without any effort on a routine basis with high accuracy and a power consumption only a few watts [2]. It seems to be general consensus that the main difference between a human brain and a computer lies in the way how data is processed. A computer works command by command in a serial fashion. Since it has to be programmed it follows an almost static, fixed, inflexible and deterministic process. The brain on the other hand relies on parallel processing of a multi-billion node network of independent neurons and each calculation can be seen as collective excitation making the brain flexible and adaptive. Further, it can learn and then rely on this learning process, which can better be described as a mem-

ory operation rather than a logic process. In contrast, a personal computer uses memory in most cases only to store data. Lately, creating so called artificial neuronal networks, which are software algorithms mimicking the functionality of our brain, has been of great scientific and commercial interest. These programs define a virtual network of interconnected nodes. Within these networks the connection strength between different nodes can be adjusted by learning processes of external input data. The developed software turned out to be incredibly successful in the recognition of faces and video footage [2].[1] Further it was used for live speech translation from English to Chinese [3].[2] On these grounds it might be possible to implement a tool that can skim publications and extract summaries and results of experimental data, compressing thousands of publications into a single, readable and understandable document.

By now, typical software emulates a brain-like behavior on a standard von Neumann CMOS [3] hardware architecture. This means parallelism has to be generated artificially by iterations. A method like this is very inefficient and due to the mismatch between task and chip operation mode also extremely power consuming. Having a hardware rather than a software solution would be a better approach. The first reported, silicon-based hardware implementation of a neuronal network on CMOS technology was presented with the 'TrueNorth' by IBM in 2014 published in Science [4].

In the context of hardware solutions, memories based on resistive switching materials (RSM) - so-called resistive switching random access memory (ReRAM) - are more promising than the commonly used silicon-based devices. The reason is that the memory switching in a ReRAM device possesses similar functionalities as a human neuron in many aspects. ReRAM is a promising candidate for novel data storage devices and logic circuits overcoming the physical limits of magnetic memories or charge based devices (e.g. FLASH). It is non-volatile, CMOS-compatible, ultra-fast and possibly scalable down to the nanometer regime. In a ReRAM cell, information is stored as the resistivity of a small volume of RS material, sometimes containing only a few atoms. By applying electrical pulses to the material, the system can be set reproducibly into either a high (HRS) or low resistive state (HRS) induced by solid-state phase transitions. Those states can be interpreted analogous to magnetic memories as binary “on” or “off”. Without any major effort ReRAM is compatible to current processor architectures. However, differing from the bipolar spin-up vs. spin-down orientation in magnetic memories, the resistivity of the volume is a continuous and not a discrete quantity. Therefore it offers the possibility to store more than a single bit per device and to increase the storage density by several orders of magnitude. The rare combination of a tunable resistance with a non-linear current-voltage response has many similarities to the operation of a neuron in a human brain. Hence, ReRAM devices enable entirely new logic concepts, which may close the gap between “Von-Neumann” processing and “Human Brain” processing opening the door for a next generation of smart and energy efficient computer systems [5].

So far, first working ReRAM devices have been implemented, but the majority of the reported RS devices suffer from reproducibility, retention and reliability issues. Often devices made out of the same material as reported in literature show switching at different experimental conditions. These

[1] Video: https://www.ted.com/talks/fei_fei_li_how_we_re_teaching_computers_to_understand_pictures

[2] Video: https://blogs.microsoft.com/next/2012/11/08/microsoft-research-shows-a-promising-new-breakthrough-in-speech-translation-technology/

[3] Complementary metal-oxide-semiconductor

discrepancies are formally attributed to different sample preparation steps. Ultimately however, they must be attributed to a lack of physical understanding of the involved transport, switching and chemical processes. Yet, for the rational design of competitive memory devices and subsequent device scaling down to the nanoscale, a deep and fundamental understanding of all involved processes is mandatory.

In this context, the collaborative research project SFB 917 "Nanoswitches" of the research center Jülich and RWTH Aachen University, including 19 different projects, was initiated on July 1st, 2011 by the Deutsche Forschungsgemeinschaft (DFG) "to understand and explore the potential of advanced nanoswitches based on such configuration changes. The overarching aim of SFB 917 is to advance the microscopic understanding of resistive switching phenomena utilizing changes in the atomic configurations, in particular in the phase and the valence of oxides and higher chalcogenides. To explore the full potential and pave the way for such an electronics technology it is mandatory to realize ultrahigh scalability, fast switching kinetics and long retention times." (http://www.sfb917.rwth-aachen.de/)

Objective of the present work

The present thesis is embedded in the framework of the SFB 917 project. It aims to elucidate switching mechanisms and the physical origin of switching in transition metal oxides (TMOs) by employing state-of-the-art, spatially and chemically resolving X-ray photoelectron emission microscopy (XPEEM). This approach can be used to extract near Fermi edge density of states (DOS) as well as chemical shifts in core-levels arising from structural and chemical changes (XPS). Further it can detect doping effects by means of spatially resolved X-ray absorption techniques (XAS). Until now, most of the previous work was performed using integral methods (e.g. two terminal resistance measurements, averaging XPS) averaging over active devices and neglecting the spatial nature of the switching process. In contrast, the XPEEM approach offers direct local access to the electronic structure of the high resistive state (HRS) and the low resistive state (LRS). It is expected to unveil the missing chemical and electronic modifications induced during the switching with a spatial resolution on the sub-micron scale. This microscopic information will be used to determine the characteristics of the switching process, which are relevant for simulations and/or for the evaluation of device failure mechanisms.

The ultimate goal is to monitor the anticipated nanoscale filament formation in a functional oxide-based ReRAM device in a time-resolved measurement during operation *(in-operando)* using XPEEM. This new type of experiment allows electrical and chemical characterization to be performed simultaneously, providing correlations between chemical modifications and the internal device resistance state, providing insight into the dynamics of the switching process.

The realization of this ultimate goal critically depends on solving the so-called "top electrode surface sensitivity dilemma" in XPEEM experiments (Sec. 6.1). This dilemma results from the high surface sensitivity of XPEEM being limited to a few nm only on the one hand and a relatively thick top electrode in a metal-insulator-metal structure on the other hand. Due to this configuration the photoexcited electrons from the buried active material are mostly blocked by the top electrode layer and cannot reach the detector. Consequently, it was of highest priority to identify experimental approaches, geometries and/or sample designs allowing to circumvent these limitations.

Outline

Following the introduction, **Chapter 2** provides a state-of-the-art review on resistive switching systems. The anticipated switching mechanisms and corresponding driving forces for resistive switching in transition metal oxides (TMO) will briefly be explained.

In **Chapter 3**, the field of materials will be narrowed down. Furthermore the electronic and structural properties of the model system $SrTiO_3$, which are the origin for the characteristic absorption behavior, will be discussed.

Chapter 4 lists the different experimental techniques being used - including XPS and XAS. Special attention is attributed to the probing depth in photoemission electron spectroscopy (PES) under different experimental conditions. Moreover the working modes of a state-of-the-art PEEM will be explained in this chapter.

The experimental section (**Chapters 5-8**) first presents characteristic, chemical fingerprints for LRS and HRS in $SrTiO_3$ derived from bulk samples and from delaminated, non-functional $SrTiO_3$ devices. These fingerprints were taken at the O K-edge and the Ti L-edge and serve as reference for the in-situ and operando experiments.

Chapter 6 shows diverse strategies to solve the "top electrode surface sensitivity dilemma" in XPEEM. Three different approaches are discussed and to each benefits and drawbacks are listed. Here, ultrathin, graphene contacted devices in combination with XAS are identified to provide the best signal contrast required in operando experiments.

Chapter 7 presents first experimental data on in-situ switched graphene contacted devices. Reversible device operation in front of the microscope serves as proof-of-concept of the derived approach. Modifications of the oxygen vacancy concentration in filamentary regions of a few 100 nm in diameter near the top electrode interface are observed explaining the change in resistivity.

Finally, **Chapter 8**, deals with the technical implementation of an operando experiment. For the first time memristive devices are monitored during operation with chemical and electronic sensitivity. A novel method was established to recalculate time dependent, two dimensional local potential distributions maps. The extracted potential distributions unambiguously prove device operation and indicate that filaments are formed under the Au leads, which are inaccessible by PEEM. These assumptions are confirmed by SEM studies of post-mortem devices providing information on how to further improve operando experiments in the future.

Chapter 9 summarizes the main findings of the thesis and provides an outlook for future experiments.

CHAPTER 2

Resistive Switching Phenomena

In the following, a general review about the research progress in the field of resistive switching in the past years will be provided and present fields of application, as well as a detailed explanation of resistive switching phenomena in oxide systems will be given. To further expand the view on the topic, the reader is referred to general reviews on resistive switching by Sawa [6], Pan [7] and Ielmini [8], to reviews of potential applications by Strukov [9] and Yang [10] and to a review on the physical driving forces by Yang [10]. A review on resistive switching focusing on transition metal oxides is provided by Waser and Aono [11].

2.1. History and state-of-the-art

The resistive switching phenomenon in general describes the reversible, hysteretic modulation of the conductivity of a thin film device in an electrical field (e.g. the application of an external voltage pulse). During resistive switching the conductivity typically changes by several orders of magnitude [10]. Generally, the change in conductivity is attributed to thermally induced phase transitions and/or redox processes on the nanoscale. Still, in many systems the origin of these phenomena remains elusive or at least under debate. Resistive switching was first reported in a series of binary oxides by Hickmott in 1962 [12]. Since then, resistive switching behavior has been reported in many other semiconducting materials. Consequently, the first period of high research activity of resistive switching phenomena took place in the 1970s and 1980s. Most of the early research focused on discussing and revealing the physical mechanism of electrically stimulated resistive switching. With the ongoing progress in microelectronics in the late 1990s, researchers recognized the potential of resistive switches to be used as an ultimate, non-volatile memory (NVM). This marks the onset of the second, technologically driven period of intensive research [7]. Nowadays, resistive switching is widely implemented in functional ReRAM (Resistive switching Random Access Memory) devices, where the geometry of a ReRAM device looks similar in all cases. In its simplest form, a few nanometer thick film of a resistive switching material is sandwiched between two metal electrodes, Fig. 2.2. This configuration is referred to as a metal-insulator-metal (MIM) structure [11, 13]. Various materials and compounds have been successfully utilized for device fabrication, including chalcogenides and transition metal oxides [10, 11, 14]. It is general consensus that even though the overall switching behavior is common to all materials, the underlying switching mechanisms strongly depend on the

material class being involved. While phase change materials (PCMs) reveal a phase transition of the host material from amorphous to crystalline state, the origin of resistive switching in oxides - especially transition metal oxides (TMO) - is attributed to the motion and redistribution of oxygen vacancies in an otherwise insulating matrix. In both cases, an externally applied electric field triggers a current, which in turn leads to a persistent modification in the atomic arrangement. The result of a switching process is then defined as one out of many thermodynamic metastable atomic configurations exhibiting long life times. Due to the statistic nature of these atomic configurations the memristive switching process progresses gradually, i.e. intermediate resistance states are observed. For memory operation in ReRAM cells, binary operation is preferred and the system is altered in between two resistance states: the low resistive state (LRS) and the high resistive state (HRS). Bi-stable operation is achieved by applying characteristic I-V cycles to a device, which tend to reproduce similar atomic configurations with each switching event. The operation changing the resistance of a device from HRS to LRS is called a 'SET' process, while the opposite process is defined as 'RESET'. Due to the non-volatile nature of the process, the specific resistance state (HRS or LRS) is retained even after the electric stimulus is removed [7]. The resistance state of a device is probed by the application of a small voltage pulse, which is referred to as 'READ' process. The amplitude is chosen as small as necessary to avoid 'read-induced' disturbance of the device state [11].

2.1.1. Characteristic I-V dependence in resistive switching materials

As the origin of resistive switching is manifold and material dependent, a first classification is based on the characteristic current-voltage (I-V) curves observed during operation, see Fig. 2.1. Two types are distinguished: Unipolar (non-polar) and bipolar. Unipolar switching requires only one voltage polarity. The switching from the LRS (on) to the HRS (off) and vice versa occurs for the same polarity of the applied voltage, but at different amplitude and for different pulse duration, Fig. 2.1a. In bipolar switching, in contrast, the switching direction is defined by the polarity of the applied voltage. One polarity switches the system into LRS, the other into HRS, Fig. 2.1b. Unipolar switching is typically related to rupture and fusing mechanisms on the nanoscale driven by local Joule heating (thermal effects), whereas bipolar switching is attributed to the movement of charged ions or defects (field driven) [10]. In bipolar devices, further information can be obtained from the sense of rotation, which depends on the contributing charge carriers and the active interface. The process can be either clockwise or counterclockwise with respect to a positive voltage applied to the top electrode, Fig. 2.1c. The observation of a superposition of both orientations in the same device at different experimental conditions as e.g. reported in Ref. [15, 16] implies a charge carrier concentration inversion or the presence of different types of conducting channels.

2.1.2. Geometric location and microscopic shape of conducting channels

How the atomic rearrangements induced during the switching process manifest microscopically depends on the material-specific driving forces and on the underlying switching mechanisms. Overall, the microscopic shape and the geometric location can be classified into either filament-type or interface-type [7, 11]. In filament-type materials the resistive switching is confined to a small, filamentary percolation path through the bulk, similar to the path of a lightning, Fig 2.2a. In interface-type devices switching takes place over the full electrode region, Fig 2.2b. Filament- and interface- types of resistive switching can be distinguished from the dependence of the cell resistance $R = R(A)$ in the LRS with respect to the electrode pad area A [7, 11]. In case of filamentary

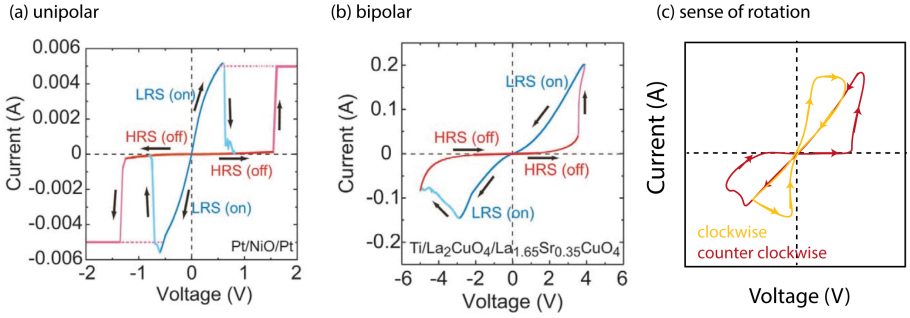

Figure 2.1. – Classification of resistive switching based on the I-V dependence: (a) unipolar switching in Pt/NiO/Pt (b) bipolar switching in $Ti/La_2CuO_4/La_{1.65}Sr_{0.35}CuO_4$ (c) sense of rotation for bipolar switching: clockwise (yellow line) or counterclockwise (red line). Images (a) and (b) are taken from Ref. [6].

switching the resistance of the full device is solely defined by the filament's cross-sectional area, which is independent of the electrode pad size (R = const.). In case of interfacial or multi-filamentary switching, the device resistance is directly proportional to the electrode pad area ($R \propto A$), because the active region (or the number of contributing filaments) is constantly increased with growing electrode size. According to this criterion most RSM systems tend to form filament-like structures [11]. Within the filamentary regions the chemical and/or crystallographic structure of the material is altered such that the conductivity is locally enhanced by orders of magnitude (defect doping, structural phase transition, etc.) making them ideal transport channels through the insulating bulk. Filaments are formed or dissolved when an external electric potential is applied to the electrodes of a MIM structure. An applied voltage has two main effects on the switching material: (i) an electric field E is formed inside the active layer promoting the movement of charged carriers and (ii) Joule heating is induced by the electric current. Electric field and Joule heating as origin for resistive switching generally coexist in all memristive switching devices. Yet, their relative importance varies depending on the device stack, the active material, electrical operation history and other parameters [10]. Given the high current densities (typical literature values $> 10^6 \frac{A}{cm^2}$) observed in the SET and RESET processes, Joule heating is expected and confirmed for both - bipolar and non-polar - device types. However, a decoupling of the thermal and electric field contributions is non-trivial, because the device resistance changes during switching and by definition thus also the ratio between voltage and current. As a consequence, the filament modulation process is governed by a dynamical and fragile interplay of changing contributions from the Joule heating and electrically driven migration of charge carriers [10]. In general, the interplay between both contributions defines the filamentary

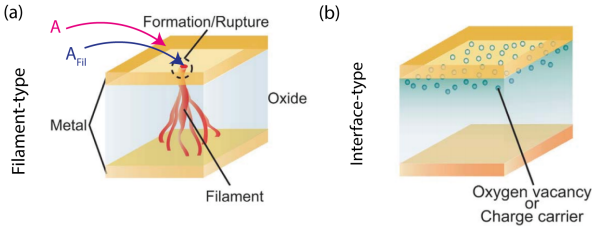

Figure 2.2 – (a) filamentary, conductive channels penetrating the insulating matrix (b) homogenous formation of charge carries in the vicinity of the metal/RSM interface. Ref. [6]

shape. According to Yang et al. the I-V dependence of a device can be used to quantify whether the dominant contribution arises from thermal or field-driven effects, Fig. 2.3. Field dominated devices typically show gradual and non-linear I-V behavior, whereas abrupt changes in the switching are typically indicative of fuse/anti-fuse processes related to thermal dominance. The evolution and shape of the filament is defined by the driving forces for the atomic/ion movement at the filament surface. The driving forces cover electric field gradients for charged defects, electron momentum transfer induced by defect-electron-collisions and motion along concentration and temperature gradients, Fig. 2.3. (For further detail see Ref. [10])

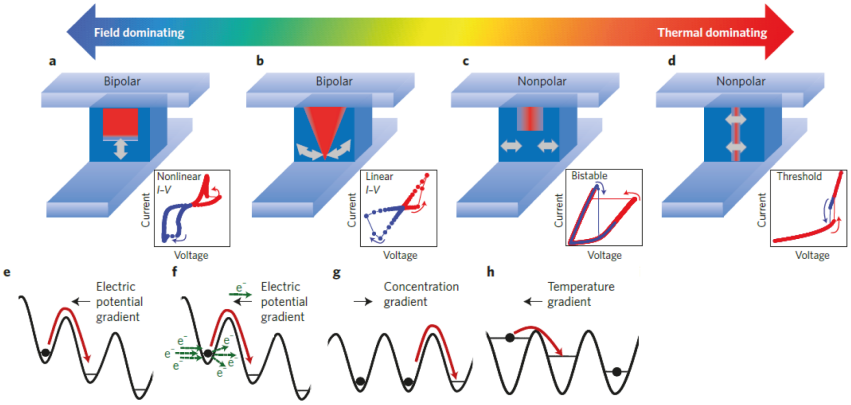

Figure 2.3. – (a-d) Expected filament structures depending on the switching mechanism and the interplay between thermal and field effects. The corresponding I-V-curves are plotted next to each of the geometries. (bottom): Summary of driving forces for ion transport across the filament: (e) field gradient (f) electron momentum transfer (g) concentration gradient (h) temperature gradient. Adapted from [10].

2.1.3. Resistance modulation and the role of interfaces for filamentary switching

The resistance of a MIM device is directly correlated with the state of the filament, Fig. 2.4. It is assumed that the conductivity in the filament is almost metallic and significantly higher than in its surrounding. Then the device resistance is only defined by the insulating layer between the filament tip - acting as a virtual cathode - and the counter electrode. Consequently, the system reaches a LRS state if the filament approaches or touches the counter electrode and the system falls back into a HRS if the filament's contact to the electrode is interrupted, Fig. 2.4a,b. In the case that the filament touches the electrode, a linear I-V behavior in the LRS is observed. If the filament tip is close to the electrode without touching it, the remaining insulating layer (e.g. the oxide) may act as tunnel barrier. Modifications of this barrier with respect to its width or its height, can affect the tunneling currents. Here, the term "tunneling currents" involves - but is not limited to - direct tunneling, Fowler-Nordheim tunneling and trap-assisted tunneling, Fig. 2.4c. All tunnel currents commonly exhibit a strong dependence on the tunneling distance. Variations of a few nanometers in tunneling distance change the transmission probability for an electron by orders of magnitude accounting for the large differences in observed device resistance between LRS and HRS. It is widely accepted

in literature that these interface effects (including Schottky barrier formation) near the filament terminator play a superior role in the explanation of the overall device resistance. Details are given in section 2.2.2.

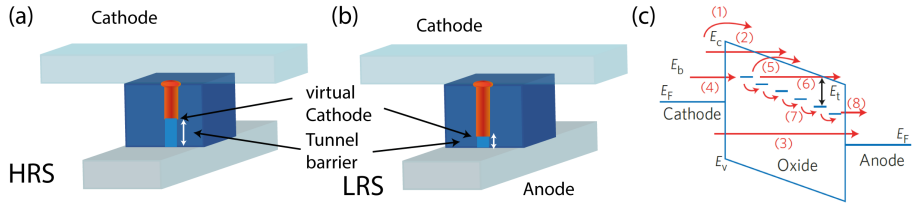

Figure 2.4. – (a) Filament state in HRS (b) Filament state in LRS (c) Tunneling contributions: (1) Schottky emission: thermally activated electrons injected over the barrier into the conduction band. (2) Fowler–Nordheim tunneling: electrons tunnel from the cathode into the conduction band; usually occurs at high electric field. (3) Direct tunneling: electrons tunnel from cathode to anode directly; only when the oxide is thin enough. When the insulator has localized states (traps) caused by disorder, off-stoichiometry or impurities, trap-assisted transport contributes to additional conduction, including the following steps: (4) tunneling from cathode to traps; (5) emission from traps to the conduction band (Poole–Frenkel emission); (6) tunneling from trap to conduction band; (7) trap-to-trap hopping or tunneling, ranging from Mott hopping between localized states to metallic conduction through extended states and (8) direct tunneling from traps to anode. Image (c) and corresponding annotations adapted from [10].

2.1.4. Dynamics of the switching process

The dynamics of the switching processes are determined by the speed at which the atomic rearrangements can take place. A recent study has shown that the switching time can be less than several nanoseconds [6], while the relaxation of the generated metastable states in the absence of an electrical field can take more than one year. Therefore, the speed of the switching process spans over 14 (!) orders of magnitude in time. One important observation from this analysis is that switching time and device retention are related properties being usually traded off against each other. Engineering devices with a small activation energy for ion hopping or redox reaction, for example, will improve the switching speed, but simultaneously reduce the retention time. [10]

2.2. Resistive switching oxides

The present thesis focuses on the investigation of resistive switching oxides. Resistive switching oxides represent a large subgroup of resistive switching materials. Commonly resistive switching is observed in metal oxides and has been reported for almost any combination of metal and oxide [10]. Part of a special group among these materials are the transition metal oxides (TMO). TMOs are binary or ternary oxide compounds of transition metals, which due to their partially filled valence bands exhibit a variety of anomalous effects including resistive switching. Stoichiometric TMOs are electrically insulating. However, TMOs have a variety of intrinsic defects (e.g. vacancies) that can alter the valence of the metal atom close to the defect site. According to Yang [10], insulating oxides can be viewed as semiconductors with native dopants, resulting from oxygen deficiency (n-type, for example, TiO_{2-x}) or oxygen excess (p-type, for example, $Co_{1-x}O$). Further, "the thermally and/or electrically activated motion of these native dopants results in chemical changes in the oxides, such as valence state change, leading to resistance switching" [10].

In the following section the more general concepts of resistive switching discussed in Sec. 2.1ff will be adapted to the special case of oxide based materials. Following the defined classification scheme, most oxide systems are of filament-type. Filament growth in oxide systems is explained by nanoscale redox-reactions promoting the creation of oxygen vacancies and their subsequent motion in electric fields [11, 17–19]. The I-V behavior in these systems is bipolar supporting the theory that field-driven ion migration effects are the predominant source of switching. The large device resistance changes between LRS and HRS of a factor 100 and more are mainly attributed to Schottky barrier modulations near the metal/oxide interface [19, 20]. Oxygen vacancy accumulation in the insulating gap between filament tip and counter electrode leads to small space charge zones and low contact resistance. Vacancy depletion on the other hand restores the transport barrier. A model combining both - ionic and electronic - contributions is known as the valence change model (VCM) .

Different oxide based systems like $SrTiO_3$, TaO_x and GaO_x have been investigated as part of this work. In the written form and for the technical implementation of an operando approach, special attention has been given to the TMO system $SrTiO_3$, which represents a model system for the valence change mechanism (VCM, see following subsection for details). The system was selected as a reference system for the implementation of the operando characterization, because of its unique absorption characteristics providing reasonable chemical contrast (chapter 5), its rather slow switching times [21] and because the system is well-characterized throughout the literature. To keep the focus of the present work on the operando PEEM characterization method development and to avoid confusion, results for TaO_x will only be shown in the rare cases, where corresponding data for $SrTiO_3$ are not available.

2.2.1. Valence change model (VCM)

The valence change model is a combined electronic and ionic model used to describe resistive switching in metal oxides [17]. While the ionic motion of oxygen vacancies is necessary to describe the charge carrier modulation and filament formation, transport of electrons over a Schottky barrier is used to describe the non-linear electronic I-V response commonly observed in these materials.

Both processes are coupled by positive or negative feedback: On the one hand, the motion and redistribution of vacancies is a thermally activated process and strongly depends on the local temperature, which can be modulated by Joule heating when electronic currents are present. On the other hand, the electronic transport through a Schottky barrier depends on the potential barrier, which is defined by the local concentration N_D of oxygen vacancies in the near vicinity of the metal electrode.

Under high electric fields or at elevated temperatures oxygen vacancies can be formed and moved within the metal oxide matrix. An oxygen vacancy is a crystallographic point defect. As for other crystallographic defects and imperfections, the position in the lattice (S) as well as the charge state (C,$\bullet = +, ' = -$) can be described in Kröger-Vink notation [22]: M_S^C, where M denotes the element or defect (V for vacancy). Oxygen vacancies are positively double charged and located at the oxygen site: $V_O^{\bullet\bullet}$. Energetically, the doubly ionized vacancies form shallow donor states located less than 0.1 eV below the conduction band and are typically depleted at room temperature [17]. An increase of the oxygen vacancy concentration N_D will lead to n-doping of the material. The Fermi level E_F shifts into the conduction band formed by the metal valence states transferring electrons that have been previously localized at the oxygen site to the metal atom. During this charge transfer process, the valence of the transition metal atom will be reduced to a lower valence (e.g. $Ti^{4+} \rightarrow Ti^{3+}$). This valence change process can be represented by a redox process in which oxygen is removed from the metal oxide according to Eq. 2.1.

$$2 \cdot M^{n+} + O_O \rightleftharpoons 2 \cdot M^{(n-1)+} + V_O^{\bullet\bullet} + \frac{1}{2} O_2 \tag{2.1}$$

As a direct consequence of Eq. 2.1., the formation of molecular oxygen is expected as a byproduct of the redox reaction. Indeed, gas bubble formation under the metal electrodes of MIM structures has been observed in different experiments [23–26] indicating the formation of molecular oxygen, see Fig. 2.5c. The combination of vacancy formation going along with the change in metal valence and the related increase in conductivity is summarized as Valence Change Mechanism (VCM). While the VCM fundamentally explains local variations of the conductivity of the oxide film due to accumulation or depletion of oxygen vacancies, it does not provide any explanation for the non-linear current voltage dependence (I-V) of a full oxide MIM device.

To fully describe reversible switching in oxide MIM devices, three process have to be accounted for: (i) Creation and annihilation of vacancies at the metal electrode interfaces. (ii) Redistribution of the inhomogeneous oxygen vacancy concentration $N_D(\vec{x})$ into filament-like structures providing a conductive percolation path through the insulating bulk. This redistribution is typically induced by migration of the charged vacancies under electric fields and temperature gradients. (iii) Electronic transport of electrons across metal/oxide tunnel barriers.

Creation of oxygen vacancies at interfaces

The creation of oxygen vacancies can be achieved by oxygen removal from the lattice O_O through the material surface into a gaseous state O_2 (g), leaving a doubly charged vacancy at the oxygen lattice site $V_O^{\bullet\bullet}$ and two free electrons e'. The oxygen inside the material is in continuous exchange with the environment/electrode. Oxygen formation in Kröger-Vink notation can be described by Eq. 2.2.

$$O_O \rightleftharpoons \frac{1}{2} O_2(g) + V_O^{\bullet\bullet} + 2 \cdot e' \tag{2.2}$$

Whether oxygen vacancies form or annihilate depends on concentration of oxygen in the environment, the temperature and the electric field strength at the interface. At ambient pressure and room temperature oxygen incorporation into the oxide is preferred, however, if the oxygen concentration on the outside is sufficiently small, e.g. by reducing the oxygen partial pressure (reducing conditions), vacancies will form at the surface. Thicker vacancy layers can be achieved for high temperatures of about 1000-1200K, where the rate of oxygen excorporation and the mobility of vacancies in the bulk increase drastically. Once oxygen depleted layers are formed under high temperatures, these vacancy layers near the surface persist even at room temperature and ambient pressure, because the process of oxygen incorporation is kinetically limited by the speed of oxygen diffusion in the material. The vacancy layer is literally frozen. The formation of oxygen vacancies can be probed by optical investigations being shown for a $SrTiO_3$ single crystal in Fig. 2.5. Crystals with many vacancies appear dark as compared to oxidized samples. The darkening arises from the occupation of the titanium conduction band (CB) states. These states are separated from the Ti t_{2g} states by a crystal field splitting of 2.2 eV (Sec. 3.3). The splitting opens an absorption channel around 2.2 eV as sketched in Fig. 2.5b. Oxygen excorporation is also observed at the oxide/metal interface of MIM devices in form of bubble formation, Fig. 2.5 [24].

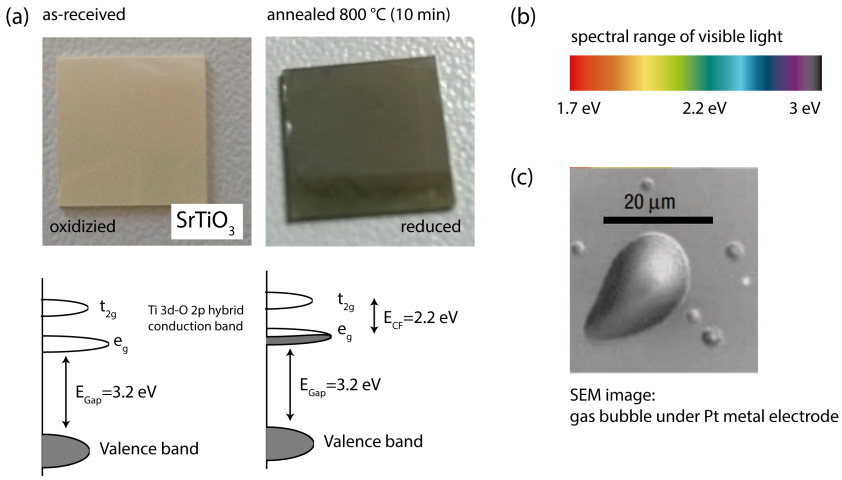

Figure 2.5. – Creation of oxygen vacancies: (a) $SrTiO_3$ single crystal as received (left) and after annealing to 800°C under UHV conditions for 10 min (right). The change in color from pearl white to brown indicates the formation of oxygen vacancies at the surface. The partial filling of the CB opens new absorption channels within the visible spectrum. (b) spectral range of visible light (c) SEM image: bubble formation underneath metal electrodes induced by vacancy formation and corresponding oxygen excorporation. See Ref. [24].

Migration of oxygen atoms and vacancies

The migration of oxygen atoms and vacancies can be treated equally as they are principally described by the same process. In electric fields the motion of both types proceeds via lattice site hopping of oxygen atoms, Fig. 2.6 [27]. The activation barrier for oxygen vacancy transport is reported to be around $W_D = 0.6 - 1.1$ eV [17, 27]. The oxygen vacancy mobility $\mu_{V_O^{\bullet\bullet}}$ is given by the combination of an Arrhenius law with the Nernst-Einstein relation [17] and is depicted in Eq. 2.3.

$$\mu_{V_O^{\bullet\bullet}} = \frac{z_{V_O^{\bullet\bullet}} \cdot e_0}{k_B T} \cdot D_0 \exp(-W_D / k_B T) \tag{2.3}$$

The mobility of the oxygen vacancies is thermally activated and thus critically depends on the local temperature. A temperature increase from $T = 300K$ to $T = 1000K$ enhances the mobility by 10 orders of magnitude. The strong temperature dependence explains the variety of observed switching times spreading from a few nanoseconds up to several minutes. The pronounced non-linearity in ionic transport defines the operation window in MIM devices and is crucial for simultaneously realizing faster switching speeds and longer retention times in memristive devices. High activation barriers increase the state stability at low temperatures, whereas low activation barriers increase the diffusion speed. The direction of oxygen vacancy migration aligns parallel with the electric field gradient, because of an effective positive charge. Ion movement with subsequent valence change is demonstrated for Fe doped $SrTiO_3$ in Fig. 2.6b. From these experiments and O_{18} tracer experiments in secondary ion mass spectroscopy (SIMS) it was further found that vacancy movement along extended defects - including linear chains of vacancies - is enhanced [17]. The diffusion coefficient along a dislocation line is about four orders of magnitude higher compared to the regular lattice and can lead to inhomogeneities in field or diffusion front growth [17].

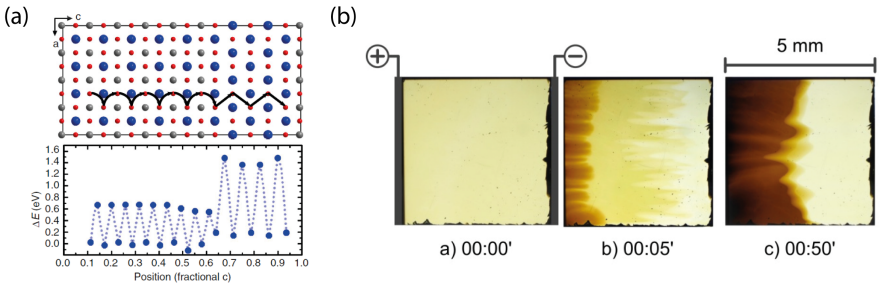

Figure 2.6. – (a) Migration of an oxygen atom across a $SrTiO_3$/SrO interface layer via lattice site hopping (black line, top). The activation energy per hop is show on the bottom. Taken from Ref. [27] (b) Electro coloration in 0.05% Fe doped $SrTiO_3$ single crystal under the application of 200 V with a current compliance of 1 mA. Adapted from Ref. [28]

2.2.2. Electronic transport across metal/insulator interfaces

The strong non-linear I-V behavior in oxide MIM devices, which triggers the migration processes and dominates the resistance change, is attributed to electronic transport across a tunnel junction. The electrode/oxide interfaces in resistive switching oxide MIM structures can be treated as a metal/insulator or metal/semiconductor hetero-junctions. In literature, contacts between metals and semiconductors are referred to as Schottky contacts named after Walter Schottky (1886-1976) [29]. Due to a work function difference between the metal ϕ_M and the oxide layer ϕ_{Ox} a potential barrier ('contact potential') is formed at the interface. The potential barrier arises from the formation of a depletion region in the vicinity of the interface, Fig. 2.7a. Electrons are transferred from the doped insulator towards the metal and vice versa until both Fermi levels are aligned. These rearrangements of the electrons go along with a local band bending $E_{CB}(x)$ due to uncompensated donor/acceptor ions in the semiconductor. The Schottky barrier height Φ_B is predicted by the

Schottky-Mott rule based on the vacuum work function of the metal ϕ_M and the electron affinity χ_{Ox} of the semiconductor (oxide), Eq. 2.4:

$$\Phi_B \approx \phi_M - \chi_{Ox} \tag{2.4}$$

Prediction of the correct barrier height based on Eq. 2.4 often fails due to different interface effects, like Fermi-level pinning. However, the general trend of higher metal work functions leading to higher barriers prevails [29]. Vacancy doped oxide systems are n-type semiconductors and the shape of the potential barrier is defined by donor (vacancy) density N_D in the depletion region x_d. It is assumed that all shallow donors within the region (e.g. oxygen vacancies) are ionized at RT, which leads to an upward band bending near the interface. Space charge regions in the metal can be neglected due to the large number of free electrons in the metal. In most Schottky barrier descriptions a constant charge density N_D within the semiconductor is assumed for the potential calculation and electron contributions are neglected [29]. This "depletion approximation" leads to a linear electric field $E = \frac{q \cdot N_D \cdot x}{\epsilon_s}$, where q is the electron charge, x is the distance from the interface and ϵ_s is the dielectric constant of the n-doped oxide. According to Gauss theorem such an electric field gives rise to a quadratic potential decrease. In the depletion approximation, the depletion layer width x_d and the conduction band offset $E_{\mathrm{CB}}(x)$ within the depletion region can be expressed by Eq. 2.5 and 2.6, where V_a represents an externally applied voltage, N_D the donor (oxygen vacancy) density in the oxide near the interface and Φ_B the Schottky barrier height as derived from Eq. 2.4.

$$x_d = \sqrt{\frac{2 \cdot \epsilon_s \cdot (\Phi_B - V_a)}{q \cdot N_D}} \tag{2.5}$$

$$E_{CB}(x) = \Phi_B - \frac{q \cdot N_D}{2\epsilon_S} \cdot x^2 \tag{2.6}$$

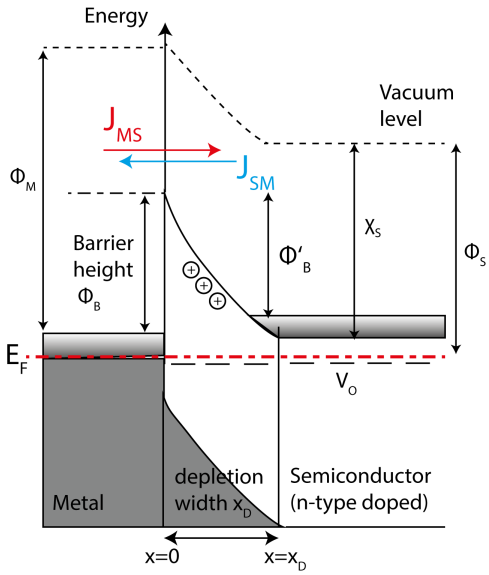

Figure 2.7 – Formation of a potential barrier at the metal/n-type oxide interface. Electrons between the metal and the doped oxide are transferred until the Fermi level is adjusted. If $\Phi_M > \chi_s$ electrons are transferred from the oxide to the metal leaving a depleted, space-charge zone of thickness x_D, which is defined by the oxygen vacancy concentration N_D in the oxide

In the steady state the currents from metal to semiconductor J_{MS} and from semiconductor to metal J_{SM} compensate each other, Fig. 2.7. These compensating currents across the potential barrier consists of classical and quantum-mechanical contributions: Classic transport is observed for 'hot' electrons with a kinetic energy above the barrier height $E > E_F + \Phi_B$ passing from one side to the other. This process is called "thermionic emission" (TE) and dominates for high and wide barriers, where the thickness of the depletion layer x_D is much larger than the wavelength λ of the electrons ($x_D \gg \lambda$). Quantum mechanical tunneling of electrons through the potential barrier on the other hand becomes progressively more important for $x_D \approx \lambda$.

Due to the quadratic band bending in the space charge region, the top of the potential barrier depicted in Fig. 2.8 is thinner than the bottom, which leads to different tunneling conditions for electrons with different energy. The tunneling probability for thermally excited electrons ($E_F < E < E_F + \Phi_B$) is drastically enhanced. The process is called 'thermally assisted tunneling'. Direct tunneling occurs at the Fermi level $E \approx E_F$. In the presence of an external electric field the effective barrier height Φ_B and the barrier width x_d are modified by electronic effects as for example Image-Force barrier lowering [19, 29, 30]. Especially for a high electric field these field-driven effects lead to a strong band bending. In this case, field induced electron emission becomes the main source of the observed currents. In many publications, "thermally assisted tunneling" and "direct tunneling" are relabeled to "thermionic field-enhanced emission" (TFE) and "field emission" (FE), respectively, to account for the additional electric field dependence. Overall, the total current density across the junction is given by the sum of all contributions $J = J_{TE} + J_{TFE} + J_{FE}$, Fig. 2.8a. Detailed descriptions of the different electronic transport channels across a metal/n-type semiconductor interface can be found in E. H. Roderick [29] and Sze [30, p. 166 ff.]. The analytical equations for the two extreme cases of purely thermionic emission (TE) and purely field emission (FE) for a forward bias V_F are given below

$$J_{TE} = A^{**} \cdot T^2 \cdot \exp\left[\frac{-q \cdot \Phi_B}{k_B T}\right] \cdot \left(\exp\left[\frac{-q \cdot V_F}{k_B T}\right] - 1\right) \qquad \text{(Thermoionic Emission)}$$

$$J_{FE} \approx \frac{A^{**} \cdot T \cdot \pi \cdot \exp[-q \cdot (\Phi_B - V_F)/E_{00}]}{c_1 \cdot k_B \cdot \sin(\pi \cdot c_1 \cdot k_B T)} \qquad \text{(Field Emission)}$$

where

$$E_{00} = \frac{q\hbar}{2} \cdot \sqrt{\frac{N_D}{m* \cdot \epsilon}}$$

$$c_1 = \frac{1}{E_{00}} \log\left[\frac{4(\Phi_B - V_F)}{\phi_n}\right]$$

A^{**} denotes the effective Richardson constant, T the temperature, Φ_B the Schottky barrier height, k_B is the Boltzmann constant and q is the electron charge. N_D is the donor density in the semiconductor, m^* the effective electron mass and ϵ the dielectric constant. In the picture of the Schottky barrier, the weighting of the tunneling contributions to the total current strongly depend on the barrier width x_D, which in turn is defined by donor density N_D in the vicinity of the interface. Fig. 2.8b demonstrates, which transport mechanism dominates for a specific donor density. Below $N_D < 10^{18} \frac{1}{\text{cm}^3}$ transport is solely dominated by thermionic emission (TE). Between $10^{18} \frac{1}{\text{cm}^3} < N_D < 10^{20} \frac{1}{\text{cm}^3}$ contributions of thermally assisted field emission (TFE) are taken into account. For values above $N_D > 10^{20} \frac{1}{\text{cm}^3}$ also direct tunneling is observed (FE). Each additional transport channel lowers the contact resistance

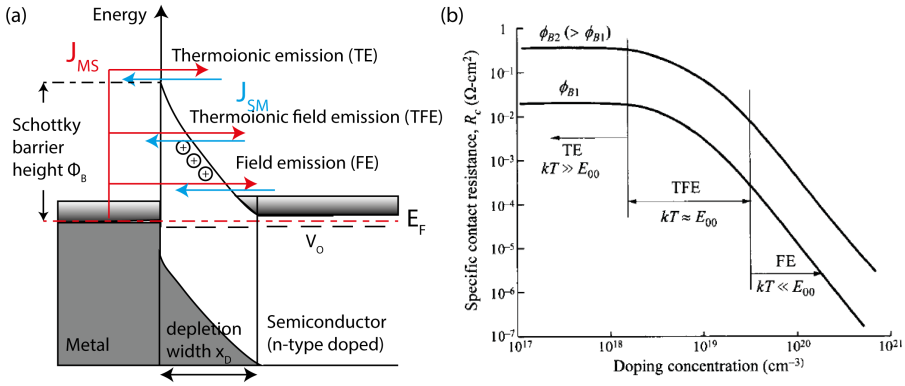

Figure 2.8. – (a) The three dominating transport mechanisms across metal/oxide junctions: Thermionic emission (TE), Thermally assisted field emission (TFE) and Field emission (FE). (b) the relative contribution of each transport mechanism depends on the doping concentration in the vicinity of the interface. Reproduced from [30]

of the interface by orders of magnitude. The strong correlation between donor density N_D and the contact resistance of a Schottky junction is exploited in resistive switching devices. Modification of the donor density by formation, depletion and migration of oxygen vacancies as described in the previous section are the key in understanding the pronounced resistance contrast. High doping concentrations lead to very thin barriers according to Eq 2.5, enabling tunneling processes and representing the LRS. Low doping concentrations lead to an increasing barrier thickness suppressing tunneling effects and representing the HRS.

2.2.3. Unified compact model for VCM devices

A typical VCM device consists of a metal-insulator-metal stack. One electrode forms a Schottky contact with the oxide ($\phi_M > \chi_{Ox}$), while the other electrode is selected to form an ohmic contact ($\phi_M \approx \chi_{Ox}$) with the oxide. Combining the concepts of oxygen vacancy formation and migration with the electron transport properties across MI interfaces, the different steps in operation of a VCM device are illustrated in Fig. 2.9. The device starts with a pre-formed, conductive filament (A), which was formed by creation and modulation of the oxygen vacancy concentration inside the oxide layer by an initial forming step. In subsequent switching cycles the filament is used to control the oxygen vacancy concentration in the vicinity of the Schottky barrier. In a SET process (B) oxygen vacancies are moved into the gap region by electrical forces. The increase in donor density decreases the contact resistance enabling a high current injection. The LRS persists after removal of the electric field and even if the field direction is reversed (C). In the RESET process under reversed polarity the charged vacancies are repelled from the interface and the electrostatic barrier is re-established. The donor density at the interface is gradually decreased and the system slowly returns to the HRS (D).

The RESET process is gradual, because the current I and the donor density N_D form a negative feedback loop: With increasing barrier height, the total current is reduced. With decreasing current also the local temperature decreases. Decreasing temperatures in turn reduce the mobility of the oxygen ions slowing the barrier increase. This is in contrast to the SET process, which forms a positive

feedback loop: The decreasing barrier height in this case increases the device current I, which further heats up the system. The elevated temperatures increase the vacancy mobility, speed up the process of vacancy accumulation. and in this way assist barrier reduction. The complex interplay between

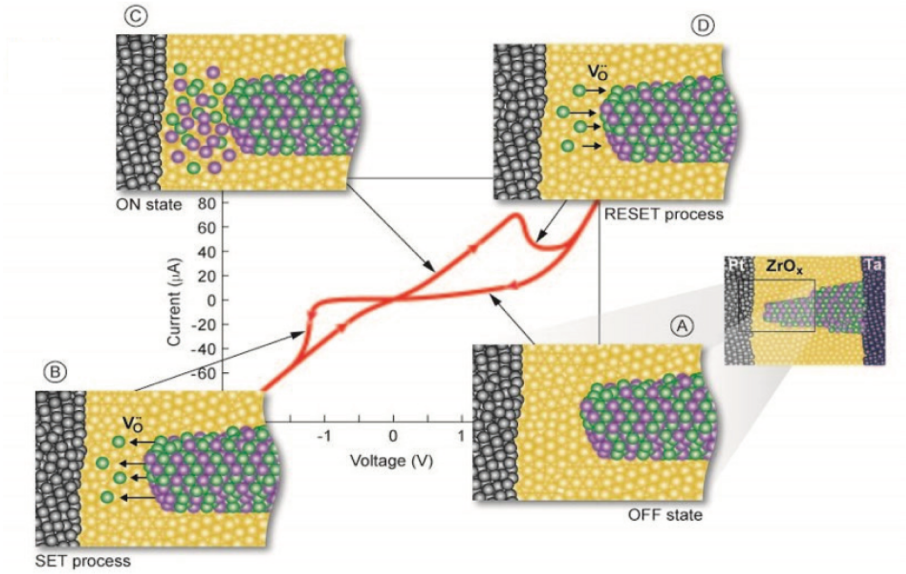

Figure 2.9. – Compact model for VCM in resistive switching in oxides. A complete OFF/ON/OFF cycle for a Pt/ZrO_x/Ta MIM device is plotted on the left (A to D). Black balls represent atoms of the electrode; yellow balls are insulating regions in the oxide. Green balls depict oxygen vacancies and purple balls describe valence changed metal atoms. The center graph shows a simulated I-V curve based on the VCM model. Adopted from [31]

donor density N_D, potential barrier width x_d, device current I, local Joule heating (T,$\dot{\text{T}}$) and the applied voltage V cannot be solved by any analytical approach. Thus, device operation has typically to be simulated. Drift/Diffusion simulations by S. Menzel based on the transport mechanisms depicted above show good agreement with observed I-V characteristics of VCM devices [19]. Still, to provide realistic simulations, filament diameters and charge carrier concentrations have to be determined experimentally from microscopic investigations.

CHAPTER 3

The model oxide system $SrTiO_3$

"The perovskite oxides have been in the focus of over 50 years of investigation, primarily due to their wide-ranging functionality and the fascinating interplay between their crystal structures and properties" [32]. One of the most prominent perovskite oxides is Strontiumtitanate $SrTiO_3$ (short: STO). STO single crystal surfaces have been investigated previously due to their relevance in sensor applications, photo catalysis and as substrates for the epitaxial growth of high-Tc superconductors [33]. In view of the large amount of data and publications being available for this material, $SrTiO_3$ also became a model system for the study of valence change (VC) in transition metal oxides. Similar to other oxides the electrical properties of STO can be modulated from a band insulator to metallic conduction by self-doping with oxygen vacancies acting as shallow donors. Moreover, STO has characteristic and pronounced absorption lines within the soft X-ray region making it a promising material for the elucidation of the dynamics of VC, observed by photoemission-based techniques being the scope of the present work.

3.1. Crystal structure

$SrTiO_3$ crystallizes in a cubic unit cell in a so called ABO_3 perovskite structure with a lattice constant of 3.905Å [32], Fig. 3.1a. Within the unit cell, the Ti atom is located at the B site in the center and is surrounded by six O atoms in octahedral configuration. This configuration is referred to as TiO_6 octahedron. The bonding between the Ti central atom and the oxygen neighbors is assumed to be ionic, leaving the Ti atom in an ionized state of Ti^{4+}, while the oxygen atoms are in a O^{2-} charge state. The A sites at the unit cell corners are occupied by Sr^{2+} ions. Along the [001] direction of the crystal the system can be described by as a stack of alternating SrO and TiO_2 layers. The TiO_6 octahedron configuration is the reason for a characteristic splitting of the Ti 3d conduction band, giving rise to a broad variety of physical phenomena - including resistive switching- and will be discussed in more detail in Sec. 3.3.

3.2. Electronic properties of $SrTiO_3$

Bulk STO crystals are insulators having a band gap of $E_G \approx 3.2$ eV. Donor doping by intrinsic defects like oxygen vacancies or extrinsic substitution of the A site cation can induce n-type doping going

(a)

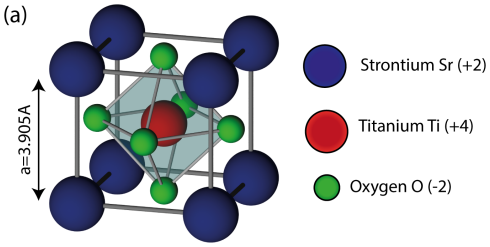

(b)

Property	Value
lattice parameter a [nm]	0.3905
density $[\frac{g}{cm^3}]$	5.2
melting point [°C]	2080
dielectric constant ϵ $[\epsilon_0]$	300
thermal conductivity $[\frac{W}{m \cdot K}]$	12
optical band gap E_G[eV]	3.2

Figure 3.1. – (a) $SrTiO_3$ unit cell. The TiO_6 octahedron is shaded in green. (b) Physical properties of bulk $SrTiO_3$

hand in hand with an increased conductivity. A good example for extrinsic donor doping is Nb:STO. In the case of Nb:STO a doping of 0.5 weight percent Nb into the STO systems - with Nb replacing the Sr sites - leads to almost metallic conductivity. Similar effects are observed for oxygen deficient $SrTiO_{3-\delta}$.

The electronic properties of $SrTiO_3$ can be derived by comparing the electronic configurations of the three contributing elements in their atomic state with their electron configuration in the compound.Elemental Sr, Ti and O have the electronic configurations [Kr]$5s^2$, [Ar]$4s^2 3d^2$ and [He]$2s^2 2p^4$, respectively (Fig. 3.2a). In the $SrTiO_3$ compound, the system minimizes the total energy by redistributing electrons between the different species until all atoms have closed valence shell configurations. In this case the O 2p states are entirely filled and the Ti 3d states are completely depleted, Fig. 3.2b. These states can be referred to as valence band (VB) and conduction band (CB) of STO, respectively. The optical gap is defined by the energetic distance between $E_G = E(\mathrm{Ti\,3d}) - E(\mathrm{O\,2p}) \approx 3.2\,\mathrm{eV}$. The basic model of electron redistribution already qualitatively explains the insulating behavior and crystal structure, even though it does not include band formation, hybridization of orbitals or any other form of electron-electron interaction.

The aforementioned effects can be accounted for by density functional theory (DFT). A site projected DFT calculation performed by Piskunov 2004 [34] is shown in Fig. 3.2c. The calculation shows the site projected and the total density of states (DOS) close to the Fermi energy E_F at $E = 0$ for STO. In this context, site projected means that the total density of states is projected onto the elemental contributions. Only weak interaction between Ti 3d and O 2p bands is observed, which corresponds to a strong ionic bonding and explains the good agreement between the simple valence shell model in 3.2b. The DFT calculations confirm that the valence band (VB; $E < E_F$) is mainly dominated by O 2p states, while the conduction band (CB; $E > E_F$) is formed by unoccupied Ti 3d and Ti 4s states. The Sr 5s states are significantly located above the Fermi level E_F and hence do not contribute to conduction. The major difference between the calculations and the electron redistrubtion model is that the sharp energetic levels of the atomic picture become modulated by band dispersion and minor hybridization of orbitals becomes visible. Further, the calculated Fermi energy for DFT is shifted towards the CB onset, whereas in the other case it would be located within the optical gap.

Electron transport is facilitated by the number of occupied and unoccupied states close to Fermi energy only. Fully occupied or completely empty bands do not contribute to conduction [35, p. 250]. In stoichiometric $SrTiO_3$ the VB is completely filled and the CB is empty leading to the insulating

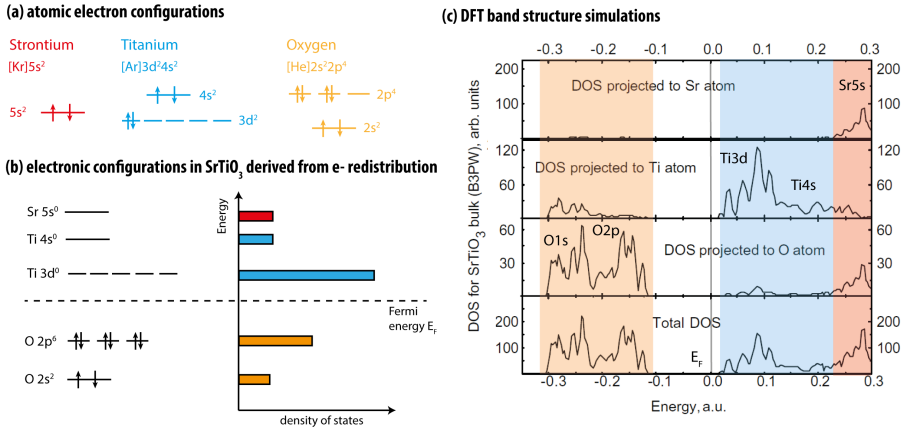

Figure 3.2. – (a) elemental electron configurations for Sr, Ti and O (b) occupied and unoccupied states in $SrTiO_3$ derived from combination of non-interacting atomic orbitals (c) DFT-calculated site projected density of states (DOS) for bulk $SrTiO_3$ sorted by elements. From top to bottom: Strontium, titanium and oxygen partial contributions as well as the total density of states. The colored overlays represent the anticipated orbitals. Modified from Piskunov et al. [34]

behavior. In oxygen deficient $SrTiO_{3-\delta}$, however, oxygen is removed from the lattice and oxygen vacancies $V_{\ddot{O}}$ are created. Oxygen vacancies act as shallow electron donors related to energetic states 0.1 eV below the conduction band [36]. Thermal activation of electrons from these states leads to a partial filling of the Ti 3d states going along with a reduction of the Ti atoms from $Ti^{4+} \rightarrow Ti^{3+}$ near the defect site [17]. The occupation of Ti 3d states is correlated with a shift of the Fermi level into the CB providing a locally enhanced conductivity and explaining why the valence change of the TM can account for resistive switching.

3.3. Structural and electronic correlations: Crystal field splitting in SrTiO3

The DFT calculations depicted in Fig. 3.2c show that bonds in STO have strong ionic character (charge transfer). Further, only weak hybridization between the Ti 3d and O 2p orbitals is observed. The ionic character of the bonding expresses itself in strong electron localization at the atoms and goes along with an electron transfer from the Sr, Ti cations, to the O anions. While Ti and Sr are reduced to Ti^{4+} and Sr^{2+}, the 6 electrons are distributed among the three O atoms, leaving each of them with a net charge of O^{-2}. This net charge distribution within the unit cell gives rise to an electrostatic field referred to as the crystal field (CF), Fig. 3.3a. The crystal field breaks the rotational symmetry and can give rise to energetic splittings. To calculate these splittings, the distribution of the charge is assumed to be located at the atomic sites (point charge model approximation). For crystals with ionic character, the crystal field theory (CFT) in combination with a point charge model predicts crystal field parameters of the correct sign and correct splitting ratios for the energy levels. The theory explains many of the properties of transition-metal complexes with a reasonable degree of accuracy and is employed throughout literature.

In an isolated Ti atom the five 3d orbitals (d_{yz},d_{xz} ,d_{xy} ,$d_{x^2-y^2}$,d_{z^2}) are degenerate in energy due to rotational symmetry of the atomic potential. The shape of each of the 3d orbitals is shown in Fig. 3.3b. In the presence of an octahedral crystal field this degeneracy is lifted and the energy levels split into 2-fold e_g and 3-fold t_{2g} states according to the symmetry of the TiO_6 octahedron, Fig. 3.3c. The splitting ratio of 2 : 3 between the two levels is a direct consequence of the symmetry of the crystal field and can be derived without further calculations from considerations of point group symmetries [37]. The lobes of the $d_{x^2-y^2}$,d_{z^2} orbitals point towards the negatively charged oxygen ions. Electrons in these orbitals experience strong repulsion. The occupation of these states and is thus energetically less favorable. The lobes of the d_{yz},d_{xz} ,d_{xy} orbitals in contrast point towards the Sr atoms and experience less repulsion, making these configurations energetically more favorable. The energy difference Δ_O (O: octahedral) between the two states, is known to be $10 \cdot Dq$. The calculation of the exact value for $10 \cdot Dq$ strongly depends on the "effective" charge Z_{eff} of the central metal atom as well as on the bond distance to the ligands. The value for $10 \cdot Dq$ is usually treated as a semi empirical parameter, taken from experiments [37]. Literature values of Δ_O reported for $SrTiO_3$ in tetravalent (Ti^{4+}) configuration with an lattice constant of $a = 3.905$Å are in the order of $\Delta_O = 2.1 - 2.4$ eV [38–40].[1] Applying the same symmetry arguments to the 2p orbitals, which are aligned along the coordinate axes, it can be concluded that octahedral crystal fields only splits the 3d states, while the 2p states remain degenerated [41].

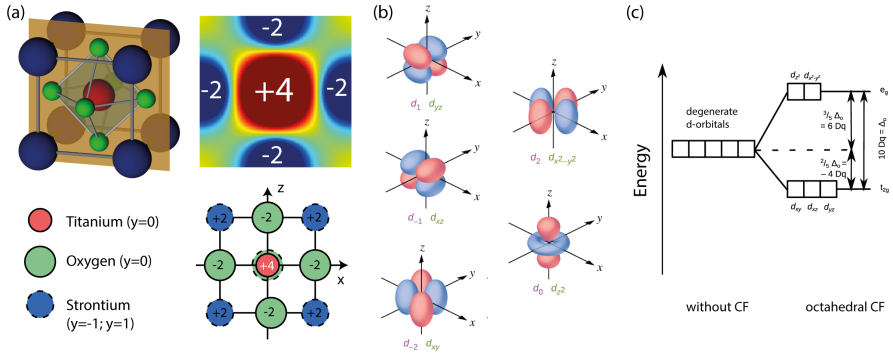

Figure 3.3. – (a) Octahedral crystal field (point group symmetry O_h) in $SrTiO_3$. The equipotential map shows the symmetry of the field. The assumed charge distribution is shown on the bottom (b) Shape of 3d orbitals: The lobes of the $d_{x^2-y^2}$and d_{z^2} orbitals are pointing along the axes of the coordination system towards the negatively charged O^{2-}, whereas the lobes of d_{xy}, d_{yz},d_{dx} orbitals are all oriented at a 45° angle to the coordinate axes. (c) term scheme illustrating the energetic splitting of the 3d orbitals in an octahedral crystal field (CF).

In summary, $SrTiO_3$ shows strong coupling between crystal and electronic structure, which manifests itself in form of a crystal field splitting of the Ti 3d orbitals. The orbital splitting of the Ti 3d states leads to a characteristic X-ray absorption behavior. As will be shown in the following, the absorption

[1] More generally, the splitting of orbitals under arbitrary crystal fields can be described within the framework of crystal field theory (CFT), which was established 1932 by John H. van Vleck in order to explain magnetic and optical properties of 3d transition metals. A detailed theoretical description of the model is given by C. J. Ballhausen, 1962 [37] and by Sugano et al. [41]. For investigations performed in this thesis, the example for an octahedral field will be sufficient.

behavior depends on the valence state of the Ti and thus can provide a tracer for the formation of oxygen vacancies in resistive switching. By simulating the Ti L-absorption edge ($2p \rightarrow 3d$) the characteristic shape for each of the valence states was determined.

3.4. Simulations of the Ti L-edge absorption

The absorption process from the occupied Ti 2p into the unoccupied Ti 3d – O 2p conduction band states was simulated using the charge transfer multiplet tool CTM4XAS [42].[2] First, the energy levels of a free standing, single atom - not accounting for hybridization and band dispersion in solids - are calculated. Subsequently, the transition probabilities between the different atomic orbitals are calculated for spherical symmetry by applying selection rules. In a final step the symmetry of the atomic potential can be defined, being relevant to account for the octahedral crystal field induced by the oxygen neighbors. Ti L-edge absorption spectra were calculated for tetravalent (4+) and trivalent (3+) Ti in octahedral crystal field, Fig. 3.4a & b, for the given initial and final state configurations, where L denotes the core hole created during the emission process.

$$\underbrace{2\mathrm{p}^6\mathrm{3d}^0}_{\text{initial state}} \rightarrow \underbrace{L2p^5\mathrm{3}d^1}_{\text{final state}} \quad (\mathrm{Ti}^{4+})$$

$$\overbrace{2\mathrm{p}^6\mathrm{3d}^1} \rightarrow \overbrace{\mathrm{L2p}^5\mathrm{3d}^2} \quad (\mathrm{Ti}^{3+})$$

The obtained energies and the corresponding transition probabilities are represented by black bars, Fig. 3.4a. For comparison with experimental data discussed in chapter 5, the spectra were artificially convoluted with Voigt functions to account for lifetime Γ and resolution broadening σ. For tetravalent Ti, a peak dependent life time broadening Γ was assumed accounting for an Coster-Kronig Auger decay leading to shortened lifetimes of these states [39, 40, 43]. The experimental resolution broadening $\sigma = 0.25\,\mathrm{eV}$ as well as the value of the crystal field splitting $\Delta_O = 2.2\,\mathrm{eV}$ were derived from best fits to experimental spectra. The value obtained for Δ_O is in good agreement with reported literature values [44, 45]. The main difference between the absorption spectra of tetravalent (Ti^{4+}) and trivalent (Ti^{3+}) Ti arises from different initial and final states. While tetravalent Ti has an empty 3d shell, the partial filling of the 3d orbital in trivalent Ti states causes a fine splitting of the multiplets leading to a strong modulation of the simulated, trivalent spectrum in Fig. 3.5b. Compared to the characteristic line shape of the tetravalent spectrum, the trivalent spectrum is rather flat and has only two pronounced absorption lines around 457.5 eV and 463 eV. These characteristic features of the Ti absorption spectra may serve as indirect fingerprints for the presence of oxygen vacancies, because in the picture of VCM the presence of vacancies is coupled to a change of the metal valence.

To quantify the magnitude of the expected changes in a XAS experiment for a certain amount of trivalent Ti, superpositions of tri- and tetravalent spectra have been simulated for different Ti^{4+}/Ti^{3+} ratios, Fig. 3.5. For less than 10% of Ti^{3+} being equal to about 5% of oxygen vacancies, no significant changes in the spectra can be observed, Fig. 3.5a. For increasing concentrations above 20%, however, a shoulder begins to form around the second peak at 458 eV and the valley-to-peak ratio between the

[2] CTM4XAS is a code based on atomic multiplet calculations that is typically used to describe optical dipole transitions between atomic orbitals for different charge states (e.g. Ti^{4+},Ti^{3+}). The software is optimized for XPS and XAS simulations of transition metal oxides.

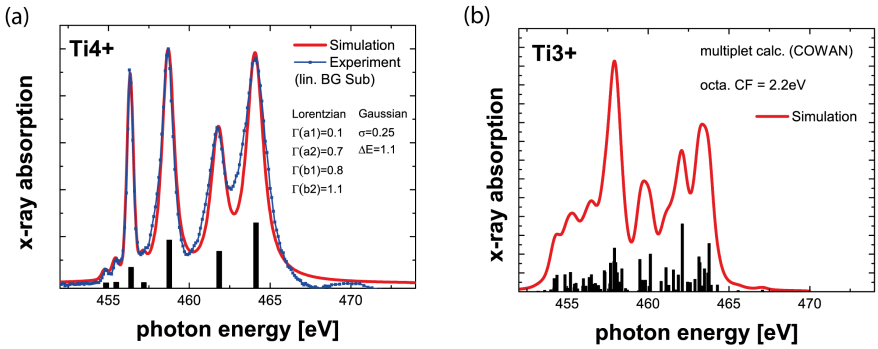

Figure 3.4. – (a) Atomic multiplet calculations for tetravalent Ti in octahedral symmetry (black bars) using CTM4XAS. The crystal field splitting is set to Δ_O =2.2 eV. The simulated transition probabilities are artificially broadened (red) to match experimental X-ray absorption spectra of stoichiometric $SrTiO_3$ (blue) (b) the same simulations performed for trivalent Ti.

peaks around 462 eV and 464 eV, and the valley at 463 eV steadily decreases, providing a promising chemical contrast for in-situ and operando detection of vacancy formation.

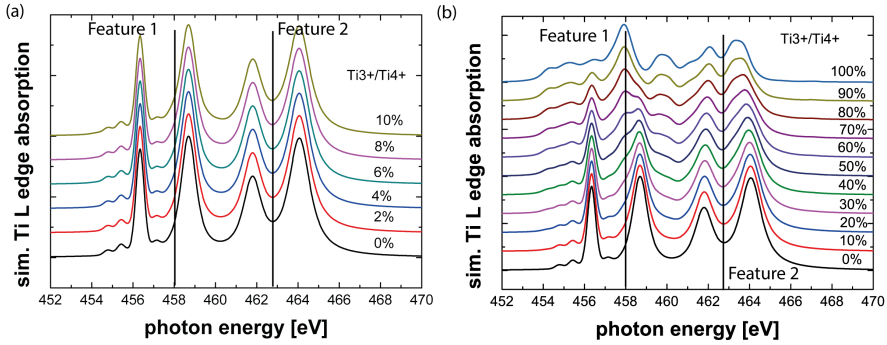

Figure 3.5. – Superpositions of Ti L-edge spectra for Ti^{4+} and Ti^{3+} in octahedral configuration (Δ_O =2.2 eV) for a varying Ti^{3+} fraction (a) 0 – 10 % Ti^{3+} in 2 % steps and (b) 0 – 100 % Ti^{3+} in 10 % steps

Note however, that the simulated trivalent Ti spectra have to be handled with caution, because they were performed under the assumptions that (a) the octahedral crystal field stays intact and (b) the field does not change in strength when an oxygen vacancy is formed. A formation of an oxygen vacancy means that one oxygen atom is removed from the unit cell and the octahedral symmetry is inevitably reduced to a square pyramidal symmetry (point group: C_{4v}). In presence of an isolated vacancy the Ti and Sr atoms can be displaced by as much as 1.4%. [36] For vacancy clusters, displacements are expected to accumulate. Therefore, both assumptions only hold true for small vacancy concentrations.

CHAPTER 4

Photoelectron emission spectroscopy & microscopy

In the past decades photoelectron spectroscopy (PES) has proven to be one of the most powerful tools in solid state physics and materials science to probe the chemical and electronic structure of a given material. The method is based on the photoelectric effect first observed by Heinrich Hertz in 1887 [46] and later explained, invoking the quantum nature of light, by Albert Einstein [47] in 1905. Einstein was rewarded with a Nobel Prize in 1921 "for his services to theoretical physics, and especially for his discovery of the law of the photoelectric effect". [48] The effect explains the interaction between light and matter, specifically, it describes the emission of an electron bound in the solid to vacuum due to the interaction with a single, quantized photon. The photon in this two particle process is completely absorbed and its full momentum as well as its energy are transferred to the electron, obeying the laws of momentum and energy conservation. For low photon energies in the ultraviolet up to the soft X-ray region the momentum transfer of the photon can be neglected as it is small compared to the electron momentum and the situation can be simplified to an energy balance as given in Eq. 4.1:

$$h\nu = E_{\mathrm{B}} + E_{\mathrm{kin}} + \Phi \tag{4.1}$$

The photon energy $h\nu$, which is transferred to the electron, is split into three contributions: (i) the binding energy E_{B} describing the energy that needs to be provided to free the electron from the nucleus, (ii) the work function Φ describing the energy that needs to be provided to bypass the potential barrier at the crystal surface and (iii) the kinetic energy E_{kin} the electron has left after emission into vacuum. The binding energy of an electron is a direct consequence of the chemical bonding in the crystal and plays a significant role in chemical analysis. The binding energy cannot directly be measured, but according to Eq. 4.1 the information is encoded in the kinetic energy distribution of the emitted photoelectrons for monochromatic excitation. Thus, the real significance of the photoemission approach became evident when first electron spectrometers with sufficient energy resolution of a few eV became available. A major personality in this context was Kai Siegbahn together with his coworkers. By developing novel electron spectrometers and integrating them to photoemission experiments, they were able to filter the photoemitted electrons with respect to their kinetic energy and to extract chemical information out of the kinetic energy distribution by

comparing emission peaks to the electron binding energies in an atom. Due to the capability to chemically distinguish different materials by this method, the term ESCA (electron spectroscopy for chemical analysis) was born. In 1981 Siegbahn was rewarded the Nobel Prize for his “contribution to the development of high-resolution electron spectroscopy" [49].

Generally, electrons in a solid are defined by four degrees of freedom, which can be recovered from the analysis of the photoemitted electrons: A spatial coordinate $\vec{x}$ defined as the point of emission, a direction and velocity defined by their momentum $\vec{k}$, a defined spin orientation $\vec{s}$, and a kinetic energy E_{kin}. The analysis of the various attributes of the photoemitted electrons is referred to as photoelectron emission spectroscopy (PES) & microscopy (PEEM).

The principal experimental configuration of a photoemission experiment has not changed since the pioneering works almost 100 years ago: It consists of a monochromatic light source and an electron analyzer [50]. While first experiments were limited to the binding energy analysis of the emitted photoelectrons $I(E_\mathrm{B})$, modern instruments provide access to additional properties of the electron: the spatial origin of the electrons $I(\vec{x},E_\mathrm{B})$ can be accessed by PhotoEmission Electron Microscopy (PEEM), the momentum distribution $I(\vec{k},E_\mathrm{B})$ is discriminated by angular resolved photoemission spectroscopy (ARPES) and the spin component can be measured by further discrimination of the electrons according to their spin in a spin-resolved photoemission experiment (spin-PES). The latest generation of spectrometers combining spectral and spatial information are called spectromicroscopes (see 4.5) and will be used in the present work. These instruments principally allow to resolve all four properties in a single experimental design due to a set of electron-optical components, which conserve the phase space information.

4.1. Three-step model of photoemission

In a simple picture the full photoemission process from excitation to vacuum emission can be described in three individual steps (Excitation, Transport and Transmission) within the so-called *three-step model*, Fig. 4.1 [50]. The three-step model is not accurate in a quantum mechanical sense, however, it is very intuitive and can be used to qualitatively explain the most important features of measured photoemission spectra, such as the work function cut off Φ at low kinetic energies and the high surface sensitivity defined by the electron emission depth. More sophisticated models for quantitative description of the emitted electrons are based on one-step photoemission calculations, where the three steps are treated as a single quantum mechanical process [51]. For the purpose of this work, however, a description of the photoemission process in the framework of the three-step model is sufficient.

- **Excitation (Fig. 4.1 Step 1):** The first step is the photo-excitation process. It describes the interaction between the photon and the electron via the photoelectric effect. The excitation depends on the photon energy, the photoionization cross section and the light polarization. A quantum mechanical description of the excitation process is given in Sec. 4.2.

- **Transport (Fig. 4.1 Step 2):** Once the electron is excited from a core level into an energetically higher unoccupied state above the Fermi level, the nearly free electron moves within the crystal. In the solid it undergoes several scattering events with other electrons, with phonons or with

lattice defects. The scattering can be either elastic (change of direction without loss of energy) or inelastic (energy loss). The average distance between two scattering events can be described by the elastic or inelastic mean free path of the electron, λ_{MFP} or λ_{IMFP}, respectively.

- **Transmission (Fig. 4.1 Step 3) :** If the electron reaches the surface of the material, it has to overcome a potential step formed by a surface dipole. Only if the kinetic energy along the surface normal exceeds the potential barrier, the electron can be transmitted into vacuum. Electrons not fulfilling this condition will be reflected at the material/vacuum interface. In this sense the potential barrier acts as high pass filter for electron kinetic energies and leads to refraction. Reflected electrons will not leave the crystal giving rise to a sharp emission onset known as the work function cut-off.

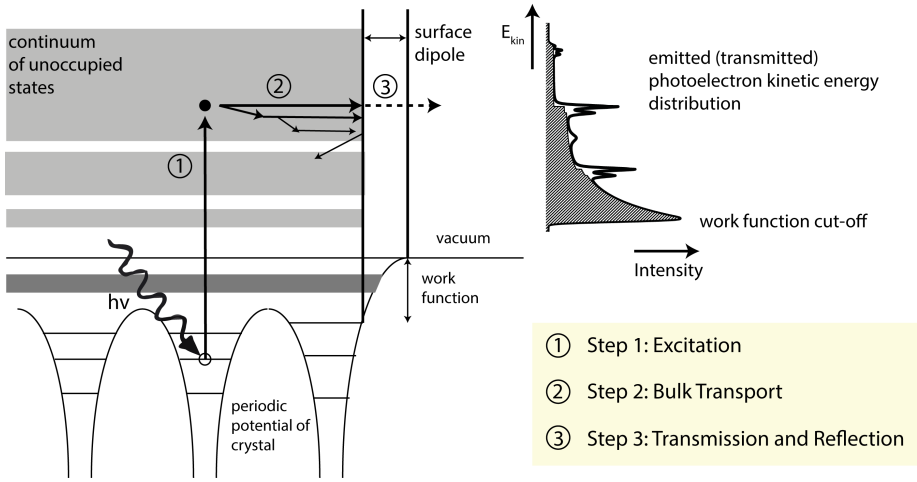

Figure 4.1. – Three-step model of the photoemission process: (1) A photon with energy $E = h\nu$ is absorbed by a bound electron in the solid, which in turn is excited into the continuum of unoccupied states. (2) During its travel through the crystal the electron undergoes elastic and inelastic scattering events. (3) When the electron reaches the surface it has to overcome a surface potential barrier before being transmitted into vacuum. The kinetic energy distribution of the emitted electrons is a replica of the electronic states in the crystal. Image inspired by [50]

4.2. Quantum mechanical description of the excitation process

In a quantum mechanical picture the excitation process in the *three-step model* can be described as a perturbation of the electronic N particle system with wave function Ψ by the electric field of the photon $\hat{H}_{\mathrm{Ph}}$. During this process the N particle system is transformed into a N-1 particle system after the photoelectron is excited. Usually the theoretical treatment is simplified by the following approximations: First, the many particle wave function Ψ is reduced to a single electron wave function neglecting interactions between different electrons. Second, the impinging light is often treated in

the *electric dipole approximation*, which holds if the wavelength of the electromagnetic radiation λ inducing the photoemission process is much larger than the typical size of an atom. In this case the local electric field at the position of the atom can be assumed constant during excitation. The approximation thus holds as long as $k \cdot r$ is small, where $k = \frac{2\pi}{\lambda}$ denotes the wave vector of the photon and r is the mean radius of the electron wave function in the atom. For values of $k \cdot r$ close to 1, quadrupole effects have to be taken into account and the dipole approximation breaks down. For photon energies below 10 keV, however, $k \cdot r$ is smaller than 0.2 and hence quadrupole effects can be neglected. Finally, the process is assumed to happen instantly (*sudden approximation*) so that initial and final state of the N electron system can be used and changes of the wave function caused by the excited electron can be neglected.

Applying all approximations, the emission probability $P_{i\to f}$ can be described by *Fermi's golden rule* (Eq. 4.2), which provides a theoretical prediction of the transition rates from an initial electron quantum state $|i\rangle$ into a final state $\langle f|$ with the corresponding binding energies E_i and E_f in case of a perturbation $\hat{H}$

$$P_{i\to f} = \frac{2\pi}{h} |\underbrace{\langle f|\hat{H}|i\rangle}_{=M_{fi}}|^2 \cdot \delta(E_f - E_i - h\nu) \tag{4.2}$$

In the special case of the dipole approximation the perturbation induced by light is described by $\hat{H} = \epsilon \cdot \vec{r}$, where ϵ denotes the electric field strength and $\vec{r}$ denotes the dipole direction. The delta function in Eq. 4.2 guarantees that only transitions that comply with the law of energy conservation are taken into account. Overall, the transition probability $P_{i\to f}$ is dominated by the matrix element M_{fi}, which describes the wave function overlap between initial and final state under perturbational approach. Under certain circumstances M_{fi} can be calculated and used to predict and calculate photoionization cross sections and selection rules. A detailed description will be given in the next section.

4.2.1. Photoionization cross sections $\sigma_{n,l}$

The transition probability $P_{i\to f}$ defined in Fermi's golden rule (Eq. 4.2) is governed by the matrix element M_{fi}. The matrix element M_{fi} on the other hand is defined by the spatial overlap between the initial and final state wave functions $|i\rangle$ and $\langle f|$ in case of a perturbational approach. The matrix element is maximized if the spatial overlap between the two wave functions is large and it becomes zero if no overlap is present. For an explicit calculation of the matrix element M_{fi} both states - initial and final - have to be known. In most systems the exact wave functions are unknown. On that account, very often atomic orbitals are used as initial states $|i\rangle$, while the final state $\langle f|$ is described by a free electron. In this context the probability of a photoabsorption event for an electron from a specific atomic orbital defined by the principal quantum numbers n and the azimuthal quantum number l $|\Phi_{n,l}\rangle$ into a free electron final state $\langle f|$ can be described by the photoionization cross section Eq. 4.3

$$\sigma_{nl}(h\nu) = \frac{2\pi}{h} \int |\langle f|\hat{H}|\Phi_{n,l}\rangle|^2 \cdot \delta(E_f - E_{n,l} - h\nu)\, dh\nu \tag{4.3}$$

The *partial photoionization cross-section (PPCS)* $\sigma_{nl}(h\nu)$ describes the total number of electrons excited from a specific atomic orbital in dependence on the photon energy $h\nu$. A compilation of calculated photoionization cross sections for various elements and for photon energies below 1500eV

is tabulated in J. J. Yeh [52]. Fig. 4.2 shows examples of calculations of the ionization cross section $\sigma_{n,l}(h\nu)$ for three different atomic orbitals of Strontium. The *total absorption cross section* $\sigma(h\nu)$ being defined as the absorption coefficient for a specific photon energy is calculated by adding all orbital contributions $\sigma(h\nu) = \sum_{n,l}\sigma_{nl}(h\nu)$. The modulation of the total absorption cross section is thus element-specific and can be used for chemical analysis (see X-ray absorption spectroscopy, 4.4.2).

Note, that photoionization cross sections $\sigma_{nl}(h\nu)$ decrease with increasing photon energy $h\nu$. This effect is related to the fact that the spatial modulation of the final state wave function increases for higher energies and the spatial overlap between the initial and final state gets smaller the larger the energetic distance $\Delta E = E_f - E_i$ between the two states [50]. The decreasing photoemission cross sections for shallow core levels at high photon energies play a major role in hard X-ray PEEM (as will be discussed in Chapter 6). The total cross section $\sigma(h\nu)$ is related to the attenuation coefficient of light as it also quantifies the number of absorbed photons. Thus, it can be used to calculate the penetration depth of light into the material $\lambda_P(h\nu) = \frac{1}{\rho\sigma(h\nu)}$ if the density ρ of the material is known. For soft X-rays λ_P typically reaches the order of 200 Å exceeding the typical escape depth of the electrons by a factor of 5-10 [53].

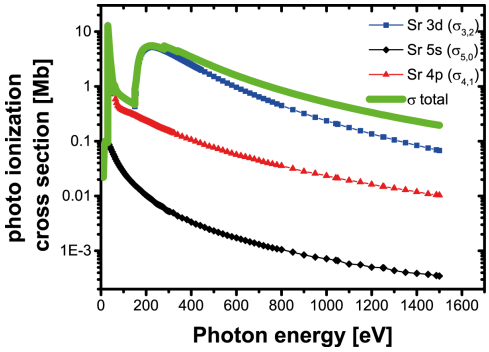

Figure 4.2 – Calculated photoionization cross sections σ_{nl} for different core levels in elemental Strontium. The total absorption cross section σ is plotted in green [52].

4.2.2. Dipole selection rules

For certain combinations of initial $|i\rangle$ and final states $\langle f|$ the matrix element M_{fi} in the dipole approximation is zero. In this case the transition is called *dipole forbidden*. The rules on which of the transitions are forbidden give the *dipole selection rules*.

The dipole selection rules are a direct consequence of the symmetry of the initial $|i\rangle$ and the final state $\langle f|$ and the perturbation $\hat{H}$ itself. They are of utmost importance in the description of X-ray absorption spectra. If non-interacting atomic orbitals are considered as initial and final states, the matrix element M_{fi} in dipole approximation can be analytically calculated. Each atomic orbital $|\Phi_{n,l,m,s}\rangle = |R_{nl}(\vec{r}) \cdot Y_{lm}(\theta,\phi) \cdot \chi(s)\rangle$ then can be decomposed into a radial part $R_{n,l}(r)$, an angular part expressed in terms of spherical harmonics $Y_{l,m}(\theta,\phi)$ and a spin component $\chi(s)$. At the same time the operator $\hat{H}$ for linearly polarized light can be expressed as $Y_{1,0}$. For the transition from one orbital $|\Phi_{n1,l1,m1,s1}\rangle$ into another orbital $|\Phi_{n2,l2,m2,s2}\rangle$ Fermi's golden rule translates into $\frac{2\pi}{\hbar}|\langle\Phi_{n1,l1,m1,s1}| Y_{1,0} |\Phi_{n2,l2,m2,s2}\rangle|^2 \cdot \delta(E_{n1,l1,m1,s1} - E_{n2,l2,m2,s2} - h\nu)$. In this special case, when two

atomic orbitals are employed as basis, it can be derived from the orthogonality relation of spherical harmonics, that for a photoemission process in *dipole approximation* the following selection rules defined in Eq. 4.4a-c. While the angular momentum l must change by 1 ($\Delta l = \pm 1$), the total spin s is not allowed to change ($\Delta s = 0$).

$$\Delta l = l_2 - l_1 = \pm 1 \tag{4.4a}$$

$$\Delta m = m_2 - m_1 = 0, \pm 1 \tag{4.4b}$$

$$\Delta s = s_2 - s_1 = 0 \tag{4.4c}$$

The selection rules explain why L- ($p \rightarrow d$) and K- ($s \rightarrow p$) edges in X-ray absorption are most pronounced.

4.3. Probing depth & Surface sensitivity

In the transport step of the *three-step model* (Fig. 4.1 Step 2) the excited electrons propagate through the crystal and undergo elastic and inelastic scattering events. While the elastic scattering only affects the direction of the propagation, inelastic scattering leads to an additional loss of kinetic energy. The latter equals to a loss of the chemical information, because a proper recalculation of the binding energy from photoemission spectra according to Eq. 4.1 is not possible anymore. This is the reason why only elastically scattered or unscattered electrons, which reveal the characteristic emission energies, can be considered in the chemical analysis. Typically inelastic scattering is dominated by electron-electron interactions, but can also include losses caused by phononic or plasmonic excitations. Hence, chemical information loss will be linked to the length scales of these processes.

The average distance between two inelastic scattering events is defined by the inelastic mean free path λ_{IMFP}. For a known λ_{IMFP} the number of unscattered electrons N can be calculated in dependence of the traveled distance d by an exponentially decaying function of the initial number of excited electrons N_0, Eq. 4.5.

$$N = N_0 \cdot \exp(-\frac{d}{\lambda_{IMFP}}) \tag{4.5}$$

The exponential behavior implies that after a distance three times as large as the inelastic mean free path ($d = 3 \cdot \lambda_{\mathrm{IMFP}}$) more than 95% percent of the electrons have been scattered. Typically, this value defines the *information depth* of a photoemission experiment from which 95% of the chemically relevant signal arises.

Inelastic mean free paths can either be measured or be calculated. In 1979 Seah and Dench [54] published a compilation of experimental values for IMFPs acquired for different elements, Fig. 4.3a. Typical values for IMFPs are found in a range of $4-50$Å. The values show a strong dependency on the kinetic energy of the electrons, but only small variations between different elements. The curve has a minimum of less than 4Å for electron kinetic energies around $50-150$ eV (region of highest surface sensitivity) and increases up to several nanometers to both ends of the energy spectrum. The fact that the measured inelastic mean free path differs only negligibly for different elements, makes this curve "universal". The reason for this universal behavior is explained in [50, p. 10]: For kinetic energies E_{kin} above 10 eV the excited electrons in the solid are almost free and independent of bonding properties

evoked by the underlying crystal. Then the electrons can be described by a free-electron gas. In this case the electron energy loss function is determined by the plasma frequency, which is only a function of the electron density and similar in magnitude for all elements.

Due to the fact that photoemission experiments rely on the analysis of emitted electrons, the probing depth of **any** photoemission experiment is limited to a maximum of roughly $3 \cdot \lambda_{\mathrm{IMFP}}$, which is equal to $\approx 12-150\,\text{Å}$ [50]. The strong dependency between the electron kinetic energy and the corresponding probing depth implies that different experimental methods and conditions result in a different surface sensitivity. Standard soft X-ray photoemission typically works with electrons having kinetic energies close to the minimum of the inelastic mean free path. This method has the highest surface sensitivity and is limited to the top most layers of a material. The high surface sensitivity of a few atomic layers also stresses the importance of UHV conditions in these types of experiments as additional layers of adsorbates will strongly reduce the signal intensity. In hard X-ray photo emission (HAXPES) the electrons of shallow core levels have kinetic energies of a few 1000 eV extending the inelastic mean free path up to 6 nm [55]. For HAXPES a total probing depth of up to 18 nm can be reached. X-ray absorption mainly works with slow secondary electrons and is expected to have an intermediate probing depth of $1-4$ nm based on the experimental data provided in this thesis. In the context of the present work, these differences in the probing depth will play a major role in chapter 6, where strategies are developed to circumvent the high surface sensitivity of the photoemission process in order to image chemical changes in layers of resistive switching materials buried below an metal top electrode.

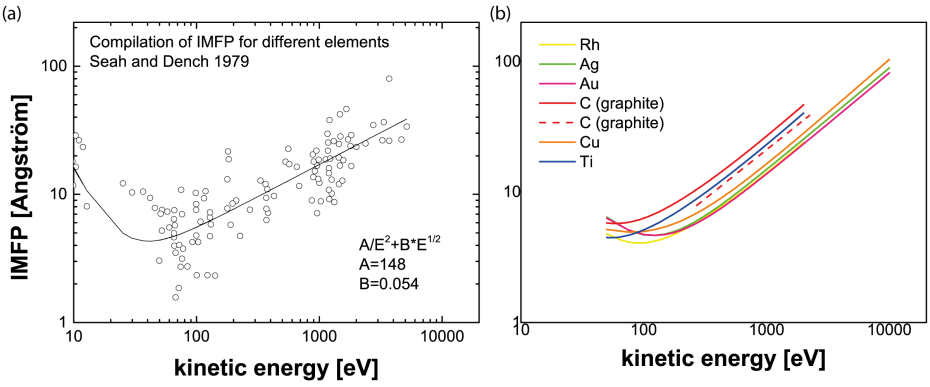

Figure 4.3. – "Universal curve" of photoemission: (a) experimental inelastic mean free path for different elements in dependence of the kinetic energy of the photoemitted electrons. The data was compiled by Seah and Dench in 1979 (digitized from [54], white dots). The black curve is a functional fit of the form: $\frac{A}{E^2} + B \cdot \sqrt{E}$. (b) inelastic mean free path calculated for different elements using the Penn algorithm summarized in NIST Standard Reference Database 71, see Ref. [56].

For reasons of completeness it has to be mentioned, that Powell and Jablonksi [57] consider the data acquisition in Seah and Dench [54] as unreliable and question the universality of the curve. Therefore, in a more sophisticated approach Tanuma, Powell and Penn [56] performed calculations of the inelastic mean free path for kinetic energies between 50 eV – 30 keV based on the Penn algorithm

and experimental optical data of the dielectric function. [1] Indeed, their results show a weak material dependence, Fig. 4.3b. Yet, a direct comparison between the experimental results of Seah et al. and the simulations of Tanuma et al. (Fig. 4.3) shows great consistency in the general trend and the expected magnitude of the IMFPs. With respect to the aims of the present work, both groups state the same: the escape/probing depth of photoelectrons is limited to the first few nanometers of a material and increases for higher kinetic energies. Further the limited probing depth results from the fundamental physical process of electron-electron scattering and thus can never be avoided.

4.4. Electron Spectroscopy for Chemical Analysis (ESCA)

In the previous sections the fundamentals of the photoemission process have been described. Now, the focus is shifted towards the material properties that can be derived by analyzing the emitted electrons using X-ray photoemission spectroscopy (XPS) or X-ray absorption spectroscopy (XAS). While XPS analyzes the kinetic energy distribution of the emitted electrons and can be used to probe the occupied states, XAS analyzes the absorption characteristics of a material by varying the photon energy and is used to probe the unoccupied states. The two approaches are complementary to each other and both provide highly element-selective analysis. Details on each of the techniques will be given in the following section.

4.4.1. X-ray photoemission spectroscopy (XPS)

In an XPS experiment the sample is illuminated by monochromatic light of energy $h\nu$ and the emitted kinetic energy distribution $I(E_{\mathrm{kin}})$ of the electrons is measured, Fig. 4.4a. For a fixed photon energy and known work function Φ, the measured kinetic energy distribution $I(E_{\mathrm{kin}})$ can be used to calculate the corresponding binding energy (XPS) spectrum $I(E_{\mathrm{B}})$ according to Eq. 4.1. The binding energy spectrum is a replica of the occupied states in the solid filtered by the photoemission process. It consists of a set of characteristic emission lines defined by the electronic structure of the material under investigation. Peaks in emission are observed whenever the condition $E_{\mathrm{kin}} = h\nu - E_B - \Phi$ (Eq. 4.1) is fulfilled. Thus, each peak is related to a transition from a binding orbital into vacuum. As binding energies E_{B} are unique for each specimen, evaluation of binding energy positions can be used for chemical analysis. Calculated and experimental reference values for binding energies are tabulated and can be found in databases [58].
A typical XPS spectrum is shown in Fig. 4.4b. The spectrum can be classified into three distinct regions: **Region I** is called valence band (VB) region and describes electrons close to the Fermi level with binding energies of up to 20 eV. In this region the effects of the atomic potentials are less pronounced, the electrons are delocalized and the electronic wave functions of neighboring electrons start to overlap. The interaction between the wave functions leads to the formation of energy dispersive bands. These interactions define the chemistry and bonding in a material. The VB region is populated by electrons originating from all contributing elements of the material. Due to the strong interaction and the large number of states in the vicinity of the Fermi level the measured features are smeared out and strong modulations are observed. The VB contains all information on the chemical bonding, electronic and optical properties. Very often the observed features can only be explained by DFT calculations. **Region II** is called the core level (CL) region starting from $E_B \approx 20\,\mathrm{eV}$

[1] The calculations using a similar version of the algorithm are summarized in the NIST Standard Reference Database 71 provided by Powell and Jablonski

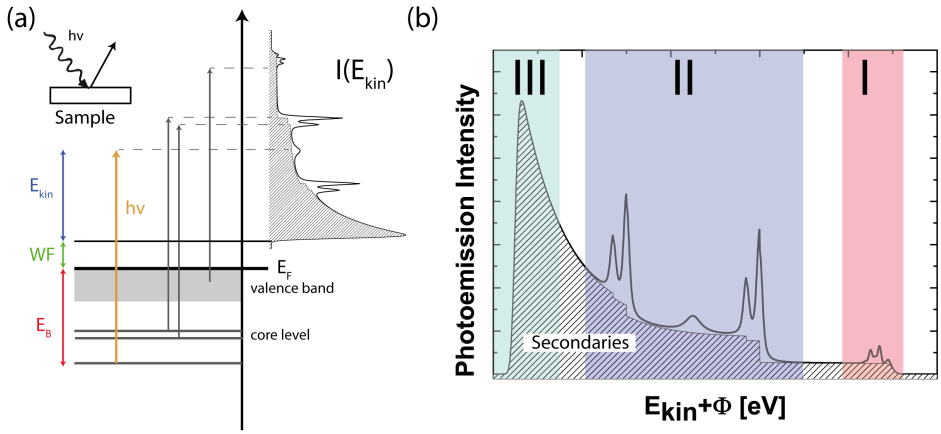

Figure 4.4. – (a) Scheme of a photoemission process. The photon energy (yellow) is transferred to an electron bound in the solid. Some of the energy is consumed to overcome the binding energy E_B (red) and the surface potential Φ (green). The remaining energy is left in form of kinetic energy E_{kin} (blue). (b) Schematic photoemission spectrum: The measured electron kinetic energy E_{kin} is plotted versus the intensity I of the photoemission signal. Three characteristic regions can be distinguished, which are explained in the text.

extending upwards in energy. The CL region is mainly characterized by sharp emission peaks with distinct binding energies. The wave functions of electrons in this regions are localized to the atomic core and they do not interact directly with other wave functions. Hence, their properties are directly related to the specific element and can be used as element selective probes. Intensity and energy of these peaks are typically used to identify the material composition. **Region III** reveals an exponential increase of the emission intensity for smallest kinetic energies before the intensity sharply drops to zero. The main intensity in this region stems from low-kinetic electrons, also known as secondary electrons, because they have been created by multiple, inelastic scattering events of the photoexcited electrons. As for this reason the region is referred to as the *secondary edge*. The hard cut off at the secondary edge is caused by the work function Φ. Electrons with energies smaller than $E < E_B + \Phi$ are reflected at the potential step (Fig. 4.1b) and cannot leave the crystal. The work function Φ is a material and surface dependent property. Typical values are in the range of $\Phi = 2.3 - 6\,\text{eV}$.

Peak intensity analysis formula of core photoelectron emission

If the material under investigation consists of more than one atomic species ($Q > 1$), the measured emission spectrum is a superposition of each of the contributing elemental spectra $I = \sum_Q w_Q \cdot I_Q(E_{kin})$, where Q denotes the number of different elements. The spectral weight w_Q of each contribution can be used to calculate the composition of the material. A full analysis of peak positions, peak areas, chemical shifts and the spin-orbit splittings allows a highly accurate discrimination of different elements, bonding configurations as well as compositional analysis.

The intensity of a core level photoemission line contains viable information on the chemical state and composition of a material. Equation 4.6 provides a theoretical framework to describe the expected

number of detected photoelectrons emitted from an atom species Q with atomic quantum numbers n and l [59]. The equation takes into account the photon intensity of the impinging light $I_{h\nu}$ with polarization vector $\vec{\epsilon}$, the transmission of the electron analyzer T, as well as material parameters given by the density ρ_Q and the photoionization cross section σ_{Qnl} (Sec. 4.2.1).

$$I(Q,n,l) = \int_0^\infty \int_0^\infty \int_0^\infty \underbrace{I_{h\nu}(x,y,z,\vec{\epsilon})}_{\text{photon intensity}} \cdot \underbrace{\rho_Q(x,y,z)}_{\text{material density}} \cdot \underbrace{A \cdot \exp\left(-\frac{z}{\lambda_{\text{IMFP}}(E_{kin}) \cdot \cos\theta}\right) \cdot \frac{1}{m_Q}}_{\text{effective volume}} \times \underbrace{\frac{\sigma_{Qnl}(h\nu,\vec{\epsilon})}{d\Omega}}_{\text{photoionization cross section}} \cdot \underbrace{T(E_{\text{kin}},\Omega(\phi,\theta))}_{\text{analyzer transmission}} \cdot \mathrm{dx\,dy\,dz} \quad (4.6)$$

The surface sensitivity of PES - as discussed in Sec. 4.3 - is considered by reducing the *probed volume* $V = \mathrm{A} \cdot \mathrm{z}$ (z = sample thickness) to an *effective volume* employing the depth-dependent attenuation coefficient (see Eq. 6.1). A is defined as the illuminated area and λ_{IMFP} is the inelastic mean free path. θ is the angle between the emitted electrons and the surface normal. The transmission function T of the analyzer is mainly determined by the acceptance angle $\Omega(\theta,\phi)$ and the kinetic energy of the electrons E_{kin}. Conversion losses within the electron detectors (e.g. channeltron, imaging unit) are usually not accounted for.

4.4.2. X-ray absorption spectroscopy (XAS)

In contrast to XPS, where electrons are excited from the solid with a *fixed, monochromatic photon energy* and the kinetic energy spectrum of these electrons is measured, in X-ray absorption spectroscopy (XAS) *the photon energy is tuned* and electrons from a fixed kinetic energy range are detected. As explained in subsection 4.2.1 the light absorption due to photoelectric effect for a specific photon energy can be explained by the total absorption cross section $\sigma(h\nu)$, which results from Fermi's golden rule and is modulated by the electronic structure. At certain photon energies steep increases in the total absorption will be observed, Fig. 4.5a. These steps are element specific and called absorption edges. An absorption edge is observed whenever the photon energy becomes large enough to overcome the binding energy of an electron ($h\nu > E_{\text{B}}$). Above these energies, core level electrons can be emitted into an unoccupied state above Fermi by photon absorption, while at the same a core hole is generated.

The generated core hole itself has a typical lifetime of about $\tau = 10^{-15} s$ before it is refilled by electrons residing at lower binding energies. During this transition energy is released is released in form of radiation (direct or indirect radiative decay) or by an Auger process, Fig. 4.5b. In the latter case the excess energy is transferred to another electron, which is then emitted from the material as Auger electron. Both - the emitted electrons and the emitted X-rays - can again lead to formation of new core holes, which are similarly refilled by the same mechanisms. In the end, the initial energy of the incoming photon is dispersed from a single high kinetic electron on to a large number of low-kinetic electrons after a cascade of secondary Auger and radiative decay processes. Thus, by collecting the emitted electrons (photoelectron yield) at different $h\nu$ it is possible to measure the photo-absorption $\sigma(h\nu)$ using photoemission-based techniques.

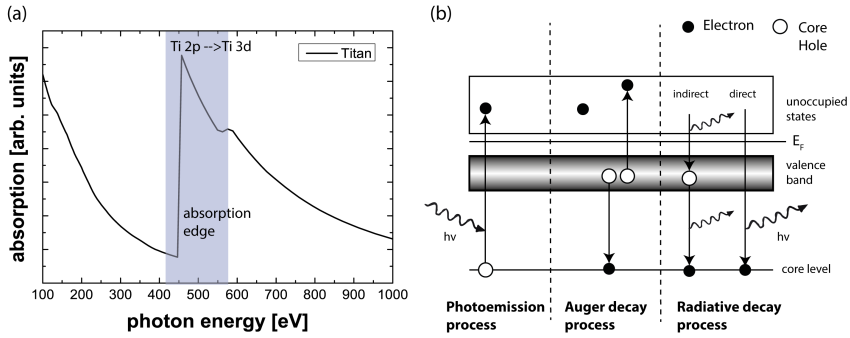

Figure 4.5. – (a) Calculated photon absorption coefficient $\sigma(h\nu)$ for elemental Ti plotted (source: Center for X-Ray Optics). The absorption edge around 458 eV corresponds to the transition from a Ti 2p core level into an unoccupied Ti 3d state. (b) Photoexcitation and core hole relaxation processes: (left) If the photon energy $h\nu$ matches the binding energy E_B, the photon is absorbed and the core level electron is emitted in the unoccupied states. (center) Auger processes: Electrons from lower binding energy can relax into the hole and transfer the excess energy to adjacent electrons. (right) Radiative decays: Electrons can relax into the core hole under the emission of photons.

The detection of the photoelectron yield is classified into different modes, Fig. 4.6. In the total electron yield mode (TEY) all emitted electrons independent of their kinetic energy are detected. In partial electron yield (PEY) only electrons with specific kinetic energies are considered for analysis. The PEY mode can be further distinguished into Auger electron yield (AEY), where only the Auger electrons are measured and secondary electron yield (SEY), where the signal is acquired integrating over the inelastic background. The two modes differ in surface sensitivity and detectable intensity. The AEY has low signal intensities and high surface sensitivity, because it only contains unscattered electrons of the Auger decay channel. The SEY on the other hand contains contributions from all decay channels - including radiative decay. The fact that secondary electrons are end products of decay cascades makes SEY less surface sensitive and leads to a signal amplification. Similarly as it was explained for XPS, also in the case of photoemission based XAS the surface sensitivity is limited by the electron escape depth.

4.5. Photoemission electron microscopy (PEEM)

The study micro-scale redox processes in resistive switching transition metal devices one does not only require *chemical selectivity* but also *sub-micron spatial resolution*. Micro-structural information can be embedded into XAS or XPS experiments by extending spectroscopy to spectromicroscopy, which requires to additionally measure the point of origin $\vec{x}$ of each of the photoemitted electrons with a high accuracy. This strategy is realized in a photoemission electron microscope (PEEM). The working principle of a PEEM is analogous to an optical microscope, but instead of imaging and magnifying visible light information, the lateral intensity distribution of photoelectrons $I(\vec{x})$ is imaged. Magnetic and electrostatic lenses are used to manipulate the trajectories of the photoelectrons. The spatial resolution of a state-of-the-art PEEM [60] is typically in the order of 50 – 150 nm and can reach down to 20 nm under ideal conditions.

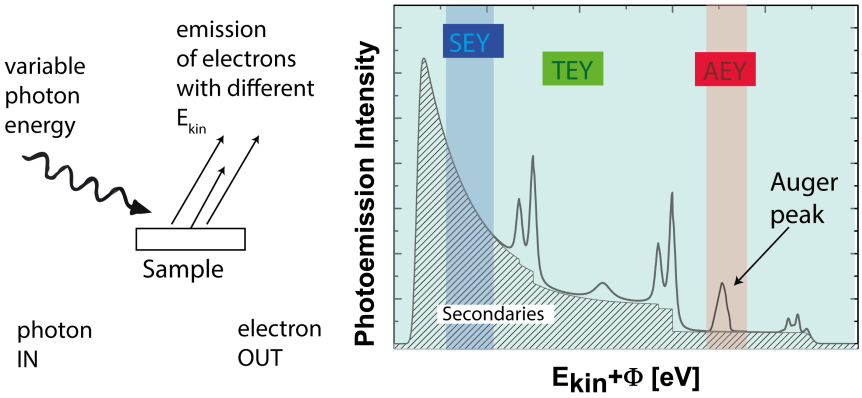

Figure 4.6. – XAS modes defined by the photoelectrons being detected. Total electron yield (green, TEY): the full spectrum of electron kinetic energies is taken into account. Secondary electron yield (blue, SEY): Only electrons near the work function cut-off are considered for analysis. Auger electron yield (AEY): only specific auger electrons are analyzed.

In a PEEM being combined with an energy-filtering element, like a hemispherical analyzer, the kinetic energy of the electrons can be detected and spatially resolved chemical analysis $I(\vec{x},E_{kin})$ (XPEEM) becomes feasible, Fig. 4.7. These instruments are called energy-filtered PEEM (EF-PEEM) or spectromicroscopes and provide chemistry-sensitive real-time images with high spatial resolution. In the course of this thesis spectromicroscopes fabricated by different manufacturers (Specs, Elmitec, Focus) have been used. Even though the technical realization is quite different between the companies, the general layout of these instruments is similar.

A typical spectromicroscope consists of four main components (sketched in Fig. 4.7): An **objective lens** (2), **projective lenses** (3), **electron energy filtering elements** (4) and **electron detection** (5) units. The **objective** is used for a first magnification. By applying a high voltage between sample and the objective lens, the so called extractor field, an immersion lens behavior is realized [61]. In this way the acceptance angle of the microscope is increased to almost 90° and the number of collected electrons is maximized. The objective has a defined focal length and generates an real space image in the image plane (point b) and an image of the angular distribution in the back focal plane (point a). Either of these images is picked up by a set of projective lenses which further select and magnify the region of interest (ROI) and decelerate the fast electrons to match the pass energy of the analyzer. The energy filtering is usually obtained in a dispersive element. In these elements the trajectory of the electrons depends on their kinetic energy, similar to a prism in light optics. A mechanical slit in the dispersive plane is used to select electrons within a defined energy offset ΔE around the pass energy E_{P}. Electrons with the wrong trajectories will be cut from the beam. At the same time ΔE defines the energy resolution of the instrument. For a hemisphere type of geometry (4), ΔE can be calculated from geometric parameters and is typically between 20 – 400 meV in modern spectromicroscopes. A second magnification takes place after the filtering process by another set of projective lenses. Finally, the weak electron signal is amplified by a two-dimensional multichannel plate (MCP) and

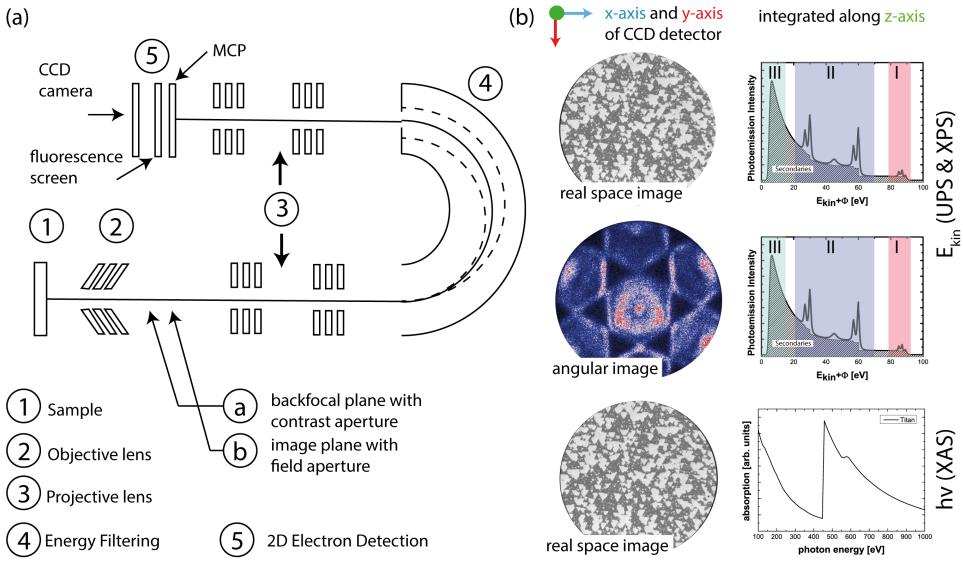

Figure 4.7. – (a) Typical electron optical layout of a spectromicroscope (b) most common modes of operation: (top) spatially resolved XPS and UPS, $I(E_B,\vec{x})$, (center) angle resolved photoemission spectroscopy $I(E_{kin},\vec{k})$ (ARPES), (bottom) spatially resolved XAS $I(E_B,h\nu,\vec{x})$. Explanations of the different modes are given in the text.

converted into light by a fluorescent screen. The screen in turn is recorded by a CCD camera (5). All instruments have additional deflector and stigmator units within the optical path to compensate image aberrations and to align the optical axis.

Depending on the lens configurations spectromicroscopes can be either used for real space or for reciprocal (angular) space analysis. In **real space mode**, x- and y-axis of the recorded CCD image encode the spatial coordinates on the sample. In **reciprocal space mode** x and y of the recorded CCD image encode the angles of electron emission. If these two types of images are taken for different kinetic energies (z-axis), one speaks of real space XPS (EF-PEEM) or momentum microscopy (ARPES), respectively. If real space images are acquired at fixed kinetic energy for varying photon energy (z-axis) it is called XAS-PEEM. The most relevant and common modes of operation are tabulated in Table 4.1.

Acquisition and analysis of EF-PEEM data

In a typical spectromicroscopic experiment a real space image of the photoemitted density $I(x,y)$ is acquired for different kinetic energies of the electrons E_{kin} or for different photon excitation energies $E_{Ph} = h\nu$. The output is a three dimensional (volumetric) data stack $I(x,y,E)$, Fig. 4.8. The image size and the point resolution are defined by the pixel matrix of the CCD camera. The field of view (FoV) and the magnification are defined by the electron optics and adjusted to reveal the desired features in the image. The dimensionality of the data set can be reduced to a single dimension by confining the ROI to a single point $P(x,y)$ and its surrounding $P(x+\delta x, y+\delta y)$. The integrated intensity in this area then becomes a function of the energy only $I(x = \text{const.}, y = \text{const.}, E)$ and reflects the electronic

Experimental configuration	Method	Mode of operation
without energy filter	PEEM	Photoelectron emission microscopy. Photoemission intensity as function of origin $I(\vec{x})$
	TEY XAS	Total electron yield X-ray absorption. Photoemission intensity as function of origin and photon energy $I(\vec{x},E_{Ph})$
with energy filter	EF-PEEM	Energy filtered photoelectron emission microscopy. Photoemission intensity as function of origin and electron kinetic energy $I(\vec{x},E_{kin})$. Corresponds to spatially resolved XPS.
	SEY XAS PEEM	Secondary electron yield X-ray absorption. Intensity as function of origin, photon energy and electron kinetic energy $I(\vec{x},E_{Ph},E_{kin})$
	ARPES (micro ARPES)	Angular resolved photoelectron spectroscopy. Intensity as function of electron momentum and kinetic energy $I(\vec{k},E_{kin})$

Table 4.1. – Modes of operation in a spectromicroscope

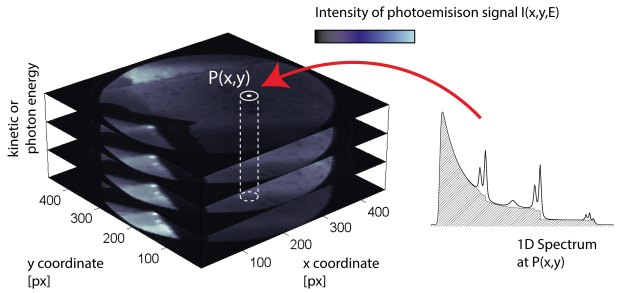

Figure 4.8 – **Data analysis** Images of the spatial intensity I(x,y) distribution are acquired at different photon or kinetic energies E. The three dimensional data set I(x,y,E) can be reduced to one dimension by defining regions of interest, e.g. P(x,y), and subsequent spatial averaging.

features of this specific region. It is the modern equivalent of a standard PES spectrum except for the fact that it can be tracked back to a well-defined and confined region in space being selected by microscopic means. The comparison of different regions in a 3D data set can thus be used to identify chemical composition variations or to distinguish local changes in the electronic properties. Changes can also be visualized in two dimensions in form of color coded images. For this purpose constant energy images are acquired at binding energies that correspond to a specific element. In a second step constant energy images for different elements are then merged in different channels of a RGB image. The composite image clearly reveals the lateral distribution of the different elemental contributions, Fig. 4.9.

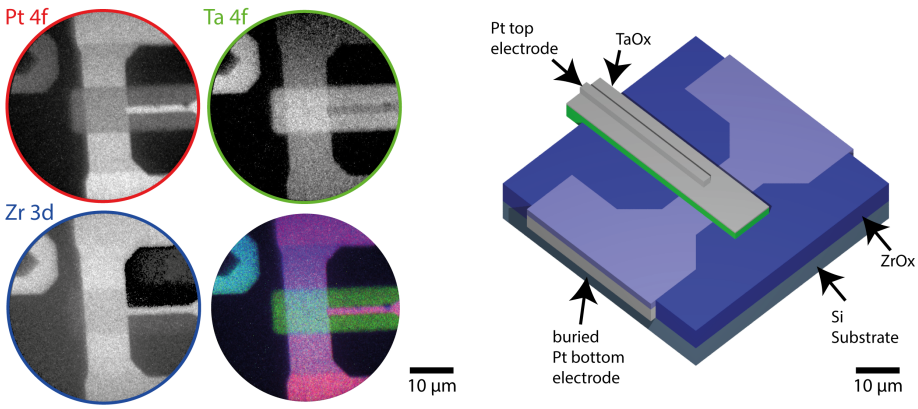

Figure 4.9. – Chemical Analysis using EF-PEEM: Photoemission intensity distributions $I(E_{\text{kin}},x,y)$ at different binding energies related to Pt 4f, Ta 4f, Zr 3d. The composite image reveals the distribution of the different elements.

4.6. Photoemission spectromicroscopy using synchrotron light

Most important for micro-spectroscopic investigations are the quality and the properties of the impinging light, as for example the photon energy $h\nu$, the polarization, the intensity in the investigated FoV and the monochromaticity. These properties of the light define the number of accessible core levels, the probing depth, the experimental resolution and the intensity of the photoemitted electrons. The highest accessible binding energy, for example, is given by the photon energy according to $E_B = h\nu - \Phi$. Further, the photon energy defines the accessible absorption edges. If in the photo excitation process a photon energy spectrum is used over a single photon energy, the measured photoemission spectrum $I(E_{\text{kin}})$ will be a superposition of all contributing photon energies in the spectrum $I(E_{\text{kin}}) = \int_{h\nu} I(E_{\text{kin}},h\nu)$. This leads to experimental broadening or crosstalk effects of the acquired photoemission spectra, decreasing the signal quality and hampering the analysis. Hence, it is of utmost importance for XAS and XPS experiments to have highly monochromatic light ($\frac{E}{\Delta E} > 10^3$) with well-defined polarization. In addition, the acquisition of chemical sensitive, time and spatially resolved spectra with acceptable statistics in XPS or XAS requires high photon fluxes in the order of $10^{12} - 10^{14}\,\frac{Photons}{s}$ over large spectral regions (UV to hard X-ray). This tunability of the photon energy is most important for absorption spectroscopy, where the photon energy $h\nu$ has to be tunable over several tens of eV with a energy resolution of better than 200 meV. These high standards for XAS-PEEM and spatially resolved XPS can only be met by a synchrotron radiation facility. A synchrotron is a large scale, ring-shaped particle accelerator in which charged particles (e.g. electrons) are accelerated close to the speed of light. These particles are kept on polygonal orbits of several hundreds of meters in diameter by bending magnets. During the bending process the particle experiences an acceleration which results in the emission of synchrotron radiation. This effect is further exploited in undulators, where electrons are intentionally forced to oscillations perpendicular to their movement induced by the *Lorentz force* exerted by alternating magnetic fields. The emitted photon energies $h\nu$ in this process depend on the magnitude of the magnetic field $\vec{B}$ in the undula-

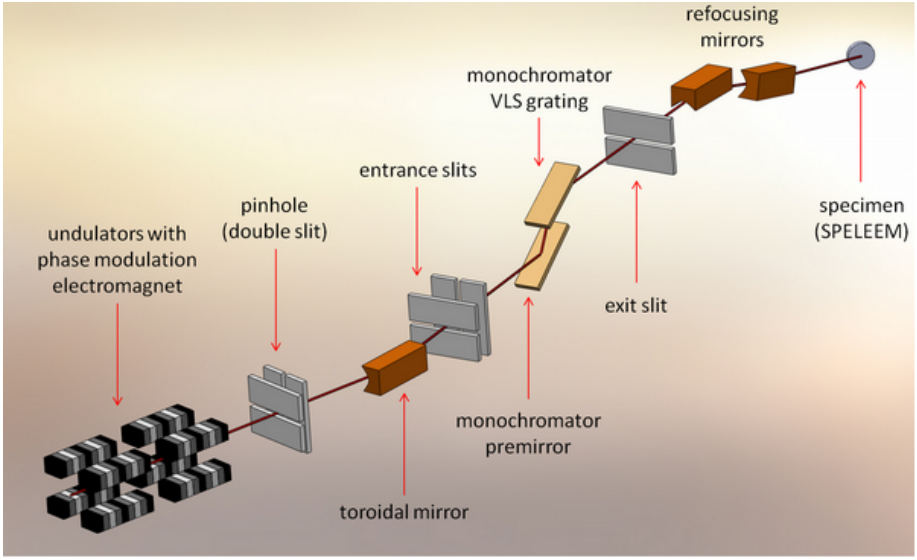

Figure 4.10. – Scheme of a soft X-ray synchrotron beamline (BL): (i) Synchrotron radiation is generated in the *undulator* of an electron accelerator facility. (ii) Horizontal and vertical slits in the front-end of the BL are used for beam shaping and collimation. (iii) The beam is monochromatized to a single photon energy $E_{Ph} \pm \Delta E$ by a *variable line space (VLS) grating*. The angle of reflection at the grating is wavelength dependent and results in a energy dispersive plane. (iv) The monochromator *exit slit* is positioned at a defined angle with respect to the grating. The slit opening selects parts of the dispersive plane and defines the accepted band width ΔE. (v) *Refocusing mirrors* are used to micro focus the beam onto the sample. Image adapted from [62]

tor and the square of the kinetic energy of the orbiting electrons $\propto E^2_{\text{center}}$, which depends on the operation mode of the facility. Typically orbiting energies range from $E_{\text{center}} = 1.5 - 10\,\text{GeV}$ resulting in photon energies up to $h\nu > 10\,\text{keV}$. The central synchrotron radiation wavelength emitted during this process can be tuned by modifying the magnetic field inside the undulator. This is achieved by opening or closing the gap between the magnet rows of the undulator. Once emitted, the synchrotron radiation is further monochromatized by gratings and focused on to the sample by curved mirrors in the beamline according to a scheme depicted in Fig. 4.10. The experiments being described in this thesis were performed at different synchrotron facilities and end-stations. The main specification of each of the beam lines and the corresponding end stations are summarized in Table A.1 in Appendix A and will be referred to in the experimental section.

Part II.

Experimental Results

CHAPTER 5

Chemical and spatial fingerprints of resistive switching in $SrTiO_3$

The ultimate aim of the present work is to image chemical changes induced by the resistive switching process and even to further monitor these changes in a time-resolved manner during operation (i.e. "operando") using photoemission based techniques. For this purpose it is mandatory to first identify chemical and spatial changes/contrast going along with the switching process from LRS to HRS. In the presence of oxygen vacancies, a priori, chemical shifts and occupation modifications are primarily expected for the TiO_6 octahedron. Possible fingerprints are thus expected to manifest in binding energy shifts of the Ti and O XPS core levels, line shape modifications of the Ti L- and O K-XAS as well as local shifts of the work function and the Fermi level due to changing occupation of the conduction band.

The present chapter will begin by reviewing fingerprints of oxygen vacancies and valence change in the TM atom being identified in literature, Sec. 5.1. Afterwards XPS and XAS studies for a controlled reduction of single crystals are presented using standard photoemission, Sec. 5.2. Both - the identified fingerprints in literature and the spectra acquired in the single crystal experiments - will serve as references for the quantification of vacancy concentrations in thin film devices.

In a next step, the attention was shifted towards the characterization of resistive switching devices using the same techniques, Sec. 5.2. Therefore, STO MIM thin film devices were fabricated. The devices were ex-situ switched and delaminated under UHV conditions. Using XPS and XAS PEEM, chemical fingerprints of the stationary low resistive (LRS) and the high resistive states (HRS) with a spatial resolution of a few 100 nm were derived. For the HRS no significant deviations from the bulk absorption could be identified. For the LRS characteristic changes in the Ti L-edge and the O K-edge are observed in confined filamentary regions of $0.5 - 1.5\,\mu m$. The filament substructure was studied in more detail in Sec. 5.2. The identified spatial and chemical fingerprints between LRS and HRS provide a viable contrast mechanism being required for in-situ and operando characterization.

5.1. Fingerprints of oxygen vacancies $V_O^{\cdot\cdot}$ and Ti^{3+} in literature

Several studies in the past decade dealt with the question of how small concentrations of oxygen vacancies $V_O^{\cdot\cdot}$ or the valence state of the Ti central atom in $SrTiO_3$ can be probed using spectroscopic techniques. The results of the two most relevant studies for the present work are summarized in the following.

In the study of Müller et al. (2004) [63] ultra-thin films of oxygen deficient $SrTiO_{3-\delta}$ were investigated by means of electron energy loss spectroscopy (EELS), Fig. 5.1a. EELS and XAS, both describe the excitation of a core level electron into the unoccupied conduction band and thus can be directly compared. The main difference between both techniques is that in EELS the transition energy is provided by a high kinetic electron, whereas in XAS the energy is gained by absorption of the X-ray photon. In their study, EELS spectra of the Ti L- and the O K-edge were measured for three, different amounts of vacancy concentrations: 0 % ($\delta = 0$), 4.33 % ($\delta = 0.13$) and 8.33 % ($\delta = 0.25$). For both absorption edges, the authors find strong modifications of the spectral line shape with increasing oxygen vacancy content: The O K-edge flattens out and the characteristic four-peak Ti L-edge - resulting from crystal field splitting - disappears being replaced by a spectrum characterized by two peaks with maximum intensities around 457.5 eV and 463 eV.

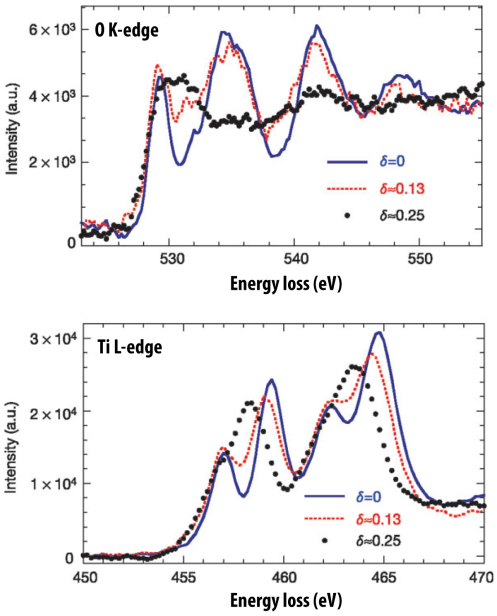

(a) Electron energy loss spectra (EELS) of the O K-edge and the Ti L-edge for different oxygen deficient $SrTiO_{3-\delta}$ films acquired from TEM measurements. Adapted from Ref. [63]

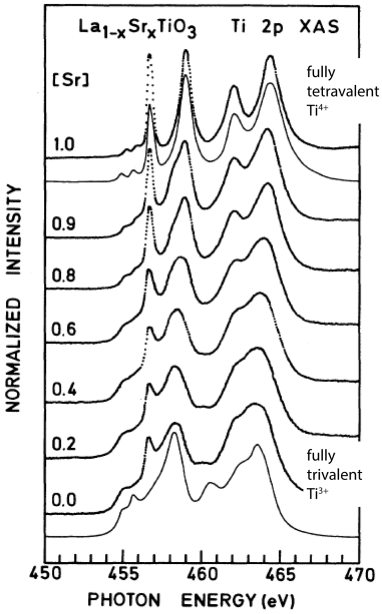

(b) Evaluation of the Ti L-edge absorption line shape for increasing Ti^{3+} concentrations. Taken from Ref. [38]

Figure 5.1. – Vacancy and valence change induced modifications of the X-ray absorption line shapes for titanium and oxygen indentified in literature by experiments on bulk samples.

The second study presented is a Lanthanum (La) substitution series performed on stoichiometric $SrTiO_3$ single crystals by Abbate et al. (1991) [38], Fig. 5.1b. In this study, the Sr atoms were gradually replaced by La atoms to modify the valence state of the central Ti atom from tetravalent (Ti^{4+}) to trivalent (Ti^{3+}). While in $SrTiO_3$ systems the valence states are +2 for Sr and +4 for Ti, the valence states in $LaTiO_3$ are +3 for La as well as for Ti. A steady substitution $La_xSr_{1-x}TiO_3$(x=0..1) from Sr rich towards La rich compounds thus will represent the transition from tetravalent Ti to trivalent Ti.[1] As a matter of fact, the absorption spectra show a strong dependence of the La:Sr ratio and the La rich phase seems to resemble the absorption spectra calculated for trivalent Ti in octahedral configuration (Sec. 3.4). Note that the findings on $LaTiO_3$ can only be partially transferred to systems containing oxygen vacancies, because in the substitution experiment the crystal structure and the symmetry of the crystal field remains intact, whereas in case of high oxygen vacancy concentrations structural changes must be expected.

Both experiments predict strong modification of the absorption line shapes already for small vacancy concentrations below 10% (20% Ti^{3+}) and thus may be used as quantifiers for the vacancy/Ti^{3+} concentrations observed in our experiments.

5.2. Chemical fingerprints of reduced STO single crystals

To obtain quantitative reference spectra of the absorption behavior at the Ti L- and O K-edge in the presence of oxygen vacancies, a $SrTiO_3$ single crystal was step-wise annealed up to 1000°C under UHV conditions in the PEEM microscope in BESSY, Fig. 5.2a.[2] Under reducing conditions and at elevated temperatures the defect equilibrium shifts in favor of vacancy formation and thus oxygen vacancies start to form at the sample surface (see Sec. 2.2.1). Absorption spectra of the O K-edge and the Ti L-edge were acquired between subsequent annealing steps, Fig. 5.2b&c. Based on two spectra with well-characterized Ti^{3+} concentrations, the Ti^{3+} fractions of each of the annealed states were interpolated from superpositions of these references. Further details on the calibration process are given in the supplementary information of Ref. [1]. For vacancy concentrations below 5% (equal to 10% Ti^{3+}) only minor changes are observed for the Ti L-edge, being in agreement with simulations carried out in Sec. 3.4. In contrast, the O K-edge is much more sensitive. In between 0-6% of oxygen vacancies (0-12% Ti^{3+}) a pronounced decrease of the hybridized Ti 3d - O 2p states (peak A) at 530 eV is observed. This decrease is attributed to a partial filling of the t_{2g} states in the conduction band. The strong correlation between spectral shape and calibrated Ti^{3+} fraction was exploited in the following way: If the peak A intensity is normalized to the almost constant peak B2 - representing a hybridization between O 2p and Sr 4d - a linear trend between the A/B_2 ratio and Ti^{3+} fraction is obtained, Fig. 5.2d. This A/B_2 peak ratio in the O K-edge serves as quantifier for the oxygen vacancy concentration in subsequent experiments.

Another experiment on STO single crystals was performed at the Nanospectroscopy beamline in Triest in order to identify fingerprints in XPS, Fig. 5.3.[3] This time a $SrTiO_3$ single crystal was subjected to varying oxygen partial pressures while being exposed to a high intensity soft X-ray

[1] A similar valence change occurs also in the case of O vacancy formation in resistive switching. In this sense the amount of trivalent Ti can serve as an indirect probe of the O vacancy concentration.

[2] The corresponding beamline specifications are tabulated in Appendix Tab. A.1

[3] The corresponding beamline specifications are tabulated in Appendix Tab. A.1

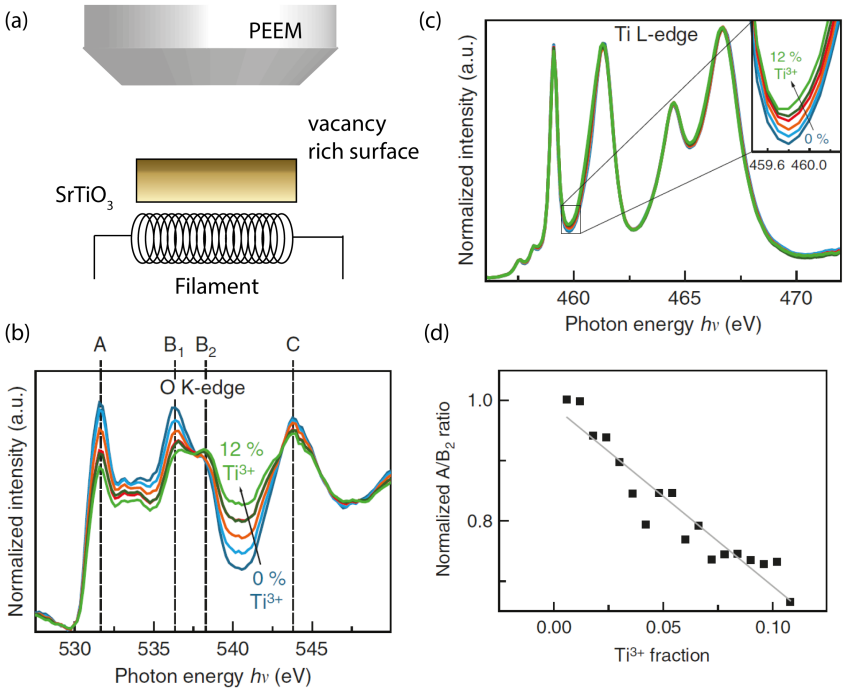

Figure 5.2. – (a) experimental setup for in-situ annealing (b) evolution of the Ti L-edge line shape with increasing Ti^{3+} content (c) evolution of the O K-edge line shape with increasing Ti^{3+} content. (d) A/B_2 peak ratio in the O K-edge with respect to the Ti^{3+} fraction. Adapted from Bäumer, Schmitz et al. [1].

radiation ($I_{\mathrm{Ph}} \propto 10^{10} \frac{\mathrm{Ph}}{s \cdot \mu m^2}$). Similar to the heating procedure the partial pressure in combination with the beam can be used to induce vacancy formation. During the experiment the Ti $2p_{1/2}$ XPS signal was monitored, Fig. 5.3a. Within the course of the experiment, the oxygen partial pressure was several times adjusted from $p_{O_2} \propto 2 \cdot 10^{-10}$ mBar to $p_{O_2} \propto 5 \cdot 10^{-7}$ mBar by regulation the oxygen flow using a leak valve. For highly reducing conditions ($p \propto 10^{-10}$ mBar) a shoulder at a binding energy of $E_B = 461$ eV next to the main line at $E_B = 463$ eV appears being representative for the formation of Ti^{3+}, respectively oxygen vacancies, Fig. 5.3b. The peak area ratio analysis between the two peaks reveals a change of the Ti^{3+}concentration from 0 % ($p_{O_2} \propto 10^{-7}$ mBar) to about 18 % ($p_{O_2} \propto 10^{-10}$ mBar) corresponding to about 0% and 9 % of oxygen vacancies going along with the formation of Ti^{3+}. A partial occupation of the conduction band and in-gap states can be derived from valence band spectra, Fig. 5.3c. Both effects - the formation of Ti^{3+} and the occupation of CB states - are attributed to the oxygen excorporation/formation of oxygen vacancies at the sample surface under beam exposure. From the temporal evolution of both peak intensities we derive that the process is directly correlated to the oxygen partial pressure and is reversible, Fig. 5.3d. The experimental data suggests that in addition to the XAS line shape modifications, Ti $2p_{1/2}$ XPS can be a viable fingerprint for oxygen vacancies, too. At the same time, the data indicates that $SrTiO_3$ surfaces directly exposed to the intense X-ray beam may be significantly reduced during the investigation.

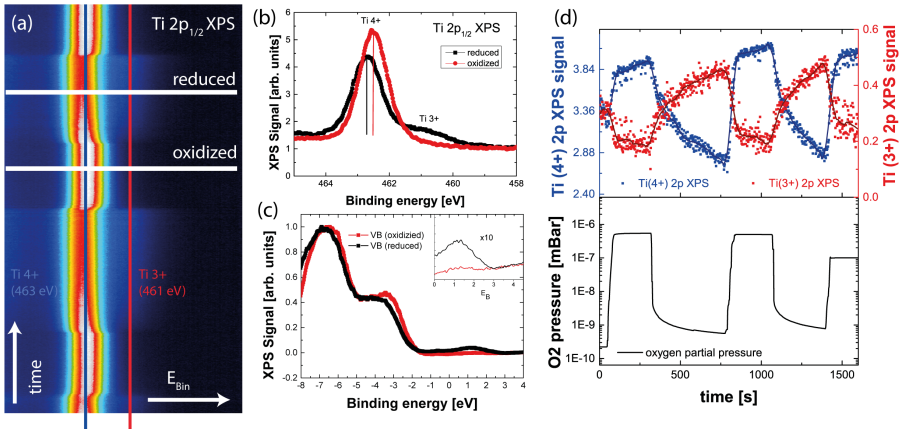

Figure 5.3. – Reduction of a $SrTiO_3$ single crystal under X-ray irradiation and UHV conditions. (a) Waterfall plot of the Ti $2p_{1/2}$ XPS signal vs time. The vertical blue line corresponds to Ti^{4+} ($E_B = 463$ eV). The vertical red line at $E_B = 461$ eV corresponds to Ti^{3+} (b) Ti $2p_{1/2}$ XPS for reducing (black) and oxidizing (red) conditions. For reducing condition a Ti^{3+} shoulder becomes visible. (c) Filling of the conduction band and in-gap states under reduction. (d) Evolution of Ti^{3+} and Ti^{4+} XPS intensities for different oxygen partial pressures. The oxygen partial pressure is plotted for reference in the bottom panel.

5.3. Chemical fingerprints in delaminated STO MIM devices

While the single crystal experiments provide spectral fingerprints for vacancy formation under reducing conditions, it remains unclear, whether these fingerprints are identical to the ones induced by the resistive switching process. In order to chemically characterize the different resistive states in memristive $SrTiO_3$ devices a set of functional thin film metal-insulator-metal (MIM) structures was prepared.

The fabricated MIM structures consisted of a few nm thin layer of $SrTiO_3$, which was epitaxially grown of a conductive $Nb:SrTiO_3$ single crystal substrate. In a subsequent step, arrays of $10\,\mu m \times 10\,\mu m$Au top electrodes were structured on top of the STO film by photo lithography, Fig 5.4a. [4] In a subsequent step specific arrays of devices on a single wafer were programmed into either low resistive (LRS) or high resistive (HRS) states by ex-situ switching using a current compliance of 50 mA. An exemplary I-V curve of a single $SrTiO_3$ device is shown in Fig. 5.4b. The device shows a pronounced hysteresis loop between LRS and HRS. Positive voltages turn the system into the LRS ('ON') state, whereas negative voltages switch it back to the HRS ('OFF'). The averaged measured ON/OFF ratio for the devices under investigation was in the order of $\frac{R_{HRS}}{R_{LRS}} \approx 10^3 - 10^5$.

According to the VCM model (see Sec. 2.2.1), the switching process between LRS and HRS is driven by the movement of oxygen vacancies, which modify donor concentrations in the vicinity of the top electrode/oxide Schottky contact. Thus within this picture, oxygen vacancies are expected to accumulate at the top electrode interface in the LRS and a depletion is expected for the HRS. These interfacial changes should appear in XPS and/or XAS and manifest in changes similar to the ones

[4] The stoichiometric $SrTiO_3$ thin films were epitaxially grown on a single crystalline $Nb:SrTiO_3$ substrate by pulsed laser deposition (PLD). Thin film growth and lithography were performed by C. Bäumer, PGI-7, FZ Jülich.

observed for the single crystals. Due to the high surface sensitivity of soft X-ray XPEEM, however, a removal of the metal top electrode is necessary in order to access this interfacial region. Electrode removal was achieved by a UHV delamination step prior to investigation. which is described in detail by A. Köhler [23]. In this procedure the pre-switched devices were covered by a metallic delamination layer. The delamination layer forms a strong mechanical bond to the top electrode and removes it once the layer is pulled off. In our study, the delamination layer was removed with an adhesive copper tape, which was pulled mechanically from the structures with a wobble stick under UHV conditions, Fig. 5.4d Step 1-3.

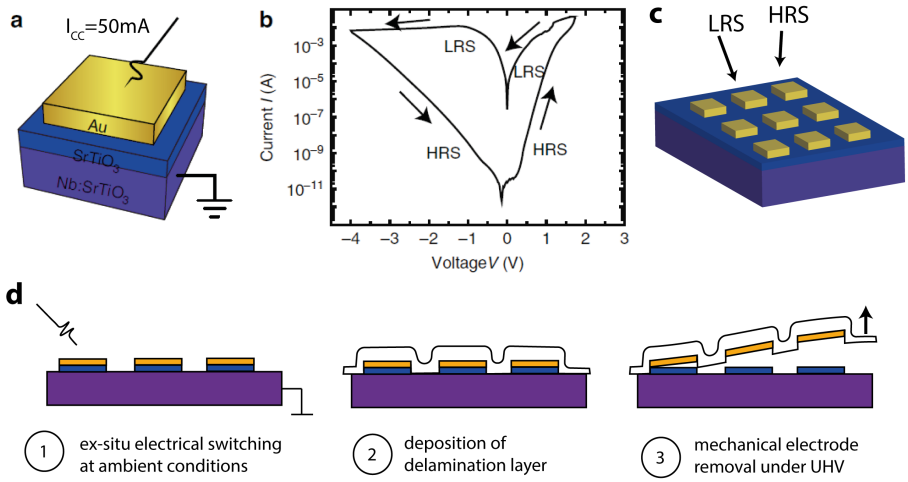

Figure 5.4. – (a) Schematic of an Au/STO/Nb : STO thin film device structured by lithography, (b) I-V characteristics of a typical device (a,b) adopted from Bäumer, Schmitz et al. [27]. (c) Different devices on a single chip were programmed into LRS or HRS (d) Sample preparation and UHV delamination: (1) Samples are connected by a tip and switched ex-situ (2) The full wafer is cover by a metallic delamination layer (3) The metallic overlay together with the top electrode is detached from the RSM by mechanical force.

The success of the delamination process was verified by work function and Au 4f XPS scans of the freshly delaminated surface in threshold photoemission (see Appendix A). A statistical analysis of multiple devices reveals that electrode removal is successful in less than 50% of the investigated devices. Even though being successful in exposing the interface region and in attaining sufficiently clean thin film surfaces for some devices, the presented delamination procedure has significant drawbacks when being applied to functional devices. The process is highly destructive. It modifies the surface morphology and it exposes a non-equilibrium state to vacuum. Further, devices after delamination are non-functional and probing of the device resistance state after delamination is not possible anymore. Alternatives to the delamination process leaving the device operational will be discussed in chapter 6.

5.3.1. Ti $L_{2,3}$-edge XAS-PEEM

X-ray absorption PEEM (XAS-PEEM) experiments at the Ti L-edge were performed in SEY on the prepared and delaminated devices. The experiments were carried out at the NanoESCA PEEM at

Elettra, Trieste. [5]. Two types of devices were investigated: (i) devices in the HR state and (ii) devices in the LR state. For each experiment the field of view was reduced to 15 µm × 15 µm to contain only a single device. The photon energy $h\nu$ of the incident light was varied from 454 eV to 468 eV equivalent to the energy of the transition from the Ti 2p core level to the unoccupied conduction band formed by Ti 3d-O 2p hybrid bands. At each photon energy the lateral intensity distribution of the photoemitted electrons was detected $I(h\nu,x,y)$. The acquired 3D data set $I(x,y,h\nu)$ for a HRS device is exemplary

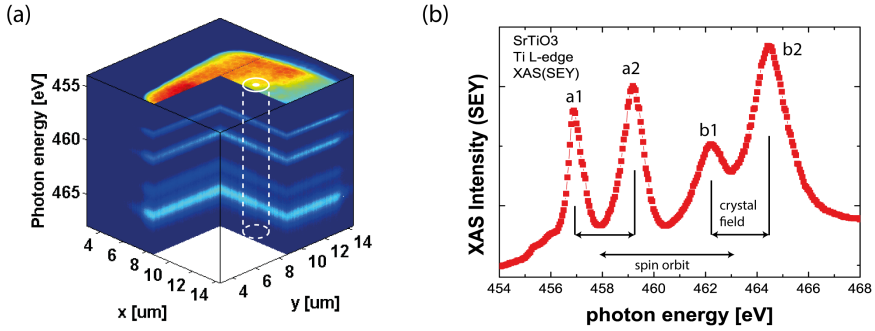

Figure 5.5. – (a) Ti L-edge XAS-PEEM scan of a single, delaminated device in the HRS plotted in three dimensions. The x- and y-axis define the spatial coordinates. The z-axis encodes the photon energy. The area indicated by the white line was chosen for a cut along the photon energy (z-axis), plotted on the right. (b) The Ti L-edge XAS line shape of the chosen region is characteristic for tetravalent titanium in an octahedral configuration.

plotted in Fig. 5.5a. The data was normalized to the photon flux $I_0(h\nu)$, which was recorded during the measurement from the drain current of a gold mesh positioned in the beamline. Further, the full image stack was divided by a bright field image taken at the pre-edge ($E_{\mathrm{Ph}} = 454$ eV) to remove beam profile and detector inhomogeneities. The Ti L-edge line shape extracted from the pad region shows the characteristic absorption line shape of the stoichiometric, tetravalent titanium (Ti^{4+}) consisting of seven peaks and is in good agreement with spectral line shapes observed in literature [38,40,45,64]. The HRS device shows a homogenous absorption behavior and no spatial modifications have been observed. The four main absorption lines were labeled according to the scheme depicted in Tab. 5.1. A detailed analysis of the different contributions is given by Ikeno [44] and de Groot [40].

	Peak	initial state	final state
L_3-edge	a1	$2p_{3/2}$	t_{2g}
	a2	$2p_{3/2}$	e_g
L_2-edge	b1	$2p_{3/2}$	t_{2g}
	b2	$2p_{3/2}$	e_g

Table 5.1. – Main transitions involved in each of the corresponding peaks

The Ti L-edge absorption scans have been repeated for devices set to a LRS state, Figure 5.6. In the center of the PEEM image acquired at a photon energy of 450 eV, a crater/filament like region can be identified. Such regions were not observed for devices in the HRS. Ti XAS spectra were extracted

[5] The corresponding beamline specifications are tabulated in Appendix Tab. A.1

from the crater region and for reference also from the surrounding. The spectra were corrected for a linear background and normalized to the maximum of peak a1, Fig. 5.6b. While most of the pad area exhibits the same spectral features as observed for the HRS, deviations could be observed in a confined area of a few micron in diameter within the crater region. The differences in spectral shape are characterized by a reduced peak-to-valley ratio for the peaks b1 and b2 around 463 eV and the presence of an additional shoulder appearing at a photon energy of 458 eV. The peak positions seem to correspond to the energetic positions of trivalent Ti in an octahedral crystal field, simulated in Sec. 3.4. Thus, the experimental XAS line shape in the crater region can be qualitatively compared to the standard defined by the La/Sr substitution experiment of Abbate [38] in Fig. 5.1b and to the simulations of the Ti L-edge in Sec. 3.4. Best agreement between the experimentally measured line shape and the substitution experiment was found for 10 – 20 % La content providing a very rough estimate of 5 – 10% of oxygen vacancies within the crater region.

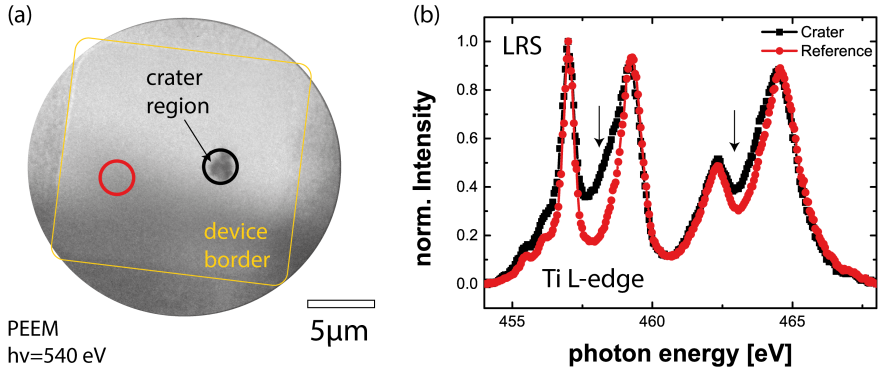

Figure 5.6. – (a) XAS-PEEM image showing a modified region of approximately 1 µm in diameter in an else homogenous matrix. (b) XAS spectrum of the Ti L-edge extracted from the crater region (black) compared to a reference spectrum extracted from the unaltered surrounding (red) Arrows indicate possible Ti^{3+} contributions.

5.3.2. O K-edge XAS-PEEM

Similar to the Ti L-edge absorption experiments, O K-edge XAS-PEEM stacks were acquired for delaminated $SrTiO_3$ devices for the LRS and HRS by scanning the photon energy from 520 eV to 560 eV. For the HRS only negligible spectral changes within the pad area are observed. Thus, further analysis was limited to devices in the low resistive state (LRS). For convenience, the analysis was performed on the same device as already discussed for the Ti L-edge. The spectra depicted in Fig. 5.7b show the filamentary region compared to a reference spectrum taken from an unaltered $SrTiO_3$ region. All spectra are I_0 corrected. A linear baseline corresponding to the pre-edge slope was subtracted. Subsequently, the data was normalized to peak B_2 at $h\nu = 536$ eV as the acquired spectra were too short for a proper post-edge normalization. For the given normalization scheme, a decrease of the peak A intensity correlated to the hybridized Ti 3d - O 2p states was observed indicating the presence of vacancies. However, at the same time, an additional background within the photon energy range of 535 eV - 550 eV appeared, which was not observed for the single crystals. This region is dominated by hybridization of the O 2p states with Sr 5s and Ti 4p orbitals and principally is not expected to transform upon valence change. Independently on the point of normalization,

the spectral differences between crater and reference region remain clearly visible indicating the differences are real. Yet, the A/B_2 peak ratio, which is used for vacancy concentration estimation, changes with the selected point of normalization. As for these reasons, the O K-edge for the presented device was only used as qualitative measure for the anticipated spectral changes and not used in any quantitative analysis of the oxygen vacancy concentration.

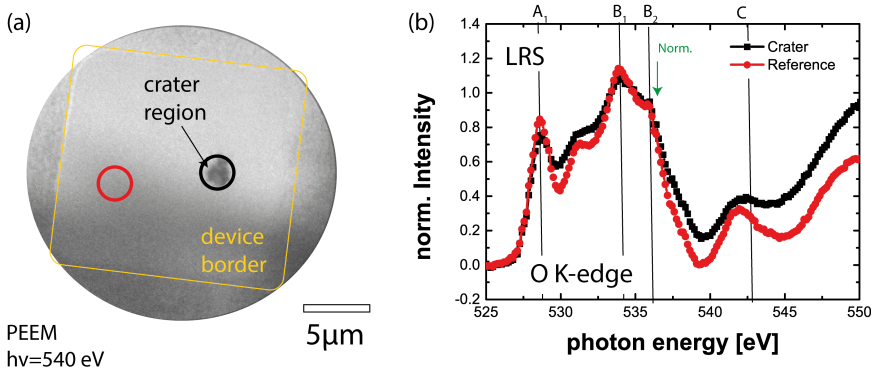

Figure 5.7. – (a) XAS-PEEM image showing a modified region of approximately 1 µm in diameter in an else homogenous matrix. (b) XAS spectrum of the O K-edge extracted from the crater region (black) compared to a reference spectrum extracted from the unaltered surrounding (red). The spectra are normalized to peak B_2.

5.3.3. Work function contrast

In addition to the two XAS fingerprints, a third chemical fingerprint of the LRS was identified in the work function Φ. The analysis of the photoemission work function cut-off for the LRS device revealed four distinct regions, Fig. 5.8a: (i) the unaltered $SrTiO_3$ thin film (grey) within the device area, (ii) regions that have been ion etched during lithography and therefore are referred to as 'amorphous' and (iii) filamentary regions in the device center - subdivided into the center (blue) and the rim (red). The work function spectra, Fig. 5.8b, of the latter two are related to the switching process: In both spectra the measured work function is significantly lowered as compared to the unaltered thin film even though the material composition should be identical. As a result, the photoemission onset is shifted by $\Delta E_1 = 700$ meV for the rim and by $\Delta E_2 = 1.2$ eV for the central part of the filament. The regions having lower work functions match the regions showing fingerprints of trivalent Ti^{3+} in the Ti L- and O K-XAS, Fig. 5.8c. Thus, the work function shifts can potentially be explained by a shift of the Fermi level E_F due to occupation of in-gap or conduction band states induced by oxygen vacancy formation (Sec. 5.2). The partially filled CB states are energetically closer to the vacuum level E_{Vac} and hence the surface potential barrier $\Phi = E_{Vac} - E_F$ for the highest occupied levels becomes smaller, Fig. 5.8e. However, the observed spectral shifts are too large to be solely explained by doping effects. Hence, additional band bending effects, as for example observed by other groups during the investigation of p/n-doped silicon heterojunctions [65] are considered. In context of the present work, the work function contrast could only be used in delaminated devices, as the active area of the resistive switching device must be in direct contact with vacuum.

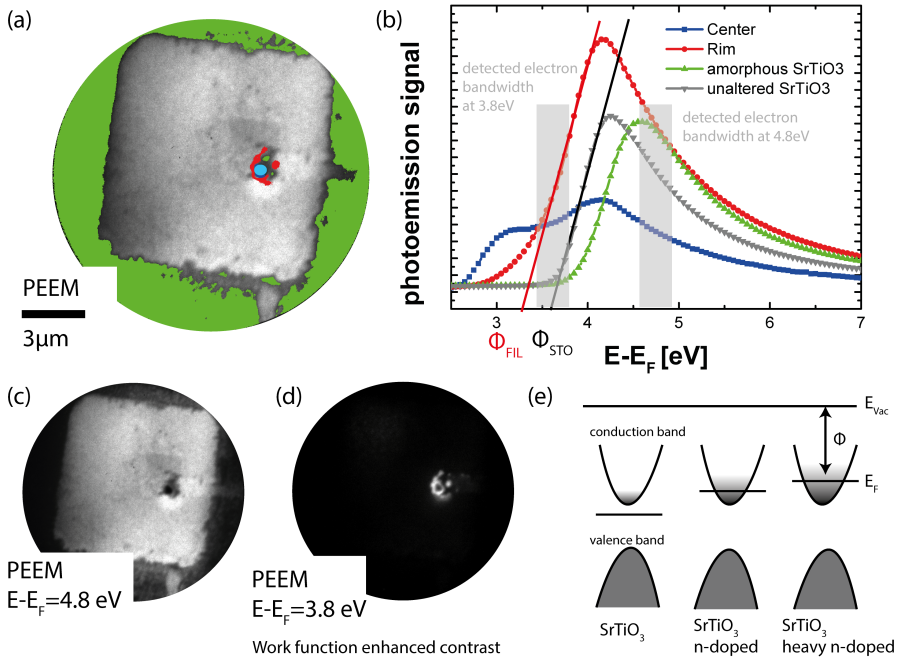

Figure 5.8. – (a) PEEM image of an LRS device with different regions of interest indicated by color. (b) Work function profiles extracted from the corresponding regions. The emission onset in the filamentary region (blue) and its surrounding (red) seem to be significantly reduced as compared to the unaltered region. PEEM images acquired at (c) $E - E_F = 4.8\,\text{eV}$ and (d) $E - E_F = 3.8\,\text{eV}$. For $E - E_F = 3.8\,\text{eV}$ the intensity distribution between filament and surrounding is inversed. (e) Model to explain work function shift by partial filling of the conduction band in the filamentary region.

5.3.4. Ti 2p XPS and VB spectroscopy

Spatially resolved investigations of the Ti 2p XPS and the valence band (VB) were performed for the delaminated devices, but discarded due to low-signal intensities and resulting low statistics. The high statistics from the single crystals experiments in Sec. 5.2 unfortunately could not be reproduced for the delaminated devices. The reasons are twofold: The single crystal XPS was acquired in a *dispersive plane* mode. Within this mode spatial and angular information are integrated and a broad bandwidth of electron kinetic energies ΔE can be collected at once. Further, the detected signal was collected from areas as large as $A_{Crystal} = 400\,\mu\text{m}^2$. In contrast, the signal of the filamentary regions stems from $A_{Filament} \approx 4\,\mu\text{m}^2$ and in the spatially resolving mode, the kinetic energies are scanned in steps of δE. For the same acquisition time, the detected signal intensity between the two modes can differ by a factor as large as $c = \frac{A_{Cyrstal}}{A_{Filament}} \cdot \frac{\Delta E}{\delta E}$, typically being above $4000 - 10.000$.

5.4. Spatial fingerprints and filament substructure

The filamentary regions observed in different delaminated LRS devices are circular to elliptic in shape, having diameters ranging from 500 – 1500 nm, Fig. 5.9(b,c). In most cases the positions of the filaments were identical to the needle tip contact points during ex-situ switching. For LRS devices the filamentary region is darkened, for the HRS device only a faint silhouette is visible (red arrow in Fig. 5.9a).

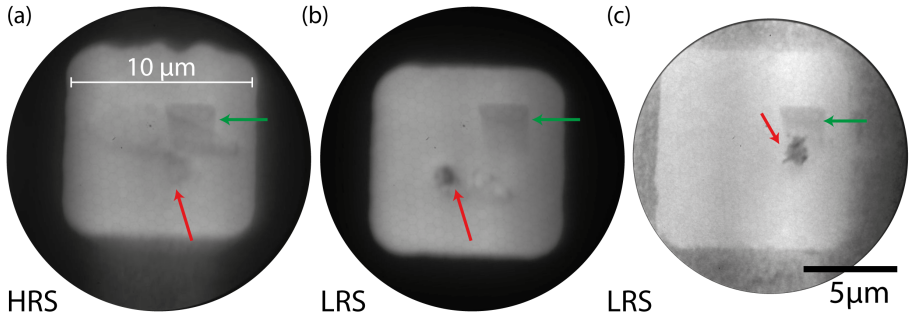

Figure 5.9. – PEEM images at the work function cut off ($E - E_F = 4.8$ eV) for different devices: (a) device in HRS (b) device in LRS (c) second device in LRS. In all three devices a circular region can be identified (indicated by a red arrow). A green arrow marks an experimental artifact in the MCP.

For the LRS device described in the previous sections, the WF difference between the filament Φ_{FIL} and the unaltered thin film Φ_{STO} was exploited as additional filter in the imaging process in order to select only electrons being emitted from the filamentary region. The working principle of the filter is based on the fact that the work function defines the onset of electron emission. For kinetic energies lower than the work function of the material, no emission is observed. By limiting the instrument to only accept electrons within a specific energy range ΔE, i.e. using the energy filtering capability of the instrument, the imaged absorption signal was limited to specific regions defined by the work function. This mode of operation will be referred to as *work function enhanced contrast*.

The concept of the novel *work function enhanced contrast* mode is illustrated in Fig. 5.8c&d. Image 5.8c shows a PEEM image acquired within a kinetic energy range around $E - E_F = 4.8 \pm 0.4$ eV. For this detected energy range electrons are emitted from all regions of the sample. This is also the range that was used for XAS measurements presented in the previous section. Image 5.8d shows a PEEM image where the filtering energy of the EF-PEEM was adjusted to detect only electrons within an kinetic energy range around $E - E_F < 3.8 \pm 0.4$ eV. This energy range is below the emission onset of the STO film Φ_{STO} and hence electrons from this region cannot yet be emitted into vacuum. The signal within the film region is suppressed and the electron emission contributions of filament core and filament rim dominate the acquired intensity. As a consequence the contrast between filamentary and non-filamentary regions is significantly enhanced.
Given this new configuration, the XAS experiments at the Ti L-edge and at the O K-edge were repeated. The results are shown in Fig. 5.10a&b. A direct comparison between the normalized Ti L- and O K-edge spectra acquired around $E - E_F = 3.8$ eV and the spectra taken around $E - E_F = 4.8$ eV for the same device reveals an interesting feature: The spectral line shape observed in the crater

(filamentary) region measured at 3.8 eV deviates from the observed line shape at 4.8 eV. The spectral shape within the surrounding pad region, however, remains similar for both energies. The XAS line shape of the filamentary region at 3.8 eV was again compared to the standard defined by the substitution experiment of Abbate [38], Fig. 5.1b. It fits to a Ti^{3+} fraction of 50 % or more, rather than to the previously estimated 20 % or less at $E - E_F = 4.8$ eV. The Ti^{3+}/oxygen vacancy concentration is a fixed quantity and does not depend on the kinetic energy of the observed electrons. For this reason, the observed spectral changes must be related to the imaging process itself. The situation may be explained under the assumption that the observed macroscopic, filamentary region is composed of nanoscale island/filaments with different oxygen vacancy concentrations.

The influence of nanoscale oxygen vacancy rich islands within the filamentary region on the detected photoelectron yield is illustrated in Fig. 5.10c. For the energies around $E - E_F = 4.8$ eV both - islands and film - emit electrons and a superposition of tetravalent and trivalent signal is detected. For the energies around $E - E_F = 3.8$ eV the signal mainly arises from the islands and only the trivalent contribution is detected. Therefore, we conclude that the filament has a substructure, which cannot be resolved by PEEM, but which can be indirectly probed using work function enhanced contrast.

There is a set of prominent experimental data published in literature [64, 66] supporting the existence of nanoscale and mixed valence islands/filaments on the surface. Lenser et al. [64], for example, show Scanning Electron Microscopy (SEM) and XPEEM data of micron-sized filamentary areas, which are composed of multiple active and inactive nanoscale filaments, Fig. 5.11(a-c). Dudy et al. [66] extracted charge carrier densities for reduced bulk $SrTiO_3$ crystals from Fermi surface maps acquired by ARPES. They report that the experimentally determined charge carrier densities deviate from the expected values of a homogenous system (Fig. 5.11d). They argue their observations with decomposition of the system into Ti^{3+} rich islands. Finally, the experimental data may help to bridge the gap between filament diameters determined in PEEM and filament sizes observed in AFM/STM studies. As an example Szot. et al [24] present conductive tip atomic force microscopy (C-AFM) studies of a $SrTiO_3$ single crystal. In their study they find nanoscale conductive dislocation lines in the range of $1 - 10$ nm being distributed over the full crystal surface. These dislocation lines are identified as oxygen vacancy rich nanofilaments.

We must assume that the spatial fingerprints identified in the PEEM experiments are not related to a single filament, but rather have to be attributed to clusters of nanosized filaments, the internal structure of which cannot be resolved by the present PEEM methodology.

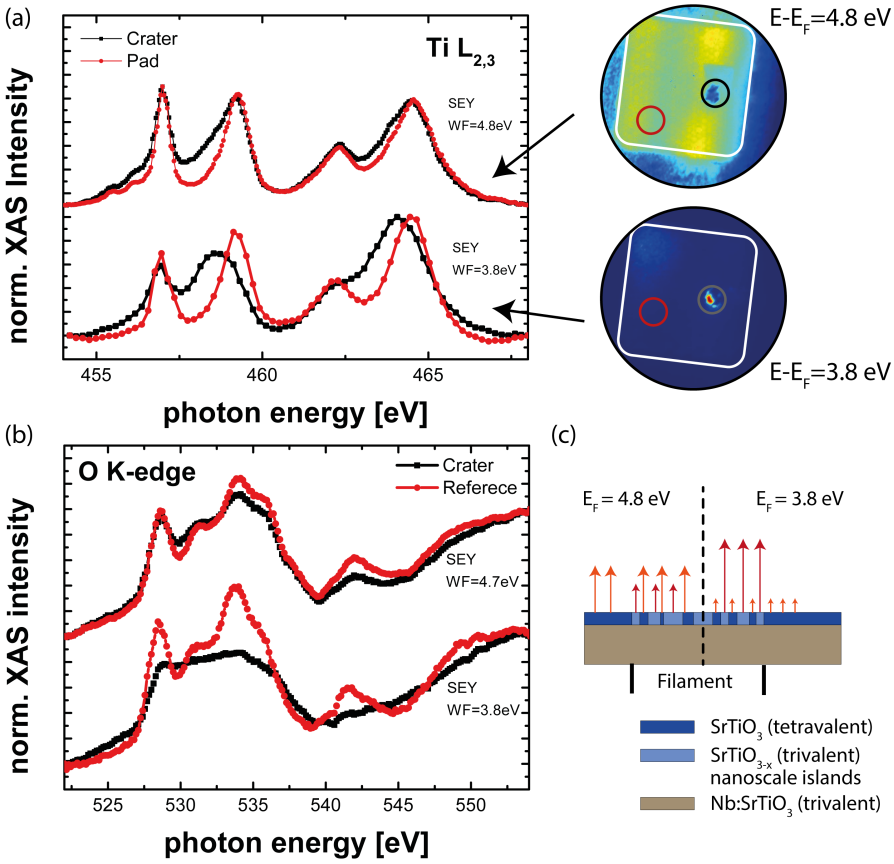

Figure 5.10. – (a) normalized Ti $L_{2,3}$-edge XAS and (b) normalized O K-edge XAS acquired in SEY for secondary electrons around $E - E_F = 4.8\,\text{eV}$ (top) and $E - E_F = 3.8\,\text{eV}$ (bottom). Red lines represent reference spectra acquired in the pad region, black spectra were extracted from the crater/filament location as indicated in the PEEM images. The spectral shape of tetravalent Ti regions (red) remains unchanged, while the trivalent, filamentary region (black) shows pronounced features at 458 eV and 463 eV for the Ti L-edge and a total flattening of the O-K edge. (c) The presence of nanoscale, vacancy rich islands embedded in a matrix of stoichiometric $SrTiO_3$ can explain the difference in the absorption line shapes between the two different energies. Details are provided in the text.

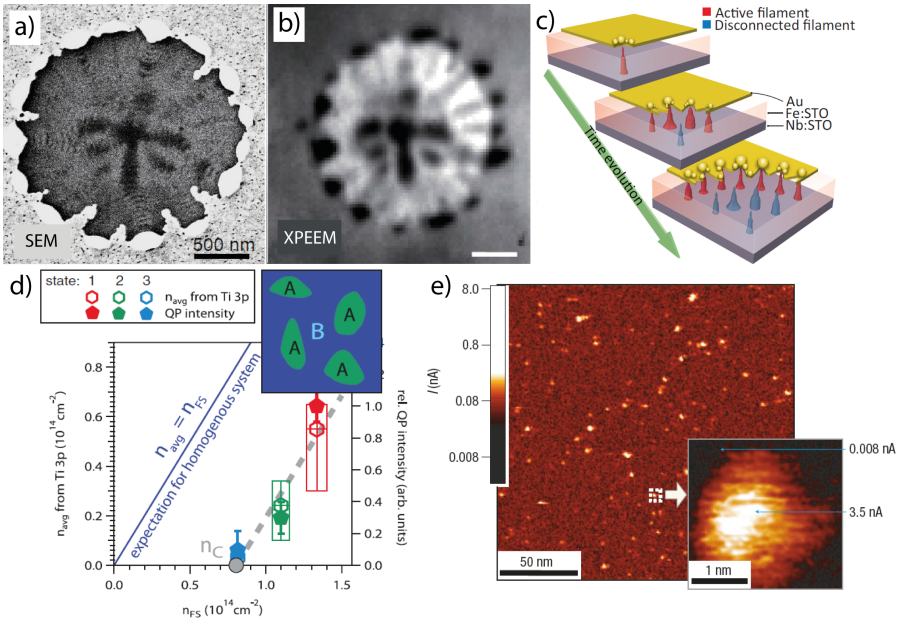

Figure 5.11. – (a) SEM image of a micron sized filamentary area in Fe : $SrTiO_3$, (b) high resolution XPEEM XAS image of the same device imaged at a photon energy $E_{Ph} = 459.9$ eV characteristic for tetravalent titanium (Ti^{4+}) (c) Multi filament model to explain large filamentary areas. A detailed explanation is given in [64]. (d) Mismatch between the expected charge carrier density (blue line) for a homogenous surface reduction of $SrTiO_3$ single crystals and the charge carrier densities measured from Fermi surfaces (data points). The deviation is explained by the presence of Ti^{3+} rich islands (inset) [66]. (e) LC-AFM study on a $SrTiO_3$ single crystal surface: Observation of nanoscale conductive filaments with diameters of a few nm [24].

CHAPTER 6

Novel approaches and device concepts for in-situ and operando resistive switching

In the previous chapter it has been demonstrated for the example of delaminated devices that photoemission microscopy is suitable to detect spatially confined chemical changes induced by nanoscale redox processes during resistive switching. A drawback of this approach is that it is destructive and neither electrical switching nor electrical testing is possible afterwards. Furthermore, the information acquired from delaminated devices can only be interpreted as statistic ensemble and it does not yet provide information about filament growth, filament localization or reproducibility of the switching process. The delamination process itself will alter the results as it removes the protecting top electrode and exposes a highly reactive surface in a non-equilibrium state to vacuum. In literature, the device state is assumed to stay constant during the delamination process, which is most probably not the case. Many groups have, for example, observed beam induced damages during synchrotron measurements. In 2012 Yang and co-workers summarize the situation in their review on resistive switching materials as follows: "The microscopic picture of how exactly these factors drive the mobile species to actuate a particular type of switching are still under debate. Therefore, experiments that could visualize the switching in real time and at nanoscale resolution and with chemical and/or structural information would be extremely valuable, such as those using in-situ transmission electron microscopy and in-situ scanning transmission X-ray microscopy." [10]

Access to resistive switching devices during operation using chemical sensitive PEEM techniques (e.g. XPEEM, XAS-PEEM) is highly desirable as it would offer completely new insights on the switching dynamics. However, the main issue with operando XPEEM is the high surface sensitivity of the photoemission process, which limits the information depth to the first few nm of the sample surface. The limited probing depth is in conflict with the fact that in an operational MIM structure (Fig. 6.1) the active region is covered by a metal top electrode, which is essential for the device operation.

The following chapter is intended to explain and to discuss different approaches on how to electrically contact and switch a device inside of a PEEM in such a way that PEEM measurements are simultaneously possible. After a thorough analysis of the factors limiting the information depth in

our experiments in Sec. 6.1, the further three sections present different approaches to tackle the challenges as well as their technical realization: (i) hard X-ray PEEM (HAXPEEM) in Sec. 6.2, (ii) lateral device structures in Sec. 6.3, and (iii) ultra-thin top electrodes in Sec. 6.4. In addition to the technical implementation of these approaches, the sections provide first experimental data. The last section (Sec. 6.5) compares the different approaches in terms of suitability for time-resolved experiments balancing pros and cons for each approach.

6.1. The top electrode surface sensitivity dilemma

The high surface sensitivity of photoemission-based experiments is not a result of the penetration depth of the light. Instead, it arises from the strong inelastic scattering of photoelectrons inside a solid. The information depth of an XPS experiment depends on the number of primary (un- or elastically scattered) electrons and therefore is typically defined as function of the inelastic mean free path (IMFP,λ_{IMFP}) (Sec. 4.3). The information depth of SEY-XAS in turn is limited by a complex combination of the initial Auger electron escape depth and the escape depth of the secondary electrons generated by inelastic collisions. The interplay between the two quantities is material- and energy-dependent and cannot be easily generalized. For both methods and despite the details of the underlying processes, however, the total intensity $I(E_{\text{kin}},d,\theta)$ of chemically relevant electrons that can be detected from a layer buried beneath an electrode can be described by an exponentially decaying function, Eq. 6.1:

$$I(E_{\text{kin}},d,\theta) = I_0 \cdot \exp\Big(-\frac{d}{\lambda(E_{\text{kin}}) \cdot \cos\theta \cdot \cos\alpha}\Big) \tag{6.1}$$

Here, I_0 equals the signal intensity expected for the uncovered layer. The product $d \cdot \frac{1}{\cos\theta}$ is the effective escape length to the surface given by the electrode thickness d and the angle θ defined as the angle between surface normal of the sample and the electron analyzer ('geometry factor'). For experiments in normal emission ($\theta = 0°$) with small acceptance angle α the termcos$\theta \cdot \cos\alpha$ can be approximated to 1. ('Straight line approximation'). Finally, $\lambda(E_{\text{kin}})$ describes an energy-dependent attenuation length, where E_{kin} is the electron kinetic energy. If the energy dependent attenuation length $\lambda(E_{\text{kin}})$ is known, Eq. 6.1 can be used to estimate the electrode thickness d_{max}, which still provides the required signal intensity from the buried layer for meaningful analysis.

For XPS, $\lambda(E_{\text{kin}})$ can be approximated by the inelastic mean free path $\lambda_{IMFP}(E_{\text{kin}})$, which according to Seah et al. [54] is almost material independent and can be described by a single "universal" curve. For spectroscopy within the UV and soft X-ray region (SX-XPS) the IMFP of valence band electrons is of the order of $\lambda_{\text{IMFP}}(10-1500\,\text{eV}) \approx 0.5-2\,\text{nm}$. For hard X-ray excitation (hard X-ray photoemission electron spectroscopy, HX-XPS) the inelastic mean free path of these electrons is increased up to $\lambda_{\text{IMFP}}(3-10\,\text{keV}) \approx 3-8\,\text{nm}$. [55]

For XAS based techniques $\lambda(E)$ is a priori unknown, because it depends on the material composition and stacking. Therefore it has to be measured. Generally, however, the kinetic energy of an Auger electron for a defined transition is constant and systems with similar material compositions tend to have similar escape length. Based on reference values derived from Abbate [67], Schroeder [68] and Franzer [69] the average attenuation length for Ti L-XAS ($E_{\text{kin}} = 456\,\text{eV}$) and O K-XAS ($E_{\text{kin}} = 530\,\text{eV}$) is expected to be in the order of $\lambda \approx 0.6-2.6\,\text{nm}$.

Figure 6.1b shows calculations of the expected relative signal intensities $I(d)/I_0$ stemming from an interface buried by a top electrode of thickness d. The signal damping is plotted for each of the three experimental methods used in the present work. The lower and upper bounds of each curve are defined by the lowest and highest reported values of $\lambda(E_{\mathrm{kin}})$, i.e. 0.6 nm and 2.6 nm for XAS. The region within the lines represents a confidence interval. The plot reveals the dilemma for resistive switching MIM devices with metal top electrodes (TE) of several nanometer in thickness: On one hand, a stable and homogenous top electrode is mandatory to facilitate the switching process, but on the other hand, a several nanometer thick electrode suppresses most of the chemically relevant signal. Assuming that a 90% loss in the initial intensity defines the lower detection limit, then the corresponding maximum electrode thickness d_{90} can be calculated. In case of soft X-ray XPS (blue) and XAS (red) the TE thickness must be below $d_{90} \leqq 2-4$ nm. For hard X-ray excitation the same signal attenuation is expected for a top electrode thickness of $d_{90} \approx 12-14$ nm, see Fig. 6.1. As a consequence, any top electrode with more than 15 nm thickness is practically non-transparent for electrons carrying chemically relevant information.

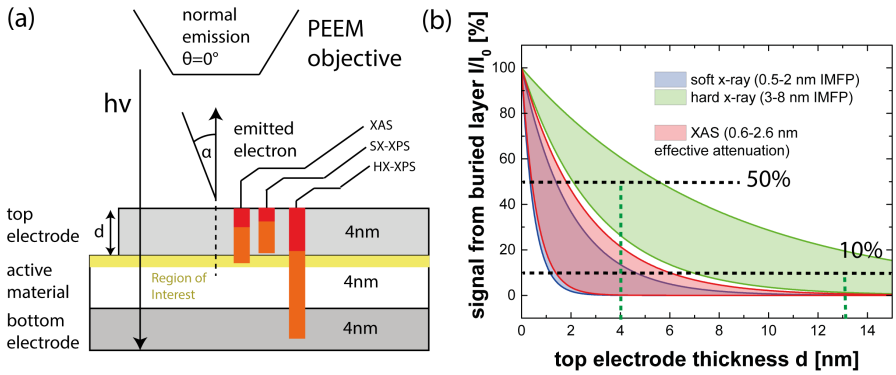

Figure 6.1. – (a) Sketch of a typical MIM structure and relevant parameters of a photoemission experiment. The yellow region under the electrode is the region of interest. The probing depth for the different methods SX-XPS, HX-XPS and XAS is exemplary indicated for a 4 nm thick top electrode by color coded bars. The red component represent 50% signal loss, the brighter one represents 90% signal loss. (b) simulated signal intensity of a buried layer covered by a top electrode of thickness d. The simulations are based on Eq. 6.1 using the attenuation coefficients discussed in the text.

The top electrode dilemma can be resolved, if the ratio between electrode thickness d and the attenuation length $\lambda(E_{\mathrm{kin}})$ in Eq. 6.1 gets smaller than $\frac{d}{\lambda} < 1$. Then, the detected signal is increased to an acceptable level of more than $\frac{I}{I_0} > 70\%$. Based on this observation two possible options on how the information depth can be tuned in order to reach the active region of MIM structures can be imagined: First, the damping length λ is increased. Second, the top electrode thickness d is reduced. Likewise, a combination of both approaches will provide positive, synergistic effect. These theoretical considerations can be implemented experimentally as outlined in the following.

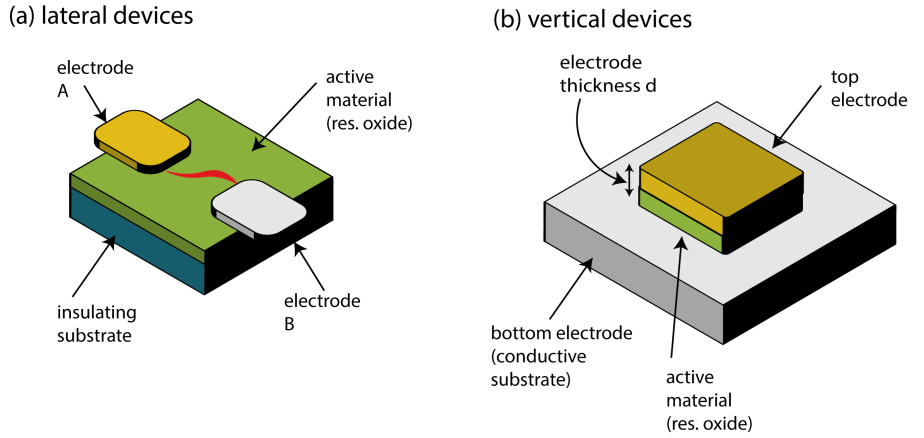

Figure 6.2. – Device geometries for operando PEEM. (a) In the lateral geometry the contacts are arranged in-plane. Signal can be collected from the active region without attenuation. (b) In vertical structures a top electrode of thickness d covers the active layer. Switching takes place at the TE/RSM interface.

Option 1: Maximizing the attenuation length λ: In XPS, the IMFP of electrons and thus the damping length $\lambda(E_{\text{kin}})$ can be tuned by using higher photon energies. Electrons excited by hard X-rays to several keV in kinetic energy can escape without disturbance from several nm below the surface. This bulk sensitivity of hard X-ray photoemission spectroscopy (HAXPES) is well-known and it is commonly used in standard photoemission experiments to probe buried layers. Recently, also PEEM using hard X-rays (HAXPEEM) has been demonstrated [55]. Unfortunately, the photoemission cross section σ of shallow core levels being relevant to chemical characterization is highly suppressed for hard X-ray excitation. The reduced cross sections lead to weak signals and increased acquisition times. A detailed discussion of **HAXPEEM** and its application to top electrode contacted devices will be given in section 6.2.

Option 2: Minimizing the top electrode thickness d : The thickness of the electrode d can be reduced to the order of the attenuation length λ. In fact, the smallest $d = 0$ - equal to zero attenuation - can be achieved if the electrode is moved into a **lateral device geometry**, Fig. 6.2a. This configuration seems favorable for photoemission, but the change in the geometry also affects the electric field distribution and turns the electric field in-plane**.** This change of the geometry has severe impact on the switching process as will be shown in Sec. **6.3**. In turn, if the standard vertical stacking is maintained, Fig. 6.2b, the electrode thickness has to be less than or equal to $d \approx \lambda \approx 2\,nm$, which requires the fabrication of **ultra-thin, electron transparent top electrodes,** Sec. **6.4**. The ultimate limit in feasibly electrode thickness is defined by monolayer materials.

6.2. Approach 1: Hard X-ray photoemission electron microscopy (HAXPEEM)

One option to overcome the surface sensitivity of PE without modifying the sample design is to exploit the energy dependence of the inelastic mean free path $\lambda_{\mathrm{IMFP}}(E_{\mathrm{kin}})$. The IMFP and accordingly the attenuation length λ depend on the kinetic energy of the photoemitted electrons, which can be increased using hard X-ray photon excitation, HAXPES. Within the present thesis, the onset of hard X-rays excitation will be defined around a photon energy $h\nu = 2\,\mathrm{keV}$ following the classification scheme of Drube et al. [70]. When photons with $h\nu > 2\,\mathrm{keV}$ are used, the photoelectrons from the valence band and shallow core levels with binding energies less than 50 eV end up with kinetic energies $\mathrm{E_{kin}} = \mathrm{hv} - \mathrm{E_B}$ well above $E_{\mathrm{kin}} = 1.5\,\mathrm{keV}$. For these kinetic energies the inelastic mean free path $\lambda_{\mathrm{IMFP}}(1.5\,\mathrm{keV})$ is expected to be at least 2 nm (see "Universal curve", Sec. 4.3). Using even higher photon energies within the range of $h\nu = 6-10\,\mathrm{keV}$, the IMFP further increases up to $\lambda_{\mathrm{IMFP}} = 4-8\,\mathrm{nm}$ resulting in an overall electron escape depth of $3\cdot\lambda \approx 12-24\,\mathrm{nm}$.

The general idea of HAXPES is not new and "due to its relatively unlimited electron escape depths, HAXPES has emerged as a powerful tool that has general application to the study of the true bulk and buried interface properties of complex materials systems..." [59]. Further, "HAXPES has opened up other research areas [...] like the study of realistic prototypical multilayer device structures under both ambient and operando conditions" [59]. In the context of resistive switching, HAXPES has already been successfully applied to devices based on HfO_2 [71, 72] and $SrTiO_3$ [73]. Both experiments clearly show the intermixing of different valence states at the interface during the initial filament formation process. In the authors opinion, however, the switching induced changes between LRS and HRS reported in Ref. [71] remain dubious, because the observed spectral variation only marginally exceeds the noise threshold. An explanation for the low contrast can be attributed to the fact that in most oxides the resistive switching process is localized to small, confined, sub-micron region. As HAXPES is a spatially averaging method - averaging over the entire device - the filamentary contributions to the spectra may be present, but obscured by the larger background signal arising from the surrounding, unaltered material.

These experimental uncertainties may be ruled out by a spatially resolving the HAXPES signal, which can be achieved by combining a hard X-ray excitation source with a modified, photoelectron emission microscope, HAXPEEM. All experiments related to the HAXPEEM approach have been performed at the hard X-ray beam line P09 at PETRA-III (DESY, Hamburg) in combination with a FOCUS NanoESCA [1]. A detailed description of the microscope, its transmission function and characterization of spatial resolution for the operation in the hard X-ray regime is given by M.Patt [55, 61]. The following section provides selected exemplary experimental data on TaO_x/ZrO_x and $SrTiO_3$ MIM devices in order to quantify the probing depth of HAXPEEM and to evaluate its capability of being applied in time-resolved experiments. [2]

[1] Beamline specifications are given in the last column in Appendix Tab. A.1

[2] For the evaluation of the electron escape depth data of ZrO_x/TaO_x crossbar experiments are taken for reference, because the crossbar structures have a well-defined vertical electrode spacing of 12 nm between the top and bottom electrode. Knowing this distance the attenuation length can be calculated from the intensity ratio of top and bottom electrode.

The gain in information depth in HAXPES and HAXPEEM comes at a cost. The atomic photoionization cross sections σ_{nl} of VB electrons for hard X-ray (10 keV) excitation - defining the likelihood of a photoemission event to occur - are decreased by 3 – 6 orders of magnitude as compared to soft X-ray excitation (1 keV). This effect leads to a significant lowering in the counting statistics going along with an increase in acquisition time. The decrease of the cross sections for a specific orbital can be approximated by $\sigma_{nl}(E_{kin}) = (E_{kin})^{-3.5-l}$, where l is the angular momentum and n is the principal quantum number [59,70]. More specifically, the photoionization cross sections for different atomic orbitals in the photon energy range from 1 keV to 150 keV have been calculated and tabulated by Scofield [74]. The expected low electron yield in HAXPEEM impacts on energetic and spatial resolution and may present an insurmountable obstacle for time-resolved measurements.

6.2.1. Evaluation of HAXPEEM probing depth

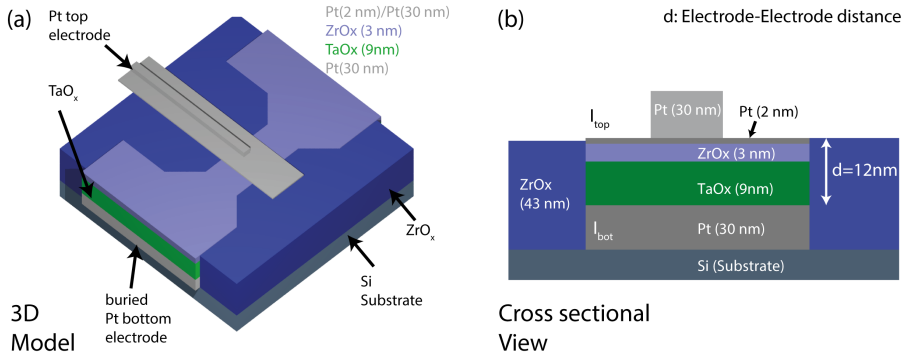

Figure 6.3. – (a) Three-dimensional representation and (b) cross sectional representation of TaO_x/ZrO_x crossbar devices with $Pt/ZrO_x/TaO_x/Pt$ layer stacking.

Functional TaO_x/ZrO_x hetero structure crossbar devices, Fig. 6.3, were utilized for the characterization of the HAXPEEM probing depth by an overlayer approach. [75] The investigated devices consisted of a Pt(30 nm)/Pt(2nm)/ZrO_x(3 nm)/TaO_x(9 nm)/Pt(30 nm) layer stack and were fabricated by A. Kindsmüller from IWE, RWTH Aachen University. The Pt top electrode was designed to be as thin as 2 nm to maximize electron transmission. An additional 30 nm thick Pt finger was deposited in the center of the top electrode to improve the mechanical and thermal stability. The Pt top and Pt bottom electrodes are separated by a spacer of $d = 3 + 9 = 12$ nm of oxide material. For the recalculation of the attenuation length λ, the XPS signal of the top electrode was assumed to be undamped, while the XPS signal of the bottom electrode is attenuated by 12 nm of oxide material. The energy dependence of the attenuation length $\lambda(E_{\mathrm{kin}})$ of the TaO_x/ZrO_xoverlayer was calculated according to Eq. 6.1 by comparing the emitted Pt 4f intensity of the bottom electrode $I(\mathrm{Pt\,4f})_{\mathrm{bot}}$ to the emitted Pt 4f intensity of the top electrode $I(\mathrm{Pt\,4f})_{\mathrm{top}}$ for different photon energies $h\nu$[3]:

$$I(\mathrm{Pt\,4f})_{\mathrm{bot}} = I(\mathrm{Pt\,4f})_{\mathrm{top}} \cdot \exp\left(-\frac{d \cdot \cos\theta}{\lambda\left(h\nu - E_{\mathrm{Bin}}\right)}\right) \tag{6.2}$$

[3]The kinetic energy is related to the photon energy according to $E_{\mathrm{kin}} = h\nu - E_{\mathrm{B}}(\mathrm{Pt\,4f})$

In this configuration d is defined by the electrode-electrode distance i.e. $d = 12\,\text{nm}$. For the given HAXPEEM setup, the acceptance angle θ of the microscope is smaller than 5° [55] and hence $\cos\theta \approx 1$, allowing to treat emission in the *straight line approximation*.

The procedure of calculating the attenuation length λ using a microscopic approach is illustrated in Fig. 6.4. First, a spatially resolved Pt 4f XPS spectrum ($E_\text{B} = 70 - 78\,\text{eV}$) for a given photon energy $h\nu$ was acquired in a field of view (FoV) containing both electrodes, Fig. 6.4a. From the acquired 3D data set, the Pt 4f intensities $I(\text{Pt4f})_{bot}$ and $I(\text{Pt4f})_{top}$ were extracted from the bottom and the top electrode regions, Fig. 6.4b. Each spectrum was fitted by CasaXPS using a fixed f orbital peak ratio of 4 : 3 and constant peak broadening. In a final step the attenuation length $\lambda(h\nu - E_\text{B}) = \frac{d}{\ln(R)}$ was calculated from the fitted peak area ratio $R = \frac{I(\text{Pt4f})_{bottom}}{I(\text{Pt4f})_{top}}$ of the $\text{Pt4f}_{7/2}$ main line at a binding energy $E_\text{B} = 72.5\,\text{eV}$.

The procedure was repeated at three different photon energies: $h\nu = 3000\,\text{eV}$, $h\nu = 4000\,\text{eV}$ and $h\nu = 5500\,\text{eV}$. The resulting energy dependent attenuation length $\lambda(E_\text{kin})$ is plotted in Fig. 6.4c. The error of the measured λ is based on a 5% error margin assumed for the overlayer thickness. The error in photon energy is negligibly small (< 0.3%). The experimentally observed attenuation length for HAXPEEM are increasing with photon energy matching the anticipated decreasing surface sensitivity. For the highest photon energy of $h\nu = 5500\,\text{eV}$ an attenuation length of $\lambda \approx 6.6\,\text{nm}$ was derived. This corresponds to a maximum *probing depth* of $P = 3 \cdot \lambda \approx 19.8\,\text{nm}$. A comparison of the measured attenuation length with experimentally determined values of the IMFP in Cr covered Au (purple) [55] and with simulated IMFPs (dashed-lines) shows good agreement, Fig. 6.4c.

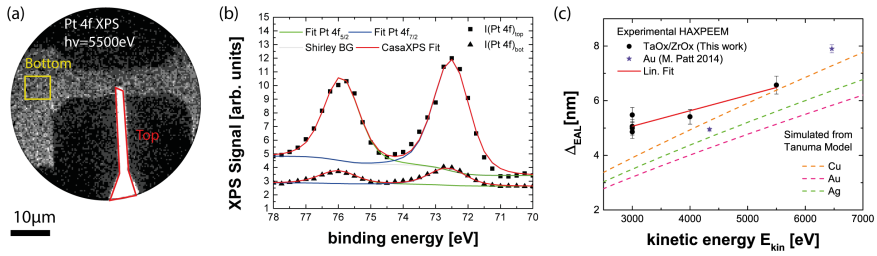

Figure 6.4. – (a) HAXPEEM image at the Pt 4f core level for hard X-ray excitation with $h\nu = 5500\,\text{eV}$. The image shows a buried Pt bottom electrode (yellow) and an exposed Pt top electrode (red). (b) Corresponding XPS spectra for regions defined in the PEEM image. The spectra were background corrected (Shirley) and fitted by CasaXPS. (c) The attenuation coefficient λ was calculated from intensity ratios of the Pt 4f intensities for different photon energies and plotted with respect to the kinetic energy of the electrons. Experimental values of previous experiments [55] (purple) and simulated IMFPs (dashed) are plotted for comparison.

Our results on the probing depth for the three hard X-ray photon energies confirm that HAXPEEM, indeed can be used probe any point of the 12 nm thick $\text{TaO}_\text{x}/\text{ZrO}_\text{x}$ oxide layer buried beneath a 2 nm thick Pt top electrode.

6.2.2. Interface-Sensitivity and HAXPEEM performance

The variable probing depth obtained for different photon energies was further used to characterize the vertical composition of the buried TaO_x layer of a formed device in the LRS and to identify

the photon energy being most sensitive to the interface. At the same time the data served as a performance measure of the HAXPEEM approach. For this purpose, spatially resolved Ta 4f spectra ($E_B = 20-34\,eV$) were taken at increasing photon energies, with each photon energy probing deeper into the material. Spectra were extracted from $10 \times 10\,\mu m^2$ regions at the junction (black) and from the pad region (red), Fig. 6.5a. While the junction region is expected to be modified by the forming step, the pad region serves as unaltered reference. Qualitatively, two different contributions can be identified in the measured Ta 4f spectra, Fig. 6.5b. A pronounced double peak structure around $E_B = 28-30\,eV$ corresponding to the Ta 4f core level of fully oxidized Ta_2O_5 and a broad shoulder starting around $E_B = 23\,eV$ related to the under stoichiometric TaO_x and metallic phases. The ratio of the two contributions defines the chemical composition. To quantify the changes in composition of

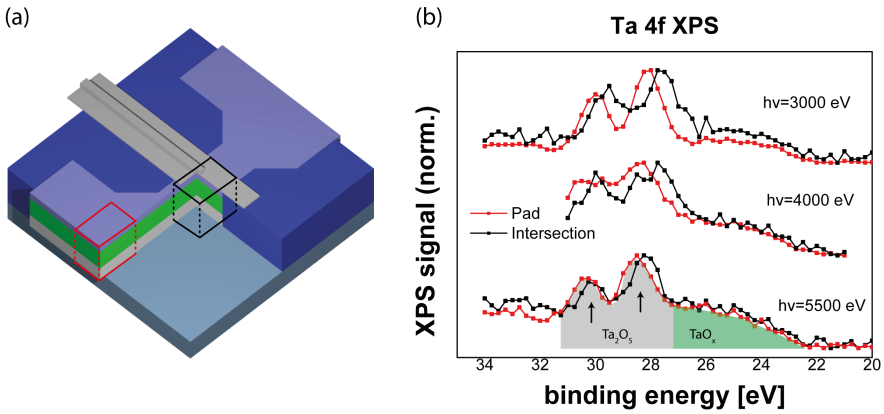

Figure 6.5. – (a) Cross section of a $ZrO_x(3\,nm)/TaO_x(9\,nm)$ device. Different regions of interest (ROI) are indicated: The junction region, where switching induced changes are expected is marked in black. Reference spectra were taken in the red region of the pad. (b) Ta 4f XPS taken at different photon energies for the two regions. Charging effects can be observed by (i) shifts in the spectra in between the two regions, which are attributed to inhomogeneous charging of top and bottom electrode and (ii) general sample charging inducing a shift of the full spectrum as it is observed for energy corrected scans at $h\nu = 4000\,eV$.

the TaO_x layer, compositional analysis of the Ta 4f spectra at different photon energies was performed by multi-peak fitting using CasaXPS. In the fitting procedure three peak doublets were modeled on a Shirley background. The doublets account for metallic components (Ta, Ta^0), sub-oxide components (TaO) and the main oxide (Ta_2O_5) as described in [76]. The peak ratios $Ta_{4f_{7/2}}/Ta_{4f_{5/2}}$ of each doublet were set to 4 : 3 according to the spin-orbit multiplicity of 4f orbitals. The binding energy positions of the peaks were set relative to the metallic $4f_{7/2}$ line according to values reported in [76]. The peak broadening was fixed for each of the doublets and amounts to $\approx 1.5\,eV$. Fits of the junction area are shown in Fig. 6.6a. While metallic contributions are negligibly small, a shift from Ta_2O_5 rich to TaO rich phases can be observed for increasing photon energies, Fig. 6.6b.

Taking into account the previously derived probing depth of each photon energy, an accumulation of Ta_2O_5 is expected near the ZrO interface, whereas TaO is mainly found near the Pt electrode. Highest sensitivity to the ZrO_x/TaO_x interface is found for a photon energy of 3000 eV, highest sensitivity to the Pt/TaO_x interface is expected for 5500 eV. The acquired data set provides essential

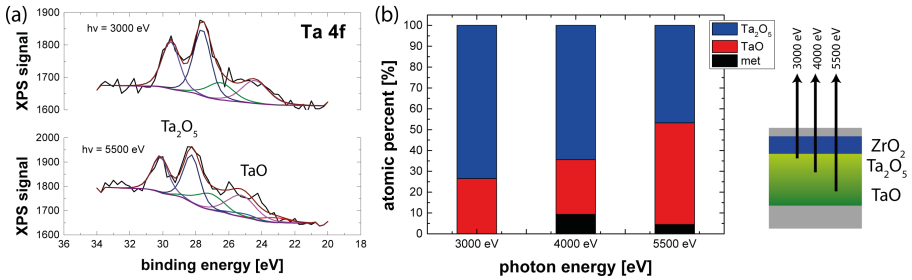

Figure 6.6. – (a) Ta 4f XPS spectra of the junction area (black) for $h\nu = 3000\,\text{eV}$ and $h\nu = 5500\,\text{eV}$. (b) Fitted relative contributions of Ta, TaO and Ta_2O_5 for different photon energies. For higher photon energies an increasing contribution of the TaO component is observed.

information on the performance of the HAXPEEM approach. The acquisition time for each point of the Ta 4f spectra was $t_{dwell} = 125\,\text{s}$. On average each scan took around 3h. Even after long exposure the spectra exhibit fluctuations in the order of $5-10\%$ of the main peak intensity. In addition to the low signal to noise ratios, energetic shifts of the spectra can be observed. Two kind of shifts are observed: (i) shifts between the two regions, which are attributed to inhomogeneous charging of the two electrodes and (ii) shifts of the full spectra, which can be seen from deviations of the core level positions in reference to literature. The latter effect was most pronounced for the photon energy of 4000 eV so that the spectra had to be manually shifted to their corresponding binding energies. The combination of charging effects and small signal to noise ratios hampers a quantitative analysis of the data.

6.2.3. Expected and measured signal intensities

The data sets for TaO_x/ZrO_x devices in the previous section were acquired with exposure times of several minutes per image. Still, the data is dominated by strong so-called *salt and pepper* noise within the images, Fig. 6.4a, going hand in hand with a large point to point variance in the extracted spectra, Fig. 6.6a. These observations are not limited to this specific material system, but could also be observed for $SrTiO_3$ and GaO_x thin film devices investigated with the same experimental setup. Consequently they seems to be intrinsic to the approach. This significantly affects the viability of the approach towards time-resolved experiments. While the HAXPEEM approach is capable of imaging XPS signal arising from buried regions underneath metal electrodes as thick as 10 nm, quantitative analysis is compromised by low signal to noise ratios accompanied by space and sample charge effects. These effects limit energetic and spatial resolution to a degree at which a meaningful analysis of percentile changes becomes practically impossible. In order to make the HAXPEEM approach a viable option for in-situ or even operando approaches, it is of utmost importance to identify causes responsible for the low signal to noise ratios. Thus, an analysis was performed for the current experimental configuration based on a simplified peak intensity analysis formula of core photoelectron emission, Eq. 4.6 [59], repeated here:

$$I(Q,n,l) = \int_0^\infty \int_0^\infty \int_0^\infty \underbrace{I_{h\nu}(x,y,z,\vec{\epsilon})}_{\text{photon intensity}} \cdot \underbrace{\rho_Q(x,y,z)}_{\text{material density}} \cdot \underbrace{\mathrm{A}\cdot\exp\left(-\frac{z}{\lambda_{\mathrm{IMFP}}(E_{kin})\cdot\cos\theta}\right)\cdot\frac{1}{m_Q}}_{\text{effective volume}} \times \underbrace{\frac{\sigma_{Qnl}(h\nu,\vec{\epsilon})}{d\Omega}}_{\text{photoionization cross section}} \cdot \underbrace{T(E_{\mathrm{kin}},\Omega(\phi,\theta))}_{\text{analyzer transmission}} \cdot \mathrm{dx\,dy\,dz} \quad (6.3)$$

This equation is well-established and widely used for peak intensities analysis. Without further proof, one of the main reasons for the observed low signal to noise ratio can be identified in the photoionization cross sections σ_{nl} of VB electrons for hard X-ray excitation. These cross sections σ_{nl} are lowered by 3 – 4 orders of magnitude in the hard X-ray regime as compared to excitation with soft X-ray (Sec. 4.2.1). Further reasons can be found in the energy-dependent transmission function T of the analyzer, which is significantly reduced for higher kinetic energies. In the following, Eq. 6.3 will be explicitly evaluated for the Ta 4f core level emission in the current experimental setup at $h\nu = 4000\,\mathrm{eV}$.

- **Photon intensity $I_{h\nu}$ and kinetic energy E_{kin} of the emitted electrons**: At a photon energy of $h\nu = 4000\,\mathrm{eV}$ the photon flux of the HAXPES beamline P09 at DESY is $\approx 10^{13}$ photons per second. These photons are distributed over a spot size of $300 \times 100\,\mu\mathrm{m}^2$, which results in an expected photon intensity of linearly polarized light $I_{h\nu} = 3.3 \times 10^{20}\,\frac{Ph}{s\cdot m^2}$. The kinetic energy of the emitted Ta 4f 7/2 electrons is $E_{\mathrm{kin}} = 3978.4\,\mathrm{eV}$ and was calculated from the binding energy $E_B(\mathrm{Ta\,4f}) = 21.6\,\mathrm{eV}$ [58] and the photon energy.

- **Number of emitting atoms N:** The number of emitting atoms $N = \rho_{\mathrm{Q}}\cdot\mathrm{V/m}$ can be calculated by multiplying $\frac{\rho_{Ta}}{m_{Ta}}$ with the effective probing volume $V = \int_0^\infty \mathrm{A}\cdot\mathrm{z}\cdot\exp\left(-\frac{\mathrm{z}}{\lambda_{\mathrm{IMFP}}(\mathrm{E_{kin}})\cdot\sin\theta}\right)\mathrm{dz}$. The density of Ta is $\rho_{\mathrm{Ta}} = 16.7\frac{g}{cm^3}$, which corresponds to $\frac{\rho_{Ta}}{m_{Ta}} = 3.34\cdot10^{21}\,\frac{atoms}{cm^3}$ (atomic mass $m_{\mathrm{Ta}} = 180\,u$). For a spectromicroscope the area A is equal to the field of view under investigation. In a typical experiment, a field of view of 70µm in diameter was chosen ($\mathrm{A_{FoV}} = 2\times\pi\times(\frac{70}{2})^2\,\mu\mathrm{m}^2 = 8.83\cdot10^{-5}\,\mathrm{cm}^2$). In first approximation the term $\int_0^\infty z\cdot\exp\left(-\frac{z}{\lambda_{\mathrm{IMFP}}(E_{kin})\cdot\sin\theta}\right)\cdot\mathrm{dz}$ can be replaced by the maximum probing depth defined as $3\cdot\lambda_{\mathrm{IMFP}}(E_{\mathrm{kin}} = 3978.4) \approx 15\,\mathrm{nm}$ if the detectable emission angle θ is small and thus $\sin\theta \approx 1$. The effective volume is then given by $V = A_{FoV}\cdot3\cdot\lambda_{\mathrm{IMFP}}(3978.4\,\mathrm{eV}) = 1.3\cdot10^{-10}cm^3$. In total, the effective number of emitting atoms N amounts to $N = \frac{\rho_{\mathrm{Ta}}}{m_{\mathrm{Ta}}}\cdot V = 3.34\cdot10^{21}\,\frac{atoms}{cm^3}\cdot1.3\cdot10^{-12} = 4.42\cdot10^{11}$ atoms.

- **Photoionization cross section σ_{nl}:** The subshell photoionization cross section for Ta 4f core level at a photon energy $h\nu = 4000\,\mathrm{eV}$ is 1500 Barn $= 1.5\cdot10^{-25}m^2$. [4]

- **Transmission of the microscope $T(E_{\mathrm{kin}},\Omega(\phi,\theta))$:** For kinetic energies around 4000 eV the acceptance angle θ of the microscope using a contrast aperture of 500 is less than 10° [55]. The small angle reduces the transmission to $T(4000\,\mathrm{eV}) \approx 2\cdot10^{-3}$ [55]. Other effects reducing the signal intensity like conversion effects in the imaging unit or phase space reduction by the analyzers are neglected. In any case, these effects would only further decrease the transmission.

[4] The cross section value is tabulated in Ref. [74].

Evaluation of Eq. 6.3 for the present experimental configuration leads to Eq. 6.4. For a photon energy of 4000 eV, XPS from the shallow Ta 4f core level of a 70 μm FoV is expected to result in about 44.000 detected electrons per second. This value defines an upper limit because losses due to the energy filter and imaging unit are not yet taken into account.

$$I(\mathrm{Ta\,4f}) = \underbrace{3.3\cdot10^{20}\frac{Ph}{s\cdot m^2}}_{\text{photon intensity I}} \cdot \underbrace{4.42\cdot10^{11}\,\mathrm{atoms}}_{\text{effectively contributing atoms N}} \cdot \underbrace{1.5\cdot10^{-25}m^2}_{\text{cross section}} \cdot \underbrace{2\cdot10^{-3}}_{\text{microscope transmission}} \approx 43.750\,\frac{el}{s} \quad (6.4)$$

The detector of the HAXPEEM end station is a CMOS camera detecting 600 by 600 pixels [55], from which effectively only $N = 200\times200\times2\times\pi \approx 250.000$ pixels are used for detection. Division of the detected electron intensity I(Ta 4f) by the number of pixels yields the average intensity per pixel $I_{Pix} = \frac{I(Ta4f)}{N} = 0.175\frac{el}{s\cdot pixel}$. On average 0.176 electrons per pixel and second are detected. The calculated low intensities are in accordance with the measured intensities in single event counting mode by Patt [55]. Projected from measured high resolution HAXPEEM scans, single image acquisition times of minimum 10 min are required for acceptable signal to noise ratios leaving space for interpretation of percentile chemical changes on the micron scale. Single images with comparable statistics, which were taken at Au 4f core level used for characterization of the probing depth and spatial resolution in Patt et al. [55], were taken with acquisition times as long as 150 min per image. As a full XPS-PEEM spectrum consists of multiple, single images taken at different energies around the core level, a high resolution HAXPEEM scan of a single core level takes at least $t_{Scan} = 560\,\mathrm{min} \approx 10\mathrm{h}$. Compared to an average beam time slot of 72 h this limits the experiment to a very few, selected scans and presents in the current configuration an insurmountable obstacle for time-resolved studies, where XPS spectra have to be acquired at different times during the switching process.

6.2.4. Viability of the HAXPEEM approach for time-resolved studies

The question whether HAXPEEM can become a viable option for time-resolved studies of buried interfaces is directly related to the technical question if the electron yield of the microscope can be increased. Equation 6.3 identifies the limiting factors: The density ρ, the cross sections σ_{nl} and the probing depth $\propto \lambda_{\mathrm{IMFP}}$ are limited by physical processes and cannot be changed. The field of view A is determined by the feature size of the expected changes and also is not accessible to increase the yield. The only remaining adjustable parameters for an increased yield are thus the photon intensity $I_{h\nu}$ and the transmission function T of the microscope.

The transmission of the microscope T is related to the acceptance angle, which is below 10° for high kinetic energies of the electrons, because the immersion lens effect of the microscope is drastically reduced [55, 61]. One way to increase the acceptance angle of the microscope is to increase the accelerating field. Higher accelerating fields, however, are problematic as direct field emission from the sample will set in for fields in the order of $E = 10^8\frac{V}{m}$ and the arcing probability is enhanced, whereas accelerating fields in the current setup are already in the order of $E = 10^7\frac{V}{cm}$ and field emission is observed for sharp edges.

The second option is to increase the photon intensity $I_{h\nu}$ on the sample. The current photon flux $\Phi \propto 10^{13} \frac{Ph}{s}$ of the P09 beamline [77] is given by the undulator and the monochromatizing elements. In the current experimental setup the total flux is dispersed over an area of $300 \times 400\,\mu m^2$ due to out-of-focus conditions. Micro-focusing of the beam spot down to the desired field of view ($20 \times 20\,\mu m^2$), the overall intensity can be increased by a factor of 75 up to $I_{h\nu} = \frac{\Phi}{A_{Spot}} \approx 2.47 \times 10^{22} \frac{Ph}{s \cdot m^2}$ as compared to $I_{h\nu} = 3.3 \times 10^{20} \frac{Ph}{s \cdot m^2}$ in the current configuration. The intensity is inversely proportional to the acquisition time. A gain of 75 in intensity would decrease the acquisition time by the same amount. Micro-focusing is planned for upcoming experiments at the newly build P22 end station being expected to go into operation at the end of 2017.

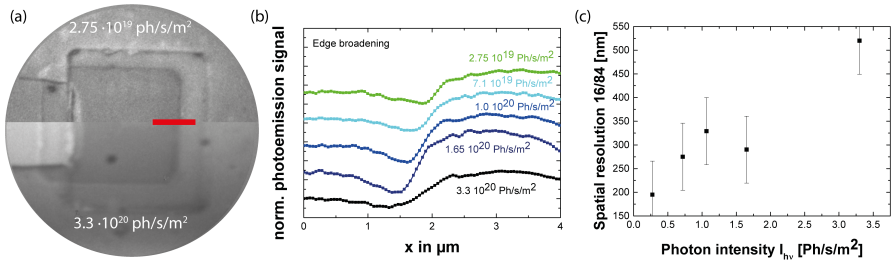

Figure 6.7. – (a) XPEEM images at the secondary cut-off acquired for two different photon intensities. The bottom part of the image is blurred and shows intensity modifications related to space charge effects. (b) corresponding line profiles of the edge marked by the red line for different photon intensities. (c) The spatial resolution derived from the line shapes according to the 16/84 criterion.

However, there are two more major challenges arising from the increase in photon flux. Already for the current experimental setup, the average photon intensity on the sample leads to *space* and *sample charging effects*. Both effects limit the achievable spatial and energetic resolution. Space charge effects describe spatial image blurring due to the Coulomb interaction between the emitted electrons [78, 79]. These effects scale with the density of the emitted electron cloud and thus scale with the photon intensity. Further the Coulomb interaction leads to energetic broadening in the spectra. The effect of space charge induced image blurring is illustrated by an XPEEM image series of a graphene contacted $SrTiO_3$ device. PEEM images were acquired close to the secondary cut-off measured at different photon intensities $I_{h\nu}$, Fig. 6.7a. In this experimental series the photon intensity was attenuated from initially $I_{h\nu} = 3.3 \cdot 10^{20} \frac{Ph}{sm^2}$ down to $2.75 \cdot 10^{19} \frac{Ph}{sm^2}$ by inserting absorbing Al foils of variable thickness into the X-ray beam. In between the scans the microscope settings were not altered. The spatial blurring can be quantified from line profiles taken along step edges on the sample, Fig. 6.7a & b. These line profiles were used to calibrate the spatial resolution according to the 16/84 criterion.[5] The analysis of line scans at different photon intensities indicates a loss of spatial resolution by a factor of 3 if the full beam intensity is used, Fig. 6.7c. This effect can be expected to be even more pronounced for higher fluxes. Electron optical simulations suggest that fast, high kinetic energy electrons are spatially separated from the slow kinetic electrons and experience less of the Coulomb interaction. Further, due to the lens arrangement of focus lens and objective, slow

[5] The 16/84 criterion is usually applied for step broadening effects. It defines the distance between the point of 16% step height and the point of 84% step height as the resolution broadening of a step function.

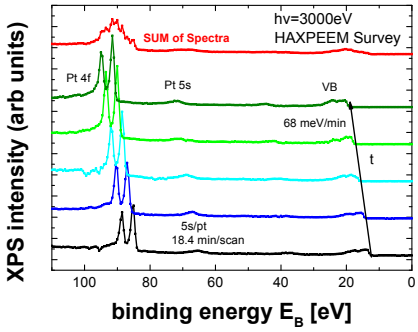

Figure 6.8 – Sample charging effects observed during HAXPEEM ($h\nu = 3000\,\text{eV}$) survey scans of Pt/TaOx/Pt devices. Each scan took 18.4 min and a linear shift between subsequent scans can be observed. This indicates a constant charging of the sample surface with 68 meV/min.The red line is representative for a long exposure spectrum.

electrons are reflected at the objective lens. This would limit the broadening effects to the secondary electron region. Quantitative characterization of the spatial resolution broadening for high kinetic electrons, however, is yet missing due to the lack of statistics. A proper characterization may be performed once the new beam line is operational.

A second effect related to the photon intensity and observed during measurements is sample charging. This effect materializes as a continuously increasing shift of the acquired XPS spectra over time complicating the interpretation of long exposure images. Fig. 6.8 shows a set of valence band spectra measured at the Pt electrode. The acquisition time for each scan was about$\approx 19\,\text{min}$. The scans are chronologically ordered from top to bottom. A steady shift of the full spectrum to higher binding energies by $68\,\frac{\text{meV}}{\text{min}}$, which is related to charging of the sample under beam, can be clearly identified. Sample charging effects are well known for insulating and semiconducting materials [80]. Unfortunately, functional MIM devices need good and large insulating layers to electrically separate top and bottom electrode and sample charging is likely to be observed. Similar to the space charge effect, sample charging also scales with the photon intensity.

6.3. Approach 2: Planar Devices

Planar (lateral) device geometries present an alternative to the weak signals acquired in HAXPEEM, because they enable characterization by high intense XAS and medium bright SX-XPS. In this configuration the two electrodes connecting the active region are placed in the same plane of the device, Fig. 6.2a. Since in this approach the area, where the switching - and thus the chemical changes - are expected is exposed, lateral devices seem to fit the requirements of operando PEEM best. The distance between the two electrodes is typically of the order of $d_{lat} = 1 - 20\,\mu m$ and thus safely within the spatial resolution limit of a PEEM. Further, the device fabrication process is simple as it does not involve complex lithographic steps, as for example the additional deposition of insulating layers.

Three different experiments using lateral $SrTiO_3$ devices have been reported in literature [81–83]. While Peng and co-workers [81] put their focus on the electric characterization of different electrode configurations, Janoush et al. [82] and Andreasson [83] use X-ray absorption techniques to evaluate the role of oxygen vacancies during the initial formation process, Fig. 6.9d. All three experiments confirm that switching in lateral geometry is feasible, but none of the mentioned experiments investigates the reversible switching between LRS and HRS.

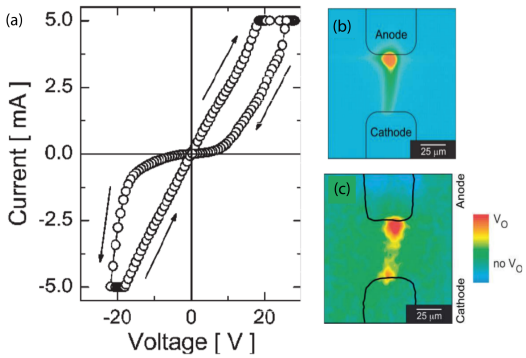

Figure 6.9 – Lateral Cr-doped $SrTiO_3$ resistive switching device. Images are adapted from ref. [82]. (a) I-V curve for switching cycle (b) thermal distribution during operation derived from infrared emission (c) oxygen vacancy concentration recalculated from Cr x-ray fluorescence. For details see ref. [82]

Based on the reported results and specifications of the aforementioned publications, multiple sets of lateral $Pt/SrTiO_3/Ti$ devices were designed to evaluate the suitability of a lateral device structure for real time XPEEM, Fig. 6.10a. However, already for the first generation of devices a severe problem, which completely disqualified lateral devices for the operando XPEEM characterization of the switching process, was identified from initial characterization experiments, literature research and simulations of cooperating partners [20, 21]. In contrast to the initial filament formation step, which takes place over the entire distance between the two electrodes (Fig. 6.10b) and which is addressed in the publications of Peng, Janoush and Andreasson, the subsequent resistive switching between the LRS and the HRS is accomplished by the modification of the oxygen vacancy concentration on a confined, nanoscale distance of less than 10 nm in the vicinity of the electrode/STO Schottky contact [21]. The situation is illustrated in the inset of Fig. 6.10b: While the filament spans over the full electrode-electrode distance, switching takes place only at the filament terminators.

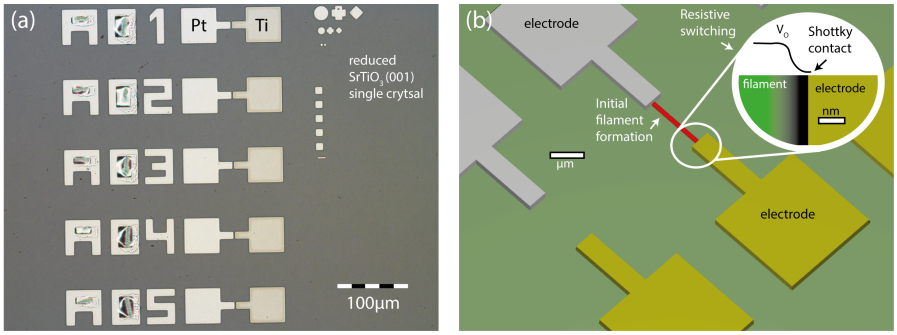

Figure 6.10. – (a) Optical microscope image of first generation lateral Pt/$SrTiO_3$/Ti devices. The structures were designed according the pioneering work of Peng et al. (b) Schematic drawing of an in-plane device after an initial formation process: a filament of several µm has formed between the two electrodes (red). The subsequent ON/OFF switching process is linked to the modification of the oxygen vacancy concentration $V_{\ddot{O}}$ in the vicinity of the electrode filament interface (inset). The switching induced changes take place on a nm scale.

As the expected changes on the nanometer scale cannot be resolved with the present spatial resolution of an XPEEM ($\delta_r > 20$ nm) and we additionally found surface reduction of $SrTiO_3$ under intense beam irradiation for uncovered SrTiO single crystals (see Sec. 5.2), the focus of the studies was shifted away from lateral devices towards the investigation of vertical structures. Still, it is important to mention that due to the small signal loss, lateral geometries are the most suitable for time-resolved measurements in XPEEM and should be used whenever the feature size is large enough to be detected.

6.4. Approach 3: Ultra-thin, electron transparent top electrodes

In the last approach the advantages of the layered vertical geometry were combined with the high signal intensities expected for XAS by the fabrication of devices with ultra-thin, almost electron transparent top electrodes. In order to make an electrode transparent for SX-XPS and XAS signals the thickness has to be decreased below 2 nm. Below 2 nm the signal damping is expected to be less than 60%, see 6.1. These thicknesses, however, corresponds to only a few layers of electrode material. Thus, electrode fabrication in this regime is complicated, because thin-film growth is dominated by interface effects and often inhomogeneous island and/or polycrystalline growth modes are observed. The contact resistance, the capability of the electrode to store oxygen as well as optical and mechanical properties critically depend on the thin film quality. As for this reasons homogenous top electrodes are of utmost importance for proper device operation.

To match the criteria for operando resistive switching experiments, the top electrode does not only have to be very thin, it furthermore has to be flat, continuous and conductive; the work function Φ has to be large enough in order to facilitate a Schottky contact with the $SrTiO_3$. The material should not react with oxygen and it should have a low atomic number Z to minimize absorption effects. The absorption spectrum between 400 – 600 eV should be featureless to allow a clear identification of the

$SrTiO_3$ signal at the O K- and Ti L-edges, see Fig. 6.11. Due to the high electric load and the related Joule heating induced by the switching process, the material should have a melting point T_m above 500°C [84].

These material specifications narrow down the field of applicable elements. Two candidates have proven suitable: First, metallic thin film electrodes consisting of 2 nm Rh ($Z = 45, \Phi = 4.98\,\text{eV}, T_m =$ 1966°C) and, second, ultra-thin graphene top electrodes ($Z = 6, \Phi = 4.89 - 5.16\,\text{eV}$ [85], $T_{\text{Sub}} = 3700$°C).

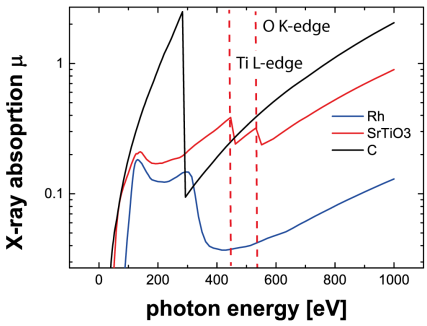

Figure 6.11 – X-ray absorption coefficient μ for rhodium (Rh, blue) and carbon (C, red). Both materials exhibit a nearly linear absorption in the vicinity of the oxygen K- and titanium L-edge excluding signal interference. Data tables from: [86]

6.4.1. XAS attenuation length for Rh electrodes

To find the best compromise between electrode thickness and transmission in case of Rh electrodes, the so far unknown attenuation length λ for XAS for the given geometry was experimentally determined by overlayer experiments in SEY XAS-PEEM. Therefor, signal intensities of the O K-edge absorption acquired from a bare sapphire Al_2O_3 substrate have been compared to the same spectra acquired from two sapphire substrates with well-defined Rh layers on top. The two Rh overlayer thicknesses were determined by X-ray reflection measurements (XRR) to be $d = 2.68$ nm and $d = 3.71$ nm, respectively, Fig. 6.12a. All three acquired O K-edge XAS spectra were corrected using a linear background. To compensate for background subtraction induced errors, two peaks instead of one (Peak 1 at 539 eV and Peak 2 at 544 eV) were used for the estimation of the attenuation length. The peak intensity of the bare substrate was used as reference for the expected intensity of a free standing layer, whereas the spectra for the other two samples were assumed to be damped by the Rh. For the 3.7 nm overlayer, a signal attenuation of nearly 400 was observed and the O K-edge could hardly be distinguished from the Rh background.

Assuming that the decrease in intensity can be modeled by Eq. 6.1, the attenuation length at Peak 1 (539 eV) was derived to $\lambda(539\,\text{eV}) = -\frac{d}{\ln\frac{I}{I_0}} \approx 0.78$ nm from exponential fitting. Repeating the procedure for Peak 2 resulted in $\lambda(544\,\text{eV}) = 0.84$ nm, Fig 6.12b. The average value $\lambda = 0.8$ nm agrees well with the lower limit of the literature values, Sec. 6.1. The results verify that a buried oxygen rich interface can be detected using SEY-XAS through 3.7 nm of top electrode material with an intensity loss of 99%. This findings set tight constraints for the layer thickness. A fabrication process limited tolerable compromise between electrode quality and electron transparency was found for a thickness of 2 nm .

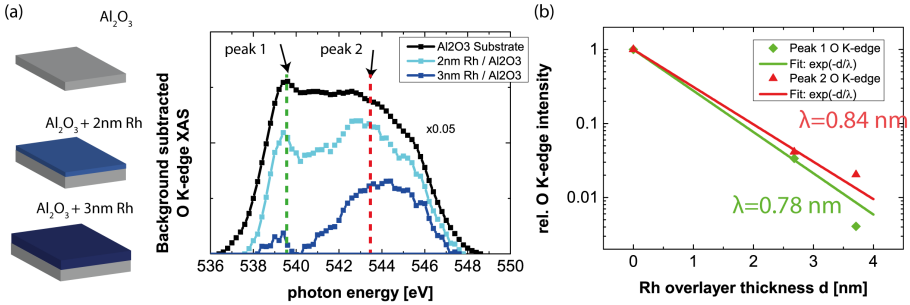

Figure 6.12. – Determination of the XAS attenuation length for the O K-edge in Rh electrodes (a) background subtracted O K-edge absorption spectra for the bare sapphire substrate (black, scaled by 0.05), for a 2.68 nm Rh overlayer (cyan) and for a 3.71 nm Rh overlayer (blue) (b) Intensity extraction at peak 1 and peak 2 with subsequent exponential fitting results in a $\frac{1}{e}$ distance of about $\lambda = 0.8\,\text{nm}$

6.4.2. Electron transparency of fabricated, thin-film devices

With respect to the electrode thickness, graphene monolayers provide an unparalleled alternative to Rh. Graphene is a quasi two-dimensional, one atom thick ($d = 345\,\text{pm}$), sheet material consisting of carbon in a hexagonal coordination. Due to three strong in-plane σ bonds, the material shows a very high mechanical stability and a delocalized π-electron system perpendicular to the surface is responsible for a very high sheet conductivity of $15.000\frac{\text{cm}^2}{\text{Vs}}$. The two dimensional structure in combination with the high electronic conductivity makes graphene an ideal photoelectron-transparent electrode.

Thus, two types of ultra-thin film top electrode designs have been fabricated and tested: (a) 2 nm Rh and (b) structured graphene monolayers. The device geometries of each of the two types are schematically depicted in Fig. 6.13. In both geometries STO thin films were deposited on Nb:STO substrates by pulsed laser deposition (PLD). On top of the STO film either the metal (Rh) or graphene electrodes were structured by photo lithography. Micro-structured Au leads with a small overlap to the graphene/Rh were used to electrically contact the top electrode to an external power supply. In both configurations the Au lead is insulated from the STO film by a thick insulating ZrO film, which has an opening ("window") of a few µm×µm at the top electrode location.

For the graphene device fabrication process, micrometer sheets of graphene monolayers are mandatory. In 2009, Li et al. [87] demonstrated large-area synthesis of high-quality and uniform graphene films by chemical vapor deposition (CVD) on a thin, heated copper foil. The same technique was applied in the device fabrication process of devices investigated in this thesis. During the optical lithography the copper film was removed by chemical wet etching. The graphene sheets were then transferred to the pre-structured $SrTiO_3/Nb:SrTiO_3$ samples using a well-established wet transfer process [88]. After the graphene transfer the remaining lithography steps were performed by standard photo lithography. Additional information on the device fabrication process is provided in the supplementary information of the publication by C. Bäumer, C. Schmitz et al. [1], in the PhD thesis of C. Bäumer [89] and the master thesis of R. Valenta [90]. [6]

[6] Prototypical devices in vertical geometry have been fabricated by C. Bäumer, R. Valenta and co-workers from PGI-7, FZ Jülich. The graphene monolayers were grown by S.P. Rogers, University of Illinois. The graphene devices depicted in

PEEM images of the finalized electrode designs are presented in Fig. 6.13a. The features visible in PEEM are mapped to the corresponding parts of the device geometry. Corresponding Ti L- and O K-edge SEY-XAS spectra for both types of devices are shown in Fig. 6.13b. The direct comparison between the SEY-XAS line shapes of the two samples reveals two main features. First, the signal to background ratio for graphene is much larger as compared to the Rh electrodes. Second, the O K-edge signal from underneath the graphene electrode reproduces the line shape of bulk $SrTiO_3$ with more detail than the corresponding signal of the Rh top electrode device. Especially, the important Ti 3d - O 2p hybridization feature around a photon energy of 531 eV cannot be identified in case of the Rh electrodes. The changes in line shape are attributed to the increasing contribution of oxygen absorbed on the surface of the Rh electrodes, which is present in any beamline. Due to the strong damping of the STO signal the relative contribution of these adsorbates is enhanced. While graphene electrodes have a signal loss of less than 35% and mostly the active $SrTiO_3$ layer is probed, the signal loss of the Rh electrodes is around 80% and only a fraction of the underlying $SrTiO_3$ layer can still be detected.

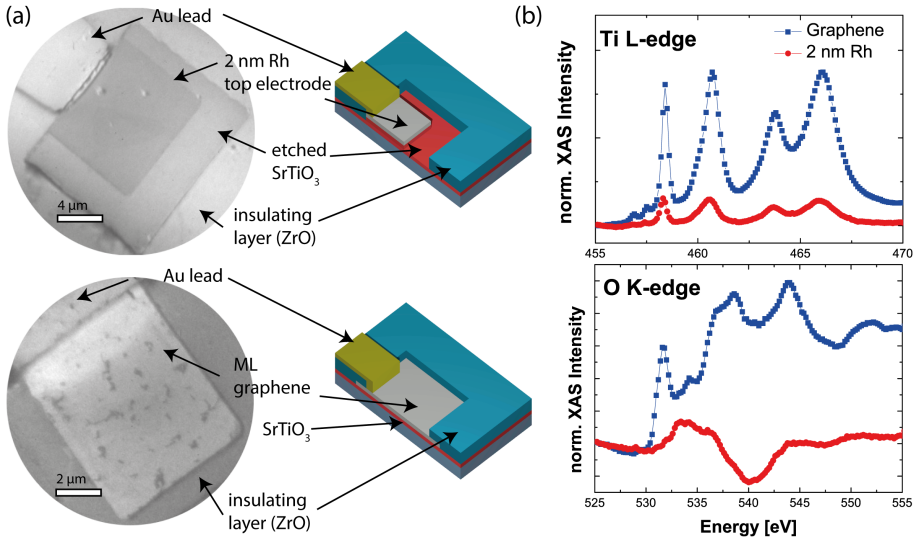

Figure 6.13. – (a) Vertical MIM $SrTiO_3$ devices: XAS images of 2 nm Rh (top) and 1ML graphene (bottom) electrodes. (b) Ti $L_{2,3}$-edge absorption spectra and O K-edge absorption spectra collected from underneath 1 ML graphene (blue) and 2 nm Rh (red). In contrast to the Rh overlayer, the graphene top electrode exhibits less absorption and shows more details of the Ti $L_{2,3}$ and especially of the O K-edge line shape. The average transmissivity of the graphene electrodes was calculated to be 7 – 10 times larger as compared to the Rh electrodes.

Some of the devices were used to derive the damping coefficient λ. The Rh devices, for example, provide open access to etched STO regions near the electrode, Fig. 6.13. These regions have been

this section were utilized within the publication "Quantifying redox-induced Schottky barrier variations in memristive devices via in operando spectromicroscopy with graphene electrodes" [1].

used as references for the intensity that would have been expected for an electrode-free region I_0. During the course of the experiments the intensity ratios between the measured intensity I_d at the electrode and the intensity in the electrode-free surrounding I_0 has been calculated for many different devices. In all cases the Rh thickness was assumed to be the nominal value of 2 nm. In the case of the graphene top electrode the I_0 was measured in the regions where the graphene layer was incomplete. Here, the graphene layer was assumed to be a monolayer of 345 pm thickness, while the surrounding was assumed to be graphene-free. All values were cast into a single plot, Fig. 6.14a. The data points show a strong scatter, which is mainly attributed to the uncertainty in thickness. Additionally, the calculated intensity ratios expected from the attenuation length ($\lambda = 0.6\,\text{nm} - 2\,\text{nm}$) reported in literature [67, 68, 91] are indicated by the black lines. The majority of measured values falls within the region spanned by these values. The average value of the full data set - including G and Rh electrodes - is $\lambda = 1.6\,\text{nm}$ (dashed line).

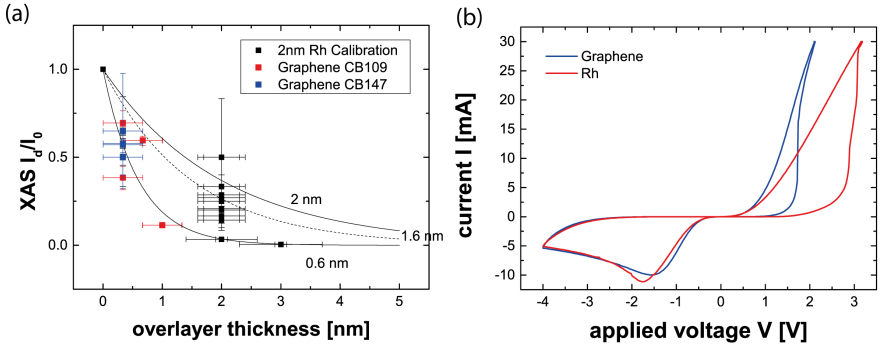

Figure 6.14. – (a) Collection of experimentally measured intensity ratios I_d / I_0 used for the calculation of the attenuation coefficient λ. As guide to the eye the lower and upper limit of the literature values are plotted as black lines. The average attenuation coefficient is in the order of 1.6 nm and shown as dashed line. (b) measured I-V curves for a LRS-HRS-LRS cycle of ultra-thin film devices. Both electrode materials show reproducible switching.

Finally, device operation for ultra-thin electrodes was verified for both device types by cycling the devices between LRS and HRS states. The typical counter clockwise switching behavior remains intact and both electrode materials show a pronounced switching hysteresis, Fig. 6.14b. Overall, the thin-film electrode devices in combination with XAS provide a very promising approach to study operando switching in PEEM with good signal to background ratios and without significant modifications of the switching properties.

6.5. Summary and Outlook

For the in-operando characterization of functional RSM it is essential to have a working electrode. Unfortunately, the presence of a top electrode leads to a strong damping of the chemically relevant signal. Based on a simple, exponential decay function the expected signal damping was modeled and three experimental approaches were identified to bypass the physical limitations imposed by the photoemission process.

It was demonstrated that photoelectron emission microscopy using **hard X-rays** can be used to image interfaces buried underneath thin top electrodes. Practically, however, the approach is limited by the low photoionization cross sections of VB electrons in the hard X-ray regime. Basic calculations of the expected signal intensity confirm the observed low count rates of $0.17\frac{el}{s \cdot pixel}$ leading to aquisition times of several hours per scan for a good signal to noise ratio in high-resultion scans measurement. This poses an insurmountable obstacle for time-resolved measurements, where XPS scans need to be taken at different time steps. Experimental modifications to increase the signal-to-noise ratio and to decrease the acquisition time have been discussed in view of enabling time-resolved measurements using HAXPEEM at all. The photon intensity can and will be improved by micro-focusing the X-ray beam in the new beam line P22 in late 2017. However, the higher intensity will eventually increase the observed space and sample charge effects. While sample charge effects can be reduced by sophisticated sample grounding, it still has to be evaluated if and how space charge effects affect the spatial resolution for the high kinetic electrons. In case they do, space charge effects can be reduced by increasing the repetition rates or the bandwidth of the excitation source. All these reasons render the spatially resolved operando characterization of devices in the current configuration as not yet possible. To put our results into context, both techniques HAXPEEM and time-resolved HAXPES (tr-HAXPES) have been classified as "future directions in hard X-ray spectroscopy" by a recent state-of-the-art review (2016) of Weiland et al. [92]. The successful combination of both techniques would be a great leap forward and enable completely new fields of science. So far, only a single group at the free electron laser Spring-8 Angstrom Compact Free Electron Laser reports having achieved time resolution in HAXPES (tr-HAXPES), but still without any spatial resolution [79].

In the **lateral device geometry** the active material is directly exposed providing the best signal to noise ratio. Unfortunately, the expected lateral feature size of the switching fingerprint is below $< 10\,\text{nm}$ and cannot be resolved by PEEM. Further, device initialization was found to be complicated due to the large electrode spacing and X-ray beam damages are expected.

Two types of **ultra-thin, electron transparent top electrodes** were designed and implemented into functional devices: 2 nm Rh thin films and devices with graphene monolayers as top electrodes. Both electrode materials match the tight specifications for electrical switching and photoemission observation. It was demonstrated that both device types behave electrically similar to devices with thick electrodes. Further, both devices show interfacial signals of the Ti L- and the O K-edge in XAS. The average attenuation length for O K- and Ti L- XAS was determined to be around $\lambda \approx 1.6\,\text{nm}$. The monolayer graphene exhibits an outstanding electron transmission of around $50-70\%$.

In the case of $SrTiO_3$, a combination of XAS and ultra-thin graphene top electrodes by now provides the best results for in-situ and operando charcterization of working devices. This assertion is based on a matrix of different, multidimensional aspects that need to be considered for a $SrTiO_3$-based devices. The matrix, which summarizes the results from chapter 5 & chapter 6 is condensed in Tab. 6.1. Each row stands for a combination of geometry and photoemission-based method. The listed key aspects are related to device operation and expected chemical contrast, but also contain microscopy related aspects as e.g. the expected feature size. Each aspect is weighted by a color with respect to its expected suitability for time-resolved PEEM. Green cells indicate high compliance, red and orange indicate drawbacks and dark red cells disqualify the corresponding pair of geometry and method. The last column is a product of chemical contrast and expected PE intensity and

can be interpreted as a figure of merit. As long as none of the other aspects disqualifies a certain combination, the last column should be taken as reference for the suitability towards operando experiments. For example, lateral or ultra-thin devices with XAS present the best combination for $SrTiO_3$ based devices. However, the feature size in the lateral geometry is below the resolution limit of PEEM and hence only ultra-thin electrodes with XAS remain as the best approach. The reason

		Methology & Fabrication		Resistiv Switching related aspects			PEEM related aspects		
device type		method	fabrication	oper. devices	chemical [4] contrast	reported endurance	ex. feature size [5]	ex. Intensity of Interface [6]	suitabilty [7] for TR-PEEM
lateral configuration		XAS [1]	basic, optical lithography	yes, but not in this thesis [3a]	o/+	no operational devices	<10 nm, below PEEM res.	very high	++
		SX-XPS			o/-			high	+
		HX-XPS			-/--			avg./low	-
vertical configuration	thin TE > 2nm	XAS [1]	basic, optical lithography	yes, well known from Lit. [3b]	o/+	10^9 cycles, reduced under UHV	observed up to 1µm	avg./low	o
		SX-XPS			o/-			avg./low	-
		HX-XPS			-/--			low/v. low	- -
	ultra-thin TE < 2nm	XAS [1]	multi-step, optical lithography [2]	yes	o/+	$10\text{-}10^4$ cycles, red. under UHV	observed up to 1µm	high/v. high	++
		SX-XPS			o/-			avg.	o
		HX-XPS			-/--			avg./low	-

1) soft x-ray XAS < 1000 eV 2) know-how for thin electrodes required 3a) working devices reported in literature 3b) standard devices in literature
4) material dependent (here shown for SrTiO3), here it implies real chemical contrast, but also involves instrumental resolution and statistics
5) the expected feature size is based on experiments and models, the ranking is based on a comparison to PEEM resolution of 50-150nm
6) the intensity ranking is referenced to best S2N ratios for a aquistion times in the order of seconds 7) The suitability for time-resolved PEEM is a product of chemical contrast and expected signal intensity

Table 6.1. – Matrix representation of device geometries, and photoemission techniques for $SrTiO_3$. For each pair of geometry and method, selected aspects of the experimental procedure and device performance are compared. Each aspect is rated with respect to the suitability for operando experiments. Green cells stand for high suitability, orange and red cells indicate drawbacks, dark red cells disqualify the specific pair from TR-PEEM. Particularly relevant for time-resolved studies are the chemical contrast and the detected intensity of electrons stemming from the MI interface, which are summarized in the last column.

making XAS with thin electrodes most favorable for $SrTiO_3$ lies within the pronounced absorption edges of Ti and O in the soft X-ray regime and the well-established fabrication processes for vertical device structures. Ta_2O_{5-x} on the other hand does not have relevant absorption edges in the soft X-ray regime and suffers from the same drawbacks in the lateral geometry. Thus, HAXPEEM and SX-XPS in combination with vertical device geometry become the only viable options for TaO_x based devices. As the operando XPEEM is not yet established and no reference for the loss in signal to noise exists, the focus of the operando experiments as described in the following chapters will be on the high intensity G/$SrTiO_3$ based devices combined with a XAS approach.

Note, that most of the findings depicted in this chapter are of general nature. These concepts are not limited to resistive switching materials, but can also be applied to other material systems. Especially the lateral approach, which is less successful for resistive switching, is expected to present a powerful approach for systems having feature sizes above the PEEM resolution limit, i.e. $d_{feat} \gg 150\,\text{nm}$.

CHAPTER 7

In-situ characterization of G/STO thin film devices

In-situ is a Latin phrase that literally translates to "on site" or "in position". In the context of the present work, in-situ will refer to experiments where a MIM device was switched in the microscope under UHV conditions, but without being imaged during operation. This kind of experiment was designed as precursor for the real-time characterization experiments being presented in the next chapter. Compared to real time characterization, in-situ experiments can be implemented into a PEEM without major modifications. PEEM analysis is performed **before** and **after** each switching event. The benefits of the in-situ approach are that the system is isolated from external influences (e.g. oxygen exchange with the environment) and that the experimental conditions are known. By investigating the LRS and the HRS of a single device, device-to-device variations such as variation of the filament position, layer thickness or compositional variations can be excluded. As for these reasons, the reversible switching of G/STO MIM devices between LRS and HRS states can be used for the first time to not only characterize, but also to quantify the redox induced changes on a single operational device in terms of donor density (oxygen vacancy concentration) modifications. The experimentally derived donor concentrations were then used as input parameters for model simulations providing a comprehensive understanding of the device operation. Good quantitative agreement between the experimentally measured I-V characteristics and the simulated I-V curves being based on the extracted donor concentrations supports the idea of vacancy accumulation and depletion as the main source for a resistance change of more than 2 orders in magnitude.

For the first time, experimental quantities derived from PEEM measurements could directly be linked to the device resistance state providing a significant step towards the characterization of resistive switching and other functional materials during operation.

Major parts of the present chapter reference to and follow the article “Quantifying redox-induced Schottky barrier variations in memristive devices via in operando spectromicroscopy with graphene electrodes” published by C. Bäumer, C. Schmitz et al., Nat Comm. 7, 2016 [1].

7.1. Spectromicroscopical quantification of resistive switching filaments

In-situ experiments were performed on the novel, graphene contacted devices (G/STO) as introduced in Sec. 6.4. Therefore, samples were mounted to special sample holders with electric contacts. By application of a switching pulses in front of the microscope under UHV conditions the device state was altered several times between the LRS and HRS. Simultanously. the I-V response of the device under test (DUT) was measured by an external power supply. During the switching process the microscope was turned off to avoid damages to the sensitive power supply inputs caused by occasional HV discharges in the microscope. After each switching event, the microscope was turned on again and XAS spectra were acquired at the O K- and the Ti L-edge. Both edges were previously identified to be sensitive to chemical changes (see Chap. 5). As already minor differences in the donor density are expected to cause significant changes in device resistivity, special attention was given to the analysis of the O K-edge being more sensitive to small concentrations as the commonly used Ti L-edge.

While for some of the investigated devices filamentary regions could be identified within the area under the graphene top electrode, matching the spectral signatures discussed in Chap. 5, other devices did not show any signs of chemical changes, even though a pronounced I-V hysteresis was measured. In the following, a detailed analysis of one of the identified switching filaments is presented. The filament position is indicated by a black arrow in Fig. 7.1. A direct comparison of XPEEM images acquired near the O K-edge around 531.6 eV photon energy (referred to as peak A in the following) for the filament and its surrounding in different device resistance states shows spatially confined and reversible intensity modifications, Fig. 7.1 a,c,e,g. For the LRS the intensity of peak A is reduced, whereas for the HRS the peak intensity is increased. Peak A is related to the transition from the O1s level into the conduction band formed by the unoccupied Ti t_{2g} and O 2p conduction band states. Partial filling of the bands leads to a decrease of the number of possible transitions and a reduction of the XAS intensity. In turn, depletion of the bands goes along with an increase in intensity. Accordingly, the observed spectral changes are attributed to spatially confined changes of the donor/vacancy concentration.

Entire O K-edge spectra were extracted for the filamentary region ($\varnothing = 400-600$ nm) and for reference also from the surrounding area, Fig. 7.1 b,d,f,h. All spectra were normalized to peak B_2 (538 eV). The filament reveals the fingerprint of reduced $SrTiO_3$, which becomes evident when it is compared to the reference spectra of the unaltered surrounding. For the LRS I, the peak intensity of peak A is reduced within the filamentary region. The reduction is attributed to a partial filling of the conduction band. By switching the device from LRS I to HRS I the intensity difference between the reference and filament becomes significantly smaller. This indicates the annihilation of oxygen vacancies near the interface. However, even in the HRS I a finite contribution of vacancies remains present indicating a non-vanishing donor concentration. A subsequent switching cycle HRS I → LRS II → HRS II was performed to validate the assumption that the observed changes are induced by the switching process and not related to experimental artifacts. The observed and reversible intensity modulations verify that the changes indeed correspond to an active switching filament. Large carrier concentrations in the conduction band are observed for the LRS, while a lower, non-zero concentration is observed for

the HRS.

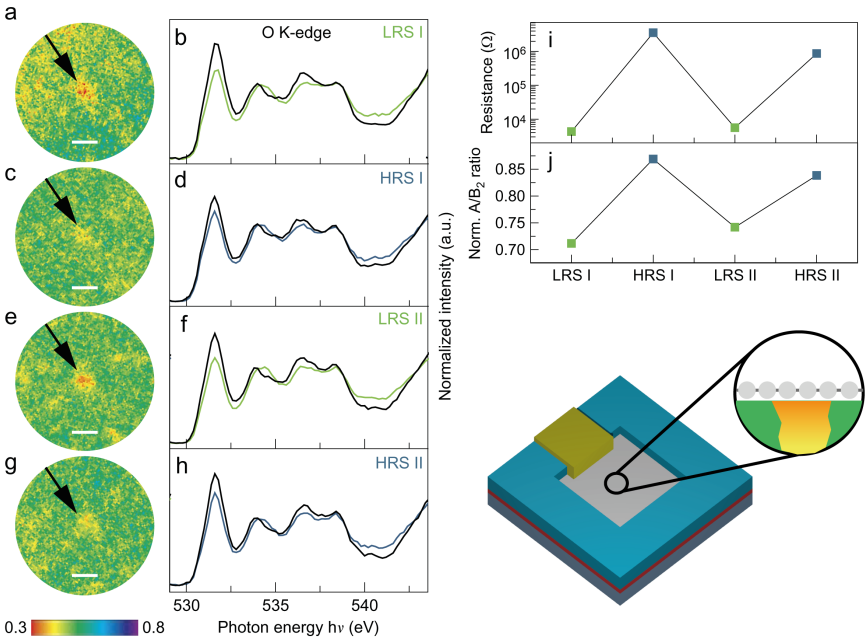

Figure 7.1. – (a,c,e,g) Spatially resolved XPEEM images at $h\nu = 531.6\,\text{eV}$ for LRS I, HRS I, LRS II and HRS II states showing a filament. (b,d,f,h) Corresponding O K-XAS spectra. Colored spectra represent signal from the filament marked by black arrow. Black lines correspond to reference spectra from the surrounding. (i) Measured resistance in each of the four states. (j) Intensity ratio A/B_2 between peak A (531.6 eV) and peak B_2 (538 eV) for the different states. Images are adapted from Bäumer, Schmitz et al. [1]. Bottom right: 3D model of the device and filament located within the graphene top electrode contact.

The changes in spectral shape were used to quantify the oxygen vacancy concentrations for each of the four resistance states. Therefore, the peak ratio A/B_2 for the filamentary region was compared to a calibration standard measured on an single crystal annealed under UHV conditions, Sec. 5. According to this calibration, the concentration of oxygen vacancies is $4.5 \pm 0.5\%$ for the LRS and $2 \pm 0.5\%$ for the HRS, which equals $9 \pm 1\%$ and $4 \pm 1\%$ of Ti^{3+}. Assuming that each trivalent Ti^{3+} atom contributes one electron to the conduction band and taking into account the density of $SrTiO_3$ ($\rho = 4.81 \frac{g}{cm^3}$), the corresponding charge carrier density in the conduction band was calculated to $n = 1.5 \times 10^{21}\,\text{cm}^{-3}$ (LRS) and $n = 6.7 \times 10^{20}\,\text{cm}^{-3}$ (HRS) [1]. Furthermore, the measured A/B_2 ratios were compared to the corresponding device resistance which was extracted from the simultaneously measured I-V curves, Fig 7.1. It was concluded that a spatially confined change of the donor concentration by a factor of $\approx 2-3$ at the G/STO interface results in a change of device resistance by more than 2 orders of magnitude.

7.2. Experiment-assisted device simulations

The experimentally determined vacancy concentrations for the LRS and the HRS as well as the filament dimensions were used as input parameters for a physical simulation of dynamic resistive switching in metal oxides using a Schottky contact barrier model. This simulation by A. Markawa[1] and S. Menzel[2] is a numerical drift-diffusion model of coupled electronic-ionic transport that accounts for current conduction across the electrode-oxide boundaries via electron tunneling and thermionic emission [20]. The model simulates the I-V response of a given device geometry based on the evolution of the oxygen vacancy distribution within the active film, the dimensions of the filament and material specific parameters. According to the model the total device resistance at low voltages is dominated by the Schottky barrier at the electrode/oxide interface and deformation of this barrier by vacancy accumulation/depletion is the driving force behind resistance modulation during resistive switching.

For the purpose of the presented work, the device under test was modeled by a graphene / 20 nm STO / Nb:STO layer stack with an embedded, vacancy rich filament of 500 nm in diameter, Fig. 7.2a. The vacancy distribution inside of the filament was modeled by a homogenous distribution of doubly ionized oxygen vacancies stretching from top to bottom of the active material, Fig. 7.2b. The oxygen vacancy density $N_D = \frac{n}{2}$ was set constant for each resistance state according to the values of the charge carrier density n derived from XPEEM. For the given configuration the Schottky barrier of interest is formed at the G/STO interface. The contact to the Nb:STO bottom electrode is nearly ohmic. In addition to the experimentally determined quantities, other, material specific parameters (e.g. work-functions, dielectric constants, diffusion energy,...) required for the simulations were taken from literature and checked to be physically meaningful. These values were not allowed to vary during the simulation and they were kept identical in the simulations of the LRS and the HRS.

The I-V response of the DUT was simulated for both resistance states. The simulations were compared to experimental, low-voltage read outs of the I-V curves acquired during the in-situ experiment, Fig. 7.2c. The analysis was limited to the low voltage regime from −200 mV to +200 mV to avoid read induced device alterations. The simulated and the measured I-V responses are in good agreement, which is remarkable as the PEEM derived vacancy concentrations are measured independently of the I-V characteristics. The good agreement between experiment and experiment-assisted simulations confirm that the model of redox-induced vacancy accumulation and depletion near the G/STO interface indeed can account for the observed resistance modulation. The model explains the changes in resistance by 2-3 orders of magnitude observed experimentally, by a spatially confined modification of the donor density by a factor of $2-3$.

Comprehensive understanding of this change in resistance can be gained from the simulation. Fig. 7.2d shows the simulated conduction band offsets resulting from the formation of a space charge layer (Schottky barrier) near the graphene/STO interface (Chapter 2). The spatial extend of this Schottky barrier and the barrier height differ for the two vacancy concentrations. For the LRS the barrier is thinned out and the barrier height is reduced. The tunnel contributions and thermionic emission are enhanced and larger currents are observed. In turn, for the HRS the barrier height is

[1] Institut für Werkstoffe der Elektrotechnik II, RWTH Aachen
[2] Peter Grünberg Institute (PGI-7), FZ Jülich

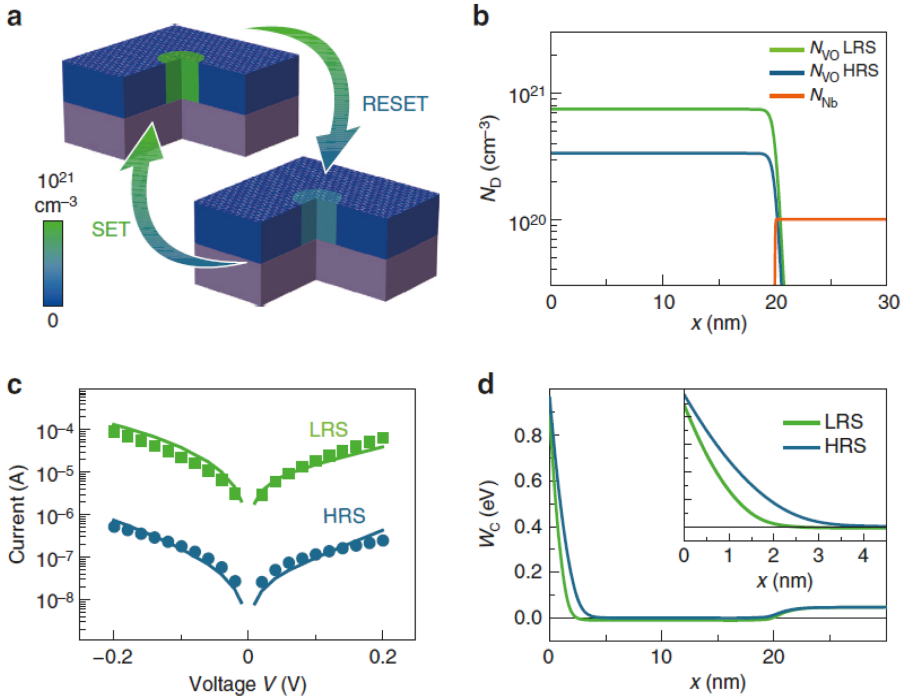

Figure 7.2. – (a) Schematic model of the simulated graphene/ 20 nm STO/ Nb:STO layer stack with embedded filament of 500 nm in diameter. The homogenous vacancy concentration inside the filament was varied between the LRS and HRS according to the derived values from the PEEM experiments. (b) Donor density profile along the filament for LRS and HRS. (c) Simulated (solid) and measured I-V response (dotted) of the device for the LRS (green) and the HRS (blue). (d) Simulated conduction band off-set for the LRS and the HRS. A pronounced modification of the Schottky barrier width and height at the graphene/STO interface (x=0) is observed in between the two resistance states. Images are adapted from Bäumer, Schmitz et al. [1].

restored by vacancy annihilation. The space charge layer region is extended and the barrier width increases. The tunneling contributions are significantly lowered. For electrons with kinetic energies 100 mV above Fermi, the barrier thickness is more than doubled from approximately 1 nm in the LRS to about 2 nm in the HRS explaining the decrease in current of more than two orders.

It has to be noted that the shape and the height of the Schottky barrier are mainly dictated by the donor concentration in the very first nanometers of the interface region. Due to the high surface sensitivity of photoemission-based techniques, this is exactly the region being probed in the PEEM measurements. Deviations of the assumed uniform donor profile in the filament, which was assumend homogenous along the full film thickness in the simulations, cannot be excluded from the experiment, because they cannot be probed by PEEM. However, the vacancy distribution far away from the interface has only minor impact on the measured I–V characteristic and can therefore be neglected. (see. Supplement [1])

7.3. Absence of chemical fingerprints in in-situ switched devices

While in some devices filament formation was observed, other devices did not show any modification within the PEEM accessible graphene region. For all devices, however, a pronounced I-V hysteresis was observed.

Statistically, filaments within the graphene top electrode were found in about 25% of the investigated devices. One possible explanation for the absence of observable filaments within the graphene region for the other devices is that switching preferably takes place underneath the Au/G contact, which due to its thickness is inaccessible by PEEM. The probability for filament formation near or underneath the Au electrode is increased due to the local Joule heating. The local Joule heating is a direct consequence of the high current density passing through the Au lead. The elevated temperatures enhance the diffusion speed of the oxygen atoms near the electrode and thus promote filament growth. This explanation is supported by thermal imaging of a 20 nm $SrTiO_3$ device showing significant heating of the Au lead during SET operation [89, p. 140 ff.]. Further evidence for filament formation underneath the electrode is given in the next chapter.

CHAPTER 8

Operando characterization of G/STO thin film devices

In chapter 5 chemical fingerprints of resistive switching in $SrTiO_3$ and especially the signals being indicative for switching have been identified based on results of non-functional, delaminated devices. In chapter 6 the top electrode dilemma has been addressed and a solution has been proposed based on the fabrication of ultra-thin graphene electrodes. It was shown that these electrodes are highly electron transparent and can be used for live imaging, while maintaining resistive switching properties. In chapter 7 first in-situ measurements in front of a spectromicroscope were discussed, which showed spatially confined and reversible variations of the O K-edge being interpreted as oxygen vacancy formation and depletion of the electrode/oxide interface. These measurements were performed on final states **before** and **after** a switching event, but not observed in real time during operation. The experiments were technically limited by the highly sensitive power supply inputs which needed to be protected against high voltage discharges between extractor lens and sample. During the time of the in-situ experiments no suitable surge protection was available and thus the high voltage was disabled during the switching process.

In the present chapter the technical implementation of a proper surge protection and a corresponding electrical contacting scheme will be presented, Sec. 8.2. Employing the novel experimental setup first experimental XAS data **during** the application of voltages to a STO thin film device were acquired. In addition to the anticipated chemical changes, the in-operando, real-time measurements go along with intensity changes that are attributed to local potential modifications in the device. The observed intensity modifications - if treated correctly - can be exploited to recalculate time dependent 2D local potential maps of the device during operation, Sec. 8.3. With a new MATLAB algorithm, XPEEM can be used as a spatially resolved, local voltage probe outperforming standard two terminal electric characterization by far. Specifications and conditions of the routine will be discussed. Once established, the procedure was further used to characterize the devices during operation and to study the electric response to different applied voltage pulse. The results unambiguously prove device operation and validate the basic suitability of the operando approach, Sec. 8.4. However, direct evidence for oxygen vacancy accumulation and/or depletion within switching filaments as observed in the previous in-situ experiments is rare. The lack of evidence can partially be attributed to an intermixing between chemical and electronic signals inherent to the novel experimental scheme,

but also to the variability of the filament position. The latter aspect is supported by SEM studies of post-mortem devices combined with the XPEEM pulse characterization results of the devices during operation, which both indicate that switching takes place underneath the Au lead, i.e. outside the region accessible by PEEM. A global summary is given in Sec. 8.2.1.

8.1. Experimental idea

The idea of the operando experiments is to combine spatial resolution, chemical sensitivity and temporal resolution in a single experiment and to image a device during operation in real-time. The experiments are expected to significantly increase the quality of experimental analysis as LRS and HRS of a single device are compared. Starting point of these experiments are the results and findings accumulated on delaminated and in-situ switched devices. Specifically, spatially resolved XAS on Ti L- and O K-edge have been established as viable fingerprints for the resistance state, while at the same time providing high signal intensities and low noise. Since the acquisition of complete XAS scans during real-time application of an external voltage pulse is technically impossible, the idea is to monitor only the specific absorption line of the O K-edge ($h\nu = 532\,\text{eV}$), which was previously identified to be linked to the formation/depletion of oxygen vacancies. In this configuration each point of a characteristic I-V curve can then be mapped to a corresponding change in the absorption intensity as schematically sketched in Fig. 8.1.

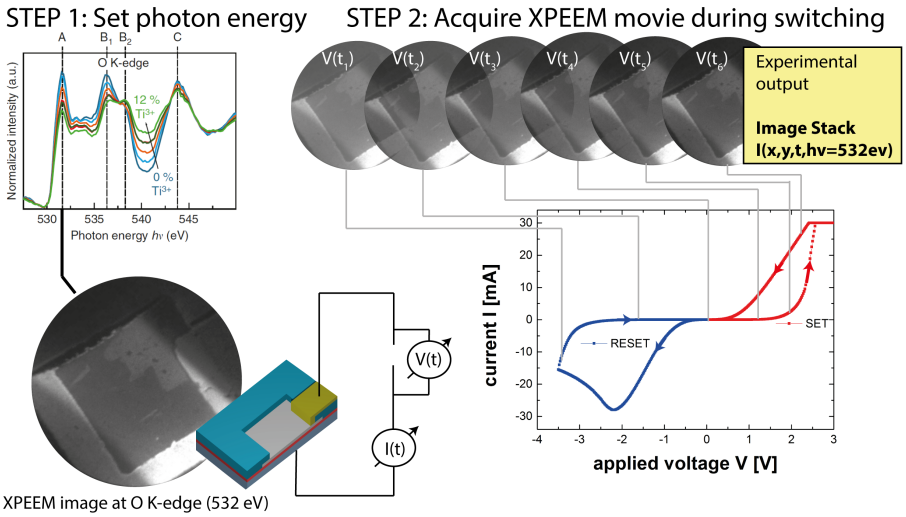

Figure 8.1. – A diagram of the operando XPEEM experiment. In Step 1, the photon energy is set to an energy sensitive to oxygen vacancy formation/depletion. In Step 2, XPEEM images at the chosen photon energy are acquired during the application of an external potential V(t). Spatial variations of the intensity can be used as tracers for changes in the oxygen vacancy concentration.

8.2. Technical implementation

Operando techniques are not yet state-of-the-art in PEEM instruments, which implies that any technical infrastructure needed to be designed, tested and implemented. The following three subsections summarize the core modifications of an ELMITEC PEEM III. While details of the sample holder design are specific to the ELMITEC PEEM instruments, the more general concepts (like the HV surge protection circuit, or the electrode configuration) can be transferred to other PEEM instruments as well.

8.2.1. Experimental Setup

The operando experiments were performed at the NanoSpectroscopy beamline at the Elettra Sincrotrone Triest, Italy, using a LEEM/PEEM III microscope [93].[1] In the LEEM/PEEM III a high voltage of 18 kV is applied to the sample, while the objective lens in a distance of a few mm is set to ground potential in order to create an immersion lens effect. For the operando characterization of MIM devices in front of a PEEM an additional, bipolar switching voltage ranging from −10 V to 10 V operated on the sample HV needs to be supplied to the devices. In our experiments the external voltage was provided by a Keithley 2611A floating on 18 kV sample potential. The electric connection between power supply and the device was realized by a modified, custom-build sample holder (see 8.2.2). The experimental configuration is sketched in Fig. 8.2. For high magnification and high spatial resolution, a high electric field of $E \approx 9 \frac{kV}{mm}$ between sample and objective lens is necessary to create an immersion lens effect [61]. In this configuration the setup is prone to high voltage arcing. To avoid serious damage to the highly sensitive equipment a special, high voltage surge protection (described in detail in 8.2.3) was mounted to the Keithley power supply outputs.

8.2.2. Sample holder design for operando experiments

A standard Elmitec holder was modified to supply the external potential V(t) to the devices, Fig. 8.3. By default the sample holder has four electrical contacts realized as insulated terminals. Usually two of the terminals are connected to a filament behind the sample and used for heating, the other two terminals are connected to a thermocouple close to the sample itself. Each of the four terminals is connected to a vacuum feed-through by a spring contact on the bottom and voltages can be supplied or read from each of the pins separately. For the operando experiments the filament and the thermocouple were removed. Instead, the two terminals on each side were electrically shortened to serve as single contacts, Fig. 8.3. Each side then was connected to a thin, else insulated wire. The other end of the wire was glued to a homemade, gold plated Al_2O_3 ceramic bond pad using a fast drying, conductive silver paint. The pads were located close to the sample and served as platform for bonding of the MIM devices. The Nb:STO substrate with the graphene contacted STO MIM devices itself was glued to the center of the sample holder by highly conductive, UHV compatible silver paste. This way the substrate had a good electric contact to the sample holder, which thus served as bottom electrode for the device. To avoid unintended short circuits between the bond wires and the sample holder cap, a 0.2 mm thick Kapton foil with a central opening as viewport was placed between the sample and the cap.

[1] The corresponding beamline specifications are tabulated in Appendix Tab. A.1

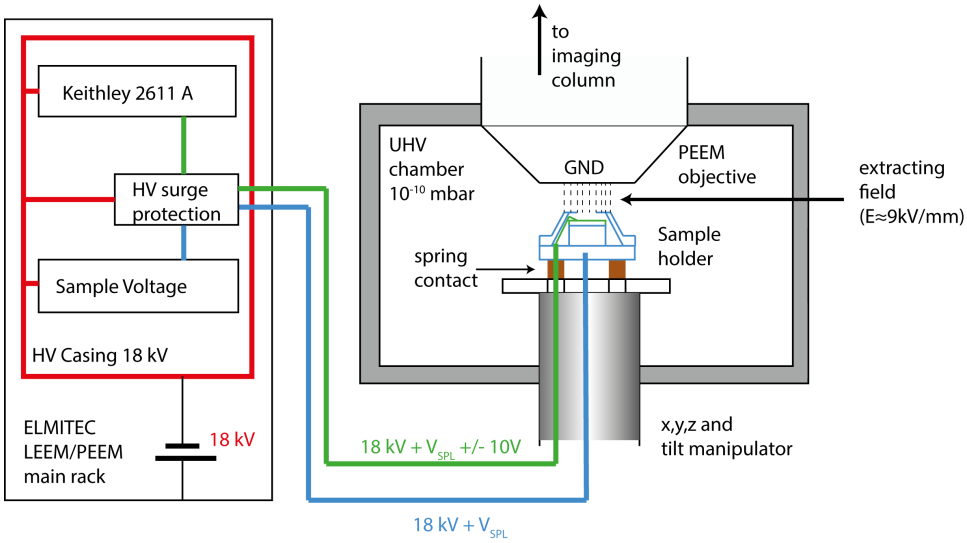

Figure 8.2. – Sketch of the experimental configuration for operando XPEEM experiments. In addition to the sample potential (blue) a second bipolar voltage (green) has to be supplied to the sample. The voltage is provided by a programmable power supply (Keithley 2611A) mounted to the HV cage of the main rack. To avoid discharge induced damages to the highly sensitive power supply a HV surge protection is placed between the sample and the Keithley output.

An important point of consideration for the sample holder design was the potential distribution on the sample surface, because in a PEEM the sample is part of the imaging process and the sample (surface) potential defines the magnification and imaging quality. For standard experiments, a homogeneous surface charging is required and achieved by biasing the sample holder to a fixed, well defined **reference potential** V_{SPL}. Any inhomogeneities in the surface potential will cause micro-lensing effects and thus further affect the operation of the energy filter in the microscope.[2]

In operando experiments the **externally applied voltage** V(t) between the top electrode and the sample substrate is - by definition - a spatially confined modulation of the sample surface potential, Fig. 8.6a. Hence, image distortions as well as operational effects on the energy filter are to be expected. For the resistive switching in the G/STO devices, only the electric field distribution inside the active $SrTiO_3$ layer is relevant, which in turn is defined by the potential difference $\Delta V = |V_{TE} - V_{BE}|$ between the top electrode (TE, Au lead) and the bottom electrode (BE, Nb:STO substrate). On these grounds the **external voltage** $V(t)$ switching the device can either be applied (a) to the top electrode ($V_{TE} = V_{SPL} + V(t)$) and the bottom electrode is kept on sample potential ($V_{BE} = V_{SPL}$) or (b) to the bottom electrode and the top electrode is kept on sample potential. Both configurations result in the same magnitude and direction of the electric field $\vec{E} = \nabla\Delta V$ within the film, if the polarity of the applied voltage$V(t)$ is adequately chosen, see Eq. 8.1. In the following, configuration (a) will be referred to as *"moving potential"* and configuration (b) will be referred to as *"fixed potential"*.

[2] How surface potentials modify the energy-filtering capabilty will be discussed in Sec. 8.3

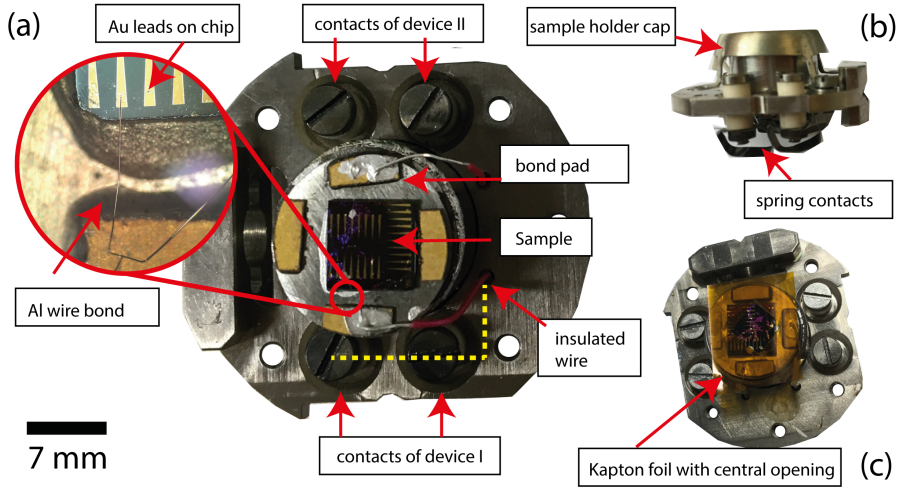

Figure 8.3. – (a) Top view of a modified Elmitec sample holder for operando measurements: The two pins on each side are interconnected (yellow dotted lines) and connected to bond pads near the sample via insulated wires. From these pads the top electrode of the device under test is bonded (magnification). (b) Side view showing the spring contacts connecting the pins to the external power supply. (c) A 0.2 mm Kapton foil is placed between sample holder cap and the mounted sample to avoid short circuits.

$$\Delta V = \begin{cases} \underbrace{V_{\mathrm{SPL}} + V(t)}_{V_{\mathrm{TE}}} - \underbrace{V_{\mathrm{SPL}}}_{V_{\mathrm{BE}}} = V(t) & \text{for "moving potential"} \\ \underbrace{V_{\mathrm{SPL}}}_{V_{\mathrm{TE}}} - \underbrace{V_{\mathrm{SPL}} - V(t)}_{V_{\mathrm{BE}}} = -V(t) & \text{for "fixed potential"} \end{cases} \tag{8.1}$$

Only regions revealing a local potential deviating from the reference potential V_{SPL} will be affected by imaging and filtering distortions. Thus, the choice of the configuration of the applied voltages defines the distorted regions in the image. Figure 8.4a shows a schematic cross section of graphene device mounted in the operando holder. Fig. 8.4b illustrates the potential distributions within the sample holder for the “moving potential” (left) and “fixed potential” (right) configuration. In the first case the top electrode potential is shifted with respect to the reference potential (blue). In the second case the top electrode potential is fixed and the substrate potential is shifted instead.

The time-dependent intensity $I(t,x,y)$ movies[3], which are acquired during an operando XPEEM experiment, have to be interpreted as a superposition of electronically ($I_V(t)$) and chemically ($I_C(t)$) induced changes, i.e. $I(t) = I_V(t) + I_C(t)$. The electronically induced changes relate to a modification of the surface potential, whereas the chemically induced intensity changes arise from the formation/depletion of oxygen vacancies during device operation. Unfortunately both, chemical changes as well as local potential modifications, have similar intensity signatures in operando XPEEM and a

[3]More details on the data sets are given in Sec. 8.3

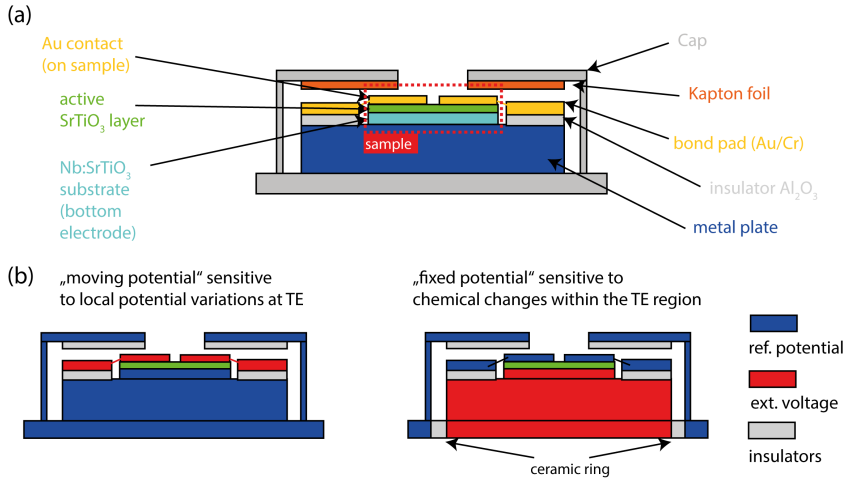

Figure 8.4. – (a) The cross section of a G/$SrTiO_3$ device mounted onto an operando sample holder. The layered Au/G/STO/Nb : STO (yellow/green/green/cyan) sample is shown in the center. The Nb : STO substrate is glued to a metal cap (blue) forming a metallic contact with the base plate. The two bond pads mounted to both sides of the sample are insulated from the metal plate and are used to electrically connect the top electrode of the device to the spring contacts. Independent on other components, the sample holder cap is always set to the reference potential. It is insulated from the other potentials by Kapton foil or ceramics. (b) Potential distributions during device operation for 'moving potential' and 'fixed potential' configurations: While the top electrode potential shifts in reference to the sample potential in the 'moving potential' configuration, it is kept fixed in the 'fixed' configuration. Both configurations generate an identical field distribution within the active layer (green), but are sensitive to different aspects of the experiment.

separation of these two intertwined signal contributions is complicated. The weighting of the two contributions, however, strongly depends on the actual configuration: If the potential of the top electrode is fixed to the reference potential, the electrically induced component $I_V(t) \approx 0$ within the top electrode region becomes negligible and changes in intensity may be solely attributed to chemical changes $I(t) \approx I_C(t)$. Alternatively, if the top electrode potential is shifted with respect to the reference potential, voltage induced effects are assumed to dominate the observed intensity modulations $I(t) \approx I_V(t)$ and chemically induced effects $I_C(t) \approx 0$ may be ignored.

Thus, by having two slightly modified sample holders and by employing the two aforementioned configurations, it is possible to physically decouple the different signal components. While the "moving potential" configuration allows one to characterize mainly the *electric potential distribution* within a working device, the "fixed potential" configuration is more sensitive to *chemical changes* within the top electrode region. On one hand, the analysis and interpretation of the electronic signal provides important information for pulse, performance and working interface characterization; whereas the analysis of the chemical signal is relevant for the basic understanding of the physical and electrochemical processes involved in switching as well as the for filament localization and switching dynamics. As the two geometries - moving and fixed potential - provide different information, both configurations have been used throughout the operando experiments. The results are presented in the experimental sections 8.4.1 and 8.4.2, respectively.

8.2.3. High voltage surge protection (HVSP)

Keithley source meter units (SMU) are established as standard tool for characterization of resistive switching materials, because a typical SMU can generate voltages in between −200 V and +200 V while simultaneously the device current can be measured over several orders of magnitude with high accuracy. The provided high dynamic range from Ampere (A) down to the nanoAmpere (nA) regime is mandatory to account for the change in resistivity stretching over several decades in magnitude arising during the resistive switching process.

For the operando experiments a SMU 2611A is mounted in the high voltage (HV) rack of the PEEM and operated floating on a high voltage of $V_{HV}(DC)$ = 18 kV, Fig. 8.5 (Photo). The Keithley is remote controlled via the LAN interface. Two bidirectional LAN↔optical fiber media converter are used to decouple the HV potential of the instrument from the data acquisition PC on ground potential. One converter is operated on the high voltage and the second converter is operated at common ground potential. One of the most demanding issues when operating a Keithley on HV is to guard the sensitive SMU from HV discharges frequently observed to occur between objective lens and sample in PEEM instruments. Therefore a custom-build, three stage surge protection was designed and manufactured consisting of a RC-component[4], two fast suppressor diodes and a high load gas discharge fuse. A detailed wiring scheme of the setup is presented in Fig. 8.5. Details and specifications of the HV surge protection can be found in Appendix A.3.

Prior to first operation the protection was successfully tested in the lab by H. Pfeiffer using a 10kV discharge tester. Additionally, it was experimentally verified that the surge protection does not affect device operation. The measured I-V curves with and without surge protection remain similar. In the course of the operando PEEM experiments the system has experienced multiple HV discharges without observed damages to the Keithley.

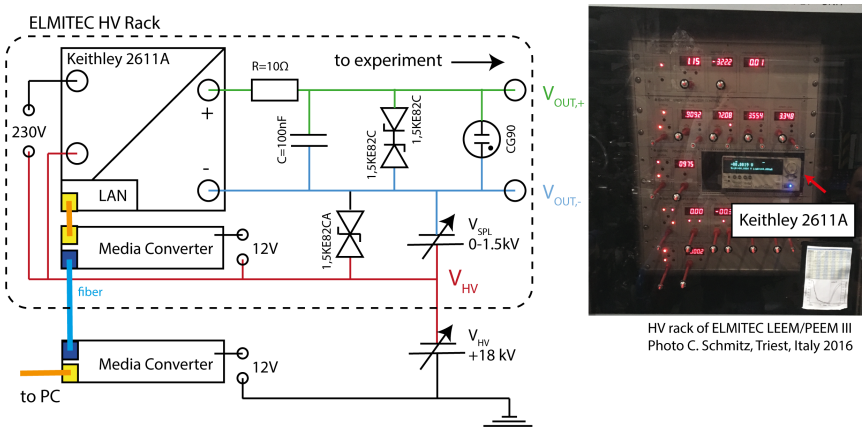

Figure 8.5. – Circuit diagram of floating Keithley 2611A power supply and data conversion scheme. The highly sensitive outputs of the Keithley are protected by a three component surge protection described in the text. Photo: Keithley mounted in the HV rack of the NanoSpectroscopy end station.

[4] An element consisting of a resistor (R) and a capacity (C)

8.2.4. Implementation of temporal resolution in operando XPEEM

Two approaches to capture the dynamics of a transient process, e.g. switching in resistive switching devices, are known: (a) real-time acquisition and (b) pump-probe techniques.

In the real-time data acquisition approach ('movie approach'), the state of the quantity of interest is probed and recorded simultaneously while the process proceeds at its normal pace. This technique is ideally suited if the acquisition time of a single frame is significantly smaller than the time of the process to be observed. Typically the acquisition time is limited by the detector, which for standard CMOS cameras is in the order of several milliseconds per frame. Thus, processes to be investigated with this approach should be rather slow and span at least over several hundred ms. The benefit of the real time approach is that only a single process is imaged, which practically allows to even image irreversible processes, e.g. thermal destruction.

Pump-probe experiments in contrast, make use of the fact that some processes are fully reversible. In a pump-probe experiment the system is first excited by a pump pulse (electrical or optical) which triggers the process and after a certain delay δt the system is probed by a probe pulse (X-ray for XAS experiments). The experiment itself is then repeated multiple times with varying delay δt. The temporal resolution in a pump-probe scheme is limited by the temporal broadening of the pulses and the control of the delay, which can be as small as a few ps. Thus, pump-probe experiments are applied to ultra-fast and fully reversible processes like the investigations of demagnetization curves of magnetic materials for which lasers are usually used [94].

The switching process in $SrTiO_3$ devices is dominated by the thermally activated kinetics of oxygen vacancies and can be separated into two temporal regimes: A slow (μs-s) and gradual field-driven regime and a second ultra-fast (ns) thermal runaway regime [95]. Due the statistical nature of the thermally activated redistribution process cycle-to-cycle variations between LRS and HRS states are observed. Furthermore, most devices show severe device degradation after a few ten to a few million cycles [96] induced by chemical decomposition of the electrode or oxygen removal. Overall, it is still under debate whether or not the processes in RSM are fully reversible.

Considering the uncertainties of reproducibility in resistive switching and the intensity loss expected when employing a pump-probe scheme, it seemed more promising to start with a real-time approach and to validate the reversibility of the switching process prior to implementation of a pump-probe scheme. Thus, all experiments performed in this thesis are based on a real-time approach as schematically shown in 8.1.

8.3. Data Analysis: XPEEM based recalculation of local potentials

The output of an operando XPEEM experiment is a movie stack $I(x,y,t,h\nu = 532\,\text{eV},E_{\text{kin}})$ acquired at a fixed photon energy $h\nu$ and detected for a fixed range of electron kinetic energies $STV - \delta E, < E_{\text{kin}} < STV + \delta E$ around a defined start voltage, STV. The detected kinetic energy range is defined by the energy filter. For $h\nu = 532\,\text{eV}$ and close to the secondary cut-off ($STV = 5\,\text{eV}$), such a stack contains the temporal evolution of the spatially resolved O K-edge XAS intensity $I(t)$ for each point P(x|y) of the sample. During the application of an external electric stimulus $V(t)$ the intensity for each point can be modulated. Explanations on the origin of these intensity modulations taking into account the working principle of EF-PEEM are given in the following. Two effects contributing to the intensity modulations were identified: local variations of the absorption behavior ('chemical contrast') and variations of the local surface potential ('electric contrast'). Special attention is paid on how the latter intensity changes can be exploited to recalculate the time-dependent local potential distribution on the surface and how electrostatic information with spatial resolution can be obtained in a non-invasive manner. Principally, the presented concept is similar to potential mapping in PEEM/LEEM as for example reported in [65, 97], however, it is not limited to static experiments. The findings were implemented into a MATLAB routine and employed for further analysis. Premises and limitations of the approach are summarized in the last paragraph of the section.

8.3.1. Recalculation of the local potential V(x,y)

In the performed operando experiments, the detected XPEEM signal compromises only a small bandwidth of emitted electron kinetic energies being defined by the reference (sample) potential and the pass energy of the energy analyzer, Fig. 8.6b&c. Thus, local potential shifts $V_{\text{SPL}} \pm V(t,x,y)$ with respect to the reference potential (e.g. induced by a static voltage, $V(t) = \text{const.}$) modify the kinetic energy of the emitted electrons and lead to an acceleration or deceleration of the electrons emitted from the region where the shift occurs, Fig. 8.6a. In this process the kinetic energy of the electrons with respect to the objective lens/analyzer is increased or decreased. Since these effects apply to all emitted electrons regardless of their kinetic energy, the full photoemitted spectrum shifts to higher or lower kinetic energies by an amount $\Delta E_{\text{kin}} = -V \cdot e$.

The direction of the spectral shift depends on the polarity of the applied external voltage$V$. If V is negative the emitted electrons are accelerated towards the objective lens and the full spectrum is shifted to higher kinetic energies (Fig. 8.6b). If V is positive the electrons are decelerated to lower kinetic energies (Fig. 8.6c). Due to the fact that the spectral shifts $\Delta E(x,y)$ only occur within regions of the sample where the local potential deviates from the reference potential, a systematic evaluation of spectral shifts for each point P(x,y) of the surface can be **exploited to recalculate local potential maps V(x,y).** In this way the XPEEM approach can be used as two dimensional voltage probe microscope. Further, by deriving 2D potential maps V(x,y) along the spatial coordinates, the lateral electric field $\vec{E}(x,y) = -\nabla V(x,y)$ distribution can be calculated.

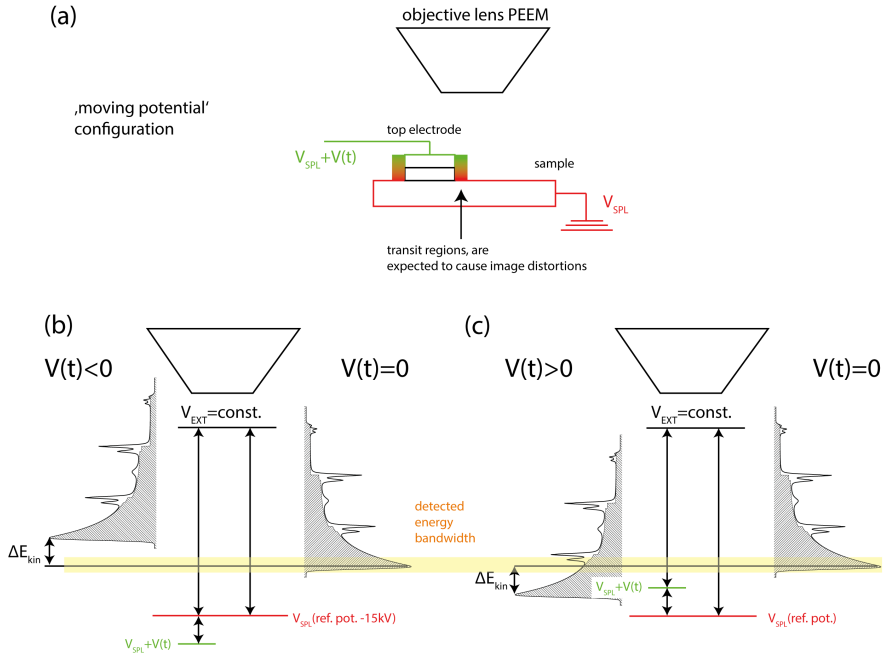

Figure 8.6. – Influence of local potential variations on the sample surface: (a) Schematic of a sample with the external potential V(t) connected to the top electrode. The top electrode is lifted to a potential $V_{\mathrm{SPL}} + V(t)$ defined by an externally applied voltage V(t) (green). The remaining sample is grounded to the reference potential V_{SPL}(red). The kinetic energy gain by the electric field of the objective lens is equal to $E_{\mathrm{kin}}[\mathrm{eV}] = (V_{EXT} - V_{SPL}) \cdot e$. Depending on the voltage polarity electrons from the top electrode are either further accelerated (b) or decelerated (c) by an amount $\Delta E_{\mathrm{kin}} = -V(t) \cdot e$. Thus in regions of applied voltage a different part of the emitted spectrum is probed.

8.3.2. Recalculation of the local time-dependent potential V(x,y,t)

Temporal resolution may be added to the experiment by acquiring PEEM emission spectra $I(E_{\mathrm{kin}},x,y,t)$ at different points in time $t = t_n$. The result is then a time-dependent local potential map $V(x,y,t_n)$. The recalculation of the time-dependent, local potential V(x,y,t) follows two steps, Fig. 8.7: First, a three dimensional XPEEM stack $I(x,y,E_{\mathrm{kin}})$ is acquired for different time steps t_n. In a next step, the induced local spectral shifts in kinetic energy $\Delta E_{\mathrm{kin}}(x,y,t_n)$ are extracted from this data set by comparing the spectra in each single point P(x,y) to the corresponding emission spectrum of a non-excited reference system (typically the PEEM stack acquired at t=0), Fig. 8.7.

The local potential $V(x,y,t_n)$ can than be calculated according to $V(x,y,t_n) = -\frac{\Delta E_{\mathrm{kin}}(x,y,t_n)}{e}$. The achievable temporal resolution Δt of this procedure is limited by the acquisition time of a single PEEM stack, which is typically in the order of several minutes. The delay of several minutes between two subsequent acquisition points renders real time data acquisition using this approach impossible. However, more than 95% of the acquired data is redundant and the performance of the procedure can be significantly enhanced **under the assumption that the shape of the emission spectrum $I(x,y,E_{\mathrm{kin}})$ does not significantly change during application of the external voltage $V(t)$.**

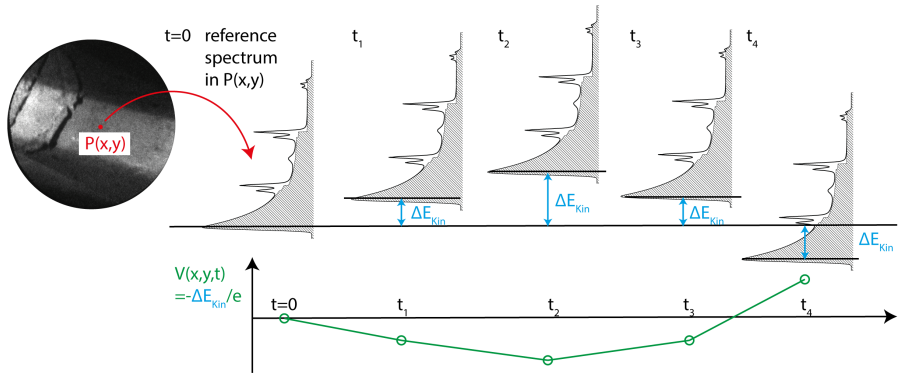

Figure 8.7. – Procedure to recalculate the local potential V(x,y,t): XPEEM image stacks $I(x,y,E_{\mathrm{kin}})$ are acquired at different points in time t_n. Then, for each time step t_n and in each pixel P(x,y) a emission spectrum $I(E_{\mathrm{kin}})$ is extracted. From the spectral shifts ΔE_{kin} (blue) between subsequent spectra the time-dependent local potential $V(x,y,t) = -\frac{\Delta E_{\mathrm{kin}}(x,y,t)}{e}$ (green) in point P(x,y) can be calculated.

Under this assumption - that the spectral shape does not change, but only shifts in energy during the application of the external voltage - it is sufficient to focus only on one spectral feature with know energy-dependence, e.g. the secondary electron edge. Details of this concept will be outlined in the following section.

8.3.3. Recalculation of local potentials from intensity modulations

The improvement in temporal resolution is based on the fact that in energy-filtered PEEM (EF-PEEM) the detected photo intensity $I(E_{\mathrm{kin}})$ depends on the kinetic energy E_{kin} of the emitted electrons. Any shift in the kinetic energy spectrum will result in a modulation of the detected intensity $I(E_{\mathrm{kin}},t)$ as sketched in Fig. 8.8.

The shift of the kinetic spectrum ΔE goes hand in hand with a change of the intensity ΔI detected by the PEEM detector. Between 2.5 V and 20 V the secondary edge is strictly (monotonously) decreasing. Positive shifts in energy ΔE_{kin} lead to increasing intensity ΔI whereas negative shifts ΔE_{kin} show a decrease of ΔI. In turn - if the underlying spectral function $I(x,y,E_{\mathrm{kin}})$ is known and bijective[5] - the function can be inverted and the measured change in intensity ΔI may be used to recalculate the shift of the spectrum ΔE_{kin}.

In the enhanced procedure, only single images instead of a full spectrum have to be acquired. This way the temporal resolution can be increased from $\Delta t \approx$ minutes down to a detector limited Δt of 300 ms corresponding to≈ 3.3 frames per second (real time).

The improved experimental procedure is performed as follows: First, a three dimensional XPEEM stack $I(x,y,E_{\mathrm{kin}})$ at the secondary electron cut-off edge (SEY) without applied voltage $V(t) = 0$ is

[5] A function is bijective if every element of the argument space is mapped to by exactly one element of the function output space and vice versa. Sometimes also referred to as one-to-one correspondence.

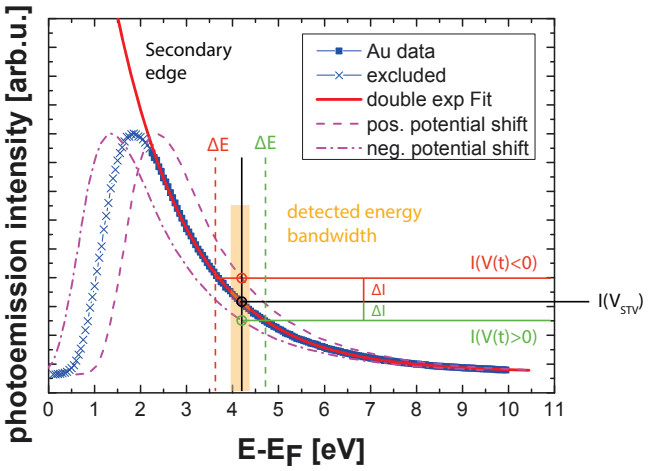

Figure 8.8. – Procedure to recalculate the local potential V(x,y,t) from intensity modulations: The blue curve shows a measured secondary edge photoemission spectrum of an Au top electrode. The spectrum has been subdivided into the cut-off region (crosses) and the tail region (squares). The latter was fitted by a double exponential fit (red). If an external voltage $V(t)$ is applied to the electrode the full spectrum is shifted in energy (purple lines). Depending on the polarity the shift is either to the left or to the right. During an experiment only a small bandwidth of the spectrum close to the start voltage is detected (yellow). In the undisturbed case the detected intensity is given by $I(V_{SPL})$ (black point). Shifts of the spectrum due to local potential variations will manifest as time and voltage dependent intensity modulations $\Delta I(V,t)$ (orange and green points). The time dependency of the intensity is measured and used to recalculate the energy offset $\Delta E = -\Delta V(t) \cdot e$ by comparison to the recorded reference.

acquired for a defined field of view in EF-PEEM. The SEY stack serves as reference for the subsequent analysis. It contains the shape and position of the secondary electron edge for each point P(x,y) and defines the $I(E_{kin})$ for voltage recalculation. In the second step the same instrumental settings are used to record a movie of the sample intensity $I(x,y,t)$ over time, while an external voltage $V(t)$ is applied. For the time-dependent measurement the start voltage (STV) - and with it the detected E_{kin} - is fixed to a value at the center of the secondary tail, so that spectral shifts in both directions can be accounted for, see Fig. 8.8.

The result of a typical experiment are two 3D data stacks: $I(x,y,E_{kin})$ at $t = 0$ and $V = 0$; and $I(x,y,t)$ at fixed E_{kin}. The two stacks contain the information on the secondary electron edge distribution $I(E)$ and the intensity modulation $I(t)$ for each single point P(x,y). If the change in intensity $I(t)$ is solely induced by a shift of the spectrum due to the presence of a local potential as previously described, both photoemission signals can be mathematically linked ($\circ$) together in order to recalculate the time dependent voltage signal $V(t)$, Eq. 8.2 (1-dimensional) and Eq. 8.3 (multidimensional).

$$V(t) = I(E) \circ I(t) \tag{8.2}$$

$$V(\vec{x},t) = I(\vec{x},V) \circ I(\vec{x},t) \tag{8.3}$$

Eq. 8.2 was solved by a MATLAB algorithm pixel-by-pixel as explained in the following. In a first step, both one-dimensional photoemission spectra $I(t)$ and $I(E)$ at a fixed point P(x,y) are normalized to their initial conditions. The time-dependent intensity $I(t)$ is normalized to $I(t=0)$. The secondary edge $I(E)$ is normalized to the start voltage $I(E=STV)$. Assuming that the relative change in intensity $\Delta I_{\mathrm{rel}} = \frac{I(t)}{I(0)}$ is due to the spectral shift $\Delta E(t) = E(t) - STV$, Eq. 8.4 must be fulfilled for any time step t. Using the Eq. 8.4 the algorithm determines the kinetic energy $E(t)$, which corresponds to the same relative intensity $\Delta I_{\mathrm{rel}} = \frac{I(E(t))}{I(STV)}$ as observed in the time-dependent intensity trace. In other words, for each time step t the relative change in intensity ΔI is mapped to the shift in energy ΔE necessary to facilitate the same relative intensity change. The time dependent local potential $V(t) = \Delta E(t)/e$ is calculated for the determined ΔE(t). An illustration plus an example of this procedure are given in Appendix A.4.

$$\frac{I(t)}{I(0)} = \frac{I(E(t))}{I(STV)} \tag{8.4}$$

The algorithm operates on a single pixel basis using one dimensional photoemission spectra, Fig. 8.9a. Application of the algorithm to each pixel P(x,y) of the acquired movie stack results in spatially and time-dependent two dimensional potential maps V(x,y,t), Eq. 8.3 & Fig. 8.9b. Except for a small mismatch between the timescales, the recalculated voltages are in good agreement with the externally applied voltages. The mismatch between the observed timescales most likely arises from an unaccounted delay caused by the image saving operation on the data acquisition PC. Analysis of real data will be presented in the sections 8.4.1 and 8.4.2.

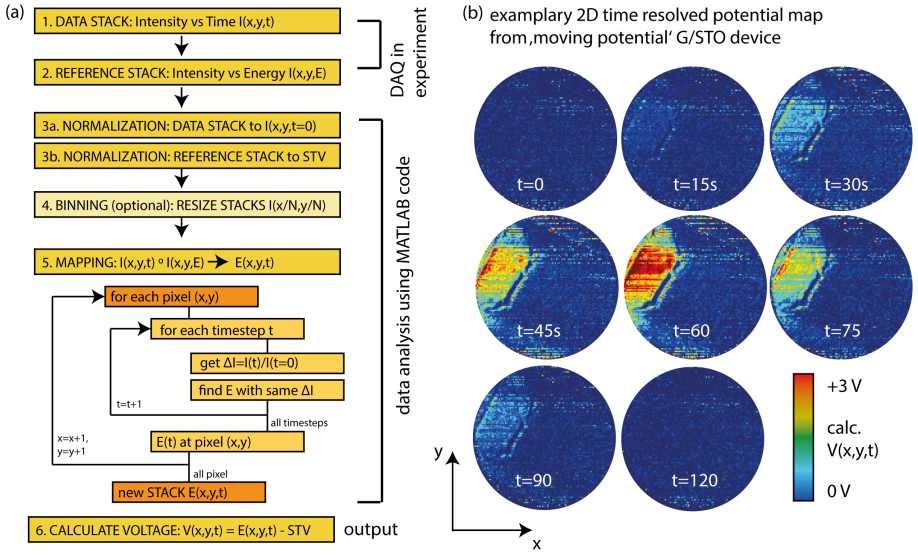

Figure 8.9. – (a) Flow sheet of potential mapping in XPEEM using the algorithm described in the text. (b) Exemplary code output: Two dimensional local potential maps V(x,y,t) of a STO MIM device during a RESET process recalculated from XAS raw data

8.3.4. Intermixing of chemical and electrostatic information in the recalculation

The formation of oxygen vacancies leads to a modified absorption behavior in the vicinity of filamentary regions referred to as chemical fingerprints. These fingerprints include intensity modulations at the O K-edge (O 1s → Ti 3d − O 2p transition, see peak A in Fig. 8.10a). For O vacancy concentrations >10% changes also include modifications of the Ti L-edge. Thus, chemical sensitivity can be added to the operando approach if the photon energy is tuned to be resonant with one of these characteristic absorption features. If the oxygen vacancy concentration is modified during the course of the experiment, the detected SEY increases or decreases, respectively. Similar to the electrostatic effects, the chemical changes will manifest as a time-dependent intensity modulation $I_{\mathrm{chem}}(t)$ such that the overall observed intensity modulation $I(t)$ must be considered as a superposition of chemical $I_{\mathrm{chem}}(t)$ and electrostatic $I_{\mathrm{static}}(t)$ contributions, Eq. 8.5 and Fig. 8.10b.

$$I(t) = I_{\mathrm{chem}}(t) + I_{\mathrm{static}}(t) \tag{8.5}$$

$$I(t) \approx I_{\mathrm{static}}(t) \tag{8.5a}$$

It the real-time acquisition approach it is not possible to disentangle both contributions. However, from previous experiments (Chapter 5) it can be expected that the chemical contributions to the intensity modifications are much smaller as compared to the electrostatic effects and that the total intensity during device operation in first order can be approximated by $I(t) \approx I_{\mathrm{static}}(t)$. Still, chemical changes can be detected. In contrast to the electrostatic effects, which are only present if a voltage is applied, chemical changes persist even after removal of the external voltage. Therefore, chemical contrast becomes visible between images before and after a switching event.

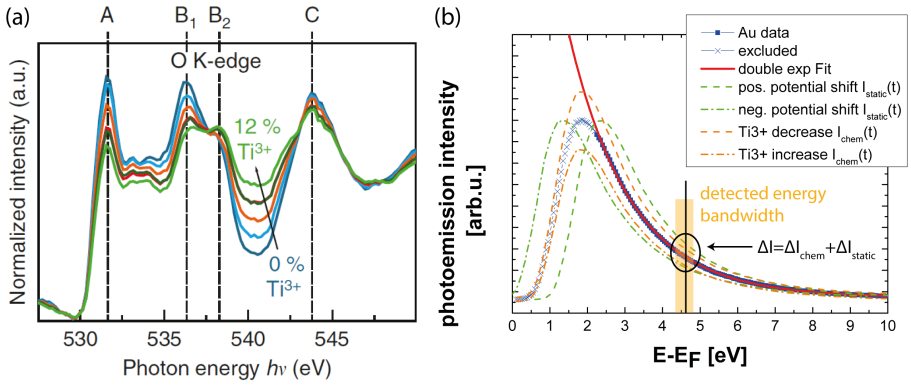

Figure 8.10. – Tracing chemical changes: (a) chemical changes in the oxygen K-edge XAS for different oxygen vacancy ($V_{\mathrm{O}}^{\cdot\cdot}$) concentrations. With increasing $V_{\mathrm{O}}^{\cdot\cdot}$/Ti 3+ concentration the SEY intensity of peak A decreases. Image taken from Ref. [1]. (b) In addition to the intensity modulations caused by spectral shifts of local potentials (green), the detected intensity I(t) is also affected if the total SEY is altered by modifications of the $V_{\mathrm{O}}^{\cdot\cdot}$ concentration (orange).

8.3.5. Limitations of the recalculation algorithm

The algorithm has three major limitations. Firstly, the approach only works if the pixel of the acquired stacks $I(\vec{x},E)$ and $I(\vec{x},t)$ describe exactly the same position on the sample. This implies that any sample and beam drift during the experiment must be corrected before analysis. Non-correctable image distortions like micro lensing effects at potential steps or image blurring will lead to faulty results. Secondly, it is assumed that the intensity changes are solely induced by spectral shifts. Intensity modulations induced by chemical changes will be misinterpreted as higher/lower local potentials (Eq. 8.5a). The problem with chemical sensitivity can be solved by using the experimental sample geometries defined in the previous section. The third and last limitation is that the reference spectrum (e.g. secondary edge) must be strictly monotonous over the full range of the expected spectral shifts. Otherwise the function is not bijective and multiple energies can account for the observed change in intensity.

8.4. Experimental results

The setup as described in the previous sections was employed to switch the graphene top contacted STO MIM devices (Chap. 6) in front of the microscope during operation. For this purpose SET, RESET and READ pulses - provided by the external power supply - have been applied to the devices in vacuum, while simultaneously the characteristic I-V curves of the devices were recorded from the Keithley output. The microscope was operated in X-ray absorption mode (XAS) and set to acquire images at the secondary emission tail at a start voltage STV of 5 ± 0.1 V. The acquisition time per image was reduced to the camera limit of 300 ms in order to capture a live XAS movie of the switching process. To be sensitive to charge carrier and Schottky barrier modulations the photon energy of the beamline was tuned to peak A of the O K-edge around 531.6 eV.

8.4.1. Real-time pulse characterization of G/STO devices in voltage mode

For operando pulse characterization and to prove the operability of the overall setup a device was mounted in 'moving potential' configuration into the PEEM. The device was switched multiple times reversibly between LRS and HRS by defined SET and RESET pulses in front of the microscope. Simultaneously, the corresponding I-V curves were recorded by the external power supply, Fig. 8.11a. Further, before and after each switching event, the device resistance was verified using a read pulse of 200 mV. For the first three resistive switching cycles ($V_{\mathrm{RESET}} = -3\,\mathrm{V}, V_{\mathrm{SET}} = 3\,\mathrm{V}, I_{cc} = 35\,\mathrm{mA}$) the device resistance alternated between $R_{LRS} = 700\,\Omega$ and $R_{HRS} = 33\,k\Omega$, Fig. 8.11b. With each additional cycle the applied voltage $V(t)$ and current compliance I_{cc} for the SET process were continuously increased to brute force filament formation, until a hard breakdown of the device at 4 V and 60 mA was observed making the device electrically shorted. The observed I-V characteristics of the sample mounted in the microscope was similar to switching under ambient conditions. No anomalies could be observed indicating no significant influence of vacuum.[6]

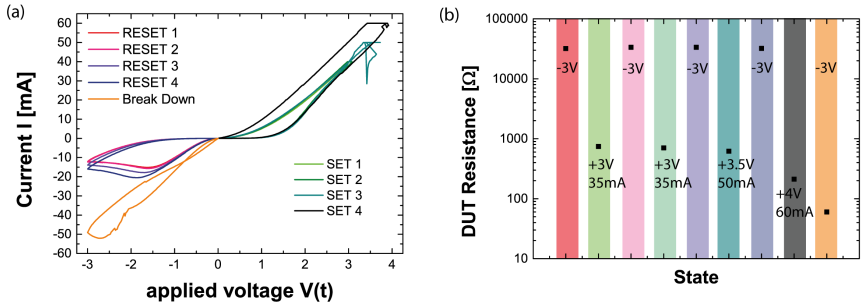

Figure 8.11. – (a) I-V characteristics of an Au/G/STO/Nb : STO device mounted in the microscope in 'moving potential configuration' and measured by the external Keithley 2611A source meter (b) READ measurements of the device resistance after each cycle (corresponding to the color scheme in a). The resistance values were extracted at +0.2 V read out voltage.

[6] At least for the first 5 cycles

Voltage recalculation from operando XPEEM

All SET and RESET switching events shown in Fig. 8.11, were also monitored during operation by time-resolved XPEEM measurements. Therefore, the field of view of the PEEM was set to ≈ 15µm containing the Au lead as well as the graphene window. Prior to the time-dependent measurements $I(x,y,t)$, a reference stack $I(x,y,E_{\mathrm{kin}})$ in dependence of the kinetic energy E_{kin} for this specific combination of microscope settings and photon energy was acquired. For the time-dependent measurements the microscope was set to continuous image acquisition in order to record a movie of the intensity distribution $I(x,y,t)$ over time with a temporal resolution amounting to $t_{\mathrm{dwell}} = 300\,\mathrm{ms}$. Both stacks were used in combination for the recalculation of the local potential distributions $V(x,y,t)$ as described in Sec. 8.3.

An exemplary operando XPEEM image series of a LRS device at different time steps t_n during the application of a −3 V RESET pulse is shown in Fig. 8.12a. The experimental operando XPEEM raw data $I(x,y,t,)$ is on top; the same data normalized to $I(x,y,t=0)$ is shown on the bottom. The normalization process removes instrumental artifacts, beam profile and highlights the regions with intensity modulations. The observed intensity modulations $I(t)$ can be related to specific features of the device according to the device scheme presented in Fig. 8.12b. The time of acquisition for each image in reference to the externally applied SET voltage pulse $V(t)$ is marked in Fig. 8.12c.

From the acquired XPEEM movie stack intensity profiles were extracted from the Au lead region, $I_{Au}(t)$, and the central graphene region, $I_G(t)$. Both profiles are plotted in Fig. 8.12c with reference to the externally applied voltage $V(t)$ and the measured current $I(t)$.[7] One can see that the intensity modulations observed in XPEEM coincide with major features of the applied voltage $V(t)$ and current pulse $I(t)$. The strongest intensity modulations are observed within the Au lead region. While the intensity at the Au lead $I_{Au}(t)$ resembles an inverted and deformed variant of the applied voltage $V(t)$, the shape of the graphene region intensity $I_G(t)$ exhibits similarities to the measured and inverted current profile $I(t)$.

In the 'moving potential' geometry the potential is applied to the Au electrode and thus strong intensity modifications near the Au lead induced by the shift in local potential are expected. On the other hand, the graphene region should exhibit similar behavior if being in good contact with the Au lead. This is not the case. Instead the extracted intensity profiles of the graphene region matches the current profile I(t) indicating an ohmic contact to the substrate. The close temporal correlation between the applied pulse parameters $V(t)$, $I(t)$ and the extracted PEEM intensity modulations, Fig. 8.12c, as well as the fact that largest changes are observed at the Au lead indicate that the observed intensity modulations are not caused by the formation/depletion of oxygen vacancies, but rather have to be attributed to electrostatic effects. These observations justify the application of the potential recalculation algorithm (Sec. 8.3) in the following.

Figure 8.13 shows the potential at the Au lead ($V_{\mathrm{Au}}(t)$, dots, orange) and the potential at the graphene contact ($V_{\mathrm{G}}(t)$, dots, purple) for a RESET (a) and a SET (b) process recalculated from the extracted intensity profiles of the operando XPEEM movie $I_{Au}(t)$ and $I_G(t)$, respectively. Additionally, the

[7] To avoid confusion between the current $I(t)$ and intensity profiles $I_X(t)$ extracted from the region x of the XPEEM stack, the intensity profiles are always labeled by a subscript

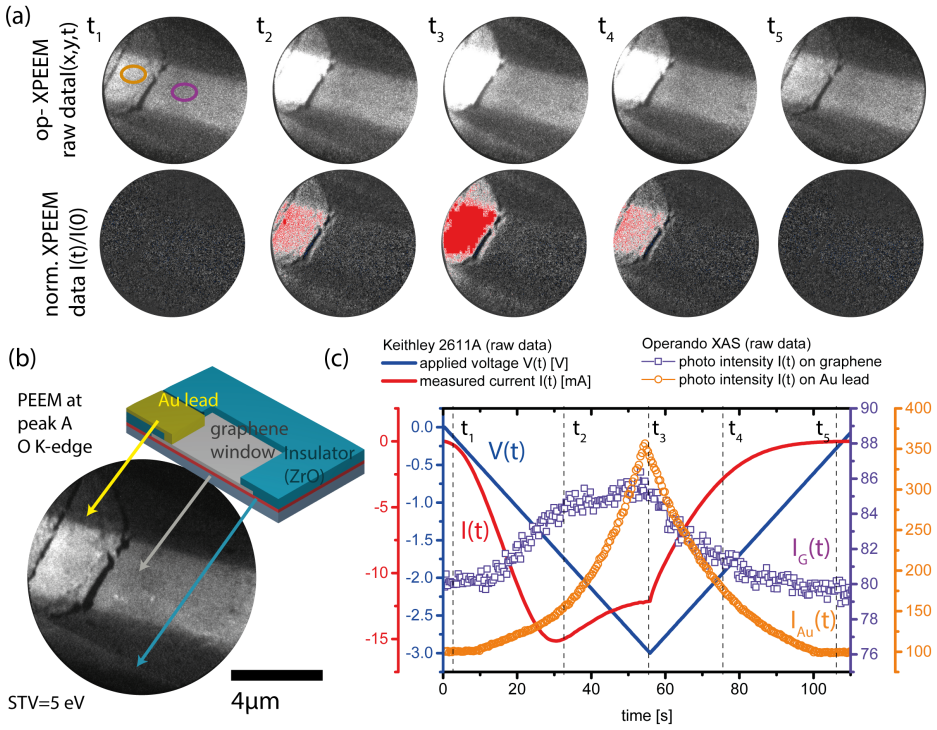

Figure 8.12. – (a) Series of XPEEM images at peak A of the O K-edge acquired at different times during a −3V RESET pulse. The snapshots show spatially confined intensity modulations of the photoemitted intensity I(x,y,t). (b) XPEEM reference image: the Au lead, the graphene window and the insulator can be identified. (c) Externally applied voltage V(t) (solid, blue), measured current I(t) (solid, red) and observed PEEM intensities for the Au lead (dots, orange) and graphene electrode (dots, purple). The latter are extracted from the corresponding regions of the XPEEM stack $I(x,y,t)$ marked in (a).

corresponding externally applied voltage $V(t)$ (solid, blue) and the current $I(t)$ (solid, red) measured by the Keithley are plotted. It is important to note that these two experimental methods to determine the potential are completely independent. One is based on electrons flowing through the device, the other relies on analyzing electrons emitted from the device. Still, both - directly measured and recalculated voltages - show reasonably good agreement with respect to shape and amplitude.

The asymmetric and non-linear shape of the current trace $I(t)$ is related to the switching process. The fact that the potential at the graphene electrode follows the current is a first solid evidence of a successful operando switching characterization using XPEEM. Further, the plateaus observed during the SET process, which are caused by the current compliance, can also be detected in the recalculated potentials. This provides additional proof that the intensity modulations are indeed dominated by electrostatic contributions. In the ideal case - if load resistance contributions can be neglected - the voltage drop at the top electrode/Au lead in 'moving potential' configuration should be identical to the externally applied voltage $V(t)$. However, especially for low resistance state of

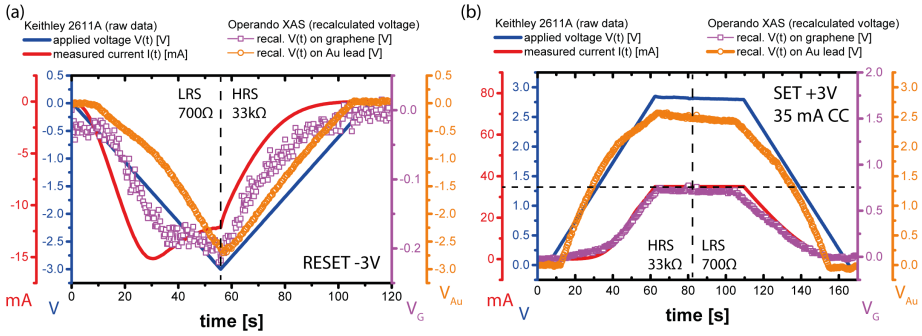

Figure 8.13. – Pulse characterization. Externally measured I-V data (solid, red & blue) and recalculated potentials at the Au lead (orange) and the graphene top electrode (purple) (a) -3V RESET operation from $R_{LRS} = 700\,\Omega$ to $R_{HRS} = 33\,k\Omega$ (b) +3V SET operation form $R_{HRS} = 33\,k\Omega$ to $R_{LRS} = 700\,\Omega$ using a current compliance of 35 mA

$R < 700\,\Omega$ ($t = 0 - 55$ s) the potential trace $V_{\mathrm{Au}}(t)$ extracted from the Au lead significantly deviates from the applied potential $V(t)$, Fig. 8.13. For the HRS ($t = 60 - 110$ s) the effect is less pronounced. It was assumed that these deviations between applied and recalculated voltage are related to voltage divider effects between the device resistance and parasitic load resistances of the setup leading to a much smaller voltage drop over the device in the LRS as it would be expected from the external measurements. Voltage divider effects are negligible if the device resistance R_{DUT} is much larger than the parasitic load resistance R_{Load} ($R_{\mathrm{Load}} \ll R_{\mathrm{DUT}}$). The become pronounced for $R_{\mathrm{DUT}} \leq R_{\mathrm{Load}}$.

Influence of parasitic resistances

The influence of parasitic resistance to device operation was evaluated by applying symmetric triangular SET and RESET cycles with increasing amplitude from 1V - 4V to a device programmed into a low resistance state (R_{DUT} at +0.2V < 700 Ω), Fig. 8.14. In the top left panel the externally applied voltage $V(t)$ (gray) is plotted versus the potential at the Au lead $V_{\mathrm{Au}}(t)$ recalculated from operando XPEEM data (yellow-red) and shown for each of the different cycles. The recalculated voltage drop shows pronounced deviations from the applied voltage in amplitude and shape. The deviations increase with increasing pulse amplitude. While the applied voltage continuously increases, the recalculated potential at the Au lead starts to saturate around 2V. Plateaus are observed in both traces if the current (bottom left panel) runs into current compliance. For the 4V RESET the potential measured at the Au lead $V_{\mathrm{Au}}(t)$ and the current $I(t)$ both become asymmetric shortly before the maximum of the half-cycle is reached. This asymmetry is induced by the non-volatile transition from LRS into HRS and indicates that a partial switching took place.

The experimental data set was compared to LT SPICE simulations in which the RS device was modeled by an anti-parallel arrangement of two diodes reproducing the bipolar, non-linear operation of a Schottky barrier, Fig. 8.14b. Before and after the device, ohmic resistors were inserted representing the expected parasitic effects by cables, wire contacts and the Au lead. An equivalent circuit model of the full setup is plotted as inset. At two points of the circuit potential traces have been extracted from the simulation. The applied voltage $V_{\mathrm{app}}(t)$ corresponds to the voltage applied to the

full circuit. The potential drop $V_{\mathrm{meas}}(t)$ was 'measured' after the first lead resistor, but before the device under test (DUT). Similar as in the case of the operando PEEM setup, applied and measured voltage have been plotted with respect to each other. The voltage drop at the device significantly deviates from the total applied voltage, showing a similar characteristic as the RSM device in the experiments. Moreover, the simulated currents exhibit a similar, but less smooth behavior.

The simulation is not intended as quantitative measure, instead is used to demonstrate the influence of parasitic load resistances. Hence, in this simple model, effects induced by the current compliance are not implemented. Further, the model does not describe a non-reversible resistive switching implying that the line shapes remain symmetric at all times. Based on the good qualitative agreement between simulations and experiment, it is assumed that the recalculated PEEM potentials differ from the externally applied potentials, because they indeed describe different points in the circuit. While the applied voltage $V(t)$ describes the voltage drop over and $I(t)$ the current flowing through the full circuit, the recalculated voltage drop at the Au lead $V_{\mathrm{Au}}(t)$ describes only the potential drop at the device.

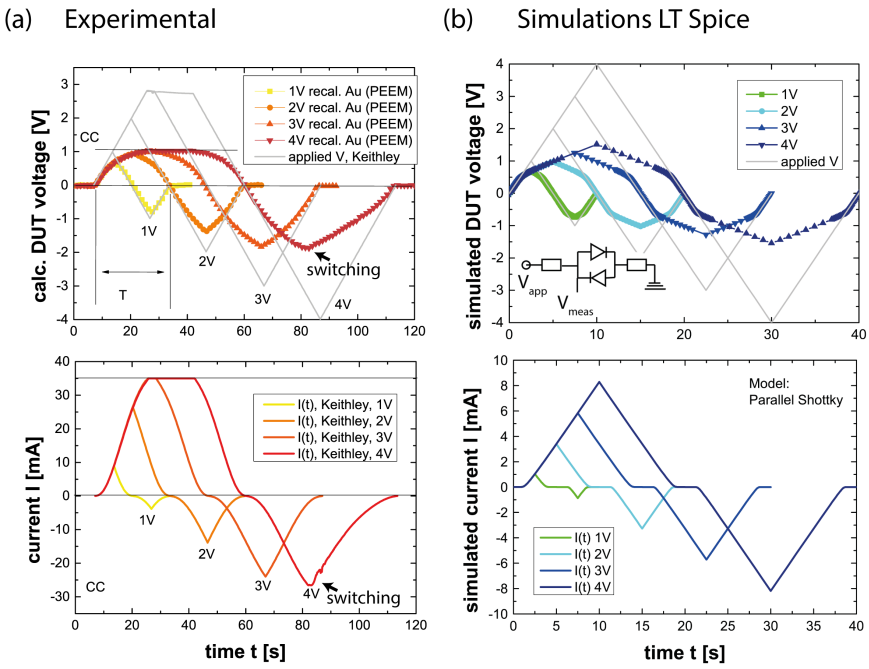

Figure 8.14. – Experiment vs. Simulation: (a) Potentials at the Au top electrode $V_{\mathrm{Au}}(t)$ derived from operando XPEEM (colored) and externally applied voltages $V(t)$ (gray); The corresponding currents $I(t)$ (Keithley) are plotted in the bottom graph. (b) In an LT SPICE simulation the resistive switching device is modeled as anti-parallel arrangement of diodes (inset). The top graph shows the simulated voltage drops behind the first load resistor $V_{meas}(t)$ (colored lines) and the simulated applied voltages $V_{app}(t)$ (grey); The corresponding simulated currents $I_{sim}(t)$ are plotted in the bottom graph.

Modeling of the internal device structure from potential distribution maps

If potential traces are not only recalculated for specific features (e.g. Au lead), but instead the values are calculated for each point of the device $V(x,y,t)$, this is what will be referred to as a potential distribution map (PDM). Fig. 8.15a shows the PDM derived from the operando pulse characterization experiments of the previously discussed devices for an externally applied voltage of $V(t) = 3\,\mathrm{V}$. These PDMs have been used to model an equivalent circuit accounting for device geometry and additional parasitic influences of the setup, Fig. 8.15b,c. According to the measured PDM in Fig. 8.15a, the graphene layer and the Au lead must be electrically separated, because they show completely different potentials. This observation may be explained by discontinuities of the graphene sheet, bad or missing contact with the Au lead or charge carrier depletion of the film by interaction with the STO film. In any of these situations the potential trace extracted from the Au lead is attributed to point A of the equivalent circuit, whereas the voltage drop measured at the graphene electrode far away from the Au lead represents point B.

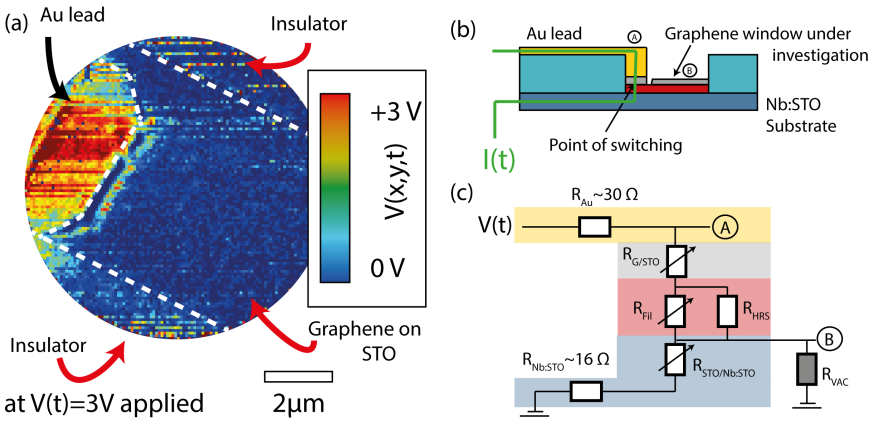

Figure 8.15. – (a) PDM in a G/STO device mounted in 'moving potential' for an applied voltage of +3V. (b) Device model to explain the extracted potential profiles. Switching occurs underneath the Au lead. The graphene window is directly not connected. (c) Equivalent circuit including lead and substrate resistance. Point A is the potential extracted from the Au lead. Point B is the potential extracted from the substrate.

The almost linear dependence observed between the recalculated voltage $V_G(t)$ and the measured current $I(t)$ for voltages above +0.3V, Fig. 8.13, implies that all elements (Nb:Substrate, cables) in series with the graphene sheet must exhibit ohmic character. Consequently, the total resistance of the Nb:STO substrate, subsequent cables and other elements in line with the device was calculated to $R_{\mathrm{Nb:STO}} = \frac{V_G(t)}{I(t)} \approx 16\,\Omega$. The combined resistance of the Au lead, the bonding contact and other elements ahead of the device, was estimated from the potential difference between the applied voltage $V(t)$ and the potential extracted from the Au lead $V_{\mathrm{Au}}(t)$ measured in current compliance to be around $R_{\mathrm{Au}} = \frac{V(t)-V_{\mathrm{Au}}(t)}{I_{CC}} \approx 30\,\Omega$.

Overall, the potential distribution in the device indicates that switching is located underneath and/or very close to the Au lead. Hence, it must be expected that resistive switching and the formation of oxygen vacancy rich filaments preferably occurs within the Au overlay region being inaccessible by PEEM. From a physical perspective, switching under the Au electrode is reasonable, because

current-driven Joule heating of the Au lead and the underlying STO thin film up to some hundred degrees significantly enhances the oxygen vacancy migration in the near vicinity. In turn, the locally enhanced migration and excorporation promotes higher filament formation rates as compared to other - unheated - parts of the device.

TEM cross sectional cuts through Au/graphene/STO/Nb:STO layer-stacked devices, thermal images of devices during operation [98], post-mortem device characterization in SEM (Sec. 8.4.4) and operando PEEM characterization of device break down (Sec. 8.4.3) point in the same direction.

Extraction of the donor concentrations and the Schottky barrier height Φ_B

If the equivalent circuit depicted in Fig. 8.15c holds true, two major implications can be derived: First, the chemical investigations will not show filament formation within the graphene region. Second, the operando XPEEM data for the first time allows to calculate the "real" voltage drop across the MIM structure by simple subtraction of the potentials $V_{DUT}(t) = V_{Au}(t) - V_G(t)$, Fig. 8.16b. "Real" in this context means without any influence of parasitic resistances picked up by cables, contacts, etc.

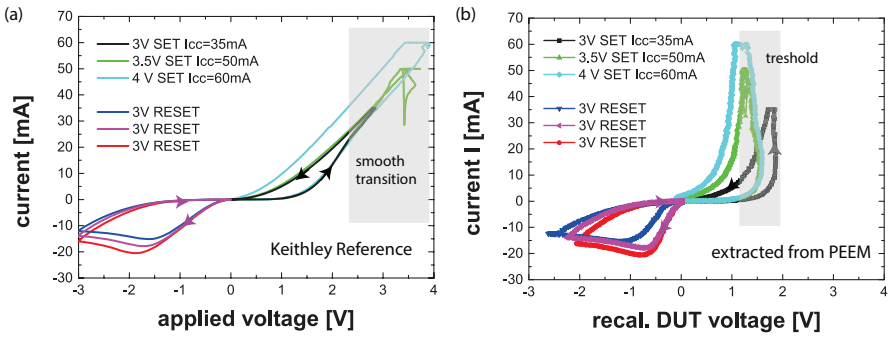

Figure 8.16. – (a) I-V curve of device operation measured by external Keithley (b) I-V curve of the DUT without parasitic influences deducted from XPEEM measurements.

By comparing the externally measured I-V curves of the Keithley (a) to the I-V curves recalculated from PEEM (b) derived potentials, the benefits of the novel approach become evident, Fig. 8.16. While the SET process measured by the Keithley shows a smooth transition, the process becomes abrupt if only the voltage drop across the device is taken into account. The abrupt change appears for certain threshold values around 1.5 – 1.9 V. Within this region the current rises to the compliance level without any observable increase of the potential drop across the device. In addition, for the RESET process it was found that even by using three times the same RESET voltage of −3 V, the voltage drop across the device was lowered with each cycle form initially −3 V to about −2 V after the second cycle. The lower RESET voltage results only in a partial RESET of the device decreasing the ON/OFF ratio with each following cycle.

The experiments point out a common problem for the characterization of resistive switching: Most authors in literature typically assume that the externally applied voltage corresponds to the device voltage. Devices undergoing a SET process, however, become highly conductive (their resistance

values decreases down to the order of parasitic resistances of a setup) and the voltages drop across the device is lowered by the potentials dropping over parasitic resistances. As a result, the switching process strongly depends on the experimental configuration. The same switching parameters for the external voltage will result in different resistance states for different experimental setups. As specifically shown for this device, even in the same setup the externally applied voltage does not represent the voltage drop across the device leading to a false characterization of switching voltages and Schottky barrier modulations. We find that the voltage values provided in many articles are not a good quantity to describe resistive switching without providing details on the parasitic influences of the setup. In contrast, the PEEM derived potentials directly measure the voltage drop across the device providing an universal, setup-independent measure of the device operation.

These universal potential profiles were used for the characterization of the expected Schottky barrier modulation. The standard procedure [30, 99, p.170] of characterizing Schottky contacts is to fit Eq. 8.6 to the experimental data in forward bias direction.

$$I = A^* \cdot T^2 \cdot \exp\left(-\frac{q \cdot \Phi_B}{k_B T}\right) \cdot \left[\exp\left(\frac{q \cdot V}{n \cdot k_B T}\right) - 1\right] \tag{8.6}$$

A^* represents the Richardson constant, T is the temperature[8] , q the electron charge. Φ_B is the Schottky barrier height and n is the so-called ideality factor. The ideality factor describes the deviations from a perfect Schottky diode, which is driven by thermionic emission only ($n = 1$). According to Sze [30, p.164] deviations of the ideality factor from unity imply a strong influence of additional tunneling contributions.

Thus, the forward bias I-V response of the extracted PEEM profiles was fitted by Eq. 8.6 describing the modulation of the Schottky barrier at the Pt/$SrTiO_3$ top electrode/oxide interface. The results of the fitting procedure are summarized in table 8.1. Notable, reversible differences in the extracted SBHs Φ_B and ideality factors n in between the LRS and the HRS were found.

		Transport at Pt/STO interface		
	Cycle	exp. $q\Phi_B$ [eV]	ideality factor n	goodness of fit R^2
LRS	I	0.820	12.88	0.989
	II	0.860	14.73	0.996
	III	0.836	13.08	0.987
	avg. + std.	(0.839 ± 0.020)	(13.56 ± 1.01)	(0.991 ± 0.005)
HRS	I	0.952	9.27	0.990
	II	0.982	9.42	0.932
	III	0.957	10.42	0.988
	avg. + std.	(0.957 ± 0.017)	(9.70 ± 0.62)	(0.970 ± 0.032)

Table 8.1. – Fit results of the measured forward currents to the Schottky equation Eq. 8.6 for three LRS → HRS cycles. The upper part is related to a LR state, while the bottom part shows the same device in the HR state.

For the LRS, the averaged measured effective Schottky barrier height is around $\Phi_B = 0.84\,\text{eV}$ with an ideality factor of $n = 13.56$. The HRS shows an averaged effective barrier height of $\Phi_B = 0.96\,\text{eV}$ and

[8] Due to a lack of experimental data T was assumed to be constant at room temperature for the fitting procedure, even though knowing that this assumption is oversimplified.

an ideality factor of $n \approx 9.7$. All fits provide an adj. R^2 close to 1 representing good agreement between fit and experimental data. Compared to the anticipated intrinsic barrier height of 1.1 eV derived from the Schottky-Mott rule, the effective barrier height is slightly lowered for the HRS and significantly lower for the LRS. The barrier lowering can be explained by the image force effect [30, p.164] in combination with the model of oxygen vacancy formation and depletion near the electrode interface. The change in the ideality factor describes the varying contributions of tunneling

During the SET process from HRS to LRS the barrier height is decreased while at the same time the ideality factor n increases. Based on these findings it is derived that during SET an oxygen vacancy rich layer must be formed at the interface, 8.17a. An increase of the vacancy/donor density N_D near the metal interface during SET explains the decrease in barrier height and it further accounts for the observed increase in tunneling contributions. The overall device resistance is reduced.

Removal of oxygen vacancies from the interface during a RESET process effectively restores the barrier height and increases the barrier width such that the amount of tunneling is again suppressed, Fig. 8.17b. The overall device resistance is restored.

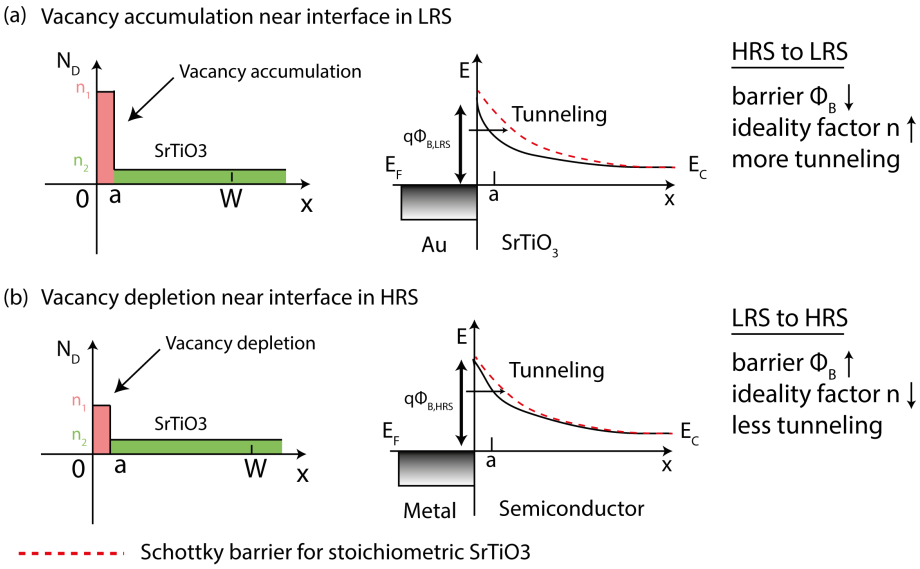

Figure 8.17. – Influence of defect density modulations at the metal/oxide interface. (a) High donor densities N_D in the electrode vicinity lower the barrier and enable tunneling. (b) A decrease of the donor density increases the barrier height and enlarges the tunneling distance. Adapted from Sze, Wiley. [30]

The effect of barrier lowering due to defects is well known and used to tune the contact resistance of metal/oxide interfaces in CMOS technology [30]. From the barrier height difference $\Delta\Phi = |\Phi_{\mathrm{HRS/LRS}} - \Phi_{B0}|$ between the measured SB values in LRS (Φ_{LRS}) and HRS (Φ_{HRS}) and the intrinsic barrier height Φ_{SB} the change in interfacial donor density $N_D \cdot a$ can be calculated according to Eq. 8.7. For the calculation a static dielectric constant $\epsilon_S = 300$ for $SrTiO_3$ was assumed. The calculated interfacial densities are $N_D(\mathrm{HRS}) \cdot a = 7.7 \cdot 10^{15}\,\mathrm{cm}^{-2}$ and $N_D(\mathrm{LRS}) \cdot a = 2.3 \cdot 10^{16}\,\mathrm{cm}^{-2}$. The spatial extension

of the vacancy rich/depleted regions a is unknown. However, due to the fact that only changes of the concentration are considered between LRS and HRS, a is less relevant and assumed constant. Overall, the two calculated concentrations differ by a factor $c = \frac{N_D(\mathrm{LRS})}{N_D(\mathrm{HRS})} = 2.98$. The value comes close to the measured charge carrier concentration ratio between LRS and HRS in chapter 7, which was determined from chemical PEEM analysis to be $c = 2.28$.

$$N_D \cdot a \approx \left(\frac{\Delta\Phi \cdot \epsilon_S}{q}\right)^2 \cdot 4 \cdot \pi \tag{8.7}$$

8.4.2. Real-time chemical characterization of G/STO devices

Operando XPEEM characterization was repeated for devices with a 'fixed potential' electrode configuration. In contrast to the devices used in the 'moving potential' configuration the Au and graphene regions are expected to remain close to the reference potential. Thus, the intensity modulations within the electrode area are expected to be more sensitive to chemical changes. The device under investigation was stably switched more than 40 times between 10 MΩ and 3 kΩ using a $-3\,V \rightarrow +4\,V$ pulse scheme, while being measured by operando XPEEM. The high OFF/ON ratio of ≈ 100 and the higher absolute values of the resistance as compared to the previous device are attributed to smaller driving currents of only 15 mA as compared to 35 mA in devices used for pulse characterization experiments. Going hand in hand with the change of the active electrode the measured I-V curves are inverted: SET is now observed for negative voltages, while RESET is observed for positive voltages.

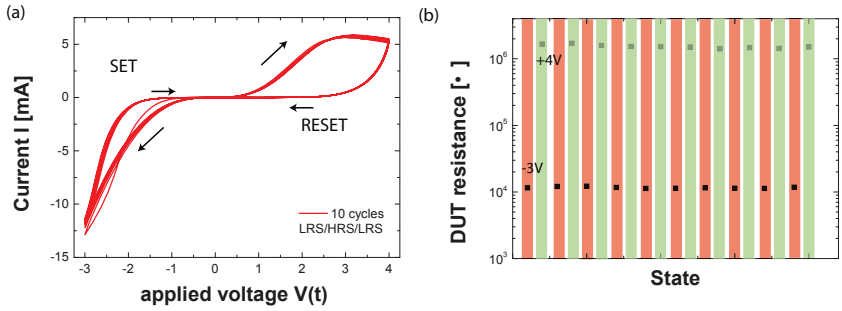

Figure 8.18. – (a) I-V characteristics of an Au/G/STO/Nb : STO device mounted in the microscope in 'fixed potential' configuration. The I-V was measured by the external Keithley 2611A source meter (b) READ measurements of the device resistance after each cycle. The resistance values were extracted at −0.2 V read out voltage.

Voltage recalculation from operando XPEEM in fixed potential configuration

The 'fixed potential' configuration is expected to be more sensitive to chemical changes within the top electrode region, because no additional potential within the electrode (Au/G) should be present. Contrary to the expectation, however, small but non-negligible contributions were also found for the graphene and Au lead regions. Hence, potential distribution maps were also calculated for this mode of operation.

A PEEM image of the device under investigation with contacted bottom electrode ('fixed potential') is shown in Fig. 8.19a. The corresponding 3D representation of the device is placed next to it. Unfortunately, the graphene electrode of the specific device was found to be inhomogeneous covering only 3/4 of the electrode area and leaving some parts of the active STO film uncovered. Snapshots of the calculated potential distribution maps within the device for different times during a LRS → HRS → LRS switching cycle are depicted in Fig. 8.19b (Steps 1-5: SET process, Steps 6-9: RESET process). As expected for the 'fixed potential' geometry strongest potential modulations are observed for the substrate region. Similar to the pulse characterization experiments, potential traces have been extracted from different regions of the sample, Fig. 8.20a. Subsequently the extracted profiles were plotted versus the externally applied voltage $V(t)$ and the measured current $I(t)$, Fig.

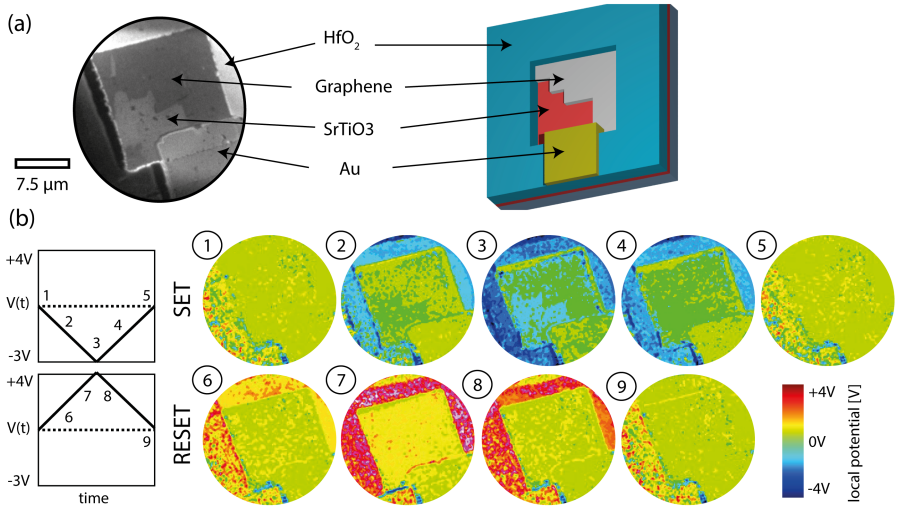

Figure 8.19. – (a) XPEEM image of a device acquired at Peak A of the O K-edge. Corresponding 3D device model (b) 2D local potential maps for operando SET and RESET recalculated from XPEEM data. Steps 1-5 show a SET process. Steps 6-9 show a RESET process. The corresponding externally applied voltages for t_1, t_2, t_3, t_4, t_5 are $V(t_n) = 0, -1.5, -3, -1.5, 0\,\mathrm{V}$ and $V(t_n) = 0, +1.5, +3.5, +3.3\,\mathrm{V}$ for t_6, t_7, t_8, t_9.

8.20b&c. Opposite to the 'moving potential' configuration, this time the Au lead follows the measured current (8.20b) whereas the HfO_2 covered substrate region reproduces the line shape of the externally applied voltage (Fig. 8.20c). Deviations for voltages above 3.5 V are artifacts from the voltage recalculation procedure: In this voltage range the work function maximum is almost reached and the function $I(E)$ becomes flat. The bijectivity of the function is lost and one intensity can be mapped back to multiple kinetic energies. Overall, all extracted potential profiles provide evidence for device operation in front of the PEEM.

While the strong modulations within the substrate region are expected and provide a good reference signal for the applied voltage, the changes in the graphene and Au lead region, on the other hand, are stronger than anticipated for the given mode of operation. In the ideal case **no** potential modulations would be expected allowing to detect the percentile chemical changes between LRS and HRS within the electrode region. However, the observed potential induced intensity modulations for the Au exceed 15 % and for the graphene region intensity modulations of more than 35 % are detected. This complicates the distinction between chemical and voltage induced effects.

The cause for the modulation within the Au lead can be found in the finite parasitic contact resistance of 33 Ω with respect to the Keithley/sample ground, which matches the values previously derived in the pulse characterization. Largest contributions to this resistance are expected from spring contacts and the thin bonding wire used to connect the devices. Again, it was found that graphene and Au lead are not on the same potential. With the same line of arguments as pursued in the previous section, it must be assumed that resistive switching is located underneath the Au electrode.

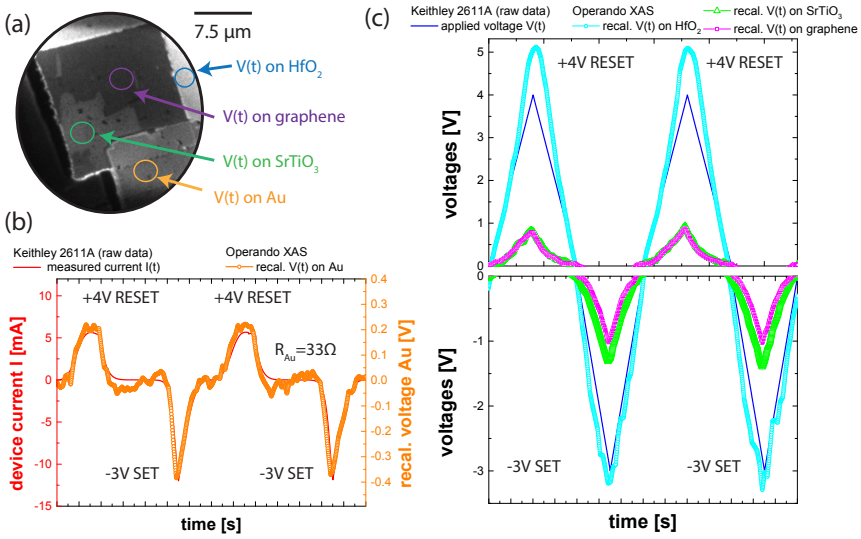

Figure 8.20. – (a) XPEEM image of device in 'fixed potential' mode. Voltage trace extraction points are indicated by color. (b) Local potential $V_{\mathrm{Au}}(t)$ at Au lead plotted vs. device current $I(t)$ measured by the Keithley. (c) Potential traces of marked regions plotted vs. externally applied voltage $V(t)$.

Due to the presence of this additional load resistance, the chemical mode cannot be used as intended and it is not possible to derive time-resolved chemical information. There is an indirect way to identify chemical changes from the calculated potential traces. The potential mapping algorithm translates intensity modulations into local potential shifts. It does not distinguish whether these intensity modulations arise from chemical or electronic changes and both signals get mixed up. When no voltage is applied any intensity signal **must** be attributed to chemical changes/and or static charging. Hence, hysteresis and reversible intensity offsets in the recalculated potential traces of graphene/$SrTiO_3$ regions around the zero crossings of the voltage can unveil the presence of chemical changes induce by vacancy formation. Oxygen vacancy accumulation is expected to cause a positive, oxygen depletion will cause a negative offset in the potential traces. Different zero voltage crossing points have been investigated, but no evidence for chemical changes was found, Fig. 8.21.

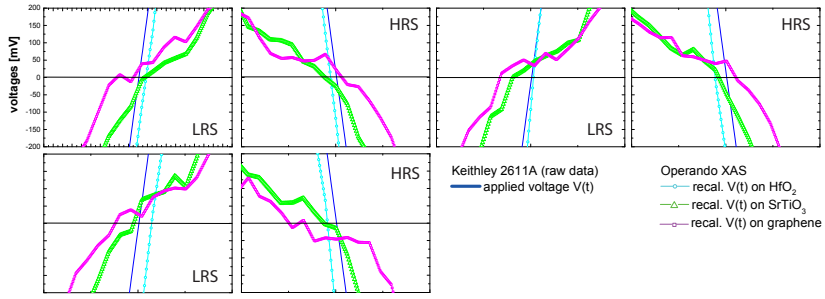

Figure 8.21. – Zoom of zero-voltage crossing points for different resistance states. Neither the potential traces of the graphene nor the potential traces of the $SrTiO_3$ region show reversible offset modifications.

Chemical Changes in static mode

The calculated potential distribution maps from the operando XPEEM experiments in both modes of operation, unambiguously prove device operation in front of the microscope. At the same time, the extracted potential profiles do not provide evidence for filament formation neither do they provide any evidence for chemical changes related to oxygen vacancy formation. To validate these findings, the same device was switched from HRS → LRS → HRS. For each of the resistance states, spatially resolved XAS spectra of the O K-edge and the Ti L-edge were acquired at zero applied bias. The full XAS stacks allow more detailed spatial and spectral analysis as compared to the low-resolution, low intensity operando experiments. They are identical to the in-situ experiments in Chapter 7. The main

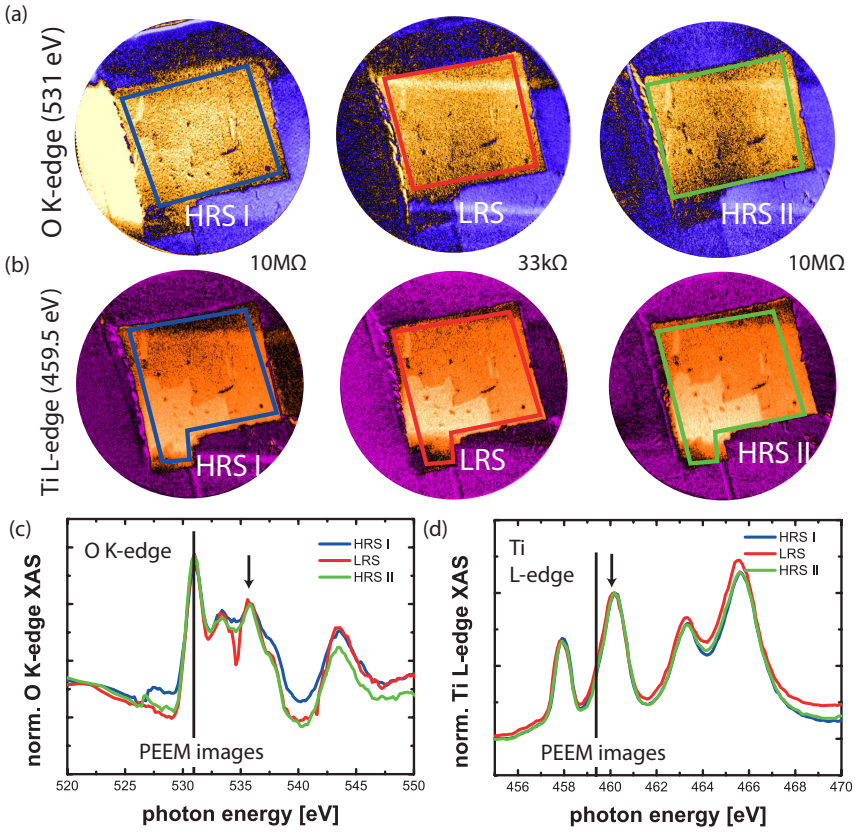

Figure 8.22. – (a) XPEEM images acquired at the main peak of the O K-XAS for the different device states. (b) XPEEM images acquired at a photon energy of 459.5 eV within Ti L-XAS for the different device states. The photon energy is sensitive to the formation Ti^{3+}. In none of the six images filamentary regions can be identified. (c) O K-XAS spectra for each state were extracted from the ROIs marked in the images. The XAS spectra are normalized as indicated. (d) The same procedure was repeated for Ti L-XAS.

findings of the experiments are summarized in Fig. 8.22. PEEM images acquired at photon energies previously identified to be most sensitive to chemical changes (O K:$h\nu$ = 531 eV, Ti L:$h\nu$ = 459.5 eV)

did not show any spatial modulations on the micron scale in between the HRS and LRS. As no filamentary region could be identified, XAS spectra were extracted for the full top electrode area. The normalized spectra show slight deviations, which are attributed to experimental artifacts, because none of these changes could be related to resistive switching.

Based on the findings it was concluded that switching filament is either too small to be detected or switching does not take place within the PEEM accessible region, but instead takes place underneath the Au/graphene overlay region.

8.4.3. Hard breakdown (HBD) experiments

Chemical and electric operando XPEEM characterization proved device operation during investigation. At the same time all methods fail to show any signatures of filamentary growth within the top electrode region. More specifically the observed experimental evidence points to a switching at the Au/STO interface underneath the Au lead. To verify whether the filament was just too small to be spatially resolved or whether the switching took place underneath the electrode, the focus of the experiments was shifted to so-called *hard breakdown* (HBD) experiments.

In this kind of experiments the current compliance was step-wise increased, allowing for thermal break down of the device. To enable higher driving currents, the SET voltage was increased from −3 V to −5 V. Larger device currents are expected to lead to higher temperatures within the filament, promoting oxygen diffusion and increasing the filament diameter. The first thermal breakdown is expected to occur near the original filament position and thus can be used as a tracer.

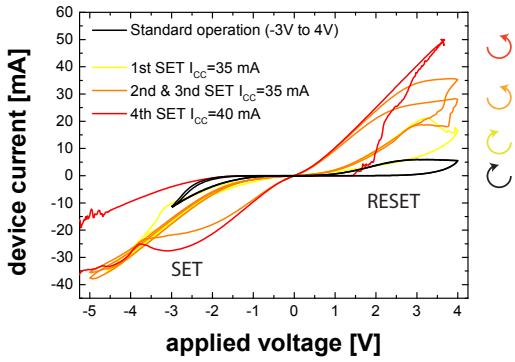

Figure 8.23 – Measured I-V characteristics of a device during hard break down. At high driving currents the sense of rotation changes from clockwise to counter clockwise. The abrupt switching observed for the last cycle (red) is characteristic for a fuse/anti-fuse process.

In the break down experiment strong modification of I-V profiles were observed, Fig. 8.23. While the device in standard operation shows LRS → HRS transition for positive voltages with a clockwise rotation, the sense of rotation changes to anticlockwise after the first cycle with increased compliance, now positive voltages induce a HRS → LRS transition. Finally, after a break down at a current compliance of 40 mA the transition becomes abrupt being indicative of fuse- and anti-fuse processes.

The full HBD experiment was simultaneously monitored by operando XPEEM. Fig. 8.24a shows the device evolution when being operated with high driving currents. The first two rows represent snapshots of two cycles at a current compliance of 35 mA. The third row shows electrode delamination observed for a current compliance of 40 mA.

A magnification of the Au electrode region, Fig. 8.24b, reveals irreversible crack or bubble formation at the gold surface (i-iv, red arrows). Further, a diffusion front moving away from the electrode becomes visible (iii, blue arrow), growing with each cycle. After the first cycle at 40 mA, a third bubble on the right side of the device appears (vi, red arrow), followed by a full, mechanical delamination or evaporation of the electrode (vii-viii) within less than 100 ms. The modifications in the characteristic I-V behavior go along with structural modifications of the electrode, which can for the first time be attributed to the specific state of the device.

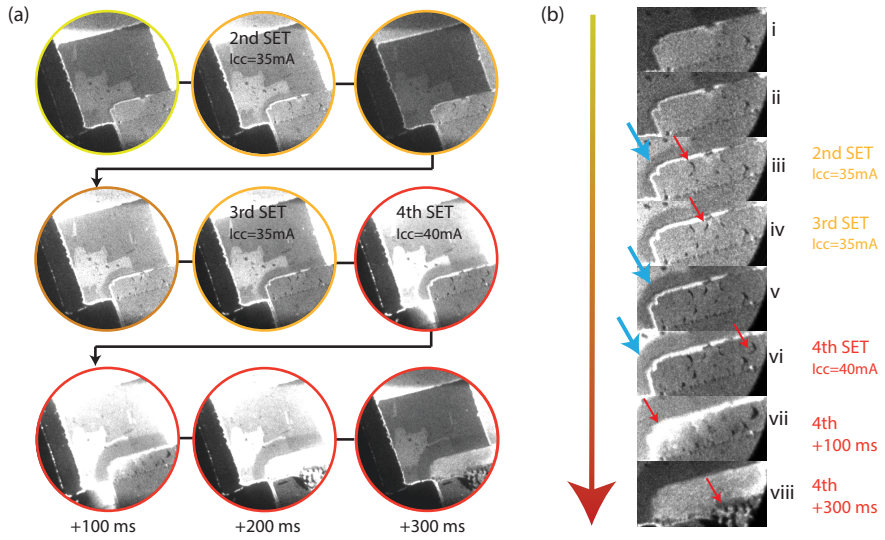

Figure 8.24. – (a) XPEEM images (peak A O-K edge) acquired at different times during a hard breakdown experiment. (b) Magnification of the electrode region. With increasing driving currents, cracks and bubbles in the electrode start to accumulate (iii-vi, red arrows) until electrode delamination is observed (vii-viii). Simultaneously with the bubble formation a growing diffusion front is observed (blue arrows).

Bubble formation at the top electrode

The increased local Joule heating - induced by the higher driving currents - increases the filament size and goes along with the excorporation of gaseous oxygen at the electrode. The process of oxygen excorporation at the anode is well documented for $Pt/SrTiO_3/Pt$ devices and covered by different articles in literature [24–26]. The molecular oxygen accumulates under the electrode and the pressure of the liberated oxygen mechanically deforms the electrode, which can be seen as bubble (shadow) formation in the PEEM images, Fig. 8.25a or for reference also for electrodes in literature, Fig. 8.25b.

Our believe is that during this process the filament is locally detached from the electrode and the initial filament becomes inactive. In the subsequent cycle a new filament is formed. Formation of the new filament takes place close to the old filament position, because the periphery of a filament is already oxygen deficient. In contrast to the first filament, the switching orientation in the surrounding is reversed as reported by Münstermann [16]. At the peak current of the second cycle, the freshly formed filament becomes detached again going along with the formation of a second bubble. With each cycle the process is repeated and the structural integrity of the electrode is weakened until finally total electrode delamination is observed, Fig. 8.24viii.

The observed bubble formation proceeds from left to right. The bubble size vary in size between 100 – 900 nm. The first bubble formation takes places at the left side marking the position of the initial filament. Subsequent filaments proceed to the right.

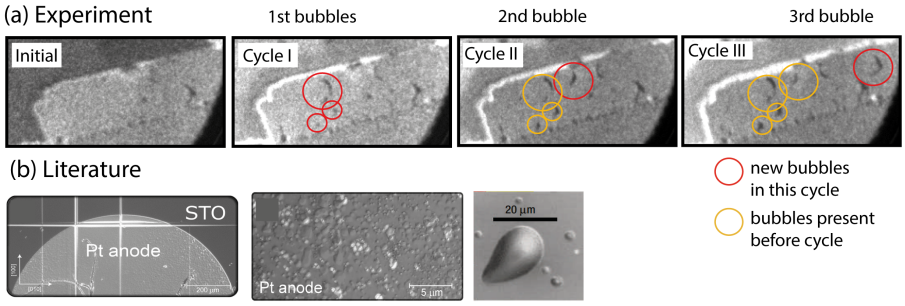

Figure 8.25. – (a) Bubble formation on the top electrode observed in operando PEEM. The bubble formation proceeds from the left to the right (b) Bubble formation reported on Pt anodes of STO MIM devices. First two images are adopted from [25]. Last image is adopted from [24].

Diffusion front formation and movement

In addition to the bubble formation, a diffusion front appears near the electrode after the second SET process at nominal $I_{CC} = 35\,\text{mA}$. The front is growing with each pulse the driving current is increased, Fig. 8.26a. The diffusion front is attributed to a depletion of oxygen near the electrode. The current induced temperature increase ΔT leads to an exponential mobility increase of oxygen atoms in the $SrTiO_3$ matrix, Sec. 2.2.1. The oxygen ions are then attracted towards the electrode due to chemical and potential gradients. At the electrode the oxygen is excorporated.

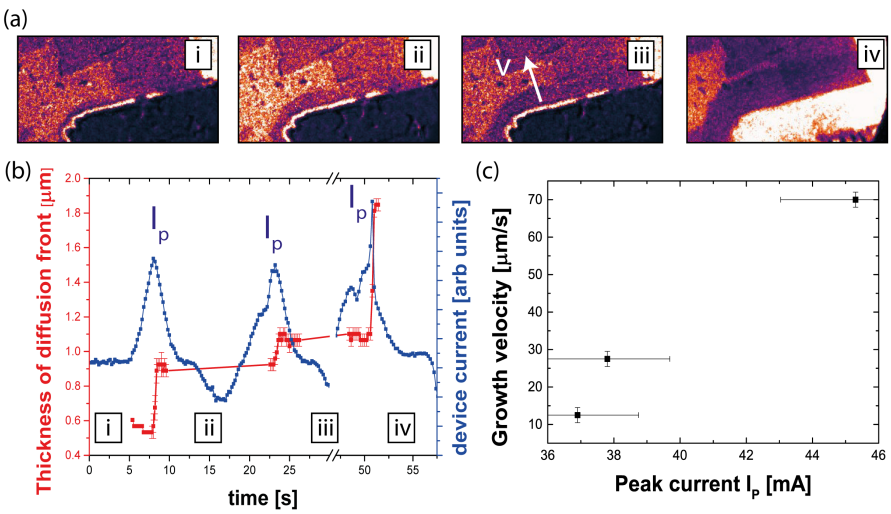

Figure 8.26. – Diffusion analysis: (a) XPEEM image series of the diffusion front evolution. The front appears as dark region near the Au electrode. (b) Temporal evolution of the diffusion front thickness $D(t)$ (red). Sharp steps are observed whenever a current maximum (blue) during the SET process is reached. (c) Growth velocity $v_\text{d} = \frac{\Delta D}{\Delta t}$ plotted versus the measured peak currents I_p.

The speed of the diffusion front growth v_d was measured form the acquired operando XPEEM movies by calculating the change of front thickness $\Delta D(t)$ with respect to time. It was found that significant front growth coincides with the measured peak currents. This observation supports the theory of current induced heating, because the dissipated power scales with $P \propto I^2$. The calculated velocity strongly depends on the peak current and ranges from $v_d \approx 12 - 70 \frac{\mu m}{s}$. Ti L- and O K-XAS spectra taken after delamination (not shown) support the idea of an oxygen depleted layer.

Model of the hard break down

Combining bubble and front formation, a model explaining the hard break down was derived based on operando XPEEM and Keithley data. It was assumed that each bubble corresponds to the location of a new filament. Consequently, the first filament was located to the left of the device. During the first SET process oxygen is excorporated from the thin film creating vacancy rich zones near the surface and detaching the initial filament from the electrode. The process is repeated in subsequent cycles. New filaments are formed until at a certain point in time the electrode is delaminated.

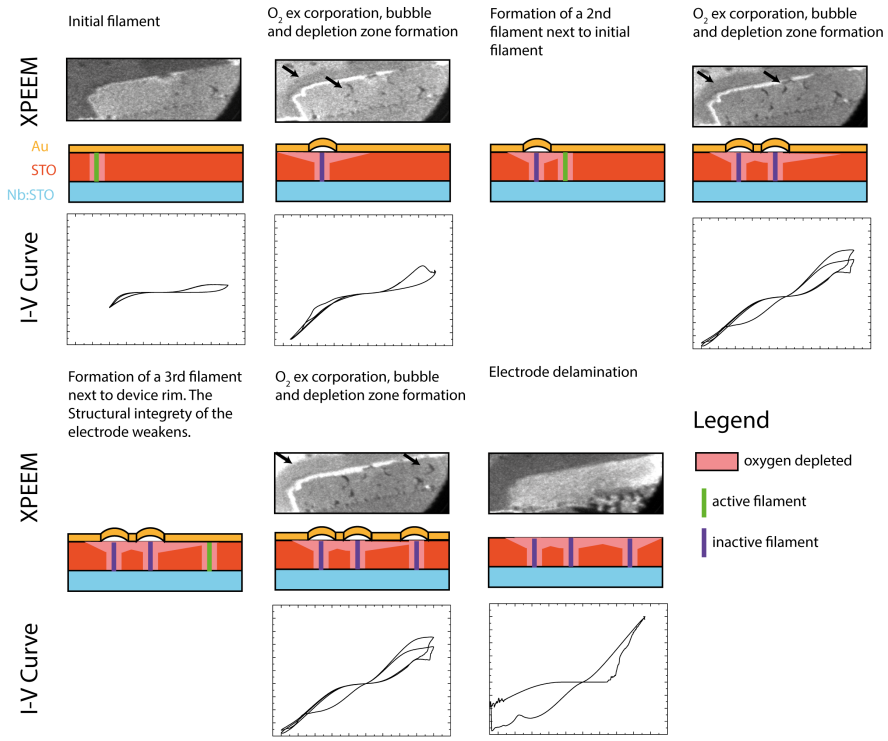

Figure 8.27. – Model of the hard break down based on microscopic and electronic observations. Each experimental situation from initial filament to delaminated electrode is represented by a schematic. Additionally, the corresponding I-V response for the system is shown for each state. The I-V characteristics changes from clockwise to anti-clockwise during the break down process. The change in the sense of rotation is attributed to a change of the switching mechanism.

8.4.4. Scanning electron microscopy (SEM) on post-mortem devices

All three types of operando XPEEM experiments unambiguously prove device operation during characterization in front of the microscope. Hence, technical issues can be excluded as reason for the fact that spatially confined chemical changes could not be observed during switching. The remaining explanations can be narrowed down to two aspects: (a) The filaments are too small to be spatially resolved by XPEEM or (b) the switching takes place underneath the Au electrode.

To shed light on this question, a batch of post-mortem (destroyed, non-functional) devices was characterized by high resolution scanning electron microscopy (SEM). SEM offers superior lateral resolution as compared to PEEM, but is less sensitive to chemical changes.

Fig. 8.28a shows a PEEM image of a device where no chemical changes could be observed during operando XPEEM characterization. The device was destroyed by a high voltage discharge in front of the microscope after characterization of multiple LRS → HRS → LRS cycles. Contrary to many other devices suffering the same fate, the device was not completely destroyed. Instead just the Au electrode was detached from the STO surface and bend upwards, thereby revealing the region underneath. Within the PEEM image Fig. 8.28a the electrode is still intact, while in the SEM image Fig. 8.28b the electrode is already delaminated.

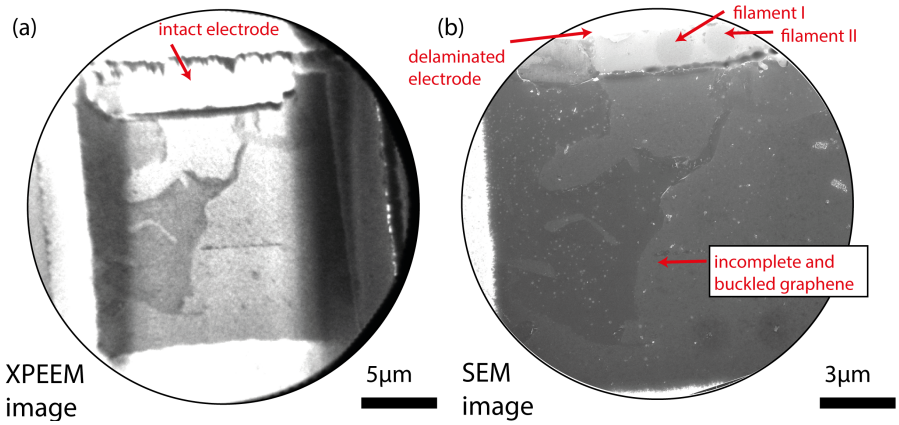

Figure 8.28. – (a) PEEM image of intact MIM device and (b) post-mortem low-magnification SEM image with delaminated electrode.

The Au covered electrode region, which was previously inaccessible for PEEM, shows two circular regions of approx. 1.6 μm in diameter in the SEM image. Further magnification of these features exhibits a substructure shown in Fig. 8.29.

The rim of the filamentary region is dominated by evenly space holes of ≈ 70 nm ('outer filaments'), while the center mainly consists of an agglomeration of holes with diameters below < 45 nm ('inner filaments'). Within the current understanding these holes are attributed to the switching filaments. The increased diameter of the outer filaments can be explained by the bubble formation process. It is assumed that filament starts forming in the center. With the increasing amount of excorporated

oxygen, more and more of the inner filaments are detached from the electrode. The driving current $I(t)$ is then distributed among less filaments leading to a significant increase of the current density $J = \frac{I}{A}$ per filament.

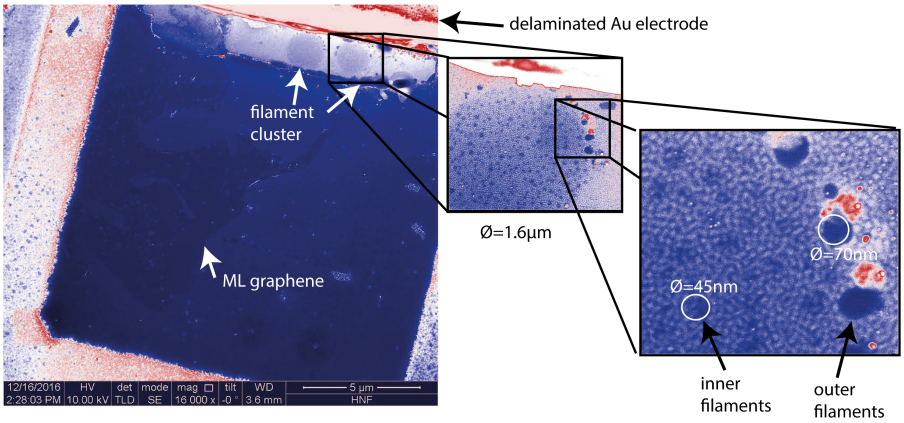

Figure 8.29. – Contrast enhanced SEM image showing a device with disconnected Au electrode. The graphene ML (dark) covers only parts of the device. Underneath the electrode two circular structures are visible. Magnification of these structures shows a further substructure in the nm regime.

The SEM observations are of great value as they are consistent with the previous PEEM measurements in four relevant points: (i) The recalculated potential distributions derived from the operando XPEEM electrical characterization prove device operation during the measurements, at the same time operando XPEEM chemical characterization fails to detect filamentary growth (Sec. 8.4.1 & Sec. 8.4.2). The discrepancy can be resolved by assuming that switching takes place underneath the Au lead. (ii) The size of the filamentary regions detected in SEM (1.6 μm) is in the same order as the filaments observed in the delaminated ($1-1.2\,\mu m$) and in-situ switched devices ($0.5-0.8\,\mu$m) in PEEM. (iii) The filamentary region shows a substructure below the spatial resolution of PEEM, which can explain the modification of the XAS line shape with start energy as was discussed in Sec. 5.4. (iv) Finally, the SEM images match the observations of the hard break down experiments, showing multiple filament clusters and evidence of bubble formation underneath the electrode before delamination.

8.5. Summary and discussion of findings

In this chapter a novel method for the XPEEM operando characterization was implemented into an existing PEEM instrument. For this purpose, two new sample holders were designed allowing to either electronically or chemically characterize a device during operation. In addition a new algorithm for the recalculation of two-dimensional, time-dependent local potential distribution maps from XPEEM data sets was developed. The developed method was then applied to graphene contacted memristive STO devices.

For the very first time the I-V traces of a device during operation could be mapped to specific chemical and electronic states of the device. The recalculated PEEM potentials distribution maps (PDM) provide solid evidence for device operation and switching during XPEEM investigations being in good agreement with the externally measured potential traces. Further, these maps provide the insight on the spatial distribution of the potentials during operation. It was found that graphene and Au never are on the same potential and switching preferably takes place underneath the Au electrode. The PDMs were used to extract the true voltage drop across the DUT, which is not identical to the applied voltage as typically parasitic resistances are present in each setup. We find that the SET process is rather abrupt happening at a threshold value around $1.5-2\,\mathrm{V}$. The extracted voltage profiles of the DUT were fitted to an idealized diode function. The potential barrier height of the $Pt/SrTiO_3$ Schottky contact was calculated to $\Phi_{B,LRS} = 0.839\,\mathrm{eV}$ for the LRS and $\Phi_{B,HRS} = 0.957\,\mathrm{eV}$ for the HRS. The vacancy concentrations of the LRS are about 2,5× larger as compared to the HRS. Absolute values could not be derived as the thickness of the accumulation layer remained unknown.

A second batch of STO devices was investigated with respect to chemically induced dynamics during operation by characterization in a 'fixed potential' geometry. In this geometry the electrode was kept on a fixed potential to avoid potential modulations. This way intensity changes within the top electrode region were expected to solely arise from vacancy formation. Unfortunately, potential modulations remained present also for this specific geometry. The reasons are unaccounted parasitic resistances of about $80\,\Omega$ in the setup leading to voltage divider effects. Despite the presence of potential modulation, the experiments were continued, but no chemical changes could be observed within the graphene region, neither for the Ti L- nor for the O K-edge. The absence of chemical features was verified by full spectral scans between two subsequent switching events. Again it was found that the Au lead and the graphene top electrode were on different potentials. The only viable explanation for the potential difference is that the graphene flake and the Au lead are not electrically connected and switching takes place underneath the Au/G overlap region.

The theory of filament formation underneath the Au lead was confirmed by a hard break down experiment. In this experiment the device was intentionally driven into thermal breakdown to expose the filament location. We find that in each break down event a new filament was formed. The formation of a filament was accompanied by the excorporation of oxygen and oxygen depletion of the filaments surrounding. Filament formation proceeds from one side to the other. After four cycles the top electrode was destabilized by cracks and bubbles and ripped apart. The I-V characteristics changes from clockwise to anti-clockwise during the break down process. The change in the sense of rotation is attributed to a change of the switching mechanism. While switching at low current compliance is driven by creation and annihilation of oxygen vacancies at the metal/STO interface, we

believe that the subsequent filaments form in regions where the switching is dominated by shifting already existing vacancies with respect to the electrode.

In the last section we used high resolution SEM on post-mortem devices. The devices investigated were devices characterized by operando PEEM for which we were not able to detect chemical changes in the electrode region and which got destroyed by high voltage arcing in front of the microscope. Within this study we found clear evidence for the formation of filament like structures within the Au/graphene overlap region. The changes were confined to regions with a diameter of about 1.6µm. Moreover, these filaments showed a filamentary substructure below the spatial resolution of a PEEM. These filaments with less than 45 nm in diameter may correspond to the nanosized islands we suspected in chapter 5.

CHAPTER 9

Summary & Future Perspectives

The results and findings of the present work can be summarized by three major milestones that were achieved on the way to a spatially and time-resolved photoemission experiment:

(i) **Identification of chemical fingerprints related to the ON/OFF states in the model system** $SrTiO_3$

(ii) **Design and fabrication of devices suitable for in-situ and operando characterization in PEEM**

(iii) **Implementation of an experimental setup for the operando XPEEM/XAS characterization of resistive switching devices during operation**

(i) Chemical fingerprints in $SrTiO_3$

First, chemical fingerprints for the formation/depletion of oxygen vacancies were identified in reduced $SrTiO_3$ single crystals. The reliable tracers and quantifiers for oxygen vacancy concentrations were found to be the XAS spectral line shapes of the O K- and Ti L- absorption edges. XAS characterization with spatial resolution (PEEM) was repeated for ex-situ switched and UHV delaminated, non-functional devices to identify a contrast between ON (LRS) and OFF (HRS) device states. For LRS devices filamentary regions with $0.5-1.5\,\mu m$ in diameter showing increased vacancy concentrations were found. Similar regions could not be identified for HRS states. It was further determined that the filamentary regions are not homogenous. Instead they consist of many nanoscale islands/filaments, which are below the current resolution limit of PEEM.

(ii) Devices for in-situ and operando studies

For the in-situ and operando characterization of functional devices, the "top electrode surface sensitivity dilemma" needed to be solved first. In functional devices, the chemical signal stemming from the active layer is damped by the top electrode. Three different approaches to reduce the signal damping were identified: (i) lateral device geometries, where d virtually becomes zero and the active region can be directly accessed, (ii) a change from soft X-ray to hard X-ray excitation in order to increase the effective attenuation length (HAXPEEM) and (iii) the use of ultra-thin top electrodes.

After thorough analysis it has been found out that only ultra-thin graphene contacted devices in absorption mode provide the signal intensities as well as chemical and spatial contrast required for operando experiments.

The novel graphene contacted devices were switched between LRS and HRS in-situ in a PEEM microscope. XAS measurements were performed before and after each switching event. For about 20% of the investigated devices similar chemical and spatial fingerprints as the ones observed in delaminated devices have been found. Within a confined filamentary region of about $0{,}5-1\,\mu$m, changes in the occupation of the hybridized Ti 3d-O 2p states at the O K-edge were identified. For the investigated switching cycles the recognized filament position remained unaltered. By comparing the measured spectral changes to an annealed single crystal "calibration" sample, oxygen vacancy concentrations of $4.5\pm0.5\%$ for the LRS and of $2\pm0.5\%$ for the HRS were estimated. According to these results the charge carrier density in the conduction band is modulated from $1.5\times10^{21}\,\mathrm{cm}^{-3}$ in the LRS to about $6.7\times10^{20}\,\mathrm{cm}^{-3}$ in the HRS. For the first time the experimentally measured chemical state could directly be related to the corresponding I-V history of the device.

(iii) Real-time operando characterization

For the real-time operando characterization, an ELEMITEC LEEM/PEEM was technically modified to supply an external voltage to a device in front of the microscope. The novel setup was successfully tested on the graphene contacted $SrTiO_3$ thin film devices. Two different modes of operation were used in the characterization: A *voltage mode* being sensitive to the potential distributions in the working devices and a *chemical mode* being sensitive to the anticipated chemical changes. Multiple SET and RESET switching processes were monitored by spatially resolved XPEEM during operation of the device with a temporal resolution of 300 ms and a spatial resolution on the sub-micrometer scale. A MATLAB algorithm, which we developed, was used to recalculate local potential maps from experimental XAS data and to extract time-dependent potential traces from different regions of a working device. The results of the potential analysis unambiguously proved device operation and were used to recalculate the change in Schottky barrier height between LRS and HRS. We found a change of barrier height from 0.86 eV in LRS to 0.96 eV in HRS being in good agreement with the previously derived vacancy concentrations. Despite of the acquired potential traces we weren't able to directly observe the evolution of filaments. The absence of chemical changes within the graphene top electrode in combination with the specific potential distribution in the device provided solid evidence for filament formation under the Au/graphene interface, inaccessible by PEEM. Filament formation under the electrode was further confirmed by hard break down experiments and post-mortem SEM characterization.

Overall, we found evidence that resistive switching in $SrTiO_3$ is indeed driven by nanoscale redox processes as described in the valence change model. Chemically altered regions with diameters of $0.5-1.6\,\mu$m could be detected. The extracted oxygen vacancy concentrations from these regions match the expected values from Schottky barrier modulations induced by vacancy accumulation and depletion at the interface. We find that for small switching currents ($<10\,$mA) the filament position stays constant whereas filament positions in hard break down experiments were changing. This work establishes the technical capability to combine spatial, temporal, chemical and electronic information in a single experiment.

Future Perspectives / Next steps

Based on our observations we determined three key challenges that need to be faced in future experiments in order to obtain the dynamics of vacancy formation and depletion from PEEM data. I would like to briefly outline these challenges in the following and address possible solutions.

(i) **Control of the filament position**

(ii) **Improvements in the chemical contrast, and**

(iii) **Extension of the experiments towards the micro- and nanosecond time domain**

(i) Controlling the filament position

Our operando and in-situ experiments showed that filament growth preferably takes place under the Au/graphene contact being promoted by local heating of the Au lead and the electric field distribution in the film. This finding explains why 80% of the devices investigated in our in-situ experiments did not show filamentary regions. It further matches the potential distributions observed in the four devices investigated during our operando studies. Consequently, filament control is one of the key challenges to be addressed. We intent to avoid filament formation underneath the Au/G interface by using a structured bottom electrode, Fig. 9.1.

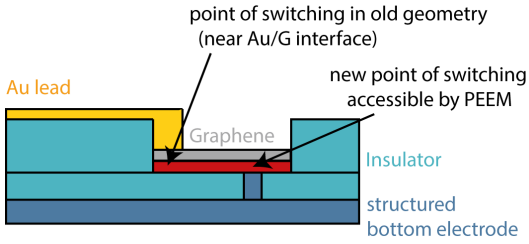

Figure 9.1 – Controlling the filament position by structuring the bottom electrode. Filament formation is expected to shift from the Au/G interface towards the point contact of the BE lying within an PEEM accessible region.

(ii) Improving the chemical contrast and signal strength

A second key challenge for time-resolved PEEM studies on resistive switching materials is to enhance the weak, percentile chemical contrast between LRS and HRS induced during resistive switching. At present the contrast is too faint to be measured with high confidence and interferes with the intensity modulations induced by local potential variations. Further the changes in $SrTiO_3$ are confined to sub-micron regions lowering the detectable signal. One possible option would be an extension of the experiments to other oxide materials, in which switching is expected to take place over the entire electrode region. Moreover, employing magnetic oxides, where the metal valence state is coupled to a specific magnetic configuration, provides additional contrast mechanisms, such as the X-ray magnetic circular dichroism (XMCD). Specifically, the experiments could be extended to LMSO ($La_{1-x}Sr_xMnO_3$) based systems which fulfills both of the aforementioned criteria. First unpublished experiments successfully demonstrate resistive switching in LSMO thin films, while at the same time providing reasonable contrast.

(iii) Switching dynamics on nanosecond timescales

Given that chemical changes induced by the switching process can unambiguously be identified within the developed real-time approach, the next plausible step would be to extend the experiments to shorter time scales. Fastest switching times are expected to reach down to nanosecond timescales. This is far below the achievable time resolution of 300 ms in the real-time XPEEM described in the present work. In order to monitor these ultra-fast changes a pump-probe technique with a temporal resolution of a few picoseconds has to be employed instead.

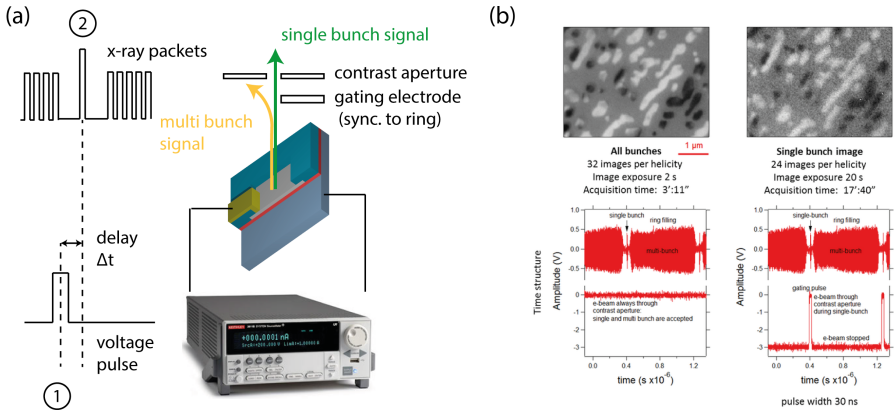

Figure 9.2. – (a) Time-resolved XPEEM using a pump-probe approach combined with a detector gating mechanism. (1) The DUT is electrically excited by an voltage pulse. (2) With a defined delay of Δt the PE intensity is probed by the single bunch (SB) of a multi-bunch X-ray pulse train. A gating electrode in the microscope is used to block out the incoming multi-bunch signal and only the single bunch signal can pass. (b) Proof-of-concept of the detector gating mechanism at the NanoSpectroscopy beam line demonstrated on magnetic domains in magnetite islands on Re(0001). Image (b) is taken and modified from [100].

Principally, the modified setup at the NanoSpectroscopy beamline already provides the essential basics for the implementation of a pump-probe experiment. The Keithley 2611A can be operated in a pulsing mode. The rise time is in the order of 75 µs and the minimum pulse width is 300 µs [101]. A detector gating scheme for time-resolved XAS (tr-XAS) was implemented in the setup by Locatelli and co-workes, Fig. 9.2a. In a proof-of-concept experiment the feasibility of the tr-XAS was demonstrated on magnetic domains in magnetite islands on Re(0001). The acquisition time for the usually very bright XAS signals for the gated SB mode increases by a factor of 432 as compared to the standard, multi-bunch operation mode, Fig. 9.2b, stressing the need for a good chemical contrast.

Based on these observations Locatelli et al. approximate acquisition times of 1h per single image for a FoV of 4 µm [100]. This equals to the accumulation of more than 60 million SB detection events [102], each corresponding to a full LRS → HRS → LRS cycle. Therefor the acquisition of a single data point in time requires more than 60 million times of switching with identical switching behavior for all cycles. Any deviation in the switching location, the strength of the chemical change or the initial and final resistance will affect the overall result. The prototypical ultra-thin top electrode devices used in the present work have had an endurance of only several thousand cycles under ambient conditions ($G/SrTiO_3 \approx 10^3 - 10^4, I_{SET} \approx 35 - 60\,mA$). Based on our experimental knowledge,

the lifetime of the device is further decreased to a few ten cycles under the reducing conditions of a PEEM experiment, e.g. UHV and X-ray illumination.

Endurance values of resistive switching oxide devices collected from several publications vary over twelve orders in magnitude, from single switching events up to several billion cycles. In two outstanding cases, namely (i) mixed TaO_x/TiO_x hetero structure devices with Ta top electrode of 100 nm thickness (Ref. [103]) and (ii) Ta_2O_{5-x}/TaO_{2-x} mixed interface structures with Pt electrodes of roughly 30 nm thickness (Ref. [96]), an endurance of more than 10^{12} cycles could be demonstrated. We attribute the high endurance of these devices to the thick top electrodes, which act as oxygen reservoirs being in constant exchange with the active material [104]. In contrast, in thin electrodes the oxygen is excorporated from the device into the vacuum and completely removed from the system. Accordingly, oxygen back filling from a reservoir into the active region is prevented.

An important step towards a successful pump-probe experiment on resistive switching materials lies within achieving a "high" ($> 10^8$ cycles) endurance for systems with the ultra-thin electrodes. Once realized, we are confident that filament evolution and growth in resistive switching materials can be monitored by PEEM.

APPENDIX A

Supplementary Information

A.1. Experimental verification of the UHV delamination process

The succes of the UHV delamination process was verfied by work function scans of the freshly delaminated surface in threshold photoemission. Examples of partially successfull delamination are shown in Fig. 1.1. The PEEM images in panel (a) show a FoV of ≈ 60 µm containing an array of nine devices for two different electron kinetic energies. Recognizably, the central device and the two devices at the bottom right show a different contrast than remaining six.

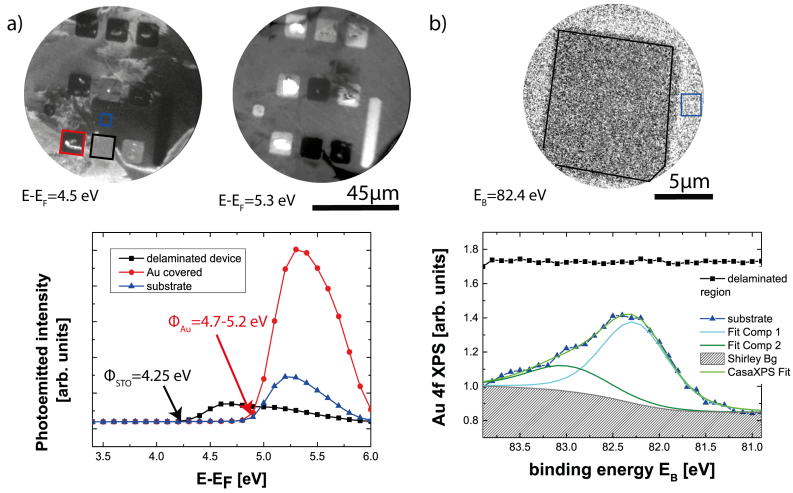

Figure 1.1. – Verification of the delamination process by PEEM & XPEEM (a) PEEM images at two different kinetic energies showing a set of nine devices. Devices with potentially removed Au electrode show a lower work function (black) than devices with remaing Au on top (red). (b) Au 4f 7/2 XPS of a delaminated device: The central pad region is gold free.

Secondary emission spectra have been extracted for both types of devices and the substrate. The devices marked by the black region starts emitting at about $\Phi_{black} = E - E_F = 4.2\,eV$, the device marked in red and the substrate start at about $\Phi_{red} = E - E_F = 4.8\,eV$. The measured work function values Φ_{black},Φ_{red} are close to the tabulated work functions of $SrTiO_3$ ($\Phi_{STO} = 4.26\,eV$ [105]) and Au ($\Phi_{Au} = 4.8 - 5.2\,eV$), hence, the contrast is attributed to a material contrast between delaminated and non-delaminated devices. The black device is delaminated, while the red device is still covered. To verify this assumption, a spatially resolved Au $4f_{7/2}$ XPS scan of a delaminated device, Fig. 1.1b, was performed to exclude other potential influences, like modifications of the surface potential or the surface morphology. The Au $4f_{7/2}$ XPS signal within the delaminated pad region remains flat proofing the absence of a gold electrode and validating the assumption. The XPS signal of the surrounding on the other hand shows a pronounced Au $4f_{7/2}$ peak, which indicates the existence of a remaining gold film on top of the substrate.

A statistical analysis of multiple device arrays according to the work function contrast reveals that the delamination process is successfull in less than 50% of the investigated devices.

A.2. Specifications of instruments and beamlines

	NanoESCA	**NanoSpectroscopy**	**BESSY UE56-1 SGM**	**PETRA III P 09**
location	ELETTRA, Trieste, Italy	ELETTRA, Trieste, Italy	BESSY, Berlin, Germany	DESY, Hamburg, Germany
beam line specifications				
type	soft x-ray		soft x-ray	hard x-ray
ring current	200 mA @ 2.0 GeV		300 mA @ 1.7 GeV	100 mA @ 6 GeV
photon energy range $h\nu$	5 – 1000 eV		55 – 1500 eV	2700 – 24.000
resolving power $\frac{E}{\Delta E}$	4000		> 10000	> 6000
photon flux $[\frac{Photons}{s}]$	$10^{11} - 10^{13}$		$2 \cdot 10^{13}$	10^{13}@ 10keV
polarization	linear (horizontal, vertical), elliptical		linear (horizontal, vertical), elliptical	linear (horizontal, vertical), elliptical
spot size source (width×height)	562 μm × 73 μm		40 μm × 40 μm	142 μm × 5 μm
spot size sample (width×height)	7 μm × 2 μm		15 μm × 30 μm	500 μm × 100 μm
spectromicroscope specifications				
type/ manufacturer	SPELEEM III, Elmitec GmbH	NanoESCA, Focus GmbH	P90 AC LEEM/PEEM, Specs GmbH	NanoESCA (HAXPEEM), Focus GmbH
imaging techniques	LEEM, PEEM, XAS, KPEEM, XPEEM	PEEM, XAS, KPEEM, XPEEM	LEEM, PEEM, XAS	PEEM, XAS, KPEEM, XPEEM
lenses	magnetic	electrostatic	magnetic	electrostatic
analyzer energy resolution ΔE	300-600 meV	50-200 meV	-	400-800 meV
lateral resolution	10 nm (LEEM), 20-30 nm (XPEEM), 40-50 nm (XAS)	50 nm (PEEM), 150 nm (XPEEM), 150 nm (XAS)	2 nm (LEEM), 20 nm (PEEM), 30 nm (XAS)	100 nm (PEEM), 150 nm (XPEEM), 150 nm (XAS)
base pressure	7.0×10^{-11} mBar	$< 1.0 \times 10^{-10}$ mBar	$< 4.0 \times 10^{-10}$ mBar	$\approx 2 \times 10^{-9}$ mBar
reference	[106, 107]	[60, 108]		[55, 108]

Table A.1. – Specifications of beam lines and end stations used in the framework of this thesis.

A.3. Specifications of the HV surge protection implementation

The negative output ($V_{\mathrm{OUT},-}$) of the SMU in Fig. 8.5 is connected to sample potential V_{SPL} and serves as reference for the imaging process (blue). The programmable voltage of the Keithley $\Delta V(t)$ is referenced to the sample potential and is provided at the positive output ($V_{\mathrm{OUT},+}$) of the SMU (green). The sample voltage V_{SPL} is controlled by the PEEM software. It can be adjusted between $0-1.5\,\mathrm{keV}$ and is part of energy filtering process. In XAS mode V_{SPL} is in the order of 1-20V.

$$V_{\mathrm{OUT},-} = V_{HV} + V_{SPL} \tag{A.1a}$$
$$V_{\mathrm{OUT},+} = V_{HV} + V_{SPL} + \Delta V(t) \tag{A.1b}$$

To avoid permanent damage to the SMU the surge protection has to guarantee that the voltage drop between the two outputs ($|V_{\mathrm{OUT},-} - V_{\mathrm{OUT},+}|$) and the voltage drop between the negative output and Keithley chassy ($|V_{\mathrm{OUT},-} - V_{\mathrm{HV}}|$), never exceeds 200V. According to Eq. A.1a and Eq. A.1b these constraints can be rewritten to

$$|\Delta V(t)| < 200\,\mathrm{V} \tag{A.2a}$$
$$\wedge\, |\Delta V_{\mathrm{SPL}}| < 200\,\mathrm{V} \tag{A.2b}$$

In case of a high voltage discharge between objective and sample, microsecond over voltages spikes ($\delta t \approx \mu s$) with spike currents of several kA are expected to appear on either one of the outputs. Therefor ultra-fast suppressor diodes (1,5KE82C, ns response time) in anti-serial arrangement between the leads short the inputs as soon as $|\Delta V(t)|$ or $|V_{\mathrm{SPL}}|$ exceed the defined threshold value of 82 V. Pulses with amplitudes above 82 V are discharged into the rack. For long lasting and high load pulses an additional gas discharge fuse (Littlefuse CG90, treshold @ 90V) is mounted, which has a slow response time, but can drain high loads without thermal destruction. Further a RC filter element consisting of a $R = 10\,\Omega$ resistor and an $C = 100\,\mathrm{nF}$ capacitor delays the voltage rise time at the power supply inputs according to it's RC time constant $\tau = R \cdot C = 1\,\mu s$ and ensures that the threshold value at the fuses is reached before the pulse peak reaches the SMU outputs.

For resistive switching applications the RC component in the filter box can alter the operation parameters of the device under test (DUT), because the resistor is placed in series with the DUT and both elements together act as a voltage divider. Further the capacitance is placed parallel to the DUT, which can reduce the voltage drop over the device for high frequency applications. The impedance of the combined system is given by Eq. A.3, where C and R are the corresponding values for the filter box components and R_{DUT} is the device resistance.

$$Z = \left(\frac{1}{R_{DUT}} + \omega C\right)^{-1} + R \tag{A.3}$$

Employing Eq. A.3 the values of the RC components ($R = 10\,\Omega$ and $C = 100\,\mathrm{nF}$) were optimized for low frequency excitation ($f < 1\,\mathrm{kHz}$) and for devices with LRS and HRS values between $100\,\Omega$ and $1\,\mathrm{M}\Omega$. Figure 1.2 shows the calculated voltage drop at the device U_{DUT} in percent of the applied external voltage U for different frequency components. For DC to 5kHz excitation the the voltage drop across the DUT varies between 90% (LRS) and 99% (HRS) of the applied voltage U. For frequencies

above 100 kHz the device voltage is reduced to less than 30% implying that for HF applications and pump-probe techniques, either the pulse parameters or the protection have to be adjusted accordingly.

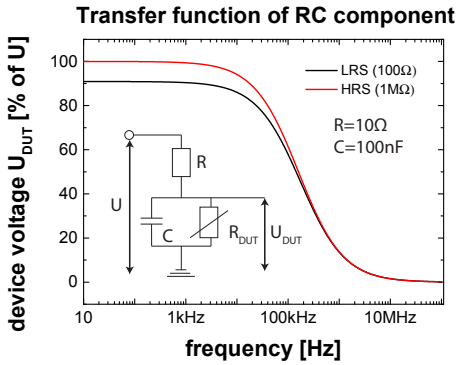

Figure 1.2 – Frequency dependent voltage drop at the device under test modified by the RC component of the surge protection. The plot shows the device voltage in percent of the applied voltage. For frequencies from DC to 5kHz the signal remains mostly unaffected. For frequencies above 10kHz the high pass behavior of the capacitor sets in.

A.4. Detailed description of the voltage recalculation procedure in XPEEM

The working principle of voltage recalculation using XPEEM is illustrated in Fig. 1.3. The top left graph (red curve) shows the temporal evolution of the relative photoemission intensity $I(t)$ at point P(x,y) normalized to t=0 during the application of an external voltage pulse V(t) (triangular,0 V; −1 V; 0 V; 1 V; 0 V). The top right graph (blue curve) shows the relative photoemission intensity $I(E)$ of the secondary edge at the same point P(x,y) normalized to the start voltage (STV). For each timestep t the relative change in intensity ΔI is mapped to the shift in energy ΔE necessary to faciliate the same relative intensity change. **Example:** At $t_1 = 10\,\mathrm{s}$ a relative intensity change of $\Delta I_1 \approx 30\%$ is observed. To achieve the same change in intensity by increasing/decreasing the kinetic energy, the spectrum must be shifted by $\Delta E_1 \approx 700\,\mathrm{meV}$ towards lower kinetic energies. According to $\Delta V_{\mathrm{calc}}(t_1) = -\frac{\Delta E_1}{e}$ the local potential at time t_1 is $\Delta V_{\mathrm{calc}}(t_1) \approx -700\,\mathrm{meV}$. The recalculated voltage $V_{\mathrm{calc}}(t)$ reproduces the externally applied and measured voltage $V(t)$ (red curve, bottom panel) fairly well. The recalculated values do not match the applied voltage exactly and show an polartity dependend asymmetry. Note, however, that these deviations are neither an experimental artefact nor caused by the recalculation routine. It turns out that calculated signal represents the real potential drop at the device lowered by voltage drops occuring at the feed lines and the bonding contact.

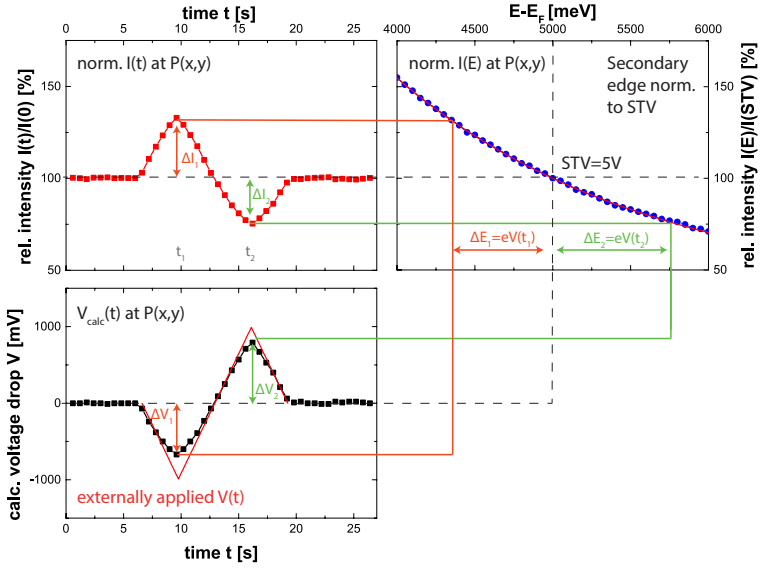

Figure 1.3. – Graphic representation of the voltage calculation procedure: The top left graph shows the temporal evolution of the relative photoemission intensity I(t) at point P(x,y) normalized to t=0 (red). The top right graph shows the relative photoemission intensity I(E) of the secondary edge at point P(x,y) normalized to the start voltage (STV) (raw data: blue, double exponential fit: red). By mapping the relative intensity change ΔI to the change in kinetic energy ΔE in the I(E) spectrum, which is necessary to achieve the same relative change in intensity, the local potential $\Delta V = -\frac{\Delta E}{e}$ (black) can be calculated for each time step t.

Nomenclature

E_B binding energy

E_{kin} electron kinetic energy

$h\nu$ photon energy

AC alternating current

AEY auger electron yield

ANN artificial neural networks

BE bottom electrode

CB conduction band

CF crystal field

CIP current in-plane

DC direct current

DOS Density of states

DUT device under test

EF-PEEM energy filtered PEEM

EUV extreme ultra violet

FoV Field of View

HAXPES hard X-ray photoelectron emission spectroscopy

HV high voltage

IMFP inelastic mean free path

JDOS joint density of states

MCP multi channel plate

MIEC Mixed ion-electron conductor

MPD mean probing depth

PCM phase change material

PDM potential distribution map

PEEM Photoemission electron microscopy

PLD pulsed laser deposition

ReRAM resistance random access memory

ROI region of interest

RSM resistive switching material

SBH Shottky barrier height

SEM scanning electron microscopy

SEY secondary electron yield

SNR Signal to Noise Ratio

STO strontium titanate (SrTiO3)

SXR soft X-ray

TE top electrode

TEY total electron yield

TM transition metal

TMO transition metal oxides

tr-PEEM time-resolved Photoemission electron microscopy

UPS ultra violet photoelectron spectroscopy

VB valence band

VCM valence change model

WF work function

XAS X-ray absorption spectroscopy

XPS X-ray photoelectron spectroscopy

Bibliography

[1] C. Bäumer, C. Schmitz, A. Marchewka, D. N. Mueller, R. Valenta, J. Hackl, N. Raab, S. P. Rogers, M. I. Khan, S. Nemsak, M. Shim, S. Menzel, C. M. Schneider, R. Waser, and R. Dittmann. Quantifying redox-induced Schottky barrier variations in memristive devices via in operando spectromicroscopy with graphene electrodes. *Nature Communications*, 7:12398, 2016. DOI: 10.1038/ncomms12398.

[2] F.-F. Li. How we are teaching computers to understand pictures. TED Talks, 2015. www.ted.com.

[3] R. Rashid. Microsoft Research shows a promising new breakthrough in speech translation technology. Tianjin and China at Microsoft Research Asia's 21st Century Computing, 2012. www.blogs.microsoft.com/next/2012/11/08/.

[4] P. A. Merolla, J. V. Arthur, R. Alvarez-Icaza, A. S. Cassidy, J. Sawada, F. Akopyan, B. L. Jackson, N. Imam, C. Guo, Y. Nakamura, B. Brezzo, I. Vo, S. K. Esser, R. Appuswamy, B. Taba, A. Amir, M. D. Flickner, W. P. Risk, R. Manohar, and D. S. Modha. A million spiking-neuron integrated circuit with a scalable communication network and interface. *Science*, 345(6197):668–673, 2014. DOI: 10.1126/science.1254642.

[5] Y. Long, E. M. Jung, J. Kung, and S. Mukhopadhyay. ReRAM Crossbar based Recurrent Neural Network for human activity detection. *2016 International Joint Conference on Neural Networks (IJCNN)*, pages 939–946, 2016. DOI: 10.1109/IJCNN.2016.7727299.

[6] A. Sawa. Resistive switching in transition metal oxides. *Materials Today*, 11(6):28–36, 2008. DOI: 10.1016/S1369-7021(08)70119-6.

[7] F. Pan, C. Chen, Z.-s. Wang, Y.-c. Yang, and F. Zeng. Nonvolatile resistive switching memories-characteristics, mechanisms and challenges. *Progress in Natural Science: Materials International*, 20:1–15, 2010. DOI: 10.1016/S1002-0071(12)60001-X.

[8] D. Ielmini and R. Waser. *Resistive switching: From fundamentals of nanoionic redox processes to memristive device applications*. Wiley-VCH, 2016. ISBN: 978-3-527-33417-9.

[9] D. B. Strukov and H. Kohlstedt. Resistive switching phenomena in thin films: Materials, devices, and applications. *MRS Bulletin*, 37(02):108–114, 2012. DOI: 10.1557/mrs.2012.2.

[10] J. J. Yang, D. B. Strukov, and D. R. Stewart. Memristive devices for computing. *Nature Nanotechnology*, 8(1):13–24, 2012. DOI: 10.1038/NNANO.2012.240.

[11] R. Waser and M. Aono. Nanoionics-based resistive switching memories. *Nature Materials*, 6(11):833–840, 2007. DOI: 10.1038/nmat2023.

[12] T. W. Hickmott. Low-Frequency Negative Resistance in Thin Anodic Oxide Films. *Journal of Applied Physics*, 33(9):2669, 1962. DOI: 10.1063/1.1702530.

[13] R. Waser and M. Wuttig. *IFF Spring School: Memristive Phenomena - from fundamental physics to neuromorphic computing*, Volume 47. Forschungszentrum Jülich, Zentralbibliothek, Jülich, 2016. ISBN: 978-3-95806-091-3.

[14] M. Wuttig and N. Yamada. Phase-change materials for rewriteable data storage. *Nature Materials*, 6(11):824–832, 2007. DOI: 10.1038/nmat2009.

[15] M. Kubicek, R. Schmitt, F. Messerschmitt, and Rupp, Jennifer L. M. Uncovering Two Competing Switching Mechanisms for Epitaxial and Ultrathin Strontium Titanate-Based Resistive Switching Bits. *ACS Nano*, 9(11):10737–10748, 2015. DOI: 10.1021/acsnano.5b02752.

[16] R. Münstermann, T. Menke, R. Dittmann, and R. Waser. Coexistence of Filamentary and Homogeneous Resistive Switching in Fe-Doped SrTiO3 Thin-Film Memristive Devices. *Advanced Materials*, 22(43):4819–4822, 2010. DOI: 10.1002/adma.201001872.

[17] R. Waser, R. Dittmann, G. Staikov, and K. Szot. Redox-Based Resistive Switching Memories - Nanoionic Mechanisms, Prospects, and Challenges. *Advanced Materials*, 21(25-26):2632–2663, 2009. DOI: 10.1002/adma.200900375.

[18] C. Lenser, A. Köhl, I. Slipukhina, H. Du, M. Patt, V. Feyer, C. M. Schneider, M. Lezaic, R. Waser, and R. Dittmann. Formation and Movement of Cationic Defects During Forming and Resistive Switching in SrTiO 3 Thin Film Devices. *Advanced Functional Materials*, 2015. DOI: 10.1002/adfm.201500851.

[19] S. Menzel. *Modeling and Simulation of Resistive Switching Devices*. PhD thesis, RWTH Aachen, Aachen, 2012.

[20] A. Marchewka, R. Waser, and S. Menzel. Physical simulation of dynamic resistive switching in metal oxides using a Schottky contact barrier model. pages 297–300. DOI: 10.1109/SISPAD.2015.7292318.

[21] A. Marchewka, D. Cooper, C. Lenser, S. Menzel, H. Du, R. Dittmann, R. E. Dunin-Borkowski, and R. Waser. Determination of the electrostatic potential distribution in Pt/Fe:SrTiO3/Nb:SrTiO3 thin-film structures by electron holography. *Scientific Reports*, 4:6975, 2014. DOI: 10.1038/srep06975.

[22] F. A. Kröger and H. J. Vink. Relations between the Concentrations of Imperfections in Crystalline Solids. *Solid State Physics*, 3:307–435, 1956. DOI: 10.1016/S0081-1947(08)60135-6.

[23] A. Köhl. *Micro-spectroscopic investigation of valence change processes in resistive switching SrTiO3 thin films*, Volume 39. Forschungszentrum Jülich, Zentralbibliothek, Jülich, 2014. ISBN: 978-3-89336988-1.

[24] K. Szot, W. Speier, G. Bihlmayer, and R. Waser. Switching the electrical resistance of individual dislocations in single-crystalline SrTiO3. *Nature Materials*, 5(4):312–320, 2006. DOI: 10.1038/nmat1614.

[25] M. Wojtyniak, K. Szot, R. Wrzalik, C. Rodenbücher, G. Roth, and R. Waser. Electro-degradation and resistive switching of Fe-doped SrTiO3 single crystal. *Journal of Applied Physics*, 113(8):083713, 2013. DOI: 10.1063/1.4793632.

[26] D. S. Jeong, H. Schröder, U. Breuer, and R. Waser. Characteristic electroforming behavior in Pt/TiO2/Pt resistive switching cells depending on atmosphere. *Journal of Applied Physics*, 104(12):123716, 2008. DOI: 10.1063/1.3043879.

[27] C. Bäumer, C. Schmitz, Ramadan, Amr H. H., H. Du, K. Skaja, V. Feyer, P. Müller, B. Arndt, C.-L. Jia, J. Mayer, De Souza, Roger A., C. Michael Schneider, R. Waser, and R. Dittmann. Spectromicroscopic insights for rational design of redox-based memristive devices. *Nature Communications*, 6:8610, 2015. DOI: 10.1038/ncomms9610.

[28] V. Havel. *Transient processes in resistive switching memory devices at ultimate time scale down to sub-nanosecond range*. Dr. Hut, 1. edition, 2016. ISBN: 978-3-8439-2597-6.

[29] E. H. Rhoderick. *Metal-semiconductor contacts*. Monographs in electrical and electronic engineering. Clarendon Press, Oxford, 1978. ISBN: 0198593651.

[30] S. M. Sze and K. K. Ng. *Physics of semiconductor devices*. Wiley-Interscience, Hoboken and N.J, 3rd edition, 2007. ISBN: 0-471-14323-5.

[31] R. Waser. *Nanoelectronics and information technology: Advanced electronic materials and novel devices*. Wiley-VCH, Weinheim, 3rd completely rev. and enlarged edition, 2012. ISBN: 978-3-527-40927-3.

[32] A. Spinelli, M. A. Torija, C. Liu, C. Jan, and C. Leighton. Electronic transport in doped SrTiO3: Conduction mechanisms and potential applications. *Physical Review B*, 81(15), 2010. DOI: 10.1103/PhysRevB.81.155110.

[33] H. Wei, L. Beuermann, J. Helmbold, G. Borchardt, V. Kempter, G. Lilienkamp, and W. Maus-Friedrichs. Study of SrO segregation on SrTiO3(100) surfaces. *Journal of the European Ceramic Society*, 21(10-11):1677–1680, 2001. DOI: 10.1016/S0955-2219(01)00091-7.

[34] S. Piskunov, E. Heifets, R. Eglitis, and G. Borstel. Bulk properties and electronic structure of SrTiO3, BaTiO3, PbTiO3 perovskites: an ab initio HF/DFT study. *Computational Materials Science*, 29(2):165–178, 2004. DOI: 10.1016/j.commatsci.2003.08.036.

[35] H. Ibach and H. Lüth. *Festkörperphysik*. Springer, Berlin and Heidelberg, 2009. ISBN: 978-3-540-85795-2.

[36] W. Luo, W. Duan, S. G. Louie, and M. L. Cohen. Structural and electronic properties of n-doped and p-doped SrTiO3. *Physical Review B*, 70(21), 2004. DOI: 10.1103/PhysRevB.70.214109.

[37] C. J. Ballhausen. *Introduction to Ligand Field Theory*. McGraw-Hill Book Company, Inc, New York, 1962. ISBN: 978-0-07-003580-6.

[38] M. Abbate, F. d. Groot, J. Fuggle, A. Fujimori, Y. Tokura, Y. Fujishima, O. Strebel, M. Domke, G. Kaindl, J. van Elp, B. Thole, G. Sawatzky, M. Sacchi, and N. Tsuda. Soft X-ray absorption studies of the location of extra charges induced by substitution in controlled-valence materials. *Physical Review B*, 44(11):5419–5422, 1991. DOI: 10.1103/PhysRevB.44.5419.

[39] Groot, F. M. d., J. C. Fuggle, B. T. Thole, and G. A. Sawatzky. 2p X-ray absorption of 3d transition-metal compounds: An atomic multiplet description including the crystal field. *Physical Review B*, 42(9):5459–5468, 1990. DOI: 10.1103/PhysRevB.42.5459.

[40] Groot, F. M. d., J. C. Fuggle, B. T. Thole, and G. A. Sawatzky. L2,3 X-ray absorption edges of d0 compounds: K+ , Ca2+ , Sc3+ , and Ti4+ in Oh (octahedral) symmetry. *Physical Review B*, 41(2):928–937, 1990. DOI: 10.1103/PhysRevB.41.928.

[41] S. Sugano, Y. Tanabe, and H. Kamimura. *Multiplets of transition-metal ions in crystals*, Volume 33. Acad. Pr, New York, 1970. ISBN: 978-0-12-431675-1.

[42] E. Stavitski and Groot, Frank M. d. The CTM4XAS program for EELS and XAS spectral shape analysis of transition metal L-edges. *Micron*, 41(7):687–694, 2010. DOI: 10.1016/j.micron.2010.06.005.

[43] Groot, F. M. d., J. C. Fuggle, B. T. Thole, and G. A. Sawatzky. L2,3 X-ray absorption edges of d0 compounds: K+ , Ca2+ , Sc3+ , and Ti4+ in Oh (octahedral) symmetry. *Physical Review B*, 41(2):928–937, 1990. DOI: 10.1103/PhysRevB.41.928.

[44] H. Ikeno, Groot, F. M. d., E. Stavitski, and I. Tanaka. Multiplet calculations of L 2,3 X-ray absorption near-edge structures for 3d transition-metal compounds. *Journal of Physics: Condensed Matter*, 21(10):104208, 2009. DOI: 10.1088/0953-8984/21/10/104208.

[45] Groot, F. M. d., M. O. Figueiredo, M. J. Basto, M. Abbate, H. Petersen, and J. C. Fuggle. 2p X-ray absorption of titanium in minerals. *Physics and Chemistry of Minerals*, 19(3):140–147, 1992. DOI: 10.1007/BF00202101.

[46] H. Hertz. Über einen Einfluss des ultravioletten Lichtes auf die elektrische Entladung. *Annalen der Physik und Chemie*, 267(8):983–1000, 1887. DOI: 10.1002/andp.18872670827.

[47] A. Einstein. Über einen die Erzeugung und Verwandlung des Lichtes betreffenden heuristischen Gesichtspunkt. *Annalen der Physik*, 322(6):132–148, 1905. DOI: 10.1002/andp.19053220607.

[48] Nobel prize commitee. Nobelprize Laureates, 1921. www.nobelprize.org.

[49] Nobel prize commitee. Nobel prize Laureates, 1981. www.nobelprize.org.

[50] S. Hüfner. *Photoelectron spectroscopy: Principles and applications*, Volume 82. Springer-Verlag, Berlin and New York, 1995. ISBN: 3-540-19108-9.

[51] J. B. Pendry. Theory of photoemission. *Surface Science*, 57(2):679–705, 1976. DOI: 10.1016/0039-6028(76)90355-1.

[52] J.-J. Yeh. *Atomic calculation of photoionization cross-sections and asymmetry parameters*. Gordon & Breach Science, Publishers, Langhorne and PA, 1993. ISBN: 2-88124-585-4.

[53] Groot, Frank M. d. and A. Kotani. *Core level spectroscopy of solids*. CRC Press, Boca Raton, 2008. ISBN: 978-0-8493-9071-5.

[54] M. P. Seah and W. A. Dench. Quantitative electron spectroscopy of surfaces: A standard data base for electron inelastic mean free paths in solids. *Surface and Interface Analysis*, 1(1):2–11, 1979. DOI: 10.1002/sia.740010103.

[55] M. Patt, C. Wiemann, N. Weber, M. Escher, A. Gloskovskii, W. Drube, M. Merkel, and C. M. Schneider. Bulk sensitive hard X-ray photoemission electron microscopy. *Review of Scientific Instruments*, 85(11):113704, 2014. DOI: 10.1063/1.4902141.

[56] S. Tanuma, C. J. Powell, and D. R. Penn. Calculations of electron inelastic mean free paths. IX. Data for 41 elemental solids over the 50 eV to 30 keV range. *Surface and Interface Analysis*, 43(3):689–713, 2011. DOI: 10.1002/sia.3522.

[57] C. Powell, A. Jablonski, I. Tilinin, S. Tanuma, and D. Penn. Surface sensitivity of Auger-electron spectroscopy and X-ray photoelectron spectroscopy. *Journal of Electron Spectroscopy and Related Phenomena*, 98-99:1–15, 1999. DOI: 10.1016/S0368-2048(98)00271-0.

[58] National Institute for Standards and Technology. NIST X-ray Photoelectron Spectroscopy Database, Version 4.1. Gaithersburg, 2012.

[59] J. C. Woicik. *Hard X-ray Photoelectron Spectroscopy (HAXPES)*, Volume 59. Springer, Cham, 2016. ISBN: 978-3-319-24043-5.

[60] C. Wiemann, M. Patt, I. P. Krug, N. B. Weber, M. Escher, M. Merkel, and C. M. Schneider. A New Nanospectroscopy Tool with Synchrotron Radiation: NanoESCA@Elettra. *e-Journal of Surface Science and Nanotechnology*, 9:395–399, 2011. DOI: 10.1380/ejssnt.2011.395.

[61] M. Patt. *Bulk and surface sensitive energy-filtered photoemission microscopy using synchrotron radiation for the study of resistive switching memories*. Jülich, 2016. ISBN: 978-3-95806-130-9.

[62] Elettra. Nanospectroscopy beamline description, 10.04.2014.

[63] D. A. Muller, N. Nakagawa, A. Ohtomo, J. L. Grazul, and H. Y. Hwang. Atomic-scale imaging of nanoengineered oxygen vacancy profiles in SrTiO3. *Nature*, 430(7000):657–661, 2004. DOI: 10.1038/nature02756.

[64] C. Lenser, A. Köhl, M. Patt, C. M. Schneider, R. Waser, and R. Dittmann. Band alignment at memristive metal-oxide interfaces investigated by hard X-ray photoemission spectroscopy. *Physical Review B*, 90(11), 2014. DOI: 10.1103/PhysRevB.90.115312.

[65] M. Lavayssière, M. Escher, O. Renault, D. Mariolle, and N. Barrett. Electrical and physical topography in energy-filtered photoelectron emission microscopy of two-dimensional silicon pn junctions. *Journal of Electron Spectroscopy and Related Phenomena*, 186:30–38, 2013. DOI: 10.1016/j.elspec.2013.01.014.

[66] L. Dudy, M. Sing, P. Scheiderer, J. D. Denlinger, P. Schütz, J. Gabel, M. Buchwald, C. Schlueter, T.-L. Lee, and R. Claessen. In Situ Control of Separate Electronic Phases on SrTiO 3 Surfaces by Oxygen Dosing. *Advanced Materials*, 2016. DOI: 10.1002/adma.201600046.

[67] M. Abbate, J. B. Goedkoop, Groot, F. M. d., M. Grioni, J. C. Fuggle, S. Hofmann, H. Petersen, and M. Sacchi. Probing depth of soft X-ray absorption spectroscopy measured in total-electron-yield mode. *Surface and Interface Analysis*, 18(1):65–69, 1992. DOI: 10.1002/sia.740180111.

[68] Schröder, Sven L. M. Towards a 'universal curve' for total electron-yield XAS. *Solid State Communications*, 98(5):405–409, 1996. DOI: 10.1016/0038-1098(96)00035-X.

[69] B. H. Frazer, B. Gilbert, B. R. Sonderegger, and G. d. Stasio. The probing depth of total electron yield in the sub-keV range: TEY-XAS and X-PEEM. *Surface Science*, 537(1-3):161–167, 2003. DOI: 10.1016/S0039-6028(03)00613-7.

[70] W. Drube. Photoelectron spectroscopy with hard X-rays. *Nuclear Instruments and Methods in Physics Research Section A: Accelerators, Spectrometers, Detectors and Associated Equipment*, 547(1):87–97, 2005. DOI: 10.1016/j.nima.2005.05.015.

[71] T. Bertaud, M. Sowinska, D. Walczyk, S. Thiess, A. Gloskovskii, C. Walczyk, and T. Schroeder. In-operando and non-destructive analysis of the resistive switching in the Ti/HfO2/TiN-based system by hard X-ray photoelectron spectroscopy. *Applied Physics Letters*, 101(14):143501, 2012. DOI: 10.1063/1.4756897.

[72] M. Sowinska, T. Bertaud, D. Walczyk, S. Thiess, M. A. Schubert, M. Lukosius, W. Drube, C. Walczyk, and T. Schroeder. Hard X-ray photoelectron spectroscopy study of the electroforming in Ti/HfO2-based resistive switching structures. *Applied Physics Letters*, 100(23):233509, 2012. DOI: 10.1063/1.4728118.

[73] S. Stille, C. Lenser, R. Dittmann, A. Koehl, I. Krug, R. Muenstermann, J. Perlich, C. M. Schneider, U. Klemradt, and R. Waser. Detection of filament formation in forming-free resistive switching SrTiO3 devices with Ti top electrodes. *Applied Physics Letters*, 100(22):223503, 2012. DOI: 10.1063/1.4724108.

[74] P. H. Scofield. Lawrence Livermore Laboratory Report UCRL-51326. 1973. DOI:.

[75] A. Jablonski and J. Zemek. Overlayer thickness determination by XPS using the multiline approach. *Surface and Interface Analysis*, 41(3):193–204, 2009. DOI: 10.1002/sia.3005.

[76] O. Kerrec, D. Devilliers, H. Groult, and P. Marcus. Study of dry and electrogenerated Ta2O5 and Ta/Ta2O5/Pt structures by XPS. *Materials Science and Engineering: B*, 55(1-2):134–142, 1998. DOI: 10.1016/S0921-5107(98)00177-9.

[77] Deutsches Elektron Synchrotron. Beamline specification P09. www.photon-science.desy.de.

[78] A. Locatelli, T. O. Menteş, M. Á. Niño, and E. Bauer. Image blur and energy broadening effects in XPEEM. *Ultramicroscopy*, 111(8):1447–1454, 2011. DOI: 10.1016/j.ultramic.2010.12.020.

[79] L.-P. Oloff, M. Oura, K. Rossnagel, A. Chainani, M. Matsunami, R. Eguchi, T. Kiss, Y. Nakatani, T. Yamaguchi, J. Miyawaki, M. Taguchi, K. Yamagami, T. Togashi, T. Katayama, K. Ogawa, M. Yabashi, and T. Ishikawa. Time-resolved HAXPES at SACLA: probe and pump pulse-induced space-charge effects. *New Journal of Physics*, 16(12):123045, 2014. DOI: 10.1088/1367-2630/16/12/123045.

[80] B. Gilbert, R. Andres, P. Perfetti, G. Margaritondo, G. Rempfer, and G. d. Stasio. Charging phenomena in PEEM imaging and spectroscopy. *Ultramicroscopy*, 83(1-2):129–139, 2000. DOI: 10.1016/S0304-3991(99)00196-5.

[81] H. Y. Peng, L. Pu, J. C. Wu, D. Cha, J. H. Hong, W. N. Lin, Y. Y. Li, J. F. Ding, A. David, K. Li, and T. Wu. Effects of electrode material and configuration on the characteristics of planar resistive switching devices. *APL Materials*, 1(5):052106, 2013. DOI: 10.1063/1.4827597.

[82] M. Janousch, G. I. Meijer, U. Staub, B. Delley, S. F. Karg, and B. P. Andreasson. Role of Oxygen Vacancies in Cr-Doped SrTiO3 for Resistance-Change Memory. *Advanced Materials*, 19(17):2232–2235, 2007. DOI: 10.1002/adma.200602915.

[83] B. P. Andreasson. *Oxygen vacancies in SrTiO3: An X-ray absorption study*. PhD thesis, ETH Zürich, Zürich, 2009.

[84] S. Menzel, M. Waters, A. Marchewka, U. Böttger, R. Dittmann, and R. Waser. Origin of the Ultra-nonlinear Switching Kinetics in Oxide-Based Resistive Switches. *Advanced Functional Materials*, 21(23):4487–4492, 2011. DOI: 10.1002/adfm.201101117.

[85] S. M. Song, J. K. Park, O. J. Sul, and B. J. Cho. Determination of Work Function of Graphene under a Metal Electrode and Its Role in Contact Resistance. *Nano Letters*, 12(8):3887–3892, 2012. DOI: 10.1021/nl300266p.

[86] B. L. Henke, E. M. Gullikson, and J. C. Davis. X-Ray Interactions: Photoabsorption, Scattering, Transmission, and Reflection at E = 50-30,000 eV, Z = 1-92. *Atomic Data and Nuclear Data Tables*, 54(2):181–342, 1993. DOI: 10.1006/adnd.1993.1013.

[87] X. Li, W. Cai, J. An, S. Kim, J. Nah, D. Yang, R. Piner, A. Velamakanni, I. Jung, E. Tutuc, S. K. Banerjee, L. Colombo, and R. S. Ruoff. Large-Area Synthesis of High-Quality and Uniform Graphene Films on Copper Foils. *Science*, 324(5932):1312–1314, 2009. DOI: 10.1126/science.1171245.

[88] C. Bäumer, S. P. Rogers, R. Xu, L. W. Martin, and M. Shim. Tunable Carrier Type and Density in Graphene/PbZr 0.2 Ti 0.8 O 3 Hybrid Structures through Ferroelectric Switching. *Nano Letters*, page 130322144812009, 2013. DOI: 10.1021/nl4002052.

[89] C. Bäumer. *Spectroscopic characterization of local valence change processes in resistively switching complex oxides*. PhD thesis, RWTH Aachen, Aachen, 2016.

[90] R. Valenta. *Resistive switching devices with ultrathin electrodes for spectroscopic investigations*. PhD thesis, RWTH Aachen, Aachen, 2016.

[91] B. H. Frazer, B. Gilbert, B. R. Sonderegger, and G. d. Stasio. The probing depth of total electron yield in the sub-keV range: TEY-XAS and X-PEEM. *Surface Science*, 537(1-3):161–167, 2003. DOI: 10.1016/S0039-6028(03)00613-7.

[92] C. Weiland, A. K. Rumaiz, P. Pianetta, and J. C. Woicik. Recent applications of hard x-ray photoelectron spectroscopy. *Journal of Vacuum Science & Technology A: Vacuum, Surfaces, and Films*, 34(3):030801, 2016. DOI: 10.1116/1.4946046.

[93] A. Locatelli, A. Bianco, D. Cocco, S. Cherifi, S. Heun, M. Marsi, M. Pasqualetto, and E. Bauer. High lateral resolution spectroscopic imaging of surfaces: The undulator beamline "nanospectroscopy" at Elettra. *Journal de Physique IV (Proceedings)*, 104:99–102, 2003. DOI: 10.1051/jp4:200300038.

[94] A. M. Kaiser, C. Schöppner, F. M. Römer, C. Hassel, C. Wiemann, S. Cramm, F. Nickel, P. Grychtol, C. Tieg, J. Lindner, and C. M. Schneider. Nano and picosecond magnetization dynamics of weakly coupled CoFe/Cr/NiFe trilayers studied by a multitechnique approach. *Physical Review B*, 84(13), 2011. DOI: 10.1103/PhysRevB.84.134406.

[95] K. Fleck, C. La Torre, N. Aslam, S. Hoffmann-Eifert, U. Böttger, and S. Menzel. Uniting Gradual and Abrupt Set Processes in Resistive Switching Oxides. *Physical Review Applied*, 6(6), 2016. DOI: 10.1103/PhysRevApplied.6.064015.

[96] M.-J. Lee, C. B. Lee, D. Lee, S. R. Lee, M. Chang, J. H. Hur, Y.-B. Kim, C.-J. Kim, D. H. Seo, S. Seo, U.-I. Chung, I.-K. Yoo, and K. Kim. A fast, high-endurance and scalable non-volatile memory device made from asymmetric Ta2O(5−x)/TaO(2−x) bilayer structures. *Nature Materials*, 10(8):625–630, 2011. DOI: 10.1038/nmat3070.

[97] J. Kautz, J. Jobst, C. Sorger, R. M. Tromp, H. B. Weber, and van der Molen, S. J. Low-Energy Electron Potentiometry: Contactless Imaging of Charge Transport on the Nanoscale. *Scientific Reports*, 5:13604, 2015. DOI: 10.1038/srep13604.

[98] Christoph Bäumer. *Spectroscopic characterization of local valence change processes in resistively switching complex oxides*. PhD thesis, RWTH Aachen, Aachen, 2016.

[99] K. G. Rana, V. Khikhlovskyi, and T. Banerjee. Electrical transport across Au/Nb:SrTiO3 Schottky interface with different Nb doping. *Applied Physics Letters*, 100(21):213502, 2012. DOI: 10.1063/1.4720516.

[100] A. Locatelli, T. O. Mentes, M. Lucian, E. Bauer, S. Pizzini, J. Vogel, P. Pittana, R. Sergo, G. Cautero, A. Carniel, and S. Bassanese. Detector Gating for Time Resolved Measurements. Trieste and Italy, 2012.

[101] Keithley Company. Series 2600 System SourceMeter: User's Manual, 2006.

[102] Elettra Synchrotron. Elettra Parameters, 2015.

[103] C.-W. Hsu, I.-T. Wang, C.-L. Lo, M.-C. Chiang, W.-Y. Jang, C.-H. Lin, and T.-H. Hou. *2013 Symposium on VLSI Technology: Digest of technical papers : 2013 VLSI Technology Symposium, Kyoto*. IEEE and ICS Convention Design, Inc., Piscataway(NJ) and Tokyo, 2013. ISBN: 978-1-4673-5226-0.

[104] W. Kim, S. Menzel, D. J. Wouters, Y. Guo, J. Robertson, B. Rösgen, R. Waser, and V. Rana. Impact of oxygen exchange reaction at the ohmic interface in Ta2O5-based ReRAM devices. *Nanoscale*, 2016. DOI: 10.1039/c6nr03810g.

[105] L. F. Zagonel, M. Bäurer, A. Bailly, O. Renault, M. Hoffmann, S.-J. Shih, D. Cockayne, and N. Barrett. Orientation-dependent work function of in situ annealed strontium titanate. *Journal of Physics: Condensed Matter*, 21(31):314013, 2009. DOI: 10.1088/0953-8984/21/31/314013.

[106] T. O. Menteş, G. Zamborlini, A. Sala, and A. Locatelli. Cathode lens spectromicroscopy: methodology and applications. *Beilstein Journal of Nanotechnology*, 5:1873–1886, 2014. DOI: 10.3762/bjnano.5.198.

[107] A. Locatelli, L. Aballe, T. O. Mentes, M. Kiskinova, and E. Bauer. Photoemission electron microscopy with chemical sensitivity: SPELEEM methods and applications. *Surface and Interface Analysis*, 38(12-13):1554–1557, 2006. DOI: 10.1002/sia.2424.

[108] M. Escher, K. Winkler, O. Renault, and N. Barrett. Applications of high lateral and energy resolution imaging XPS with a double hemispherical analyser based spectromicroscope. *Journal of Electron Spectroscopy and Related Phenomena*, 178-179:303–316, 2010. DOI: 10.1016/j.elspec.2009.06.001.

List of Publications

Accepted Publications

- **Christoph Schmitz**, Daniel Wilson, Denis Rudolf, Carsten Wiemann, Lukasz Plucinski, Sally Riess, Martin Schuck, Hilde Hardtdegen, Claus M. Schneider, F. Stefan Tautz, and Larissa Juschkin, *"Compact extreme ultraviolet source for laboratory-based photoemission spectromicroscopy"*, Applied Physics Letters (APL), Cover Story June 2016, DOI:10.1063/1.4953071

- Christoph Bäumer, **Christoph Schmitz**, Amr H. H. Ramadan, Hongchu Du, Katharina Skaja, Vitaliy Feyer, Philipp Müller, Benedikt Arndt, Chun-Lin Jia, Joachim Mayer, Roger A. De Souza, Claus Michael Schneider, Rainer Waser & Regina Dittmann, *"Spectromicroscopic insights for rational design of redox-based memristive devices"*, Nature Communications 6, 2015, DOI:10.1038/ncomms9610

- Christoph Bäumer, **Christoph Schmitz**, Astrid Marchewka, David N. Mueller, Richard Valenta, Johanna Hackl, Nicolas Raab, Steven P. Rogers, M. Imtiaz Khan, Slavomir Nemsak, Moonsub Shim, Stephan Menzel, Claus M. Schneider, Rainer Waser and Regina Dittmann, *"Quantifying redox-induced Schottky barrier variations in memristive devices via in-operando spectroscopy with electron-transparent graphene electrodes"*, Nature Communications 7, 2016, DOI: 10.1038/ncomms12398

- Christoph Bäumer, Nicolas Raab, Tobias Menke, **Christoph Schmitz**, Roland Rosezin, Philipp Michael Müller, Michael Andrä, Vitaliy Feyer, Rainer Bruchhaus, Felix Gunkel, Claus M. Schneider, Rainer Waser and Regina Dittmann, *"Verification of redox-processes as switching and retention failure mechanisms in Nb:SrTiO"*, RSC nanoscale, 2016, DOI:10.1039/C6NR00824K

- Katharina Skaja, Christoph Bäumer, Oliver Peters, Stephan Menzel, Marco Moors, Hongchu Du, Manuel Bornhöfft, **Christoph Schmitz**, Vitaliy Feyer, Chun-Lin Jia, Claus Michael Schneider, Joachim Mayer, Rainer Waser, Regina Dittmann, *"Avalanche discharge induced electrical forming in tantalum oxide based metalinsulator-metal structures"*, Advanced Functional Materials, 2015, DOI: 10.1002/adfm.201502767

Pending Publications

- CHRISTOPH BÄUMER**,** RICHARD VALENTA, **CHRISTOPH SCHMITZ**, ANDREA LOCATELLI, TEVFIK ONUR MENTES, STEVEN P. ROGERS, ALESSANDRO SALA, NICOLAS RAAB, SLAVOMIR NEMSAK, MOONSUB SHIM, CLAUS M. SCHNEIDER, STEPHAN MENZEL, RAINER WASER AND REGINA DITTMANN, *"Subfilamentary networks cause cycle-to-cycle variability in memristive devices"*, under review in ACS Nano

Talks

- Characterization of functional devices during operation using PEEM, *SFB annual meeting*, Spa, Belgium (2016)
- Approaches for operando PEEM characterization of resistive switching SrTiO3 devices under applied electric fields, *International LEEM/PEEM 10*, Monterey, USA (2016)

Poster Contributions

- Chemical investigation of buried active layers in resistive switching materials by hard X-ray photoemission electron microscopy (HAXPEEM), *DPG spring meeting* , Dresden, Germany (2014)
- Reversible switching between amorphous and crystalline phases in $Ag_3In_3Sb_{62}Te_{32}$ thin films, *International LEEM/PEEM 09* , Berlin, Germany (2014)
- Electronic structure and phase formation in resistive memory materials, *SFB Meeting*, Aachen, Germany (2015)

Band / Volume 39
Micro-spectroscopic investigation of valence change processes in resistive switching $SrTiO_3$ thin films
A. Köhl (2014), viii, 166 pp
ISBN: 978-3-89336-988-1

Band / Volume 40
Strained Silicon and Silicon-Germanium Nanowire Tunnel FETs and Inverters
S. Richter (2014), iii, 117 pp
ISBN: 978-3-95806-002-9

Band / Volume 41
Integration of Redox-Based Resistive Switching Memory Devices
F. Lentz (2014), i, 166 pp
ISBN: 978-3-95806-019-7

Band / Volume 42
Ladungstransportuntersuchungen an nanofunktionalen Bauelementen mit Diodencharakteristik basierend auf funktionalisierten Nanopartikeln
N. Babajani (2015), iv, 138, XLVII
ISBN: 978-3-95806-026-5

Band / Volume 43
Transport and Noise Properties of Nanostructure Transistors for Biosensor Applications
J. Li (2015), vii, 175 pp
ISBN: 978-3-95806-034-0

Band / Volume 44
Quantitative scanning tunneling spectroscopy of non-polar III-V compound semiconductor surfaces
M. Schnedler (2015), 122 pp
ISBN: 978-3-95806-075-3

Band / Volume 45
Model-based Algorithm Development with Focus on Biosignal Processing
Y. Yao (2015), x, 169 pp
ISBN: 978-3-95806-080-7

Band / Volume 46
Growth and characterization of crystalline rare-earth based thin oxide fims for the application as gate dielectric in nanotechnology
A. B. Schäfer (2015), xiii, 157 pp
ISBN: 978-3-95806-111-8

Band / Volume 47
TEM/STEM Investigations of Phase Change Materials for Non-volatile Memory Applications
M. Bornhöfft (2017), viii, 135 pp
ISBN: 978-3-95806-221-4

Band / Volume 48
Investigation of ternary nitride semiconductor alloys by scanning tunneling microscopy
V. Portz (2017), 140 pp
ISBN: 978-3-95806-232-0

Band / Volume 49
Redox processes and ionic transport in resistive switching binary metal oxides
K. Skaja (2017), VII, 203 pp
ISBN: 978-3-95806-236-8

Band / Volume 50
Investigation of switching mechanism in Ta_2O_5 -based ReRAM devices
K. Wonjoo (2017), iii, 138 pp
ISBN: 978-3-95806-261-0

Band / Volume 51
Development of ReRAM-based Devices for Logic- and Computation-in-Memory Applications
T. Breuer (2017), x, 179 pp
ISBN: 978-3-95806-270-2

Band / Volume 52
Resistive switching memory devices from atomic layer deposited binary and ternary oxide thin films
N. Aslam (2017), X, 172 pp
ISBN: 978-3-95806-274-0

Band / Volume 53
Operando X-ray photoemission electron microscopy (XPEEM) investigations of resistive switching metal-insulator-metal devices
C. J. Schmitz (2017), IX, 153 pp
ISBN: 978-3-95806-283-2

Information
Band / Volume 53
ISBN 978-3-95806-283-2

Mitglied der Helmholtz-Gemeinschaft

JÜLICH
Forschungszentrum